Model-Based Arterial Flow and Stroke Volume Estimation for Hemodynamic Monitoring in a Critical Care Environment.

Joel Cameron Balmer

A thesis presented as partial fulfilment of the

requirements for the degree of Doctor of Philosophy

in

Mechanical Engineering

at the

University of Canterbury

Christchurch, New Zealand

August 2019

“Nine-tenths of education is encouragement.”
– Anatole France

Acknowledgements

There are so many people whose support of me enabled this work and journey to be completed. I would like to begin by generally thanking my supervisory team, Dr Chris Pretty, Professor Geoff Chase, Dr Thomas Desaive and Dr Geoff Shaw. Without your guidance, none of this work would have been possible.

Chris, thank you for always being so approachable. Whenever I was stuck and confused, I always appreciated being able to turn to you without fear of judgement. You were always happy for me to come up to your office and start scribbling on the whiteboard. Often I was so confused it was hard enough for me to even explain my predicament, but you always patiently listened. This patience along with your lighthearted nature was often enough to help me arrive at a solution to the problem. Additionally, I am so glad for your encouragement to embrace the initial steep learning curve when developing new skills, your support in this area enabled me to learn so much more throughout this PhD process than I initially would have expected.

Geoff Chase, thank you for encouraging me to begin this journey back in early 2015. Your willingness to take me on as a PhD student helped me to believe in myself when starting this journey. Considering the sheer number of students you support, I cannot thank you enough for the effort you put into making yourself available to us all. I heard before

starting a PhD that choosing a supervisory team can prove more important than choosing a particular project. After hearing horror stories, I took this advice to heart, and it was a very deliberate decision choosing to come back and see you about the possibility of doing a PhD all those years ago. I can honestly say, I am so glad to have had such fantastic support from you and Chris both, I don't think I could have asked for more invested supervisors. Not only did you provide me with a choice of interesting projects, you also provided me funding and travel opportunities, and an overall profound experience.

To the fellow cardiovascular office crew, Dr Shun Kamoi, Dr Musabbir Khan, Dr Shaun Davidson, Jake Campbell, Liam Murphy and Rachel Smith. What a fantastic team of people to have worked with. In particular I would like to thank Shun, Shaun and Rachel, it has been a privileged to work with you three so closely. I have thoroughly enjoyed bouncing ideas around with your great minds! And to the wider office, even with people starting and finishing, the Centre for Bioengineering has remained a place of great banter and support.

A special mention must go to Alexander Amies. Not only did I begin this PhD journey needing to learn high school level physiology, I also had to navigate learning Python. From the get go you were always willing to step away from your desk to help me debug particularly confusing errors, decipher documentation and discuss Pythonic ways of doing things. You are a fantastic teacher and communicator and it was a privilege to learn from you.

To my Mum and Dad. Thank you so much for the lifelong support you have showed Lauren, Caleb and I. Everything I have achieved in my life, all stems from the phenomenal parenting I was so privileged to experience. In that sense, this thesis is as much your work as it is mine.

Mum, thank you for endlessly believing in me and encouraging me. Your belief in all peoples' potential is infectious and as I have grown up, this has become a core belief of my

own. I am so thankful for this truth you have showed me, and it now informs so much of my world view in such a profoundly positive way. You are my greatest inspiration to forever learn and teach.

Dad, thank you for the years you prioritised our family. The way you somehow balanced work with making time to be at basically every single one of your kids' events, is inspiring but also hard for me to fathom. Your ability to work hard is something I have always tried to mimic, but what inspires me more is the father you were to us as kids. You were fun, funny and enthusiastic, never pressuring us, but always believing and supporting us in anyway you could.

To my brother and sister! You guys are champs, thanks for the love and support that has grown over the years. Thank goodness we didn't stay teenagers forever! I am so glad to have you both in my life, your belief in me over the last four years has been so encouraging. So thanks heaps!

To my best mate Sam, your constant positive affirmation and close support is always felt from afar. To Elliot, thanks for always taking an interest in the dicrotic notch, I appreciated having someone to complain about it too! And to Jolyon, thanks for introducing me to climbing during this PhD process. The days on the rock proved so crucial for my well-being throughout the process.

Finally, to my wife Jemma. Thank you for supporting my decision to return to university and start this PhD. Four years ago seems like such a long time, and what a exciting journey it has been, full of experiences we never would have predicted. Thank you for loving me in my existential angst, for helping me discover who I am and who I want to be. I have loved sharing this journey with you and look forward to whatever is next!

Abstract

Cardiac and circulartory dysfunction are responsible for approximately a third of all intensive care admissions and deaths in New Zealand, reflecting similar statistics globally. Diagnosing and treating cardiovascular disease is made more difficult by the complex and interdependent nature of the circulatory system, where compounding symptomatology makes it difficult to deduce the specific underlying mechanisms triggering the dysfunction. The result is high variability and cost of care, and suboptimal outcomes.

Currently, monitoring a patient's hemodynamic state is undertaken using metrics like arterial and venous pressure, heart rate, gas exchange variables and electrocardiogram (*ECG*). While these metrics are easy to measure, they also change in response to many physiological factors. Thus, they are capable of indicating at a global level potential hemodynamic instability, but less capable of monitoring cardiac performance directly. Direct cardiac performance metrics, such as stroke volume (*SV*)/cardiac output (*CO*), are called for in consensus statements, but are difficult to measure. The trade-off between the level of invasion, accuracy and frequency/duration of monitoring, have not yet been satisfactorily mitigated.

Cardiovascular models provide a potential avenue for clinically applicable, minimally or non-additionally invasive hemodynamic monitoring. Cardiovascular models exploit the

relationship between common clinical metrics, like pressure, and the preferred but more difficult to measure cardiac performance metrics, like *SV*. The performance of a model is dictated by two facets. First, the theory of the model, often a mix of physiology and mathematics, ultimately seeking to provide a simplified/abstracted representation of the cardiovascular system. Second, how the method is actually implemented, including aspects of data acquisition, signal processing and parameter identification. The exact algorithms used in many commercial devices for monitoring *SV*/*CO*, are commercially sensitive and therefore it is often difficult to critique specific aspects of the underlying model approach. However, generally there remains an issue of commercial devices performing well in stable patients, but struggling to capture unstable hemodynamics and stable behaviour thereafter, without re-calibration of the model. Model re-calibration often involves an independent measurement of the target variable, *SV*/*CO*, thus, frequent re-calibration defeats the purpose of continuous monitoring. Equally, there can be a delay in outward indicators of hemodynamic instability, making it difficult to determine when re-calibration is required.

Thus, this thesis sought to develop a clinically applicable, non-additionally invasive cardiovascular model for estimating *SV* to overcome the limitations of similar models, both commercial and in literature. Specifically, the model developed was based on three-element windkessel theory and parameters were identified via pulse contour analysis (PCA). Identifying parameters via PCA meant the model always reflects the *current* patient state, rather than relying solely on model calibration during a prior patient state.

Most models focus on clinically relevant *SV*/*CO* measures, despite three-element windkessel theory primarily describing a relationship between the pressure and flow waveforms. Thus, this thesis developed novel end-systole detection methods to improve PCA-based parameter identification, in clinically applicable arterial pressure waveforms. Having this focus meant the model implementation reflected the model theory well, enabling it to estimate the physiologically accurate flow waveforms that other methods cannot.

Moreover, the results showed failure to derive physiologically accurate profiles meant one or more of the windkessel model assumptions had been violated. Thus, any accurate *SV* estimation from unphysiological flow waveforms, was contingent on the independent *SV* calibration, and the resulting model performance would not reflect its underlying theory. This research clearly delineates when and how these issues arise.

More specifically, a novel aspect of this thesis is its illustration of windkessel model limitations and their impact on PCA-based parameter identification. Specifically, two novel methods of end-systole detection are developed in the thesis, one specifically for detecting dicrotic notches. However, the three-element windkessel is not capable of describing reflected wave phenomena, like the dicrotic notch. Thus, the thesis illustrated the detrimental effects of dicrotic notch presence in the diastolic part of the pressure waveform for PCA parameter identification, as well as developing methods to mitigate its effect. Ultimately, the second novel end-systole detection method enabled the more clinically applicable femoral artery waveform to be used. The results showed its shape, often void of dicrotic notches, was more aligned with windkessel model theory, aiding parameter identification, as well as making the implementation more clinically applicable. Thus, the results showed how the advantages of easy end-systole detection, via the dicrotic notch, can be outweighed by its reduced compatibility with the well-accepted windkessel model and PCA parameter identification.

The analyses conducted in this research used porcine animal trials for the development, testing and validation of methods. Since the overall goal of the thesis was to develop a clinically applicable method for monitoring *SV* during periods of hemodynamic instability, the experimental protocols included clinically relevant disease states and treatments. Bland-Altman analysis showed beat-to-beat *SV* error between the model estimated and aortic flow probe measurement, had limits of agreement (95% of data) of $\pm$32%, where 90% of the data falls within -24.2% and +27.9%. Mean beat-to-beat errors $>$24% were only

associated with severe, rapid onset of a sepsis like response, which would be clinically evident.

The stated results are from the preferred model implementation in the thesis, where the only fixed model parameter was windkessel characteristic impedance ($Z_{c,w}$). Specifically, the static $Z_{c,w}$ value was found via calibration using an independent *SV* measurement, during a period of stable hemodynamics. Two methods of updating $Z_{c,w}$ on a beat-to-beat basis, were also tested, both requiring pulse transit time (*PTT*) monitoring. One method was based on the water hammer equation, while the other was a hybrid approach, using the Bramwell-Hill equation and PCA. However, these dynamic approaches to $Z_{c,w}$ identification did not cause significant improvement in the results. Thus, the additional patient burden of monitoring *PTT* on a beat-to-beat basis could not be justified.

While it is difficult to compare the model implementation presented in this thesis to commercial devices tested on different data sets, it appears the results represent a significant improvement over existing methods. In particular, the model developed in this thesis provides a physiological flow waveform in conjunction with beat-to-beat *SV*, where the former enables quantitative and qualitative verification of successful parameter identification, instilling confidence in the subsequent *SV* estimate.

Finally, successful clinical implementation of the model would significantly impact intensive care unit (ICU) practice. The patient specific manner in which the model is implemented, could enable personalised titrating/optimisation of care to quantitatively estimate cardiac function on a beat-to-beat basis, something which is not yet possible in a clinical environment.

Deputy Vice-Chancellor's Office
Postgraduate Research Office

UNIVERSITY OF CANTERBURY
Te Whare Wānanga o Waitaha
CHRISTCHURCH NEW ZEALAND

Co-Authorship Form

This form is to accompany the submission of any thesis that contains research reported in co-authored work that has been published, accepted for publication, or submitted for publication. A copy of this form should be included for each co-authored work that is included in the thesis. Completed forms should be included at the front (after the thesis abstract) of each copy of the thesis submitted for examination and library deposit.

Please indicate the chapter/section/pages of this thesis that are extracted from co-authored work and provide details of the publication or submission from which the extract comes:

Section in Thesis: Section 6.2

Publication Type: Journal Paper

Publication: "Improved pressure contour analysis for estimating cardiac stroke volume using pulse wave velocity measurement" BioMedical Engineering Online

Please detail the nature and extent (%) of contribution by the candidate:

10% candidate contribution

The candidate provided proof-reading of the original publication and detailed feedback on the clarity of the publications methods and results. Thus, as stated in the thesis, Section 6.2 covers the Kamoi model, having cited and credited the first author Shun Kamoi.

The remainder of Chapter 6 from the thesis, mainly covering the limitations of the Kamoi model, are the candidates own work and is not in the above publication, nor is it published elsewhere.

Certification by Co-authors:

If there is more than one co-author then a single co-author can sign on behalf of all

The undersigned certifies that:

- The above statement correctly reflects the nature and extent of the PhD candidate's contribution to this co-authored work
- In cases where the candidate was the lead author of the co-authored work he or she wrote the text

Name: Chris Pretty Signature: Chris Pretty (on behalf of all co-authors) Date: 28 August 2019

Deputy Vice-Chancellor's Office
Postgraduate Research Office

UNIVERSITY OF CANTERBURY
Te Whare Wānanga o Waitaha
CHRISTCHURCH NEW ZEALAND

Co-Authorship Form

This form is to accompany the submission of any thesis that contains research reported in co-authored work that has been published, accepted for publication, or submitted for publication. A copy of this form should be included for each co-authored work that is included in the thesis. Completed forms should be included at the front (after the thesis abstract) of each copy of the thesis submitted for examination and library deposit.

Please indicate the chapter/section/pages of this thesis that are extracted from co-authored work and provide details of the publication or submission from which the extract comes:

Chapter in Thesis: Chapter 7

Publication Type: Conference Paper

Publication: "Electrocardiogram R-wave is an unreliable indicator of pulse wave initialization." 20th World Congress of the International Federation of Automatic Control, Toulouse, France, 9th–14th July 2017

Please detail the nature and extent (%) of contribution by the candidate:

90% candidate contribution

The candidate developed the hypothesis, necessary algorithms for analysis, conducted the analysis and wrote the article.

Co-authors contributions varied from contributing toward the formulation of the hypothesis at a high level, acquiring the raw data used in the analysis, supporting the candidate in the form of proof reading of the article, and providing feedback on the clarity of the candidate's results presentation and discussion.

Certification by Co-authors:

If there is more than one co-author then a single co-author can sign on behalf of all

The undersigned certifies that:

- The above statement correctly reflects the nature and extent of the PhD candidate's contribution to this co-authored work
- In cases where the candidate was the lead author of the co-authored work he or she wrote the text

Name: Chris Pretty Signature: Chris Pretty (on behalf of all co-authors) Date: 28 August 2019

Deputy Vice-Chancellor's Office
Postgraduate Research Office

UNIVERSITY OF CANTERBURY
Te Whare Wānanga o Waitaha
CHRISTCHURCH NEW ZEALAND

Co-Authorship Form

This form is to accompany the submission of any thesis that contains research reported in co-authored work that has been published, accepted for publication, or submitted for publication. A copy of this form should be included for each co-authored work that is included in the thesis. Completed forms should be included at the front (after the thesis abstract) of each copy of the thesis submitted for examination and library deposit.

Please indicate the chapter/section/pages of this thesis that are extracted from co-authored work and provide details of the publication or submission from which the extract comes:

Section/Chapter in Thesis: Section 5.4.3 and Chapter 7

Publication Type: Journal Article

Publication: "Pre-ejection period, the reason why the electrocardiogram Q-wave is an unreliable indicator of pulse wave initialization" Physiological Measurement 2018

Please detail the nature and extent (%) of contribution by the candidate:

90% candidate contribution

The candidate developed the hypothesis, necessary algorithms for analysis, conducted the analysis and wrote the article.

Co-authors contributions varied from contributing toward the formulation of the hypothesis at a high level, acquiring the raw data used in the analysis, supporting the candidate in the form of proof reading of the article, and providing feedback on the clarity of the candidate's results presentation and discussion.

Certification by Co-authors:

If there is more than one co-author then a single co-author can sign on behalf of all

The undersigned certifies that:

- The above statement correctly reflects the nature and extent of the PhD candidate's contribution to this co-authored work
- In cases where the candidate was the lead author of the co-authored work he or she wrote the text

Name: Chris Pretty Signature: Chris Pretty (on behalf of all co-authors) Date: *28 August 2019*

Deputy Vice-Chancellor's Office
Postgraduate Research Office

UNIVERSITY OF CANTERBURY
Te Whare Wānanga o Waitaha
CHRISTCHURCH NEW ZEALAND

Co-Authorship Form

This form is to accompany the submission of any thesis that contains research reported in co-authored work that has been published, accepted for publication, or submitted for publication. A copy of this form should be included for each co-authored work that is included in the thesis. Completed forms should be included at the front (after the thesis abstract) of each copy of the thesis submitted for examination and library deposit.

Please indicate the chapter/section/pages of this thesis that are extracted from co-authored work and provide details of the publication or submission from which the extract comes:

Chapter in Thesis: Chapter 8

Publication Type: Conference Paper

Publication: "Accurate dicrotic notch detection using adaptive shear transforms" 10th IFAC Symposium on Biological and Medical Systems Sao Paulo, Brazil, 3rd – 5th September 2018

Please detail the nature and extent (%) of contribution by the candidate:

90% candidate contribution

The candidate developed the hypothesis, necessary algorithms for analysis, conducted the analysis and wrote the article.

Co-authors contributions varied from providing the raw data necessary for the analysis, proof reading of the article, and providing feedback on the clarity of the candidate's results presentation and discussion.

Certification by Co-authors:

If there is more than one co-author then a single co-author can sign on behalf of all

The undersigned certifies that:

- The above statement correctly reflects the nature and extent of the PhD candidate's contribution to this co-authored work
- In cases where the candidate was the lead author of the co-authored work he or she wrote the text

Name: Chris Pretty Signature: Chris Pretty (on behalf of all co-authors) Date: *28 August 2019*

Deputy Vice-Chancellor's Office
Postgraduate Research Office

UNIVERSITY OF CANTERBURY
Te Whare Wānanga o Waitaha
CHRISTCHURCH NEW ZEALAND

Co-Authorship Form

This form is to accompany the submission of any thesis that contains research reported in co-authored work that has been published, accepted for publication, or submitted for publication. A copy of this form should be included for each co-authored work that is included in the thesis. Completed forms should be included at the front (after the thesis abstract) of each copy of the thesis submitted for examination and library deposit.

Please indicate the chapter/section/pages of this thesis that are extracted from co-authored work and provide details of the publication or submission from which the extract comes:

Chapter in Thesis: Chapter 9

Publication Type: Conference Paper

Publication: "Effect of arterial pressure measurement location on pulse contour stroke volume estimation , during a rapid change in hemodynamic state" 10th IFAC Symposium on Biological and Medical Systems Sao Paulo, Brazil, 3rd – 5th September 2018

Please detail the nature and extent (%) of contribution by the candidate:

90% candidate contribution

Regarding the publication, the candidate developed the hypothesis, necessary signal processing algorithms for analysis, conducted the analysis and wrote the article. The candidate did not develop the initial windkessel model implementation in the publication. As per Thesis Chapters 6 and 9, and publications citations, the credit for the Kamoi model implementation belongs to Shun Kamoi.

However, the identification of the Kamoi model limitations in the Chapters 6 and 9 are almost entirely the candidates work. Moreover, the publication stated above does not contain any content shown in the thesis, but did loosely inform/lead to the analysis presented in the Chapter 9, as stated in Section 10.1.

Co-authors contributions to the publication varied from providing the raw data necessary for the analysis, proof reading of the article, and providing feedback on the clarity of the candidate's results presentation and discussion.

Certification by Co-authors:

If there is more than one co-author then a single co-author can sign on behalf of all

The undersigned certifies that:

- The above statement correctly reflects the nature and extent of the PhD candidate's contribution to this co-authored work
- In cases where the candidate was the lead author of the co-authored work he or she wrote the text

Name: Chris Pretty Signature: Chris Pretty (on behalf of all co-authors) Date: 28 August 2019

Deputy Vice-Chancellor's Office
Postgraduate Research Office

UNIVERSITY OF CANTERBURY
Te Whare Wānanga o Waitaha
CHRISTCHURCH NEW ZEALAND

Co-Authorship Form

This form is to accompany the submission of any thesis that contains research reported in co-authored work that has been published, accepted for publication, or submitted for publication. A copy of this form should be included for each co-authored work that is included in the thesis. Completed forms should be included at the front (after the thesis abstract) of each copy of the thesis submitted for examination and library deposit.

Please indicate the chapter/section/pages of this thesis that are extracted from co-authored work and provide details of the publication or submission from which the extract comes:

Chapter in Thesis: Chapter 10

Publication Type: Journal Paper (in review)

Publication: "Accurate end systole detection in dicrotic notch-less arterial pressure waveforms"

Please detail the nature and extent (%) of contribution by the candidate:

90% candidate contribution

The candidate developed the hypothesis, necessary algorithms for analysis, conducted the analysis and wrote the article.

Co-authors contributions varied from providing the raw data necessary for the analysis, proof reading of the article, and providing feedback on the clarity of the candidate's results presentation and discussion.

Certification by Co-authors:

If there is more than one co-author then a single co-author can sign on behalf of all

The undersigned certifies that:

- The above statement correctly reflects the nature and extent of the PhD candidate's contribution to this co-authored work
- In cases where the candidate was the lead author of the co-authored work he or she wrote the text

Name: Chris Pretty Signature: Chris Pretty (on behalf of all co-authors) Date: 28 August 2019

Deputy Vice-Chancellor's Office
Postgraduate Research Office

UNIVERSITY OF CANTERBURY
Te Whare Wānanga o Waitaha
CHRISTCHURCH NEW ZEALAND

Co-Authorship Form

This form is to accompany the submission of any thesis that contains research reported in co-authored work that has been published, accepted for publication, or submitted for publication. A copy of this form should be included for each co-authored work that is included in the thesis. Completed forms should be included at the front (after the thesis abstract) of each copy of the thesis submitted for examination and library deposit.

Please indicate the chapter/section/pages of this thesis that are extracted from co-authored work and provide details of the publication or submission from which the extract comes:

Chapter in Thesis: Chapters 4 & 11

Publication Type: Journal Paper (in review)

Publication: "Clinically applicable model-based method, for physiologically accurate flow waveform and stroke volume estimation"

Please detail the nature and extent (%) of contribution by the candidate:

90% candidate contribution

The candidate developed the hypothesis, necessary algorithms for analysis, conducted the analysis and wrote the article. The exception being, the three-element windkessel model theory, outlined in Chapter 4 and used in Chapter 11 of the thesis. The original windkessel theory was described by the likes of O Frank, N Westerhof, as credited in the thesis and publication. However, the explanations of the models and the specifics of its implementation, are the candidates own work.

Co-authors contributions varied from providing the raw data necessary for the analysis, proof reading of the article, and providing feedback on the clarity of the candidate's results presentation and discussion.

Certification by Co-authors:

If there is more than one co-author then a single co-author can sign on behalf of all

The undersigned certifies that:

- The above statement correctly reflects the nature and extent of the PhD candidate's contribution to this co-authored work
- In cases where the candidate was the lead author of the co-authored work he or she wrote the text

Name: Chris Pretty Signature: Chris Pretty (on behalf of all co-authors) Date: 28 August 2019

Publications

Over the course of this research, a number of papers have been published. The research demonstrated in these papers is based on the work presented in this thesis.

Journal Papers

- **Balmer J**, Pretty C, Davidson S, Desaive T, Kamoi S, Pironet A, Morimont P, Janssen N, Lambermont B, Shaw GM, Chase JG. “Pre-ejection period, the reason why the electrocardiogram Q-wave is an unreliable indicator of pulse wave initialization.” *Physiological Measurement* 2018.

- **Balmer J**, Smith R, Pretty C, Desaive T, Shaw GM, Chase JG . “Accurate end systole detection in dicrotic notch-less arterial pressure waveforms.” [Under Review] 2019

- **Balmer J**, Pretty C, Davidson S, Mehta-Wilson T, Desaive T, Smith R, Shaw GM, Chase JG. “Clinically applicable model-based method, for physiologically accurate flow waveform and stroke volume estimation.” [Under Review] 2019

Conference Papers

- **Balmer J**, Pretty C, Kamoi S, Davidson S, Pironet A, Desaive T, Shaw GM, Chase JG. "Electrocardiogram R-wave is an unreliable indicator of pulse wave initialization." *IFAC-PapersOnLine, 20th World Congress of the International Federation of Automatic Control*, Toulouse, France, 9th–14th July 2017.

- **Balmer J**, Pretty C, Amies A, Desaive T, Chase JG. "Accurate dicrotic notch detection using adaptive shear transforms." *10th IFAC Symposium on Biological and Medical Systems* São Paulo, Brazil, 3rd – 5th September 2018.

- **Balmer J**, Pretty C, Davidson S, Desaive T, Habran S, Chase JG. "Effect of arterial pressure measurement location on pulse contour stroke volume estimation, during a rapid change in hemodynamic state." *10th IFAC Symposium on Biological and Medical Systems*, São Paulo, Brazil, 3rd–5th September 2018.

Contents

List of Figures

List of Tables

List of Abbreviations

$\boldsymbol{A}$ cross-sectional area

$\boldsymbol{A_{cal}}$ calibrated cross-sectional area

$\boldsymbol{C}$ volumetric compliance

$\boldsymbol{C_A}$ cross-sectional area compliance or compliance per unit length

CDF cumulative distribution function

$\boldsymbol{CO}$ cardiac output

$\boldsymbol{CO_{est}}$ estimated cardiac output

$\boldsymbol{CO_{mea}}$ measured cardiac output

CVD cardiovascular disease

$\frac{d^2P}{dt^2}$ second derivative of pressure with respect to time

$\frac{dP}{dt}$ first derivative of pressure with respect to time

$\boldsymbol{dt}$ sampling interval

ECG electrocardiogram

EDAP end-diastolic aortic pressure

EDPVR end-diastolic pressure volume relationship

EDVP end-diastolic ventricular pressure

EDVV end-diastolic ventricular volume

ESAP end-systolic aortic pressure

ESICM European Society of Intensive Care Medicine

ESPVR end-systolic pressure volume relationship

ESVP end-systolic ventricular pressure

ESVV end-systolic ventricular volume

f_c cutoff frequency

f_{tb} transition band width

FIR finite impulse response

HR heart rate

ICU intensive care unit

L_c characteristic length

MAP mean arterial pressure

MRI magnetic resonance imaging

N_f filtering length, also known as the number of filter coefficients

ODE ordinary differential equation

P_{ao} aortic arch/proximal aortic pressure

P_{cvp} central venous pressure

P_{ex} excess pressure

P_{fem} femoral pressure

P_{max} maximum pressure of a beat

P_{mc} mean circulatory pressure

P_{mea} measured pressure

P_{min} minimum pressure of a beat

P_{res} reservoir pressure

P_{vent} left ventricular pressure

PAC pulmonary artery catheter

PAT pulse arrival time

PCA pulse contour analysis

PDT pulse delay time

PEEP positive end-expiratory pressure

PEP pre-ejection period

PPG photoplethysmogram

PTT pulse transit time

PWV pulse wave velocity

$\boldsymbol{Q_{ao}}$ proximal aortic blood flow

$\boldsymbol{Q_C}$ blood flow to the capacitor element of the windkessel

$\boldsymbol{Q_{est}}$ estimated blood flow

$\boldsymbol{Q_{in}}$ blood flow, modelled as flow into the windkessel/reservoir

$\boldsymbol{Q_{out}}$ blood flow out the windkessel/reservoir

$\boldsymbol{Q_R}$ blood flow across the resistive element of the windkessel

$\boldsymbol{Q_{V_{vent}}}$ aortic blood flow estimation via V_{vent}

$\boldsymbol{R}$ peripheral resistance

$\boldsymbol{r^2}$ coefficient of determination

RM recruitment manoeuvre

RWA reservoir wave approach

$\boldsymbol{SV}$ stroke volume

$\boldsymbol{SV_{cal}}$ calibration stroke volume measurement

$\boldsymbol{SV_{err}}$ stroke volume estimation error

$\boldsymbol{SV_{est}}$ estimated stroke volume

$\boldsymbol{SV_{mea}}$ measured stroke volume

$\boldsymbol{SV_{\%err}}$ stroke volume estimation error as a percentage of SV_{mea}

$\boldsymbol{t_0}$ time of start-systole

$\boldsymbol{t_{dr}}$ start of diastolic relaxation/decay

$\boldsymbol{t_{es}}$ time of end-systole

$\boldsymbol{t_{es,d^2P/dt^2}}$ weighted second derivative based estimate of the time of end-systole

$\boldsymbol{t_{es,dic}}$ time of a dicrotic notch, marking end-systole

$\boldsymbol{t_{es,dP/dt}}$ weighted first derivative based estimate of the time of end-systole

$t_{es,PTT}$ PTT based estimate of the time of end-systole

$t_{es,shear}$ estimated time of end-systole based on the minimum of a shear transform

$t_{P_{max}}$ time of maximum pressure

T_{sys} systolic duration

$T_{sys,mea}$ measured systolic duration

$T_{sys,d^2P/dt^2}$ systolic duration measured to $t_{es,d^2P/dt^2}$

$T_{sys,dP/dt}$ systolic duration measured to $t_{es,dP/dt}$

$T_{sys,HR}$ systolic duration estimated based on heart rate

$T_{sys,PTT}$ systolic duration measured to $t_{es,PTT}$

$T_{sys,shear}$ systolic duration measured to $t_{es,shear}$

$t_{w_{max}}$ time of maximum weighting

V_{res} reservoir/windkessel volume

V_{vent} left ventricular volume

VCO vena cava occlusion

$Z_{bh,cal}$ calibrated characteristic impedance updated via the Bramwell-Hill equation

Z_c (general) characteristic impedance

$Z_{c,ao}$ aortic characteristic impedance

$Z_{c,cal}$ control stage calibrated characteristic impedance

$Z_{c,ideal}$ ideal $Z_{c,w}$, back calculated from SV_{mea} and P_{ex}

$Z_{c,w}$ windkessel characteristic impedance

$Z_{wh,cal}$ calibrated characteristic impedance updated via the water hammer equation

CHAPTER 1

Introduction

1.1 Introduction

This chapter outlines the main motivation and goals for the thesis, as well as its novel aspects. Thus, some basic knowledge of cardiovascular anatomy and function will be required to understand the context of this chapter. If the reader feels they lack the necessary background knowledge, they may find it helpful to first refer to Chapter 2 Section 2.2.

1.2 Motivation

Cardiovascular disease (CVD), comprising particularly heart, stroke and blood vessel disease, accounts for ∼30% of all deaths in New Zealand (Ministry of Health, 2013) and 24.6% of intensive care unit (ICU) admissions (Kasza et al., 2013). Ischaemic heart disease alone is the second leading cause of death in New Zealand, killing 5534 people in 2011, or 18.3% of all deaths that year (Ministry of Health, 2013). The highest leading cause of death includes all form of cancer (Ministry of Health, 2013).

Cardiovascular dysfunction is not only a New Zealand issue. In the United States 31.3% of deaths were attributed to cardiovascular disease (Mozaffarian et al., 2015), and accord-

ing to the European Society of Intensive Care Medicine (ESICM), up to a third of people admitted to the ICU suffer from some form of *circulatory shock* (Cecconi et al., 2014). Circulatory shock is defined as a generalised form of acute circulatory failure associated with inadequate blood flow, resulting in inadequate tissue oxygenation (Cecconi et al., 2014).

The type of shock a patient is suffering depends on the underlying cardiovascular dysfunction (Cecconi et al., 2014), but ultimately results in oxygen demand exceeding supply to one or more of the organs:

- ***Hypovolemic***: also known as *low volume*, where inadequate blood volume leads to inadequate blood flow.
- ***Cardiogenic***: where inadequate heart/cardiac pumping performance provided by the ventricles of the heart leads to inadequate blood circulation.
- ***Obstructive***: where obstructions of the large blood vessels leads to inadequate blood flow down to peripheral vessels.
- ***Distributive***: where abnormal blood distribution in the peripheral vessels leads to inadequate blood and oxygen supply to certain organs.

For example, *septic shock*, the most common form of distributive shock, is where an infection leads to *sepsis*, where cardiac and circulatory changes result in abnormal blood flow, low blood pressure and low oxygen perfusion in tissues (Silverman and Wang, 2005; Merx and Weber, 2010). Septic shock has also been shown to reduce oxygen extraction of the coronary (heart's) circulation (Cunnion et al., 1986), and a reduction in *stroke volume* (*SV*), the volume of blood ejected by the heart per beat (Young, 2004; Merx and Weber, 2010). With sepsis already inhibiting normal circulatory function, this reduction in the heart's ability to use the oxygen supplied to it, combined with less blood being ejected per beat, leads to an increased likelihood of mortality. In addition since the heart's main function is to circulate blood, any impairment in this function often causes dysfunction for other organs, due to poor oxygen distribution (Guyton and Hall, 2011), which cascade in turn to amplify these issues.

1.3 ICU Monitoring and Management Strategies

Monitoring cardiac performance of patients in the intensive care unit is commonly undertaken by comparing arterial pressure, central venous pressure, heart rate, electrocardiogram (ECG) and gas exchange variables to physiological norms (Segal et al., 2002; Cousins and O'Donnell, 2004; Dickstein, 2005). However, variations in these measures can be caused by numerous changes in cardiovascular function, particularly in elderly patients who often have multiple medical issues (Dickstein, 2005). This variability creates uncertainty, and can make decisions on diagnosis and treatment more difficult for clinicians. In addition, the measures are imperfect surrogates for more desirable, direct measures of cardiac function, such as *SV*/*cardiac output* (*CO*), where *CO* is the flow of blood out of the heart over time, rather than per beat:

$$CO = \overline{SV} \times HR \tag{1.1}$$

Where $\overline{SV}$ is the average stroke volume over the time interval of the heart rate (*HR*). Usually *HR* is measured in beats per minute, leading to *CO* in litres per minute. Therefore, *SV* represents the superior metric when measured *beat-to-beat*, compared with the $\overline{SV}$ of *CO*.

CO/*SV* monitoring helps define the initial hemodynamic state of a patient, measure the response to therapies and monitor changes in disease progression (Gust et al., 1998; Tibby, 2003; Reuter et al., 2003; Luecke and Pelosi, 2005; Montenij et al., 2011; Cecconi et al., 2014). More specifically, ESICM stated that evaluation *and* monitoring of *CO and SV*, is essential for determining the type of circulatory shock a patient is suffering and its degree of severity (Cecconi et al., 2014). As such, the task force went on to recommend measurement of *SV* and *CO* to evaluate the *response to fluid* and *inotrope* therapies, which are core treatment modalities (Cecconi et al., 2014). For more on these therapies see Chapter 5, Section 5.2.1 and 5.2.2. However, in a clinical environment, accurately measuring *SV*/*CO* is difficult, and monitoring it even more so.

1.3.1 Stroke Volume and Cardiac Output Measurement Overview

SV/*CO* measurement techniques are covered briefly here as part of articulating the novelty of this thesis. The methods are covered in more detail in Chapter 3 and 4.

SV measures fall into two broad categories: *discrete* and *continuous*. A discrete measurement technique is limited to one-off or short-term *SV* estimation. Examples include *indicator dilution methods*, where a bolus of fluid is introduced to the blood and the resultant mixture downstream can provide a *SV* estimate. *Trans-esophageal doppler ultrasound* is another example, which is limited by the requirement of a trained operator holding the correct positioning of the ultrasound probe in the esophagus (Dark and Singer, 2004; Marik, 2013). Overall, discrete measures are less suitable for monitoring patients who are likely to experience sudden and unpredictable hemodynamic changes, which these measures will often miss.

Direct continuous methods are those that can *monitor SV* over time, at frequent sampling intervals. Examples include, *aortic flow probes* and *ventricular admittance catheters*. An aortic flow probe is placed on the aorta and measures flow velocity, computed to flow rate based on the cross-sectional area of the aorta. Ventricular admittance catheters are placed inside a ventricle of the heart and measure its changing blood volume. The highly invasive nature of these two examples limit them to experimental settings.

Cardiovascular models use commonly monitored clinical metrics and mathematical relationships to estimate physiological properties that are otherwise difficult to measure, including *SV*. In this way, they reduce invasion, but are no longer direct measurements of the variable of interest. Thus, the accuracy of models depends on the assumptions made in their theoretical formulation, *but also* on their implementations.

Some of the commercially available devices to indirectly monitor *SV* perform well in stable patients, but can fail to capture changes in *SV* during and after changes in hemodynamic state, unless a recalibration is performed (Goedje et al., 1999; Rödig et al., 1999; Gödje et al.,

2001; Hadian et al., 2010; Marik, 2013). Since unstable patients are arguably those who might benefit most from continuous *SV* monitoring, it is critical a model capture changing hemodynamics. There is currently significant room for improvement in this space.

1.4 Goals of this Thesis

This research aims to fulfil the stated goals of the ESICM, in having a low to non-additionally invasive, clinically applicable technique to monitor *left ventricular SV*. In addition, it aims to improve upon existing commercial devices and experimental methods by not only providing *SV* and *CO*, but provide a physiologically accurate aortic flow waveform, similar to the ubiquity of pressure waveform in critical care. Without the waveform, it is difficult for an interpreter to determine the validity of a single value of *SV* or *CO* from a model. The waveform provides an indication as to whether the model parameter identification is reasonable, thus invoking confidence in the resulting *SV*/*CO* estimate. In doing so it would provide clinicians with a tool to improve diagnostic and therapeutic decision-making, thereby improving patient outcomes. In addition, the method would not require proprietary external devices, relying only on common clinical metrics. This non-proprietary approach should improve the clinical applicability of the method by removing cost limitations, and the non-additionally invasive aspect should minimises additional clinician or nurse workload and patient risk.

To achieve these aims the thesis will improve upon an existing *pulse contour analysis* (PCA) method for estimating *SV*. More specifically, it will:

1. Resolve outstanding issues around the model's need for pulse wave velocity (*PWV*) (definition in Section 2.5), a metric that can be measured in a clinical environment, but is not commonly monitored.

2. Resolve the parameter identification sensitivity resulting in the prediction of unphysiological flow profiles, which are then used to estimate a potentially less accurate *SV*.

3. Establish the impact of pressure waveform measurement location on model implementation and performance.

1.4.1 Novelty of this Thesis

This thesis ultimately shows that superior start- and end-systole detection leads to improved parameter identification, significantly improving arterial flow waveform tracking, and thus *SV* estimation over existing models. The model is tested on experimental data captured during severe hemodynamic instability including circulatory failure, and is shown to monitor and track changes in *SV* during transient behaviour, without needing recalibration.

1.5 Chapter Overview

This thesis is broadly structured in the following chapters:

- Chapter 2 outlines the physiological principles and nomenclature necessary to understand the remaining chapters. It is often referred back to throughout the thesis, along with the thesis goals (Section 1.4), in order to reinforce the relevance of later chapter's analysis and discussion.

- Chapter 3 covers the current common methods by which *SV* can be measured and monitored. This was briefly covered in Section 1.3.1, but Chapter 3 will give more specific detail and qualitative comparison of methods.

- Chapter 4 covers the development of cardiovascular models that aim to simplify the complex anatomy and function covered in Chapter 2. This chapter can be seen as the foundational work, upon which the author will build. It outlines the successes but also the shortcomings of previous models, with respect to Chapters 1 and 2.

- Chapter 5 covers the experimental protocols, data and the initial post-processing that enabled the more detailed analyses of later chapters.

- Chapter 6 covers the cardiovascular model developed by Kamoi et al. (2017), which the author was involved with in the late stages of development. Having identified the Kamoi models limitations, it acts as the starting point for the author's own work.

- Chapter 7 covers the development and testing of a novel *PWV* measurement and monitoring technique, one that was hoped would improve the clinical applicability of the original Kamoi et al. (2017) method.

- Chapter 8 develops an improved dicrotic notch detection algorithm. The algorithm was developed to improve end-systole detection in the Kamoi model of Chapter 6.

- Chapter 9 implements the improved end-systole detection of Chapter 8 with the Kamoi model of Chapter 6. The improved end-systole detection uncovers new aspects of poor Kamoi model implementation. Specifically, the issues found are a combination of poor parameter identification methodology and a function of dicrotic notch presence in proximal arterial pressure waveforms.

- Chapter 10 will cover another novel end-systole detection algorithm, designed to identify end-systole in dicrotic notch-less pressure waveforms, overcoming the limitations outlined in Chapter 9. Thus, the development was specifically to serve the *SV* estimation of a three-element windkessel model, but end-systole detection is not limited to that singular use.

- Chapter 11 will the cover the latest implementation of the developed model, built from the knowledge gained in Chapters 6, 7, 9 and achieving the goals set out in Section 1.4.

- Chapter 12 will then explore the re-introduction of *PWV* on the more foundationally-sound model developed in Chapter 11, and assess whether *PWV* improves *SV*.

- Chapter 13 will conclude the thesis, summarising what the thesis aims were, which were achieved, which were not and why.

- Chapter 14 covers the future work in light of the conclusions in Chapter 13.

1.6 Summary

This chapter provides the motivation for this thesis. Namely, the desire from clinicians for clinically applicable methods of continuously monitoring *SV* and/or *CO*, to improve detection and assessment of cardiovascular dysfunction, and as a means of assessing intervention success. It briefly covers the current techniques for *SV* measurement and their shortcomings, something that will be covered further in Chapters 3 and 4. Finally it covers the goals of this thesis, to improve on existing PCA method's shortcomings, creating a method that more closely meets the needs of clinicians in a critical care environment.

CHAPTER 2

Background Physiology

2.1 Introduction

2.2 Cardiovascular Anatomy

The main function of the cardiovascular system is to transport blood around the body, supplying nutrients and oxygen, and removing waste. It consists of the heart, which contains two halves, known simply as the *left* and *right heart* respectively. Each half of the heart pumps blood around two circulations. The right heart pumps partially de-oxygenated blood to the lungs to be oxygenated, before returning to the left heart, and this is known as the *pulmonary circulation*. The left heart pumps the oxygenated blood through the *systemic circulation*, perfusing all tissue with oxygen, after which the partially de-oxygenated blood returns to the right heart. These three components are shown in Figure 2.1.

2.2.1 Heart

The heart is a muscle, known as the myocardium, which applies pressure to the blood as it contracts, reducing in volume to ejecting the blood within. It is made up of four chambers, an *atrium* and a *ventricle* pair for each of the left and right hearts, separated by the *septum*

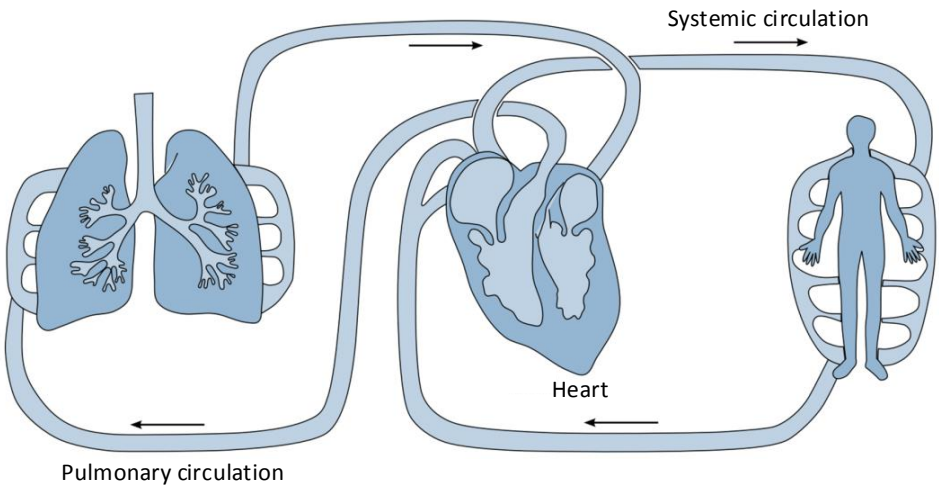

Figure 2.1: Overview of the three components of the cardiovascular system, the heart and the two circulations, systemic and pulmonary (Paeme, 2013).

as shown in Figure 2.2. The atria are priming pumps, contracting to force a final volume of blood into the ventricles under pressure. About a sixth of a second after atrial contraction, the ventricles contract, generating the main force of the heart (Guyton and Hall, 2011). The amount of blood ejected by a single ventricle's contraction is known as the stroke volume (*SV*).

Atrioventricular valves prevent backflow of blood from ventricle to atria. The right and left heart atrioventricular valves are the *tricuspid* and *mitral* respectively. The pulmonary valve prevents backflow of blood from the pulmonary system into the right ventricle. The aortic valve prevents backflow from the systemic system to the left ventricle. The valves are also shown in Figure 2.2.

2.2.2 Blood Vessels

Arteries

The blood exits the right and left ventricles into the pulmonary and aortic *arteries* respectively, as shown in Figure 2.2. Blood in the arteries is characterised as being under high pressure and moving away from the heart. The large arteries, and particularly the aorta, are also highly *compliant*, meaning they stretch, increasing in cross-sectional area when under pressure, according to Equation 2.1 (Westerhof et al., 2009; Townsend et al., 2015).

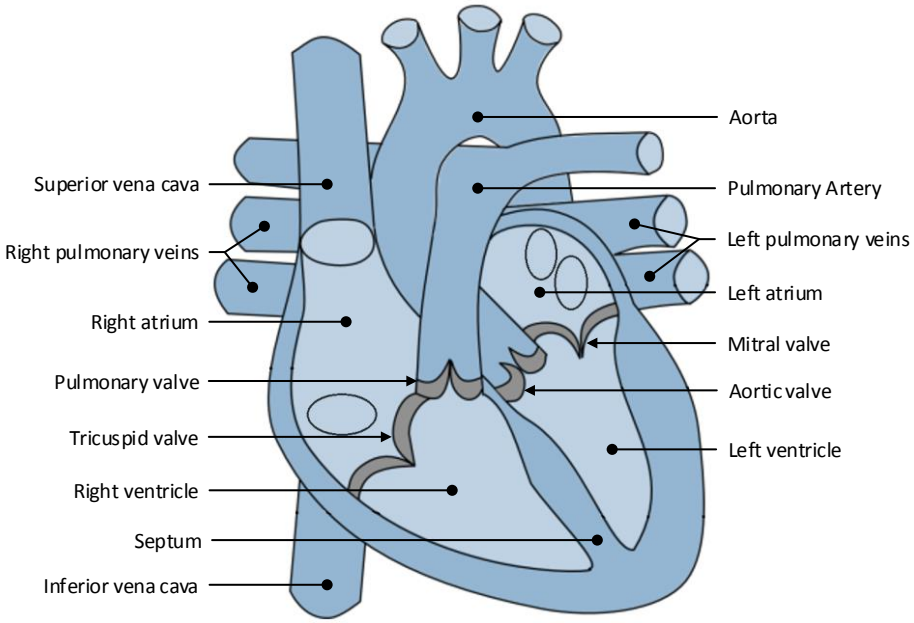

Figure 2.2: Anatomy of the heart. Showing the four heart chambers, two atria and two ventricles, the valves and major arteries and veins. Modified from (Paeme, 2013)

$$C = \frac{\Delta V}{\Delta P} = \frac{dV}{dP} \tag{2.1}$$

Where V and P are volume and pressure of a vessel, and C is the compliance. The expansion occurs during systole, when the flow rate ejected from the heart exceeds the flow to the periphery. Thus, a proportion of the SV is, in a sense, *stored*, its kinetic energy converted to potential energy in the elastic nature of the large arteries (London and Pannier, 2010). As ventricular ejection slows and eventually ends, the arterial walls begin to passively relax. This relaxation returns the wall's stored potential energy to the stored blood volume, as kinetic energy, maintaining flow to the periphery during diastole. Thus, arterial compliance enables important physiological functions, smoothing out discrete ventricular ejection to a more semi-continuous flow to the periphery, and damping the pulsatile pressure produced by the heart's intermittent ejection (Frank, 1889; Westerhof et al., 1969; Oppenheim and Sittig, 1995; London and Pannier, 2010; Townsend et al., 2015). Additionally, the distension helps minimise *resistance* to flow, with only a 2 – 4 mmHg mean pressure

drop from the aorta to the peripheral arteries (Westerhof et al., 1969; London and Pannier, 2010; Guyton and Hall, 2011).

Although Equation 2.1 is linear, there is a limit to how much the arteries can stretch. In reality, at high pressures or volumes, the arteries will begin to stiffen (reduced compliance), meaning successive increases in volume will accompany significant increases in pressure (Segers et al., 2015). Generally however, Equation 2.1 suffices, assuming a constant compliance over normal physiological ranges of pressure and volume.

As the blood moves further from the heart, it distributes down consecutively smaller and stiffer arteries, reaching the relatively low compliant *arterioles* (Nichols, 2005; Nichols et al., 2011; Townsend et al., 2015). Resistance to flow in the arterioles accounts for the majority of the total peripheral resistance within the circulatory system (London and Pannier, 2010; Townsend et al., 2015). As a result, there is a gradual modifying of the measured pressure waveform along the arterial tree, with the most significant decrease in blood pressure across the arterioles, as shown in Figure 2.3 (Westerhof et al., 2010a; Guyton and Hall, 2011).

The main large arteries of the systemic circulation are shown in Figure 2.4. This diagram is by no means exhaustive, but includes the arteries referred to in later analyses. Overall, arteries are the network ensuring blood is well-distributed throughout the body.

Capillaries

Successively smaller arterioles lead to capillaries, where oxygen exchange occurs. In the lungs, these capillaries are where oxygen perfuses into the blood, while in the systemic circulation, capillaries are where oxygen perfuses out to tissues. The delicate nature of these small vessels is why the balance of compliance and resistance upstream in the arteries is of physiological importance, ensuring adequate blood supply at the right pressure for perfusion.

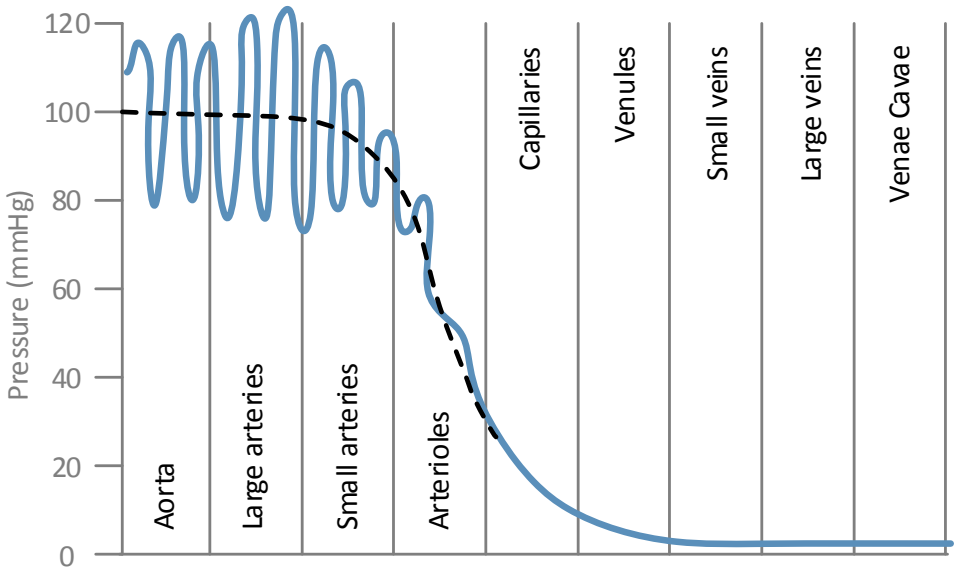

Figure 2.3: Schematic redrawn from (Guyton and Hall, 2011) showing the pressure in the systemic circulation. Note the slight increase in pulse pressure in the large arteries after the aorta, but the slightly lower mean pressure (dashed line). Additionally, there is little change in mean arterial pressure until the significant pressure drop at the arterioles.

Veins

The venous system are the blood vessels that return to the atria of the heart. At the capillaries the *venules* begin with a small diameter and as the vessels near the heart, they join to form the larger *veins*, the largest being the systemic system's vena cava, which returns blood to the right atrium. The veins are characterised by large blood volumes at low pressure that move toward the heart. The systemic circulation contains approximately 84% of the total blood volume, of which the systemic venous system contains 64% of the total blood volume or 76% of the blood in the systemic circulation (Guyton and Hall, 2011).

2.3 Cardiac Cycle

The cardiac cycle can be broken down into two stages, *systole* and *diastole*. Systole is the duration from start of ventricular contraction to end of ventricular ejection. Diastole is the duration of ventricular relaxation and filling, prior to the next cardiac cycle's systole. While contraction behaviour is similar for both the left and right heart, this section will

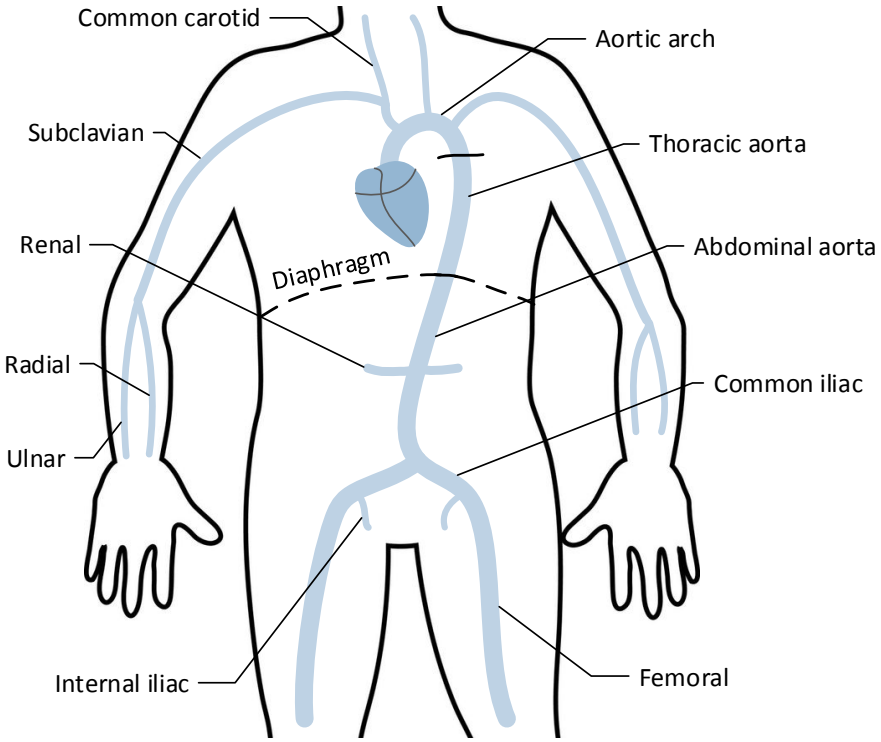

Figure 2.4: The main large arteries of the systemic system. Of particular interest to later analyses will be the arterial segment from the aorta to the femoral artery. However, discussion will include many of the other arteries shown.

use examples focusing on the left heart, since the systemic circulation is the focus of later chapters. The stages of systole and diastole are shown in Figure 2.5, and discussed in further detail in the subsections.

2.3.1 Systole

Chemical-Electrical Initiation of Contraction

Chemical reactions cause electrical signals, known as *action potentials*, to travel along the nervous system. Heart contraction is caused by an action potential changing voltage at the *sinus node*, located near the right atrium. The sudden voltage potential results in current discharging from the sinus node, through the atria and then through the ventricle, causing *depolarization*. The depolarization across the myocardium releases calcium ions resulting in muscle fibre contraction (Guyton and Hall, 2011).

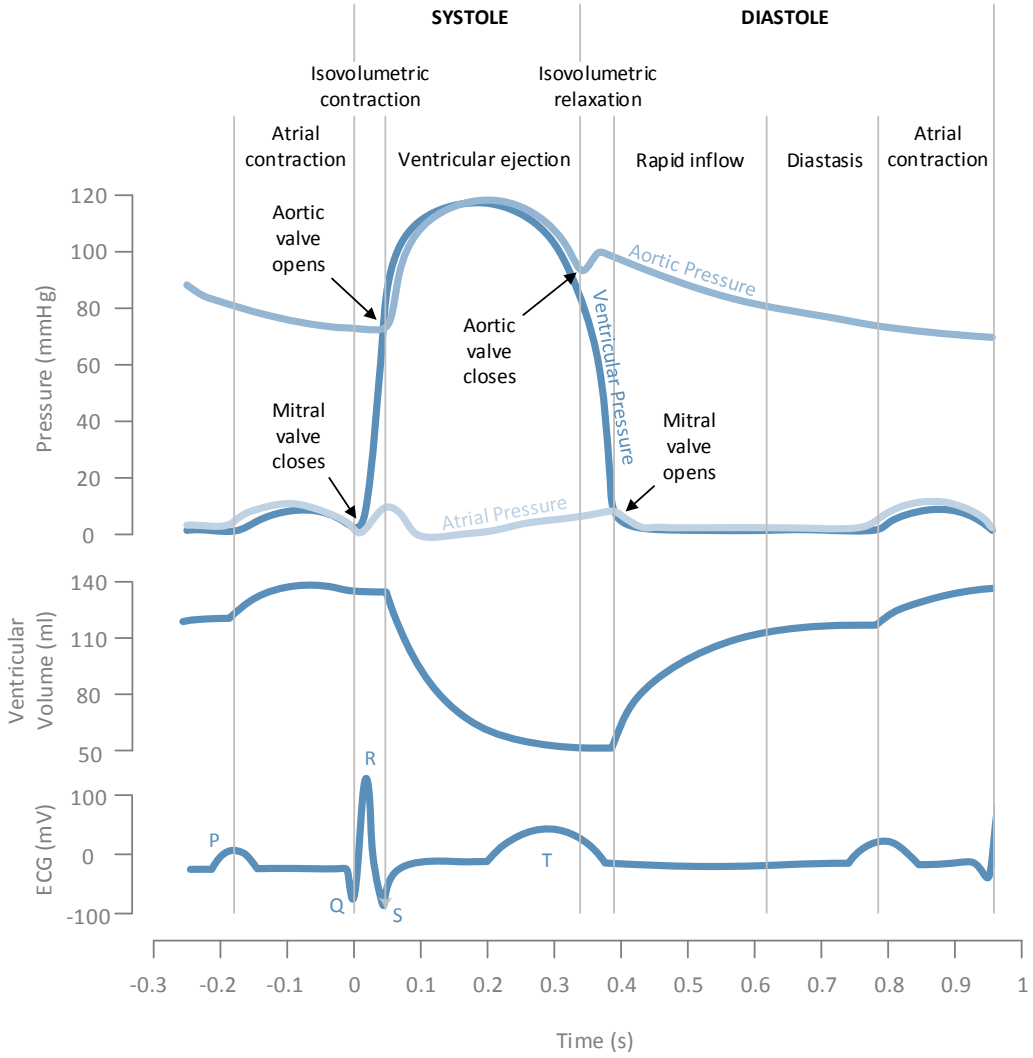

Figure 2.5: A single cardiac cycle of the left heart, showing different stages of systole and diastole.

Some of the current spreading through the tissues from the sinus node can be detected at the surface of the skin, using electrodes. The signal detected is known as an electrocardiogram (*ECG*) and can be used to indicate atrial and ventricular contraction. The *ECG* signal begins with the *P-wave*, indicating atria depolarization, causing contraction. Next the *QRS complex*, comprised of the *Q-wave*, *R-wave* and *S-wave*, indicates ventricular depolarization and contraction. Finally, the T-wave is generated by the ventricles as they *repolarize* during diastole. An example of an *ECG* signal is shown in Figure 2.6 and relative to the stages of the cardiac cycle in Figure 2.5.

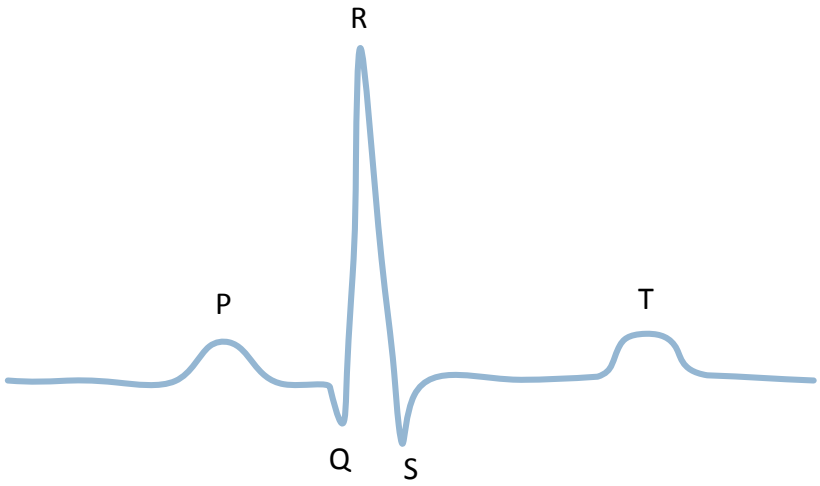

Figure 2.6: Example of an electrocardiogram (*ECG*) signal for a single beat, including the P, Q, R, S and T waves.

Since systole was defined as starting at the onset of ventricular contraction, it can be identified from an *ECG* QRS complex. By the strictest of definitions, systole starts with the Q-wave (Talley et al., 1971; Newlin and Levenson, 1979; Balmer et al., 2018c). However, since *ECG* lead locations influence both the presence of each wave and their peak prominence (Guyton and Hall, 2011), it is not uncommon for systole to be marked by either the R or S-waves (Guyton and Hall, 2011; Payne et al., 2006; Pitson et al., 1994), depending on the level of accuracy required.

Isovolumetric Ventricular Contraction

The mitral valve closes when the pressure in the left ventricle reaches the pressure of the left atrium, as shown in Figure 2.5. As the left ventricle contracts with closed mitral and aortic valves, pressure builds rapidly at constant blood volume. This ideal case is known as *isovolumetric contraction*, and lasts until the aortic valve opens.

Ventricular Ejection

When the pressure in the ventricle exceeds the pressure in the aorta, the aortic valve opens, ending the period of isovolumetric contraction, as shown in Figure 2.5. Valve opening begins a period of ejection of blood into the systemic circulation. Contraction still con-

tinues and ventricular pressure continues to increase during the early part of ejection, but at a decreased rate compared with the isovolumetric phase. During ejection, pressure in the aorta rises and tracks closely with the ventricular pressure. Initially, the rate of ejection into the aorta is higher than the flow of blood to the periphery, causing arterial expansion. The degree of this expansion depends on arterial compliance and ejection pressure, as per Section 2.2.2 (Townsend et al., 2015). As the ventricle volume falls, eventually ventricular pressure begins to fall, even while contraction continues. With up to 50% of the ejected *SV* stored in the elastic nature of the large arteries (London and Pannier, 2010), and ventricular ejection no longer exceeding blood flow to the periphery, the arterial walls begin to passively contract. As this arterial contraction occurs, the aorta remains at a higher pressure than the left ventricle, meaning the blood in the proximal aorta is driven back towards the heart. This backflow is stopped by the snapping shut of the aortic valve. Valve closure causes a *dicrotic notch* in the aortic pressure waveform, formed by wave reflection (Section 2.5) off the aortic valve (Lewis, 1906). Thus, the dicrotic notch is clearest in proximal arterial pressure signals and is often used to determine the transition from systole to diastole (Oppenheim and Sittig, 1995).

2.3.2 Diastole

Isovolumetric Relaxation

Following the ejection phase, the mitral and aortic valves are again both closed. Furthermore, the *ECG* T-wave has occurred, indicating ventricular *repolarization*, which causes relaxation of the heart muscle, decreasing pressure within the ventricle. While left ventricular ejection was occurring, right ventricular ejection was also occurring in a similar manner, but moving blood through the pulmonary system, ending with oxygenated blood filling the left atrium. Thus, as the left ventricular pressure fell through late systole and start of diastole, the left artial pressure steadily increased, as shown in Figure 2.5. When the left atrial pressure exceeds the ventricular pressure, the mitral valve opens, ending the isovolumetric relaxation.

Ventricular Filling: Rapid Inflow and Diastasis

Once the mitral valve opens, blood rapidly fills the ventricle. Thus, initially the volume rises rapidly, but as the ventricle approaches its full state, filling plateaus. This plateau in mid-diastole is known as *diastasis* and occurs just prior to atrial contraction, causing a final forcing of blood into the ventricle under atrial induced pressure. This action ends the cardiac cycle, with the depolarization process about to spread across the ventricle, beginning the next cycle's systolic contraction.

During diastole, the aortic pressure falls exponentially, as the *stored* blood volume in the arteries moves towards the lower pressure periphery. The rate of decay depends on the compliance and resistance of the arterial tree (Section 2.2.2), but can also be influenced by reflected wave behaviour, discussed in Section 2.5.3.

2.4 Cardiac Performance

As discussed in Section 2.2.1, the heart's main function is to move blood around the two circulations. It does this task by ejecting a volume of blood into each circulation per cardiac cycle, known as the stroke volume (*SV*). Section 2.3 covered the main stages of the cardiac cycle: *isovolumetric contraction*, *ejection*, *isovolumetric relaxation* and *filling*. Measured ventricular pressure and volume over the cardiac cycle forms a *PV loop*, as shown in Figure 2.7. This loop can be used to analyse cardiac performance (Sagawa, 1978; Knaapen et al., 2007; Davidson et al., 2018).

The width of the PV loop, defined by the maximum and minimum volume, is the *SV*. There are three main mechanisms through which this width and thus *SV* can change. Firstly, the heart *contractility* could change, meaning a change in its force of contraction. Second, the filling of the ventricle could change, altering the amount of blood in the ventricle at the start of contraction. This input pressure guiding filling is known as the *preload*. Finally, the load ventricular contraction must overcome to eject blood could change, known as a

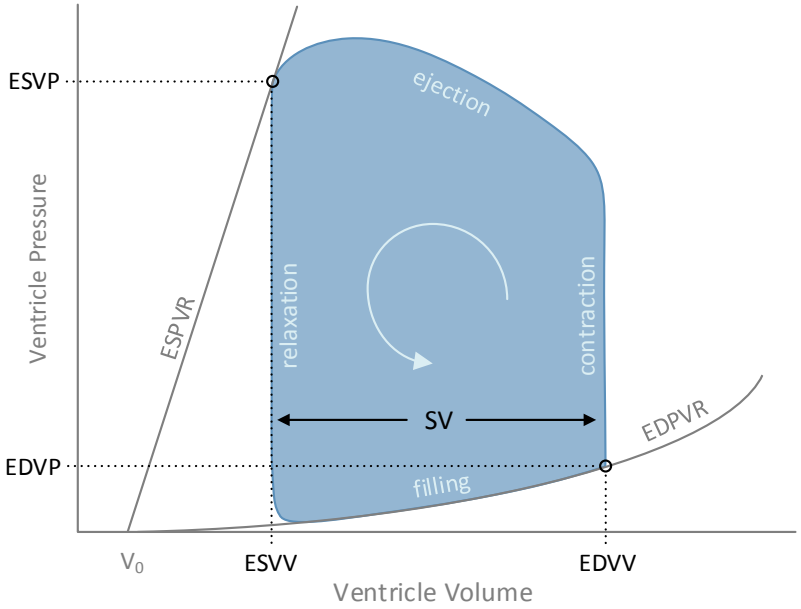

Figure 2.7: Example of an ideal PV loop for a single beat, including end-diastolic and end-systolic ventricle pressures and volumes respectively (*EDVP*, *EDVV*, *ESVP*, *ESVV*), as well as their relations (ESPVR, EDPVR) whose origin is the volume at zero pressure (V_0). By definition, stroke volume (*SV*) is the difference between *EDVV* and *ESVV*.

change in *afterload*. The following sections explore these mechanisms and their effect on *SV* through the PV loop.

2.4.1 Contractility/Inotropic State

Section 2.3.1 stated calcium ions resulted in muscle fibre contraction. More specifically, the individual contractile units of the myocardium (Section 2.2.1), are the *sacromeres*. The concentration of calcium ions available to the sacromeres is proportional to the contractile force they can produce and the velocity with which they contract (Westerhof et al., 2010b). An increase in contractile force is known as an increase in *contractility*, or an increase in the *inotropy*.

During systole, as the ventricle empties, the pressure within the ventricle would fall without the heart actively continuing to contract against the remaining volume. The change in volume over which pressure can be maintained, is dependent on the contractility. An increase in contractility decreases the end-systolic ventricular volume (*ESVV*) for the same end-systolic ventricular pressure (*ESVP*) (defined in Figure 2.7), as per Figure 2.8. In other

words, higher contractility sustains pressure in the ventricle to lower ventricle volumes. This sustained pressure increases the *ejection fraction*, defined as the proportion of the end-diastolic ventricular volume (*EDVV*) ejected as *SV*. Thus, on a PV loop, the contractility determines the ESPVR, which describes the maximum pressure development for any given *ESVV*, the *ESVP*. An increase or decrease in contractility shifts ESPVR, altering the *SV* as shown in Figure 2.8.

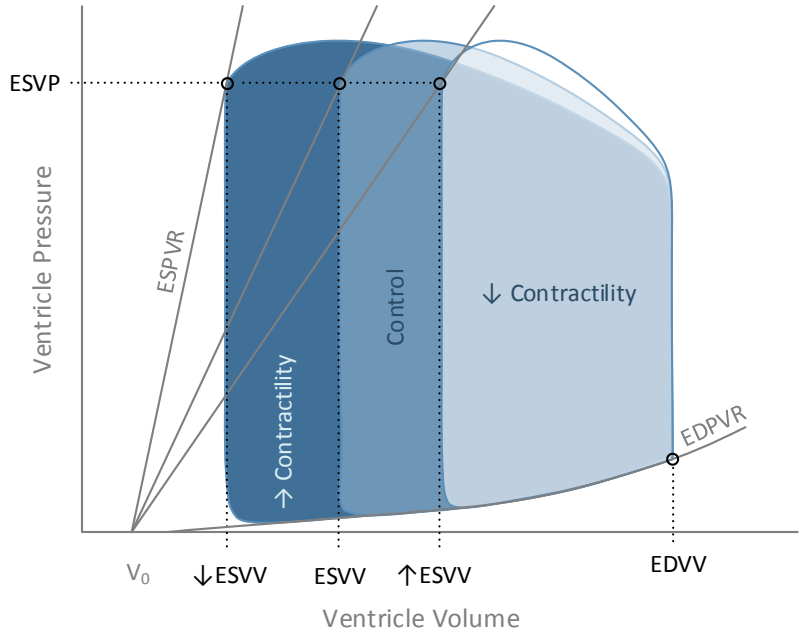

Figure 2.8: Effect of △contractility on PV loop, showing an increase in contractility leads to a reduction in *ESVV*, and visa versa.

2.4.2 Preload

Preload is defined as the stretch felt by the muscle fibres at end-diastole, as a result of filling. Specifically, it is the sarcomere length within the muscle fibres that increases as ventricular pressure and volume increase. The longer the sarcomere length, the more *myosin* heads are activated and available for contraction, which is a second mechanism through which the force of contraction can be increased (Guyton and Hall, 2011). Since sarcomere length is an infeasible measurement in most situations, surrogate measures of preload exist, such as *EDVV* and end-diastolic ventricular pressure (*EDVP*), which represent the degree to which the ventricle was stretched during the filling stage. Some of the

factors that increase ventricular filling and thus preload include:

- Decreased venous compliance, which leads to increased venous pressure and can increase the pressure gradient to the atria, increasing *venous return*, the flow rate to the atria (Guyton and Hall, 2011).
- Increased atrial contraction, increasing volume of blood forced into the ventricle prior to the atrio-ventricular valve closure described in Section 2.2.1.
- Reduced heart rate, leading to increased ventricular filling duration.
- Increased ventricular compliance, increasing the change in volume or amount of stretch for a given change in pressure.

Preload is proportional to *SV* and this relationship is commonly referred to as the *Frank-Starling mechanism* (Newlin and Levenson, 1979; Luecke and Pelosi, 2005). The Frank-Starling mechanism is illustrated for PV-loops in Figure 2.9.

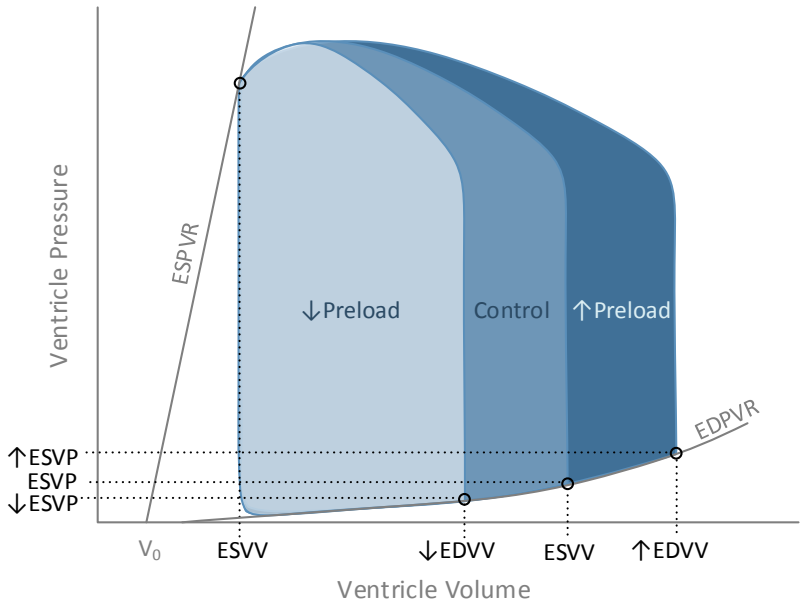

Figure 2.9: Effect of ∆preload on PV loop.

2.4.3 Afterload

Afterload is the load that ventricular contraction must overcome to sustain the ejection phase of systole. Section 2.3.1 stated left ventricular ejection begins when left ventricular pressure (P_{vent}) $>$ aortic pressure (P_{ao}). Thus, the afterload is *initially* end-diastolic aortic pressure (*EDAP*), signifying the end of diastole with respect to the aorta. *EDAP* is often a surrogate measure for afterload (Newlin and Levenson, 1979). *EDAP* changes with arterial stiffness and resistance to flow (see Section 2.2.2). Specifically, *SV* is inversely proportional to *EDAP* as shown in Figure 2.10.

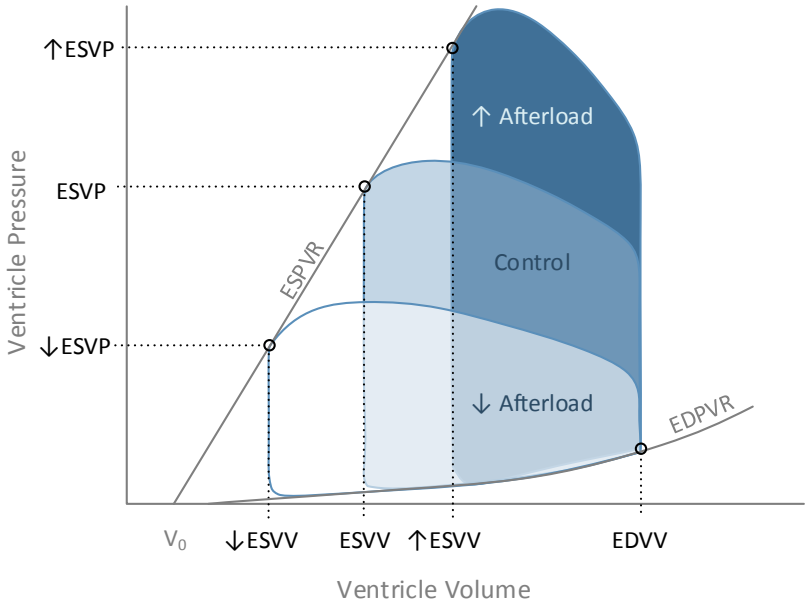

Figure 2.10: Effect of $\triangle$afterload on PV loop.

While *EDAP* provides a simple afterload surrogate, in reality the load the ventricle must eject against is changing throughout systole. This variability can be seen in Figure 2.5, with the very nature of ejection increasing P_{ao}, forcing P_{vent} to increase to maintain ejection. Therefore, other surrogate measures of afterload are also possible, for example end-systolic aortic pressure (*ESAP*) or *ESVP* (Luecke and Pelosi, 2005).

2.4.4 Changes in Cardiac Performance

Preload, afterload and contractility are dynamic variables changing in both the short and long-term to optimise cardiac performance.

Short-Term Changes in Cardiac Performance

An example of short-term changes in cardiac performance occurs during exercise, where oxygen demand increases. To meet this demand, respiration increases, but so too must oxygen delivery. The working muscles respond by dilating their blood vessels. The net effect is a reduction in systemic vascular resistance, which acts to reduce afterload, ultimately increasing the blood flow and oxygen delivery to the tissue. The afterload reduction increasing arterial blood flow, has a secondary effect of increasing flow to the venous system and back to the heart, thus increasing preload. As covered in Section 2.4.2, increased venous return leads to an increase in preload and subsequent increase in *SV* through the Frank-Starling mechanism. This intrinsic autoregulation mechanism of the heart helps it synchronise with the demands of the circulation (Guyton and Hall, 2011).

The body's autonomous nervous system can also regulate the cardiovascular system. For example the *sympathetic nervous system* can increase contractility and heart rate (*HR*), leading to an increase in both *SV* (Figure 2.8) and cardiac output (*CO*) (Equation 1.1), respectively. The *parasympathetic nervous system* can reduce *HR* and contractility as necessary (Guyton and Hall, 2011).

Long-Term Changes in Cardiac Performance

As a person ages, the stiffness of their aorta increases (Nichols et al., 2011). This stiffening leads to slow, long-term changes in cardiac performance. Specifically, Section 2.2.2 stated that arterial compliance helped minimise resistance to flow in the arteries. Thus, the opposite is also true, as compliance reduces, resistance to flow increases, representing increasing afterload on the ventricle.

To understand the inverse relationship between arterial resistance and compliance, first consider the hypothetical case of ventricular ejection into a rigid arterial tree. In order for the stroke volume to be ejected from the ventricle, it would need to displace an equivalent volume of blood in the proximal aorta further along the arterial tree. However, in doing so, the displaced blood from the proximal aorta would also need to find space further downstream. Hence, the net result is the entire blood volume of the arterial tree would need to be displaced in order to make room for the stroke volume. The average volume of blood in a human is 5 l (Guyton and Hall, 2011). Thus, in a rigid arterial tree, the ventricle would need to overcome the inertia associated with 5 l of blood to eject the stroke volume. The force necessary to displace such a significant volume is much higher than the force of contraction provided by the human heart.

Sections 2.2.2 and 2.3.1, highlighted how arterial compliance allowed some of the energy produced by ventricular contraction to expand the arteries. The higher the compliance, the larger the proportion of stroke volume *stored* in arterial expansion, thus reducing the volume of blood already in the aorta needing to be displaced further along the arterial tree. Therefore, it is the additional volume provided by the arterial expansion, that significantly reduces the inertial load on the heart (London and Pannier, 2010).

Finally, as the compliance of the aorta reduces in the elderly, a larger proportion of the energy produced by contraction, must go into displacing blood already in the aorta, further along the arterial tree. Hence, the ventricle experiences the decreased aortic compliance as an increase in proximal arterial resistance and an increase in afterload.

Section 2.2.2 also stated the compliance helped to *dampen* the pulsatile pressure. According to Equation 2.1 it is now clear that the pulse pressure is higher in elderly due to the reduction in compliance leading to less change in arterial volume (ΔV).

Reflected pressure waves are a second mechanism through which compliance increases afterload in elderly. Section 2.5 will discuss how ventricular ejection produces a pressure wave that is partially reflected back to the heart from downstream reflection sites. In

elderly, the reduced compliance leads to faster *return times* of the reflected waves. When the reflected waves return during systole, they act against the continuation of ventricular ejection. Ultimately, the increase in afterload due to reduced compliance, leads to the general trend of increasing mean arterial blood pressures with age (Nichols et al., 2011).

Other factors influencing cardiac performance are disease and interventions. Hence the desire for continuous *SV* monitoring in a clinical environment, to diagnose cardiovascular dysfunction and observe the effect of treatments, as covered in Section 1.3. Chapter 5 Section 5.2 will cover the disease states and interventions induced in the experiments associated with this thesis, along with their effect(s) on preload, afterload and contractility. The net effect being an alteration of *SV*, with the aim of capturing it with the developed model.

2.5 Arterial Wave Theory

The intermittent nature of ventricular ejection causes pressure and flow *waves* to propagate through the arterial tree. This phenomena is commonly referred to as the *pulse wave* and is the focus of this section. The pulse wave should not to be confused with pressure and flow *waveforms*, which show how pressure and flow change over time at a particular point.

2.5.1 Pulse Wave Velocity (*PWV*)

Section 2.4.4 already alluded to a relationship between compliance and the speed of the pulse wave. To understand this relationship, consider systolic ejection into a rigid versus compliant arterial tree, as was done in Section 2.4.4. In the rigid system, ejection at the aortic valve displaced all the blood along the arterial tree, in a manner that meant blood downstream moved instantaneously with the push upstream at the valve.

However, as per Section 2.3.1, aortic compliance enables flow into the aorta to exceed flow to the periphery during early ventricular ejection. The arterial expansion caused

by the net increase in blood volume begins locally in the proximal aorta, as illustrated in Figure 2.11. Thus, for a brief moment, blood in the distal aorta and distal arteries does not experience the force of ventricular ejection. As the proximal aorta expands according to its compliance (Equation 2.1), the local pressure increases. The net increase in blood volume in the proximal aorta, combined with the significant increase in local pressure gradient, eventually leads to the displacing of blood along the arterial tree. As blood is displaced from the proximal aorta, it occurs in a manner that propagates the arterial expansion and increases pressure along the arterial length, as shown in Figure 2.11. Thus, the increase in pressure due to ejection begins locally in the proximal aorta, but takes time to propagate along the arterial tree, causing arterial expansion as it does so. This propagating arterial expansion is the *pulse wave* and the expansion can be felt in large arteries near the surface of the skin, referred to simply as *the pulse*.

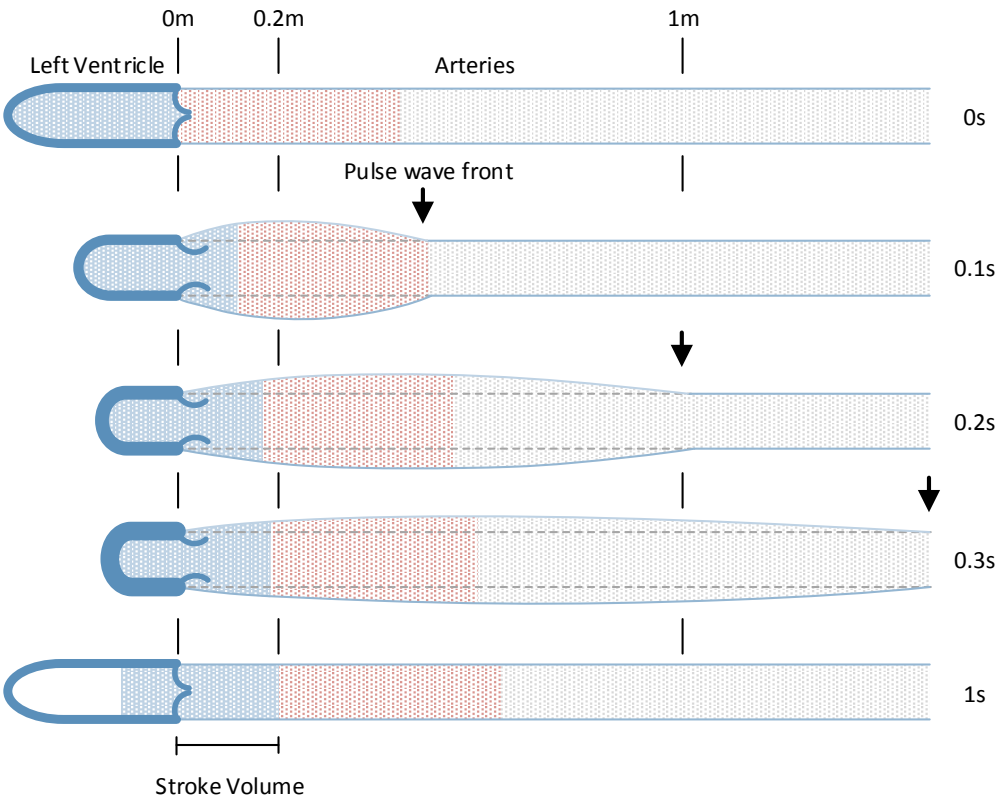

Figure 2.11: Schematic illustrating how ejection displaces blood along the arteries and expands the arterial walls (blue pattern). The red pattern is a control volume representing the blood already in the aorta, and illustrates its displacement contributing to the propagation of the pressure wave and arterial expansion further downstream. The black arrows indicate the pulse wave front in each frame, illustrating how its speed is much greater than the velocity of the bulk fluid flow (Modified from (London and Pannier, 2010)).

Finally, in light of Figure 2.11, consider the effect of reducing compliance on the pulse wave. As the compliance tends to zero, approaching the hypothetical rigid case, aortic expansion is reduced and the pressure propagates along the arterial tree faster, as a larger proportion of ventricular ejection goes into displacing blood along the arterial tree. Assuming the blood is incompressible, when compliance reaches zero, pressure can be thought of as propagating instantaneously, this limiting case is equivalent to infinite wave speed.

Figure 2.12 shows how with increasing age, aortic *PWV* increases, in response to the reduced compliance discussed in Section 2.4.4. Since it is not feasible to measure compliance directly, *PWV* is a common clinical surrogate. Specifically, when estimating arterial compliance, it is most relevant to use *aortic PWV* (Blacher et al., 1999b; Laurent et al., 2006; Nichols et al., 2011; Townsend et al., 2015; Balmer et al., 2018c). Aortic *PWV* is favoured because the aorta accounts for most of the compliance of the arterial tree, as per Section 2.2.2, and it also changes significantly over a humans lifetime as per Figure 2.12.

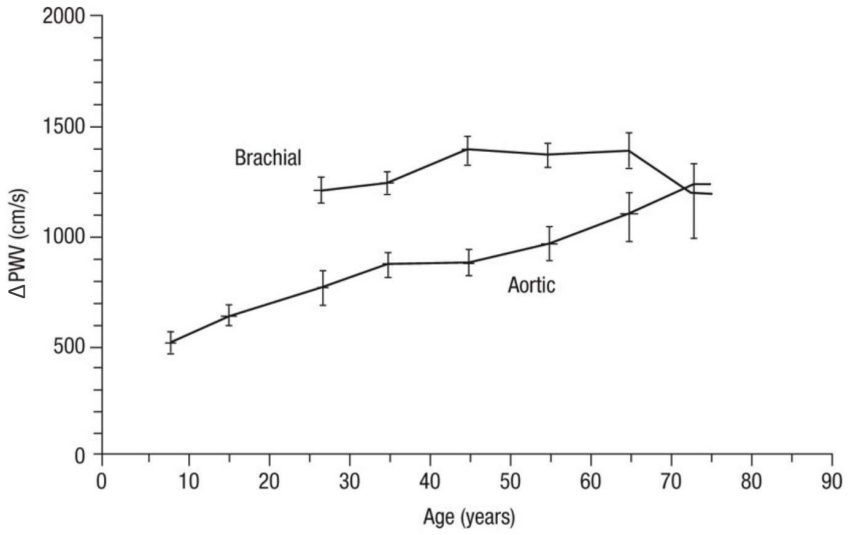

Figure 2.12: Changing aortic *PWV* (ΔPWV) with age, as a surrogate for vessel stiffness/compliance. Taken from (Nichols et al., 2011).

Finally, the inverse relationship between compliance and *PWV* is described by the Bramwell-Hill equation (Bramwell and Hill, 1922):

$$PWV = \sqrt{\frac{V}{\rho C}} \tag{2.2}$$

Where ρ is blood density, V is the vessel volume and C is the compliance according to Equation 2.1. The Bramwell-Hill equation can also be expressed in terms of area compliance, useful for vessels such as the aorta, whose area is easier to measure than its volume:

$$PWV = \sqrt{\frac{A}{\rho C_A}} \tag{2.3}$$

Where A is the vessel cross-sectional area and C_A is the area compliance, defined as:

$$C_A = \frac{\Delta A}{\Delta P} = \frac{dA}{dP} \tag{2.4}$$

Assuming the area compliance is constant along a vessel's length, the volumetric (Equation 2.1) and area compliances (Equation 2.4) are related by length:

$$C = C_A L \tag{2.5}$$

Thus, C_A is sometimes know as the compliance per unit length.

The speed of the pulse wave can be calculated using two simultaneous pressure measurements, as illustrated in Figure 2.13. When the pulse wave passes a measurement site, it causes the sudden transition from the negative pressure gradient associated with the last beats diastolic decay, to the sudden steep positive gradient of the current beats systole. This transition feature is known as the *foot* of the waveform. The time difference between each waveform's foot, is the pulse transit time (*PTT*) between the two measurement sites. If the distance (*d*) between the two measurement sites is known, the *PWV* can then be calculated:

$$PWV = \frac{d}{PTT} \tag{2.6}$$

In the aorta, *PWV* is in the range of 4–12 m s^{-1}, and is proportional to the stiffness of the artery (Murgo et al., 1980; Laurent et al., 2006; London and Pannier, 2010), where stiffness is the inverse of compliance. *PWV* is significantly faster than the bulk fluid flow through the aorta, which is on the order of centimetres per second (London and Pannier, 2010), as illustrated in Figure 2.11.

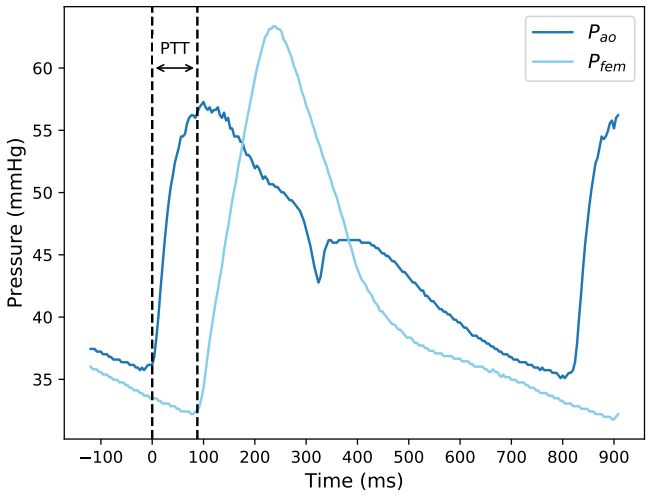

Figure 2.13: Simultaneously measured aortic arch and femoral pressures from a pig, showing the pulse transit time (*PTT*), calculated using the *foot-to-foot* method.

2.5.2 Waves in a Uniform Tube

If the arterial tree were a uniform tube of infinite length, the outgoing waves would not be reflected, and the pressure and flow waveforms would have the same shape according to *Poiseuille's equations* (Westerhof et al., 2010e; Westerhof and Westerhof, 2017). In this reflectionless system, neglecting blood viscosity *PWV* could be determined from the *water hammer* equation (Papageorgiou and Jones, 1988; Khir and Parker, 2005; Westerhof and Westerhof, 2017):

$$PWV = \frac{Z_c A}{\rho} \tag{2.7}$$

Where ρ is the density of blood, A is the cross-sectional area and Z_c is the *characteristic impedance* of the vessel. Z_c is defined as the ratio of change in pressure to change in flow, in a reflectionless system:

$$Z_c = \frac{dP_f}{dQ_f} \tag{2.8}$$

Thus, P_f and Q_f are the forward-travelling pressure and flow waves in the tube, respectively. Under these conditions, Z_c is real valued, since P_f and Q_f are in phase. If they were out of phase, the impedance (Z) would have deviated from Z_c, becoming complex, reflecting their phase difference, and Equation 2.7 would not be applicable.

When using *dP* and *dQ* measured from the proximal aorta during the steep early systolic rise, Equation 2.8 gives a reasonable approximation of aortic characteristic impedance ($Z_{c,ao}$) (Khir and Parker, 2005; Hughes and Parker, 2009). This is because in early ejection, the proximal aortic measurements are the result of the forward-travelling pulse wave, thus they have similar shape, as shown in Figure 2.14 (Khir and Parker, 2005; Laurent et al., 2006; Westerhof and Westerhof, 2017). The *PWV* then calculated by Equation 2.7 will be similar to that found using the *foot-to-foot* method of Figure 2.13.

However, the pressure and flow waveform shapes differ following their systolic rises, as shown in Figure 2.14. Thus, the uniform tube model fails to describe wave propagation and its effects on measured pressure and flow in the distributive nature of the arterial tree (Mynard et al., 2015).

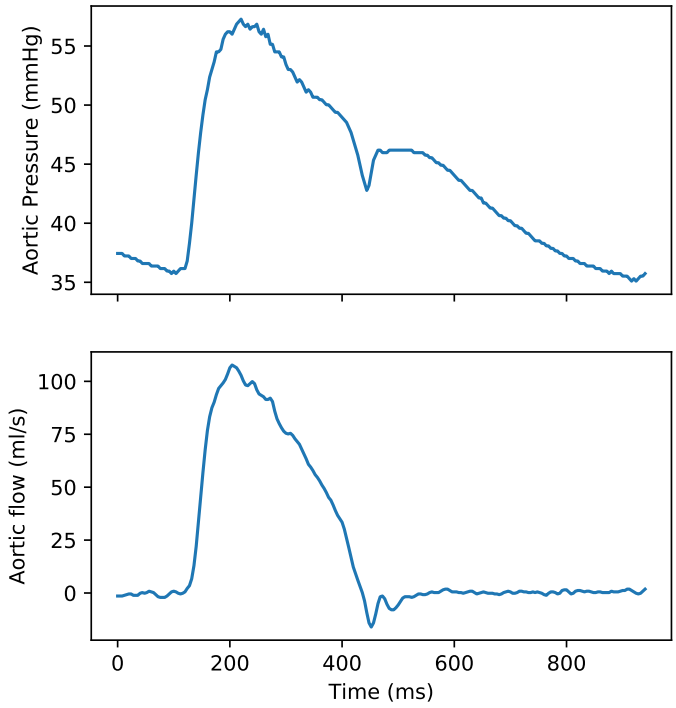

Figure 2.14: Simultaneously measured aortic arch pressure and aortic flow (using aortic flow probe) from a pig.

2.5.3 Waves and Reflections in a Network of Distensible Tubes

As covered in Section 2.2.2, the arterial tree contains many branches whose vessel properties change along their length. The aforementioned section explained how this ensured adequate pressure and flow at the capillaries to optimise perfusion, and partly explained the spatial dependencies of the waveforms. However, these changing properties also mean impedance is not constant along the arterial tree. At locations where there is an impedance mismatch, like a branching of the vessels, a proportion of the forward-travelling wave is reflected, given by a *reflection coefficient* (Γ) in Equation 2.9 (Papageorgiou and Jones, 1988; Wang and Parker, 2004; Khir and Parker, 2005; Westerhof et al., 2010e; London and Pannier, 2010; Mynard et al., 2012; Mynard and Smolich, 2014b), defined:

$$\Gamma = \frac{Z_{in} - Z_c}{Z_{in} + Z_c} \tag{2.9}$$

Where Z_c is the *characteristic impedance*, of the mother vessel, describing the forward-travelling pressure and flow waves, while Z_{in} is the *input impedance*, or impedance downstream of the mother vessel. Their difference is what causes wave reflection. In a reflectionless system, the input impedance is equal to the characteristic impedance and the system is said to be *impedance matched* (Westerhof et al., 1969). Factors that contribute to the *input impedance* include the vessel compliance, dimensions, peripheral resistance, inertia of blood volume and timing of reflected waves (London and Pannier, 2010).

Given high *PWV*, a reflected wave can return from a reflection site within the time of a single beat (Murgo et al., 1980; Westerhof and Westerhof, 2017). Thus, when measuring pressure and flow in the arteries, their resulting waveforms are due to the initial forward travelling wave, but also reflected waves. The return times of reflected waves vary, depending on the distance from their reflection sites and if the wave is in fact a compounding of many reflected waves (Laurent et al., 2006). Thus, reflected waves can be catagorised into two types: *distinct*, meaning a reflected wave's reflection site is known, or *diffuse*, meaning a distinct reflection site is unknown since the reflected wave may be a compounding of many reflected waves from many reflected sites (Westerhof et al., 2010d).

Distinct Waves

Murgo et al. (1980) identified some patients' peak systolic aortic pressure followed a point of inflection, and appeared as a secondary rise in pressure. By measuring pressure at many places along the aorta, Murgo et al. (1980) showed the inflection point would appear earlier on the systolic rise of a waveform the further the measurement was from the heart. This pattern continued until the measured waveform was from or just past the aortic-iliac branch, causing the inflection point to disappear. Murgo et al. (1980) hypothesised the aortic-iliac branch caused a *distinct* reflection site (Westerhof et al., 2010d), and the inflection point was due to the reflected wave propagating back to the heart. Supporting this theory Murgo et al. (1980) found the time it took for the inflection point to propagate along the aorta, back to the heart, was equal to the *PTT*, calculated from the *foot-to-foot* method

shown in Figure 2.13. Murgo et al. (1980) also noticed the reflected wave seemed to arrive later in systole or in early diastole in younger patients. This behaviour appeared consistent with lower *PWV* recordings in younger, more compliant arteries, where reflected waves take longer to propagate back to the heart (Laurent et al., 2006; Westerhof et al., 2010d), as breifly stated in Section 2.4.4. What Murgo et al. (1980) identified was a distinct reflection site, leading to a distinct reflected wave and its effect of increasing the measured pressure in the aorta, as shown in Figure 2.15.

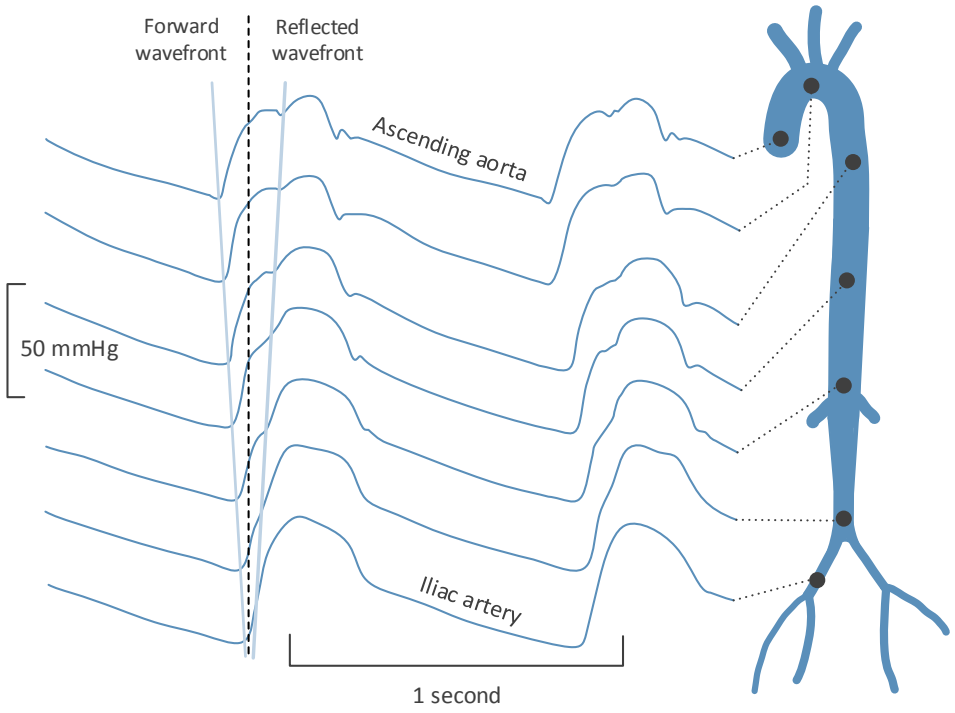

Figure 2.15: Effect of the distinct aortic-iliac reflection site on measured pressure waveforms in the aorta. Redrawn from (Murgo et al., 1980).

Diffuse Waves

Generally, the arterial tree is considered to be reasonably well impedance-matched, with mismatches low enough to cause only partial wave reflection, particularly in the central arteries (Westerhof et al., 1969). In other words, $Z_c \approx Z_{in}$, leading to a low Γ in Equation 2.9. What is often less considered, is reflected waves can also be re-reflected, and since the impedance mismatch in the backwards direction is much greater than the forward, a

significant proportion of the reflected wave would be re-reflected to once more travel in the forward direction (Westerhof et al., 1969). This phenomena is thought to focus wave reflections in the periphery, known as *wave trapping* (Wang and Parker, 2004; Khir and Parker, 2005; Mynard et al., 2015). The vast number of branches over short distances in the periphery leads to *diffuse* waves: those that combine, making it difficult to identify individually reflected waves and their distinct reflection site. Inevitably, some diffuse waves still propagate back to the heart throughout the course of a cardiac cycle.

Clinical Implication of Reflected Waves

Interventions causing vasodilation and vasoconstriction of the peripheral bed have been shown to reduce and increase reflected waves returning to the heart, respectively (Nichols, 2005; Laurent et al., 2006). The early systolic arrival of reflected waves is of clinical relevance since they increase the systolic pressure in the aorta, increasing afterload, as discussed in Section 2.4.4 (Nichols, 2005; Khir and Parker, 2005; Laurent et al., 2006).

The experimental methods of wave analysis are not of practical use in a clinical environment. However, the speed at which reflected waves return to the ventricle principally depend on *PWV*, which increases with arterial stiffness, as discussed in Section 2.5.1. While, measuring arterial stiffness directly is difficult, *PWV* serves as a suitable clinical surrogate and is used as a predictor for future cardiovascular dysfunction (Nye, 1964; Blacher et al., 1999a,b; Laurent et al., 2001; Cameron et al., 2003; Millasseau et al., 2005; Laurent et al., 2006; Nichols et al., 2011; Ben-Shlomo et al., 2014).

2.5.4 Difference in Pressure and Flow Waveforms Shapes

Finally, Section 2.5.2 and Figure 2.14 showed the measured pressure and flow waveforms had different shapes and implied this was due to reflected wave phenomena. So far, the reflected wave examples focused on pressure, where the reflected waves lead to an increase in the overall measured pressure waveform. These waves are known as *compression waves*.

Flow waves differ, having a negative magnitude upon reflection, that is, the flow waveform they cause appears inverted (Westerhof et al., 1969, 2010d; Mynard et al., 2012; Mynard and Smolich, 2014b; Westerhof and Westerhof, 2017). To understand why, consider the effect of the reflected pressure wave with its positive magnitude on flow. Flow is driven by a pressure gradient, travelling in the direction of lower pressure. When averaging the pressure along the length of the arterial tree, this pressure gradient is highest at the heart and lowest at the periphery, reflected in Figure 2.3. However, as a reflected pressure wave moves back towards the heart, back towards the region of (on average) higher pressure, it increases pressure in its local vicinity. Thus, just upstream of the reflected pressure wave is in fact a region of *lower* pressure, creating a local pressure gradient that is opposing the main flow direction. Therefore, the corresponding flow waveform it causes is negative, acting against the bulk flow direction. Alternatively, the velocity wave can be used in place of the flow wave, where a backwards travelling pressure wave causes deceleration of the fluid, reflected in a backwards travelling velocity wave of negative magnitude (Khir and Parker, 2005).

In addition, Figure 2.14 uses pressure and flow data from the proximal aorta. It shows near the aortic valve, once ejection ends, flow quickly measures zero. However, as discussed in Section 2.2.2, during diastole the decaying pressure reflects the passive relaxation of the large arteries as they expel flow to the low pressure periphery. Thus, in more peripheral sites, measured flow would remain positive through diastole (Mynard and Smolich, 2014b).

In summary, the changes in pressure and flow waveforms measured along the arterial tree *(spatial changes)*, can be understood as the result of two phenomena: firstly the changing of vessel properties, and secondly, more indirectly through reflected wave influence. The *temporal* difference between pressure and flow waveforms measured at a particular location in the arterial tree, are due to the differences in reflected pressure and flow waveforms.

2.6 Summary

This chapter covers the necessary background physiology and nomenclature to understand the analyses and discussion of later chapters. Specifically, it covered the anatomy and function of the cardiovascular system, with particular focus on the systemic circulation, since it is driven by left ventricular ejection, whose *SV* and flow waveform will be estimated in coming chapters.

Furthermore, cardiac performance, measured by preload, afterload and contractility was discussed. Understanding of these metrics is important in Chapter 5, as part of understanding the effect of interventions used in the experiments to attempt to alter *SV*/*CO*.

Finally, Section 2.5 covered arterial wave theory. Many of the models discussed throughout this thesis are *lumped* models, where arterial properties are averaged, leading to a simplification of the real cardiovascular dynamics. This aspect will be discussed further in Chapter 4, but the context of the simplifications and their implications would be lost without first having a background knowledge on the complex wave dynamics that are critical to normal cardiovascular function.

CHAPTER 3

Stroke Volume/Cardiac Output Measurement Techniques

3.1 Introduction

Chapter 1 briefly covered the need for monitoring stroke volume (*SV*)/cardiac output (*CO*), with particular focus on unstable patients in intensive care with complex disease states (Cecconi et al., 2014). It also outlined the limitations of current monitoring techniques, exposing the potential for research to improve clinical care. However, until sufficient background physiology and nomenclature could be covered, the specifics of measurement techniques was not discussed. With a more thorough understanding of the cardiovascular system from Chapter 2, this chapter examines the current state of the art in clinical and experimental methods to measure and monitor *SV* and *CO*, in more detail.

3.2 Ultrasound Techniques

3.2.1 Echocardiography

Echocardiography ("echo") is commonly used to assess cardiac performance (Pandian et al., 1994; Cecconi et al., 2014) and monitor unstable patients (Marik, 2013). Echo is an ultrasound imaging technique enabling a patient's heart to be viewed non-invasively. Ultrasound imaging involves sending sound waves, at a frequency higher than human hearing, into a medium. At any boundaries between mediums some of the sound will be reflected, due to a change in the acoustic impedance. The *echo* is then detected and based on the time between transmission and reception, and the strength of the echo, an image can be constructed.

By recording images over time, clinicians can determine a patient's *SV* and *CO* by tracking volume change of the heart (Cecconi et al., 2014). The main advantage of the technique is that it is non-invasive, explaining its routine use for diagnosis, management and follow up of patients with suspected or known cardiac dysfunction. The main disadvantages are that it is not continuous, the three-dimensional shape is inferred from two-dimensional images, and that it requires a trained operator.

Despite the low invasiveness of the method, Wetterslev et al. (2016) conducted a systematic review comparing *CO* measurements from echocardiography and pulmonary arterial catheters and found the mean error across the studies to be $> \pm$ 30% (Wetterslev et al., 2016). While the gold standard measure of *CO* is still debated (Wetterslev et al., 2016; Moise et al., 2002; Tibby et al., 1997; Peyton and Chong, 2010; Dark and Singer, 2004), the pulmonary arterial catheter is considered, at the least, a clinical standard (Wetterslev et al., 2016; Dark and Singer, 2004; Yelderman, 1990). Thus, while echo is less invasive, it also appears less accurate compared to a clinical gold standard, which itself does not have perfect accuracy (Chase et al., 2014).

3.2.2 Aortic Flow Probes

Aortic flow probes are one of the most accurate means of measuring flow in the aorta. The probes have been shown to have a correlation coefficient of $r \approx 1$ when used in a pig study involving heart bypass and a roller pump to control flow (Dean et al., 1996). Some commercial models are quoted with precisions of ±2% (Yang et al., 2013).

The probe contains a pair of ultrasonic transceivers, one upstream of the other. When the downstream transceiver emits soundwaves, to be detected by the upstream transceiver, they must travel against the flow and are slowed. When the upstream transceiver emits soundwaves, to be detected by the downstream transceiver, they travel with the flow and hence travel faster compared with their downstream counterparts. The difference between the transit times of the two transceivers can then be related to the flow velocity in the aorta and subsequently converted to a volumetric flow rate knowing the area of the vessel (Eren, 1998). By integrating flow over time, a measure of *CO* or *SV* can be found (Dean et al., 1996), as shown later in Section 5.4.4.

The main disadvantage of this technique, is it is highly invasive, since a probe must be fit physically around the aorta. For this reason it is limited to experimental studies, rather than the clinical environment. A second disadvantage is due to the probes location, it is usually placed near the root of the aorta, but some blood flow can still have passed into coronary arteries via this juncture (Yang et al., 2013; Kamoi, 2016). Finally, the angular positioning of the probes transceivers must be correct to minimise constructive and destructive interference caused by reflected waves (Eren, 1998).

3.2.3 Trans-Esophageal Doppler Ultrasound

Trans-Esophageal doppler monitoring can be used to estimate *CO* relatively non-invasively by measuring the cross sectional area of the descending aorta and the velocity of blood (Dark and Singer, 2004; Chaney and Derdak, 2002). As evident from its name, velocity is computed from the change in frequency of the emitted versus reflected sound waves,

Figure 3.1: Transonic Scisence's (Transonic, Ithaca, NY, USA) aortic flow probe, similar to the type used in the experiments discussed in Chapter 5.

known as the *Doppler* principle. While it is less invasive than the aortic flow probe, the trade-off is it is more difficult to position correctly, in the esophagus at an angle of 20° (Chaney and Derdak, 2002; Marik, 2013), rather than fixed around a vessel. A second issue with this technique, is vessels have branched off prior to the descending aorta, taking a proportion of the blood flow . As a result, a correction factor must be applied to account for the blood not passing the probe when calculating SV/CO (Chaney and Derdak, 2002; Marik, 2013).

3.3 Ventricular Admittance Catheters

Admittance Catheters measure the changing electrical conductance within the ventricle, to deduce changes in ventricular blood volume. The catheter itself is comprised of source and sensing electrodes, as well as a pressure sensor. It is placed directly into the ventricle where an oscillating voltage is then applied to the source electrodes, and the voltage difference between the source and sensors electrodes is measured over time (Transonic Sys Inc, 2013). The difference in voltage between the source and sensor is inversely proportional to the conductance according to Ohm's law.

The conducting medium between the source and sensor is both the blood and muscle fibres of the ventricle (Transonic Sys Inc, 2013). Since the aim is to measure the fluctuations in

ventricular blood volume, the conductance of the muscle fibres needs to be accounted for and its contribution removed. Further complicating the issue, muscle fibre conductance also varies with time. A time varying correction factor was developed by Wei et al. (2005), which isolates the conductance's associated with blood volume and the myocardium respectively (Wei et al., 2005). This empirical correction factor relies on an initial measure of *SV* to calibrate. Wei's Equation is then used to calculate the volume of blood measured over the duration of a beat (Wei et al., 2005). *SV* can be calculated via the difference between *EDVV* and *ESVV*, as per Figure 2.7, and discussed later in Section 5.4.4. A detailed work through of the mathematics relating the conductance to the blood volume can be found in (Porterfield et al., 2009).

Similar to the aortic flow probe, the clinical applicability of the admittance catheter is limited by its highly invasive nature. Furthermore, placing a catheter in the ventricle can impede the function of the atrial-ventricular valves (Evans et al., 2009). As a result, the risks outweigh the benefits in an ICU environment.

3.4 Indicator Dilution Methods

The general principle of indicator dilution methods, is to introduce a known amount of a substance into the bloodstream and determine *SV*/*CO* based on how the substance distributes (Tibby et al., 1997). The substance can be a dye or chemical, or fluid at a particular temperature (Tibby et al., 1997).

Thermodilution is a reliable measure of *SV*/*CO* and the most common of the indicator dilution methods. It is where a fluid of lower temperature than the blood is injected into the bloodstream and the temperature change it causes can be measured by a thermistor-tipped catheter downstream of the injection site. Typically, saline is injected into a blood vessel upstream of the hearts right atrium and the thermistor is located just downstream of the right ventricle in the pulmonary artery (Nishikawa and Dohi, 1993; Pearl M.D., Ph.D. et al., 1986; Sorensen et al., 1976). Cardiac output can be related to the temperature change

based on the Stewart-Hamilton equation:

$$CO = \frac{(T_b - T_i)V_i K}{\int \Delta T_b dt} \quad where \quad K = \frac{\rho_i S_i}{\rho_b S_b} \tag{3.1}$$

Where T_b is blood temperature before injection of the bolus, T_i is the temperature of the indicator, V_i is the volume of the indicator and K is a ratio of the density (ρ) and specific heat[1] (S) of blood and the indicator, respectively.

Equation 3.1 has many assumptions resulting in the systems between the injection site and detection site being treated as a single inflow, single outflow tube (Zierler, 1962). For example:

- Conservation of mass cannot be achieved if there is branching in the vessel between the injection site and detection site.
- The volume of indicator injected is time dependent. Only in the ideal theoretical sense can the indicator volume be injected instantaneously.

However, the violation of these assumptions and others when applying the method to a real vascular system, have been well justified (Zierler, 1962). As a result, the method is used in numerous clinical and experimental settings, including the well-known Swan-Ganz Catheter, discussed later in Section 3.4.1.

The main disadvantages of thermodilution are it is invasive and discrete, requiring additional saline injections for an updated *CO*. These disadvantages makes the technique undesirable for extended monitoring of unstable patients. Continuous thermodilution cardiac output techniques have been developed (Yelderman, 1990). These techniques can rely on direct heating of the blood, without needing to introduce an external fluid indicator. However the fluid bolus method still remains the clinical standard.

Thermodilution is not the only indicator method available. The LiDCO system (Section

[1] Specific heat is usually given the label *C*, but in this thesis *C* is already used for volumetric compliance.

3.5.2) uses a lithium dilution indicator method, which utilizes the change in concentration over time to measure the cardiac output. However this method is less common and equally invasive.

3.4.1 Pulmonary Artery Catheter (PAC)

In 1970 Dr William Ganz and Dr Jeremy Swan invented the Swan-Ganz Catheter, known today as the pulmonary artery catheter (PAC). The PAC is passed through the right heart and into the pulmonary artery with a thermistor near the tip. Through another port on the catheter the thermodilution indicator can be introduced directly into the atrium of the right heart (Sorensen et al., 1976). Hence, the PAC uses thermodilution to measure the right heart cardiac output using Equation 3.1.

Passing a catheter through the right heart is inherently highly invasive and the use of a PAC in of itself can cause additional complications for a patient (Dark and Singer, 2004; Evans et al., 2009; Matthieu et al., 2008). Previous studies have shown right heart catheterisation in patients suffering from shock, sepsis and acute myocardial infraction in the ICU, is likely to lead to significant increases in hospital cost, length of stay and mortality (Connors et al., 1996; Dalen and Bone, 1996). For patients with sepsis in combination with right ventricle dysfunction, is has been suggested PACs may be inadequate for the detection of left ventricle dysfunction (Vieillard-Baron and Cecconi, 2014).

Furthermore, PAC *CO* measurements have recently been shown to have systematic error of $\pm$26%, and are less accurate when therapies that alter *CO* are used (Yang et al., 2013). These issues makes it a suboptimal form of *CO* monitoring for patients with cardiac dysfunction, which is itself the target patient group. Despite these issues, the PAC is still considered by some as the gold standard *CO* technique, to which new technologies are often compared (Dark and Singer, 2004; Yang et al., 2013; Gust et al., 1998; Sakka et al., 2000). Others still state there is no gold standard measure of *CO*, but the PAC is simply a clinical standard (Wetterslev et al., 2016).

Despite the general acknowledgement that the PAC is a reliable discrete method, its use is declining due to it invasiveness, in favour or less invasive methods (Cecconi et al., 2014). These issues highlight the limited quality of measurement comparators in assessing new methodologies (Chase et al., 2014).

3.4.2 Transpulmonary Thermodilution

A less invasive alternative to the PAC is a similar method called transpulmonary thermodilution. This method still uses thermodilution, but with a thermistor normally in the abdominal aorta or femoral artery (Cecconi et al., 2014). Transpulmonary thermodilution still introduces the bolus upstream of the right heart but measures *CO* of the left ventricle down at the thermistor (Gust et al., 1998). Depending on the exact location of the thermistor, some introduced indicator will branch down a major artery before reaching the thermistor. Therefore, conservation of mass will be violated for Equation 3.1. While this method is less invasive, it still shares many of the same issues as the PAC. The main disadvantage being the method on its own is discrete, requiring successive indicator to be administered to get successive *CO* measurements.

In healthy patients, *CO* measurements at the right and left ventricles usually equate, although transpulmonary thermodilution does tend to result in slightly higher *CO* than corresponding PAC measurements (Tibby et al., 1997; Gust et al., 1998; Sakka et al., 2000; Godje et al., 1998; Segal et al., 2002). Transpulmonary thermodilution bias may be due to a combination of indicator loss and a reduction in heart rate (Sakka et al., 2000; Chaney and Derdak, 2002). In particular, the cold fluid can induce a temporary reduction in heart rate, the same reason room temperature indicator is argued as being preferable in the PAC (Nishikawa and Dohi, 1993). Finally, ventricle dysfunction may result in a divergence of these values (Chaney and Derdak, 2002), as could positive pressure ventilation (Goedje et al., 1999). Hence, there are several courses for potential bias and error.

3.5 Commercial Pulse Contour Analysis (PCA) Devices

Chapter 2 described how the heart provides the high pressure necessary to move blood through the circulation. Thus, there is a relationship between the pressure gradient and flow through the system. Pulse contour analysis (PCA) methods combine a measured arterial pressure waveform with mathematical models, attempting to relate the measured pressure to a continuous flow and/or *SV* estimate (see Chapter 4). They are usually non-additionally or minimally invasive, with some requiring a calibration *SV* measure to estimate patient specific model parameters, from the likes of thermodilution or similar technique (Marik, 2013). Those not requiring calibration, use a patient demographic database (i.e age, gender) to estimate model parameters (Grensemann, 2018).

Critchley and Critchley (1999) suggested acceptance of new *CO* estimation methods should be based on a maximum of $\pm$30% limits of agreement, when using Bland-Altman to compare the new method with a reference method, such as thermodilution. The $\pm$30% criterion considers the reference method to contribute $\pm$10–20% error. This criteria allows new PCA methods clinical applicability to be assessed.

3.5.1 PiCCO

PiCCO (Pulsion Medical Systems, Germany) is an improvement on PAC, as it is less invasive, sometimes being non-additionally invasive for ICU patients (Segal et al., 2002; Philips Electronics North America Corporation, 2002). The method requires central venous and arterial catheterisation, along with a transpulmonary thermodilution measurement to calibrate the pulse contour analysis parameters relating pressure and flow, to determine *CO* (Buhre et al., 1999). Specifically, thermodilution calibration relates the pressure of the catheterised artery to its compliance. The equation for *CO* is given in the manufacturers guide (Philips Electronics North America Corporation, 2002; Gödje et al., 2001), as heart rate (*HR*) multiplied by the terms that estimate *SV*. Although, as a commercial product, the exact algorithms used for the full implementation are not disclosed, representing some-

what of a black-box measurement to the user.

As long as a patient remains relatively stable, a single calibration enables *CO* to be continuously monitored using the arterial pressure pulse contour and a computer algorithm. However, re-calibration is required when there is a significant change in the hemodynamic state (Marik, 2013; Goedje et al., 1999; Philips Electronics North America Corporation, 2002; Rödig et al., 1999). Even in a stable patient, the manufacturer and other studies recommend recalibration occurs every 4-6 hours (Marik, 2013; Philips Electronics North America Corporation, 2002; Buhre et al., 1999; de Wilde et al., 2008).

Finally, as previously discussed in this section, it is sometimes desirable to limit fluid administration in unstable patients and this issue is a further drawback of all the thermodilution methods. PiCCO is no different, especially when the manufacture still recommends three transpulmonary thermodilutions per calibration (Philips Electronics North America Corporation, 2002).

3.5.2 LiDCO

LiDCO (LiDCO System, UK) is a pulse contour analysis method calibrated using a lithium bolus. It uses a change in concentration approach, rather than the thermodilution technique, as mentioned in Section 3.4. Instead of relating pressure to flow, the algorithms relate measured pressure to volume of the arterial tree (Montenij et al., 2011). This method has been shown to have similar performance when compared to other thermodilution calibrated PCA methods like PiCCO (Hadian et al., 2010; Montenij et al., 2011; Marik, 2013). Once again, recalibration is recommended every 8 hours or after acute hemodynamic changes, due to either changes in disease state or clinical intervention (Montenij et al., 2011; Marik, 2013).

3.5.3 FloTrac/Vigileo

FloTrac™ (Edwards Lifesciences, USA) is marketed as a PCA method which can calculated *CO* and *SV* variation without requiring external calibration, thus removing the invasiveness caused by indicator dilution methods (Slagt et al., 2014). Invasiveness is reduced further by using a peripheral arterial pressure line (Montenij et al., 2011). Instead of parameter identification via a calibration, it uses patient demographic and physical characteristics from the waveform. The exact algorithm the device uses is undisclosed and the method is thus difficult to critique. The device has had numerous software updates, which are said to improve performance by detecting and accounting for different hemodynamic conditions, e.g. hypertension.

Slagt et al. (2014) conducted a review of the device, drawing on data collected from 2234 patients. The results suggested the FloTrac/Vigileo was able to monitor CO with an average error less than 30% relative to a reference method, within the suggested criteria of Critchley and Critchley (1999). However, other studies have shown various FloTrac iterations have clinically unacceptable error when tracking changes in *SV* due to interventions (Hadian et al., 2010; Montenij et al., 2011; Marik, 2013), which is a critical clinical goal. It is possible the methods reliance on population demographic data favours healthy, stable patient behaviour, or introduces other biases since it is not more patient specific. Thus, in unstable patients it may be more beneficial to have patient specific model parameters, available, for example, to LiDCO and PiCCO through an initial calibration and re-calibrations as necessary.

3.5.4 esCCO

esCCO (Nihon Kohden®) is a truly non-invasive *CO* monitoring method, using an electrocardiogram (*ECG*) and photoplethysmogram (*PPG*) signals along with a pressure cuff. The arterial compliance is then estimated using a combination of pulse transit time (*PTT*), pulse pressure and patient demographic data (age, sex, height and weight) (Bataille et al., 2012).

Unfortunately, despite its non-invasive nature, the method has been shown to have poor performance, falling well outside the clinically acceptable accuracy outlined by Critchley and Critchley (1999), with errors of 49 - 61% reported (Bataille et al., 2012; Obata et al., 2017).

Using *PTT* from the periphery may be a contributor to the high errors of the device. Specifically, Section 2.2.2 discussed how compliance is mostly associated with the large arteries and particularly the aorta. Section 2.5.1 went on to explain how compliance was inversely proportional to pulse wave velocity (*PWV*), and when assessing arterial compliance/stiffness, it is most relevant to measure *PTT* along the aorta (Blacher et al., 1999b; Laurent et al., 2006; Nichols et al., 2011; Townsend et al., 2015; Balmer et al., 2017, 2018c). In contrast, measuring *PTT* to the periphery includes the stiffer peripheral arteries and arterioles, resulting in a more average arterial compliance, underestimating the compliance of the aorta (Balmer et al., 2018c).

In addition, *PTT* was measured from the *ECG* R-wave to the foot of the *PPG* signal. Thus, it is in fact not *PTT*, since the *ECG* R-wave does not signify the onset of ejection and a pulse wave, but ventricular contraction (Section 2.3.1). What has actually been measured is pre-ejection period (*PEP*)+*PTT*, where *PEP* is the duration from start of ventricular contraction, up to start of ejection. Therefore, the inclusion of *PEP* will overestimate the true *PTT*, underestimating *PWV* (Balmer et al., 2017, 2018c). Additionally, since *PEP* varies independent of *PTT*, ΔPWV would also incur error (Balmer et al., 2017, 2018c). These facts are of particular importance to this research and will be discussed in detail in Chapter 7.

3.6 Summary

This chapter summarised and analysed the common methods available to measure *SV*/*CO*. Generally, methods with high accuracy were of limited clinical use, either due to their invasiveness (flow probe and admittance catheter) and/or due to their discrete nature (PAC). PCA methods sought to overcome the limitations of more direct measures of *SV*/*CO*, by

using mathematical models and parameters to estimate a relationship between arterial pressure and flow/volume. Models with the highest accuracy tended to be those using established calibration techniques, which are still invasive, but enable these discrete measures to facilitate continuous monitoring. PiCCO is one of the more common PCA devices and has reasonable clinical accuracy, particularly in stable patients.

However there is still room for improvement in this space, particularly with regard to monitoring patients during unstable hemodynamics. Although PCA methods use a pressure waveform to infer some form of relationship to flow/volume, they return the clinically relevant *SV*/*CO* rather than an actual flow waveform estimate. However, Chapter 6 will show a PCA method whose *SV* accuracy was claimed to be clinically acceptable, but whose algorithm and implementation can lead to an unphysiological relationship between pressure and flow (Chapter 9). It is possible other commercial devices *SV* estimation is based on the same unphysiological flow waveform behaviour, but without the devices giving access to a flow waveform, it is not possible to know. However, access to a flow waveform estimate may help clinicians assess whether the resulting *SV*/*CO* estimates are derived from sound patient parameter identification, particularly following changes in patient hemodynamic state, which may not be otherwise indicated. This information may also help to indicate if and when re-calibration of the model is necessary.

The next chapter will explore the progressive development of PCA methods, which are fully described in literature as a foundation going forward in this research. The foundations of the different methods can be traced back to similar roots, but their implementation highlights their novel aspects. These models greatly influenced the development of the PCA method developed in this thesis, and likely the models implemented in the commercial devices of Section 3.5.

CHAPTER 4

Physiological Models

4.1 Introduction

Chapter 3 covered the common commercially available pulse contour analysis (PCA) based stroke volume (*SV*)/cardiac output (*CO*) monitoring devices. The exact algorithms and implementation are not fully disclosed for the commercial products, making their methodologies difficult to critique. This chapter focuses on PCA methods fully described in literature. Their description allows others to test and address their shortcomings, aiding in the development of improved models.

Often, in experimental settings, it is possible to measure and monitor dynamics not commonly measured in a clinical setting. The additional measures available in experimental settings can lead to the development of more complex cardiovascular models, which capture more of the dynamic nature of the cardiovascular system. The challenge is then taking an experimental model and implementing it in a clinically relevant manner. Since clinical relevance is one of the primary goals of this thesis (Section 1.4), this chapter focuses on those models and their implementation, leading to the development of the PCA method presented in this thesis.

4.2 The Corrected Characteristic Impedance Method

Equation 2.8 presented a method of calculating characteristic impedance as the ratio of changing pressure with changing flow. Measured pressure and flow waveforms from the aorta (P_{ao}, Q_{ao}) show how these variables change over the time of a beat. Thus, if the characteristic impedance of the aorta ($Z_{c,ao}$) was known, Q_{ao} could be estimated from the P_{ao} waveform. However, Section 2.5.2 noted Equation 2.8 applied to the forward travelling pressure and flow waves, while Section 2.5.4 explained the difference in shape between P_{ao} and Q_{ao} was due to reflected waves. This difference is why Section 2.5.2 stated Equation 2.8 is invalid when applied to the whole arterial waveform, but approximated $Z_{c,ao}$ when using only the systolic upstrokes of P_{ao} and Q_{ao}.

Wesseling (1983) recognised, even if Equation 2.8 could not exactly estimate the aortic flow waveform shape, what was clinically relevant was *SV*. Since *SV* was ejected during systole, Wesseling (1983) hypothesised a *reasonable SV* estimate could still be achieved using the whole systolic part of P_{ao}, as shown in Figure 4.1, and $Z_{c,ao}$, according to the following equation:

$$SV_{est} = \int_0^{t_{es}} Q_{est}(\tau)d\tau \approx \frac{1}{Z_{c,ao}} \int_0^{t_{es}} P_{ao}(\tau)d\tau \tag{4.1}$$

Where t_{es} is end-systole and Q_{est} is the estimated flow. Here, the use of *approximately* equal to ($\approx$) is in recognition that even though the integration happens only over systole, as previously stated, this approach will not result in a physiological accurate flow profile. However, it is still possible a $Z_{c,ao}$ value can be found that scales the unphysiological Q_{est}, such that a physiological *SV* value can be found.

For example, Jansen et al. (1990) used this method to estimate cardiac output (CO_{est}), by multiplying Equation 4.1 by heart rate (*HR*), as per Equation 1.1. $Z_{c,ao}$ was initially estimated ($Z_{c,ao,init}$) by an empirical equation, depending on patient age, *HR* and mean P_{ao}.

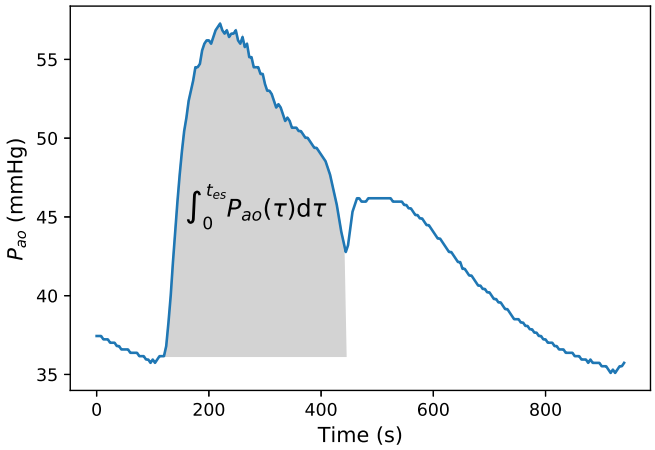

Figure 4.1: An example of the systolic area calculated as part of Wesseling (1983) *corrected characteristic impedance* method.

This method allowed an initial CO_{est} ($CO_{est,init}$). The value of $Z_{c,ao}$ was then "corrected" using a calibrating CO measure (CO_{mea}) from thermodilution:

$$Z_{c,ao} = \frac{CO_{est,init}}{CO_{mea}} Z_{c,ao,init} \tag{4.2}$$

Continuous CO could be estimated based on the calibrated $Z_{c,ao}$. Hence, Wesseling et al. (1993) later referred to this method as the *"corrected characteristic impedance"* method, which, despite its simplicity, provided evidence for the potential of PCA based models to estimate difficult to (directly) measure physiology. The fact it is possible to estimate an unphysiological flow profile, which if scaled correctly, can still provide an accurate estimate of SV, is also relevant to this thesis and will be discussed and further extended in Chapter 9.

Interestingly, PiCCO uses a *similar* approach to the corrected characteristic impedance method. While Section 3.5.1 stated the algorithms and implementation of PiCCO are not fully disclosed, the equation used to estimate CO is shown in the device documentation along with limited explanation (Gödje et al., 2001; Philips Electronics North America Corporation, 2002). It uses the area under the systolic part of the measured pressure waveform, as per Figure 4.1, along with a thermodilution calibration of model parameters. It differs

from the corrected characteristic impedance method by factoring the storage phenomena of the arterial tree, compliance, as per Section 2.2.2 (Gödje et al., 2001; Philips Electronics North America Corporation, 2002; de Wilde et al., 2008). Thus, it appears to fit somewhere between the corrected characteristic impedance method and windkessel based methods.

4.3 The Arterial Windkessel

The arterial windkessel forms the basis of many of the cardiovascular models applied to the systemic circulation covered throughout this thesis. Thus, this section covers the form and governing equations as used by the author, with variations covered in later sections relevant to specific models.

4.3.1 The Arterial Windkessel Theory

As covered in Section 2.2.2, compliance (C) of a vessel describes how its volume changes for a given change in pressure (Equation 2.1). The relatively high compliance of the large central arteries, compared to the periphery, enables them to store and release blood volume, during systole and diastole respectively. Thus, this compliance smoothes discontinuous ventricular ejection into semi-continuous blood flow through the arterial system (Frank, 1889; Westerhof et al., 1969; Oppenheim and Sittig, 1995; London and Pannier, 2010).

The storage-like behaviour of the arterial system is well described by Frank (1889), as the two-element windkessel, represented by a resistor (R) and capacitor (C) in parallel. The capacitor represents the storage or reservoir (volumetric) compliance of the arterial tree, and the resistor accounts for the pressure drop associated with the reservoir emptying into the periphery and subsequent venous system (Westerhof et al., 2009, 2010a). By *lumping* or averaging the vessel dynamics into single circuit elements, the model does not account for the wave propagation and reflections covered in Section 2.5.3 (Westerhof et al., 2009; Westerhof and Westerhof, 2017).

The two-element windkessel closely predicts a measured arterial pressure waveform dur-

ing diastole, but is a poor predictor of measured systolic pressure (Westerhof et al., 2009; Westerhof and Westerhof, 2017). Westerhof et al. (1971) sought to improve prediction by adding an input impedance element (Z_{in}) in series with the parallel *RC* circuit, to create the three-element windkessel. This additional element represents the impedance overcome by ventricular contraction to eject blood into the windkessel/reservoir component (Westerhof et al., 2009, 2010a). Since reflected waves are still not accounted for by the model, the windkessel input impedance is in fact a characteristic impedance $Z_{c,w}$, according to the definitions given in Sections 2.5.2 and 2.5.3 (Westerhof et al., 2009). Hence, it acts like, and is represented by, a resistor in Figure 4.2a, causing a pressure drop associated with the filling of the windkessel.

Specifically, Westerhof et al. (1971) showed by using aortic characteristic impedance ($Z_{c,ao}$) for $Z_{c,w}$, estimated via the water hammer equation (Equation 2.7), the three-element windkessel vastly improved pressure waveform estimation during systole over the original two-element model (Westerhof et al., 1971, 2009; Westerhof and Westerhof, 2015). In summary, the three-element windkessel model, shown in Fig 4.2a, is capable of describing global arterial tree behaviour based on pressure and flow relations in the large arteries. However, it is limited by design, in its ability to simulate spatially varying properties and dynamics (Westerhof et al., 2009; Westerhof and Westerhof, 2017).

4.3.2 Three-Element Windkessel Hydraulic Equations

For a particular beat whose start of systole is treated as time zero (t_0 = 0), the key model hydraulic equations, describing the equivalent circuit analogy of Fig 4.2a, are defined:

$$P_{mea}(t) = P_{ex}(t) + P_{res}(t) \tag{4.3}$$

where P_{mea} is the pressure waveform measured by an arterial catheter.

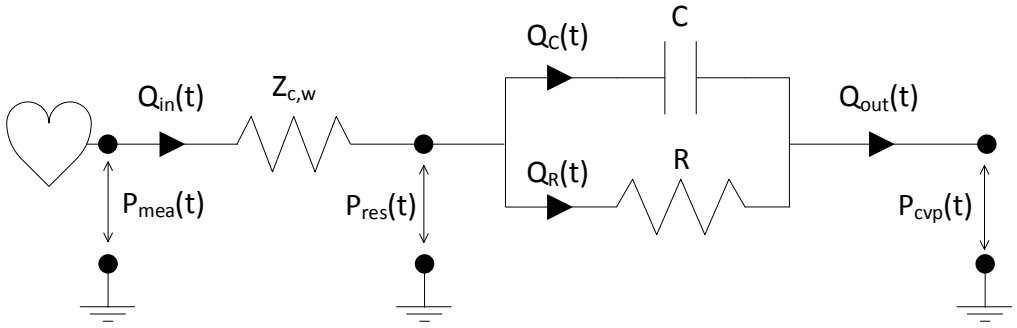

(a) Electrical circuit representation

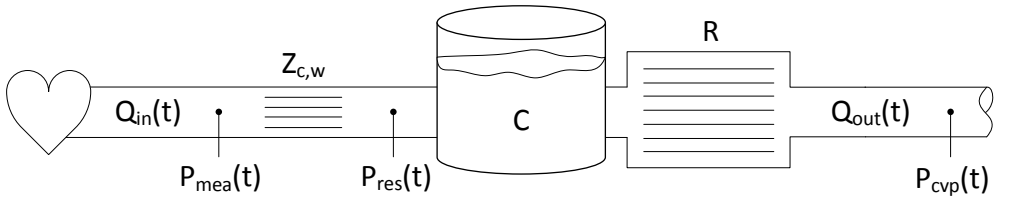

(b) Hydraulic circuit representation

Figure 4.2: The three element windkessel model. P_{mea} is the measured pressure in an artery. P_{res} is the modelled reservoir pressure and P_{cvp} is the pressure downstream of the reservoir, assumed to be the central venous pressure. Q_{in} is flow ejected from the ventricle, Q_C is the flow stored in the reservoir and Q_R is the flow out of the reservoir, equivalent to Q_{out}.

In the real arterial tree, P_{mea} varies over time and space, per Section 2.2.2. However, the lumping of arterial tree properties removes the spatial dependency, thus Equation 4.3 is assumed to vary only with time. P_{ex} is the *excess pressure* produced by ventricular contraction in order to eject blood into the reservoir (Q_{in}) (Westerhof et al., 2010a). Therefore, it is the pressure drop across the $Z_{c,w}$ element, equivalent to Ohms Law and defined:

$$Z_{c,w} = \frac{d(P_{mea}(t) - P_{res}(t))}{dQ_{in}(t)} = \frac{P_{mea}(t) - P_{res}(t)}{Q_{in}(t)} = \frac{P_{ex}(t)}{Q_{in}(t)} \tag{4.4}$$

Thus, in theory, if a measured flow waveform is used for Q_{in}, the P_{ex} waveform should share its shape, where $Z_{c,w}$ is simply the scalar relating them:

$$P_{ex}(t) = Q_{in}(t)Z_{c,w} \tag{4.5}$$

Since end-systole (t_{es}) marks the end of ventricular ejection, $Q_{in}(t \geq t_{es}) = P_{ex}(t \geq t_{es}) = 0$.

Therefore, during diastole ($t \geq t_{es}$), according to Equations 4.3, the measured pressure is simply the pressure decay associated with the emptying reservoir P_{res}. The implication of this will be made clear later in this section.

The flow, Q_{in}, can be separated into Q_C and Q_R, analogous to current in an electric circuit. Q_C is stored in the capacitor during systole and subsequently released during diastole, capturing vessel compliance. Flow out of the reservoir is the flow through the resistive element Q_R. These definitions yield:

$$Q_{in}(t) = Q_C(t) + Q_R(t) \quad where \quad Q_R(t) \equiv Q_{out}(t) \tag{4.6}$$

The pressure drop associated with the emptying of the reservoir is then defined:

$$P_{res}(t) - P_{cvp}(t) = Q_R(t)R = Q_{out}(t)R \tag{4.7}$$

Where P_{cvp} is the central venous pressure downstream of the lumped arterial reservoir, as shown in Fig 4.2a.

The changing pressure and volume of the modelled reservoir as it fills and empties is governed by its compliance, analogous to the relationship between stored charge and voltage potential of a capacitor. The volume stored in the reservoir over time (V_{res}) depends on the cumulative difference between flow in (Q_{in}) and out (Q_{out}) and thus Q_C, according to Equation 4.6. Therefore, the compliance of the reservoir can be written:

$$\begin{aligned} C = \frac{dV_{res}(t)}{d[P_{res}(t) - P_{cvp}(t)]} &= \frac{Q_C(t)dt}{d[P_{res}(t) - P_{cvp}(t)]} \\ &\approx \frac{[Q_{in}(t) - Q_{out}(t)]dt}{dP_{res}(t)} \end{aligned} \tag{4.8}$$

$$when \quad \frac{dP_{cvp}(t)}{dt} << \frac{dP_{res}(t)}{dt}$$

Equation 4.8 assumes changes in P_{cvp} are small within a given beat, relative to changes in P_{res}, simplifying the model equations. Alternatively, similar model accuracy can be achieved by assuming P_{cvp} is a constant value (Kamoi et al., 2017).

By rearranging Equation 4.8, an ordinary differential equation (ODE) describing how reservoir pressure changes through the course of a beat can be derived:

$$\frac{dP_{res}(t)}{dt} = \frac{Q_{in}(t) - Q_{out}(t)}{C} \tag{4.9}$$

Substituting Equations 4.3, 4.5 and 4.7 into 4.9, yields:

$$\frac{dP_{res}(t)}{dt} + P_{res}(t)\left(\frac{1}{Z_{c,w}C} + \frac{1}{RC}\right) = \frac{P_{mea}(t)}{Z_{c,w}C} + \frac{P_{cvp}(t)}{RC} \tag{4.10}$$

Equation 4.10 can be solved using the *integrating factor* method to describe a beat's reservoir pressure in terms of $Z_{c,w}$, R, and C:

$$P_{res}(t) = e^{-(\frac{1}{Z_{c,w}C} + \frac{1}{RC})t}\left(\int_0^t \left[e^{(\frac{1}{Z_{c,w}C} + \frac{1}{RC})\tau}\left(\frac{P_{mea}(\tau)}{Z_{c,w}C} + \frac{P_{cvp}(\tau)}{RC}\right)\right]d\tau + P_{mea}(0)\right) \tag{4.11}$$

Where $P_{mea}(0)$ is the pressure at the start of a beat (t_0 = 0). A reminder, here P_{cvp} is still shown as a variable with respect to time, but, as mentioned earlier, since its magnitude and variability is much less than arterial pressure, assuming a constant value has little impact on model performance (Kamoi et al., 2017).

Systolic Versus Diastolic Model Behaviour

Equation 4.11 describes the pressure for the entire beat, both systole and diastole, in terms of the three-element windkessel model. However, it is worth noting how this equation behaves during diastole. Returning to Equation 4.5 and how $Q_{in}(t \geq t_{es})$ = $P_{ex}(t \geq t_{es})$ = 0,

it was stated this equality would lead to P_{res} describing P_{mea} during diastole, according to Equation 4.3, yielding:

$$P_{mea}(t \geq t_{es}) = P_{res}(t \geq t_{es}) \tag{4.12}$$

Thus, for diastole only (Q_{in} = 0), Equation 4.9 would become:

$$\frac{dP_{res}(t)}{dt} = \frac{-Q_{out}(t)}{C} \quad where \quad (t \geq t_{es}) \tag{4.13}$$

And, similar to the full beat case, substituting Equation 4.7 into 4.13 gives:

$$\frac{dP_{res}(t)}{dt} = \frac{P_{cvp}(t) - P_{res}(t)}{RC} \quad where \quad (t \geq t_{es}) \tag{4.14}$$

At this point it should be no surprise the changing reservoir pressure during diastole ($\frac{\boldsymbol{dP_{res}}}{\boldsymbol{dt}}$) is only a function of parameters R and C, and downstream pressure (P_{cvp}), since during diastole the reservoir is strictly emptying, no longer being filled by ventricular contraction. This form of the ODE can be solved in a similar manner as Equation 4.10. The result is an equation describing the diastolic decay of the reservoir pressure, and, according to Equation 4.12, it also approximates the measured pressure decay:

$$P_{mea}(t \geq t_{es}) = P_{res}(t \geq t_{es}) = e^{\frac{t_{es}-t}{RC}} P_{mea}(t_{es}) + e^{\frac{-t}{RC}} \int_{t_{es}}^{t} e^{\frac{\tau}{RC}} \frac{P_{cvp}(\tau)}{RC} d\tau \tag{4.15}$$

By assuming P_{cvp} is constant over the beat, the equation can be simplified:

$$P_{mea}(t \geq t_{es}) = P_{res}(t \geq t_{es}) = (P_{mea}(t_{es}) - P_{cvp})e^{\frac{t_{es}-t}{RC}} + P_{cvp} \quad where \quad \frac{dP_{cvp}}{dt} = 0 \tag{4.16}$$

The key significance is for t $\geq t_{es}$, the three-element windkessel behaviour reverts to the same as the two-element windkessel, describing the pressure decay from $P_{ao}(t_{es})$ as an exponential decay with time constant RC (Frank, 1889; Westerhof et al., 2009). Otto Frank's two-element model's ability to accurately estimate diastolic pressure decay was discussed in Section 4.3.1 (Frank, 1889).

Calculating Q_{in} and Estimating SV

If the parameter products $Z_{c,w}C$ and RC can be found, P_{res} can be calculated according to Equation 4.11, and then P_{ex} from Equation 4.3. However, to calculate Q_{in} from Equation 4.5, $Z_{c,w}$ must be known, separately from its product with compliance in Equation 4.11. Two appropriate methods for estimating characteristic impedance were given in Section 2.5.2, the water hammer equation (Equation 2.7) and the ratio of the early systolic rise in the measured pressure and flow waveforms, per Equation 2.8. Equation 2.8 considered wave reflections negligible, consistent with the model assumptions in Section 4.3.1. Using the water hammer equation would require pulse wave velocity (PWV) and cross-sectional area to be known from the P_{mea} site. While Equation 2.8 requires flow to already be known, making it unsuitable if flow is the variable to be determined. Section 4.2 showed another method, where an initial estimate of $Z_{c,w}$ could subsequently be corrected using a calibrating measure of SV/CO.

For now, assuming $Z_{c,w}$ is found, stroke volume can then be estimated (SV_{est}) for a beat by integrating Q_{in}:

$$SV_{est} = \int_0^t Q_{in}(\tau)d\tau = \frac{1}{Z_{c,w}} \int_0^t P_{ex}(\tau)d\tau \tag{4.17}$$

Provided Q_{in} and P_{ex} are found to be zero during diastole, the integration limits of Equation 4.17 need only be the duration of systole. However, imperfect identification of $Z_{c,w}C$ and RC results in a non-zero P_{ex} during diastole, leading to a non-zero Q_{in} estimate during diastole. Thus, it is important to estimate $Z_{c,w}C$ and RC as accurately as possible, minimiz-

ing the error between P_{res} and P_{mea} during diastole. Parameter identification is specific to a given study's implementation of the method. It critically affects results, all else equal, for any identifiable model proposed. Therefore, it is discussed with respect to specific implementations in later sections and chapters, and not in general.

Applying the Three-Element Windkessel Model to an Aortic Pressure Waveform

Figure 4.3 shows Equation 4.11 applied to a measured aortic pressure waveform (P_{mea} = P_{ao}), with RC = 1.26 s and $Z_{c,w}C$ = 0.124 s. The method used to find these parameters and calculate P_{res} are developed by the author, and covered in detail in Chapter 11.

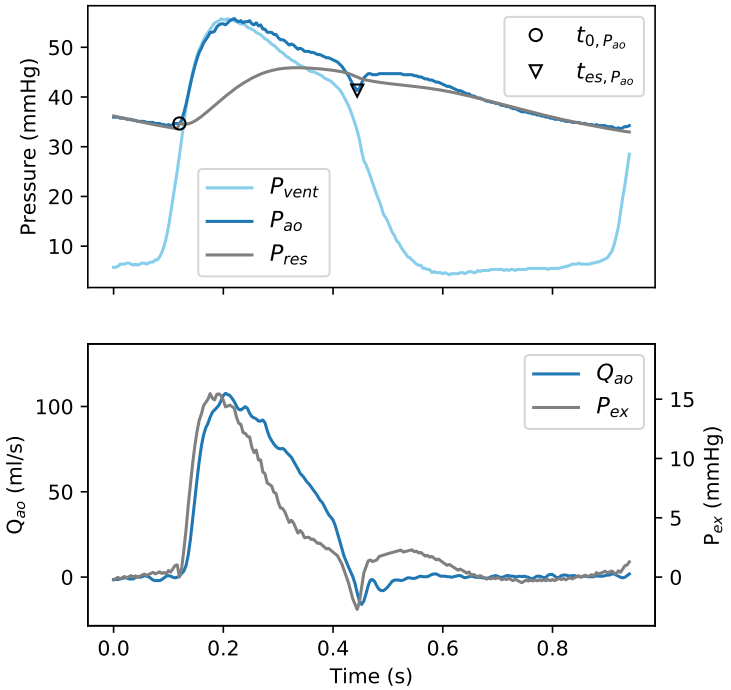

Figure 4.3: A realistic example of P_{res} and P_{ex} calculated from an aortic pressure signal (P_{ao}).

The similar shape of P_{ex} and Q_{ao} in Figure 4.3, illustrates the definition of P_{ex} given earlier in this section. Specifically, although P_{ex} is calculated from the arterial pressure waveform, it is thought of as being the pressure *in excess* of the the reservoir pressure (P_{res}), generated by ventricular contraction to eject blood into the reservoir (Q_{in}). Therefore, in theory, during ventricular ejection/systole as it's experienced in the aorta ($t_{0,P_{ao}} \leq t \leq t_{es,P_{ao}}$), Equation 4.3 could be re-written:

$$P_{mea}(t) = P_{ao}(t) = P_{ex}(t) + P_{res}(t) \approx P_{vent}(t), \quad where \quad t_{0,P_{ao}} \leq t \leq t_{es,P_{ao}} \tag{4.18}$$

Applying the Three-Element Windkessel Model to a Femoral Pressure Waveform

In a clinical environment, measured central arterial pressure is more likely to come from a region like the femoral artery, than the aorta, as it is less invasive (Cousins and O'Donnell, 2004). However, as discussed in Section 2.2.2 and 2.5.3, the pressure waveform is modified by changes in vessel properties and reflected waves as it travels away from the heart. Thus, if $P_{mea} = P_{fem}$, the modified shape and phase delay means Equation 4.18, relating P_{vent}, is no longer applicable, as shown in Figure 4.4.

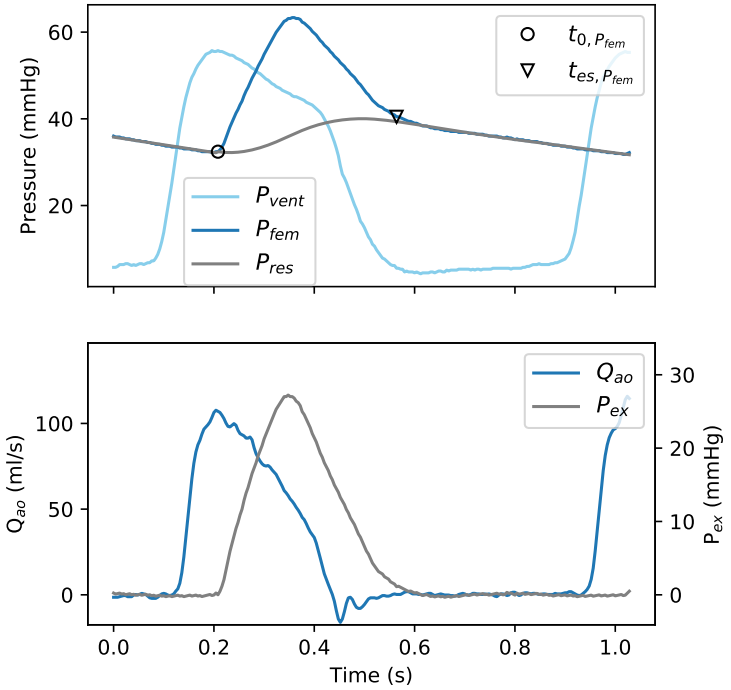

Figure 4.4: A realistic example of P_{res} and P_{ex} calculated from a femoral pressure signal (P_{fem}.

Regardless, Equations 4.11 and 4.3 can still be applied to P_{fem}, with Figure 4.4 showing P_{res} constructed with $RC = 1.78\,s$ and $Z_{c,w}C = 0.39\,s$. As expected, the ratio of P_{ex} to P_{res} has increased in the femoral signal, reflecting the slightly reduced compliance and the increase in excess pressure due to the windkessel/reservoir now being modelled using a P_{mea} further from the heart, compared to the P_{ao} waveform. Thus, the model behaviour is

as expected for different P_{mea} pulse contours (Balmer et al., 2018b), and will be discussed further in Chapter 11.

4.3.3 Three-Element Windkessel Limitations

As covered in Section 4.3.1, lumping spatially varying arterial properties into parameters $Z_{c,w}$, R and C limits the model's ability to describe spatial dynamics. Depending upon how the parameters are identified, this limitation means their identified values may not necessarily represent local arterial properties. Therefore, parameter values should be treated as relevant only within the model context (Westerhof et al., 2009, 2010a; Segers et al., 2015; Westerhof and Westerhof, 2017).

Despite this limitation, numerous studies have shown the usefulness of the three element windkessel for estimating global circulatory behaviour that is difficult to measure directly (Stergiopulos et al., 1992; Wesseling et al., 1993; Aguado-Sierra et al., 2008; Alastruey, 2010; Segers et al., 2015). The effects of these limitations are dependent on how the model is implemented, including how parameters are identified. These aspects of model structure and identification will be presented in detail, as required in later sections and chapters.

4.4 Wesseling's Three-Element Windkessel CO Estimation

Although Westerhof et al. (1971) created the three-element windkessel, it was Wesseling et al. (1993) who sought to use it as a method of estimating SV from a pressure waveform. Although the article does not define the specific hydraulic equations, as per Section 4.3.2, it refers to a figure equivalent to Figure 4.2a and states *"we would compute flow by simulating the response of a three-element model of arterial input impedance to arterial pressure"* and subsequently *"left ventricular SV is computed by integrating model flow during systole"*. Additionally, it has reference to the time constants RC and $Z_{c,w}C$ of Equation 4.11. Thus it is reasonable to believe the paper used the same fundamental theory expressed in Section 4.3.2, although the exact implementation is not specified.

For example, there is no clear explanation for how start and end-systole were identified in the study's measured pressure and estimated flow signals. The study used aortic pressure and radial pressure. It is possible end-systole was identified as the dicrotic notch in the aortic signal, as discussed in Section 2.3.1 and later in Chapter 8. However, the dicrotic notch is not visible on a radial pressure waveform under normal conditions.

4.4.1 Initial Parameter Identification

Parameter identification was not entirely based on pulse contour analysis. Instead, *cross-sectional area compliance* or *compliance per unit length* (C_A) was calculated as the derivative of Langewouters et al. (1984) equation, describing aortic area as a function of aortic pressure and maximum aortic area, (A_{max}), which itself was an empirical value based on patient age and sex. Since windkessel compliance (Equation 4.8) simulates volumetric compliance (Equation 2.1), converting C_A to C involves assuming a length as per Equation 2.5. Specifically, since the windkessel model does not have a physical length, a *characteristic length* (L_c) is assumed:

$$C = C_A L_c \tag{4.19}$$

As per Section 4.3.3, the windkessel compliance is not the true compliance of the aorta, or any specific part of the arterial tree. Instead, it is only the lumped compliance assumed to best describe the arterial tree globally. Hence, *characteristic length* is the length necessary for C_A's value to describe C as desired. Therefore a justification had to be made for the choice of L_c. Since Wesseling et al. (1993) had calculated C_A from the aorta, they also assumed L_c as a fixed aortic length of 80 cm. The fact the aorta represents most of the compliance of the arterial tree (Section 2.2.2) means this choice of L_c seems justifiable.

$Z_{c,w}$ was approximated from a combination of the water hammer equation (Equation 2.7), which depended on cross-sectional area, and the area compliance form of the Bramwell-

Hill equation (Equation 2.3) (Wesseling et al., 1993):

$$Z_{c,w} = \sqrt{\frac{\rho}{AC_A}} \tag{4.20}$$

Finally, R was initially assumed as the ratio of an assumed, generic mean pressure of 100 mmHg and a CO of 3 l min^{-1}. R was then iteratively updated per beat, based on the previous beat's measured mean pressure and modelled cardiac output (CO_{est}).

4.4.2 Calibrating Parameters with Measured Cardiac Output (CO_{mea})

Once initial parameters were identified, the initial empirically based patient A_{max} value was updated such that CO_{est} matched a CO_{mea} by thermodilution. This approach uses a similar method as used for $Z_{c,ao}$ in Wesseling's *corrected characteristic impedance* method (Equation 4.2). Calibrating the aortic area in this manner subsequently updated its dependencies, C_A and $Z_{c,w}$.

4.4.3 Estimating Flow and CO

Using the three-element windkessel and thermodilution CO calibration, Wesseling et al. (1993) managed to estimate flow profiles (Q_{est}) from the human aorta and radial artery, which appeared physiological. Thus, this approach improved upon the limitations of the *corrected characteristic impedance* method of Section 4.2. Unfortunately, the study on human patients only had access to intermittent CO measures, meaning the accuracy and physiological validity of the flow profiles could not be validated. However, the model did perform with similar accuracy to the *corrected characteristic impedance* method in estimating CO from the thermodilution measures (Wesseling et al., 1993).

4.5 The Reservoir-Wave Approach

Wang et al. (2003) rearranged Equation 4.7 for Q_{out} and substituted it into Equation 4.9 to yield the following differential equation:

$$\frac{dP_{res}(t)}{dt} = \frac{Q_{in}(t)}{C} - \frac{P_{res}(t) - P_{\infty}}{RC} \tag{4.21}$$

With the exception, instead of P_{cvp}, Wang et al. (2003) used a constant P_{∞}, which was still considered the pressure downstream of the windkessel, but whose value was the asymptotic pressure of the diastolic exponential decay. Given a long enough diastole P_{∞} would be the *mean circulatory pressure* (P_{mc}), the pressure when there is no blood flow, whose value is similar to P_{cvp} (Mynard and Smolich, 2017).

In a similar manner to the ODEs in Section 4.3.2, Equation 4.21 can be solved to give[1]:

$$P_{res}(t) = (P_{ao}(0) - P_{\infty})e^{-\frac{t}{RC}} + P_{\infty} + e^{-\frac{t}{RC}} \int_0^t e^{\frac{\tau}{RC}} \frac{Q_{in}(\tau)}{C} d\tau \tag{4.22}$$

Where, as a reminder, $P_{ao}(0)$ is the aortic pressure at the start of the beat, considered time zero (t_0 = 0).

Equation 4.22 describes the pressure of the windkessel/reservoir in terms of R and C, thus representing the two-element windkessel or the parallel RC component of Figure 4.2a (Westerhof et al., 2009). In particular, the similarities, as well as the differences, of Equation 4.22 with Equation 4.16 should be noted. Specifically:

- As mentioned, P_{∞} is used instead of P_{cvp}.
- Equation 4.22's initial condition is start-systole $P_{ao}(0)$, instead of end-systole, since the full beat is being described, as opposed to just diastole.

[1] Wang et al. (2003) mistakenly dropped the first exponential terms t, the correct solution is also shown in (Aguado-Sierra et al., 2008; Alastruey, 2010)

- The first two terms of Equation 4.22 are of the same form as Equation 4.16, describing how the pressure decays in the reservoir.

- Equation 4.22 includes the integral of inflow divided by compliance, which according to Equation 2.1, describes the increase in reservoir pressure for Q_{in}.

To solve Equation 4.22 for P_{res}, Wang et al. (2003) needed P_{ao}, Q_{ao} (for Q_{in}) and the parameters R, C and P_{∞}. The waveforms P_{ao} and Q_{ao} were measured in dogs, using a pressure catheter and aortic flow probe, respectively. The parameters, R, C and P_{∞} were found using *"fminsearch"*, a nonlinear least squared error search algorithm provided in MATLAB (Mathworks, Natick, MA, USA). More specifically, the parameters were identified using the condition outlined in Equation 4.12, with the optimization performed on the final two-thirds of the diastolic part of the measured pressure signal. This method of parameter identification is a specific example of the more general concept of *fitting* an equation to data in order to identify its parameters and will come up in later sections and chapters.

Implementing the model in this way, Wang et al. (2003) found the resulting difference between the P_{ao} and P_{res} was a pressure waveform whose shape matched the measured flow waveform. In other words, Wang et al. (2003) had found the excess pressure described by Equations 4.3 and 4.5. Wang et al. (2003) also found the ratio of P_{ex} and Q_{ao} gave a value similar to the aortic characteristic impedance ($Z_{c,ao}$).

The results of Wang et al. (2003) were supportive evidence for the the inclusion of the third impedance element to the two-element windkessel (Westerhof et al., 2009). Furthermore, it improved on Wesseling et al. (1993) (Section 4.4) by validating the estimated flow waveforms of the three-element windkessel. However, Wang et al. (2003) interpreted the result more literally, citing the pressure and flow dynamics of the real arterial tree appeared to follow a description of wave propagation given by Lighthill (1978), where measured pressure was the sum of an *"undisturbed pressure with its hydrostatic distribution"* (P_{res}) and an *"excess pressure whose gradients produce fluid accelerations"* (P_{ex}). Thus, the method in Wang et al. (2003) became known as the *reservoir-wave* approach (RWA), for which an

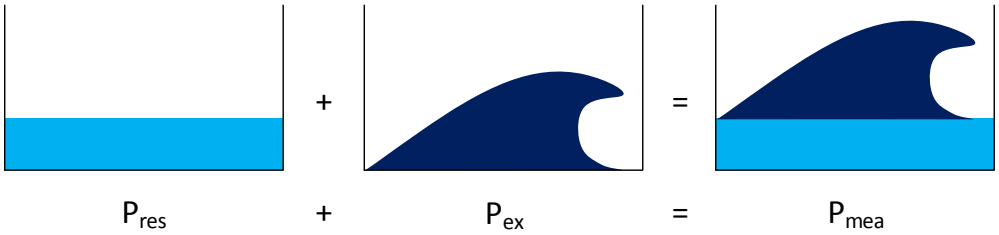

Figure 4.5: The reservoir-wave approach assumes a measured pressure can be represented as two components, a hydrostatic *reservoir* and an *excess* wave component that travels along the reservoir, much like a wave appears to travel across the surface of a body of water.

analogy is shown in Figure 4.5 (Tyberg et al., 2014; Mynard and Smolich, 2014a; Westerhof and Westerhof, 2015).

By attributing all the wave behaviour to P_{ex}, Wang et al. (2003) re-interpreted Equation 4.3 as capable of describing *both* time and spatial dynamics:

$$P_{mea}(x,t) = P_{ex}(x,t) + P_{res}(t) \tag{4.23}$$

This subtle change in the equation and its literal interpretation is what differentiates the RWA from the traditional lumped windkessel models.

4.5.1 Reservoir-Wave or Waves?

The RWA interpretation called into question a lot of the wave behaviour covered in Section 2.5. In particular, Wang et al. (2003)'s RWA concluded the difference between the shape of the measured pressure and flow waveforms had been explained by separation of pressure into reservoir and wave components. Specifically, the fact Q_{ao} had the same shape as P_{ex} implied the Q_{ao} profile was not due to reflected wave behaviour, per Section 2.5.4, but simply due to the forward travelling wave and entirely attributed to P_{ex}. With wave behaviour confined to P_{ex} and thus systole, diastolic decay of P_{ao} must be interpreted as volume-related pressure of the emptying reservoir, per Equation 4.12 - 4.16. Thus, the RWA interpretation of arterial pressure and flow dynamics concluded there is minimal reflected wave behaviour under normal conditions (Segers et al., 2012).

While this dualistic interpretation is simple and its mechanisms intuitive, it does present some inconsistencies. First, as discussed in Section 4.3.2 and seen from a comparison of Figures 4.3 and 4.4, the reservoir pressure does propagate along the arterial tree, and its waveform shape changes with respect to measurement location. Thus, P_{res} is in fact wave like, as others have also found (Segers et al., 2012, 2015; Mynard et al., 2012; Mynard and Smolich, 2014a).

P_{res} waveform shape being spatially dependent should not come as a surprise, the reasoning has already been given. Specifically:

- It is dependent on compliance, which changes throughout the arterial tree (Section 2.2.2).
- The storage of blood in the arteries was due to a rapid ventricular ejection exceeding flow to the periphery, which began by expanding the aorta and this expansion propagated along the arterial tree *making room* for the ejected *SV* (Section 2.3.1) (London and Pannier, 2010; Mynard et al., 2012).

It is only if the heart stopped beating, that pressure would equally distribute throughout the arterial tree, to the so called mean circulatory pressure (P_{mc}). This pressure would be the true *"undisturbed pressure with its hydrostatic distribution"* described by Lighthill (1978), not P_{res} as in Wang et al. (2003), (Mynard and Smolich, 2014b).

Secondly, Figure 4.3 shows in early diastole, following the dicrotic notch, it is possible for the aortic pressure to briefly rise. This phenomena is not captured by the exponential decay of P_{res} and is thus attributed to P_{ex} through Equation 4.3. However, this non-zero P_{ex} in diastole, contradicts its definition according to Equation 4.5. Specifically, since Q_{ao} = 0, P_{ex} should be zero. This issue is an example of the imperfect parameter identification outlined in Section 4.3.2. However, and in contrast, the parameters in Figure 4.3 have minimized the error between P_{res} and P_{ao} as per the condition of Equation 4.12.

Hence, if there is no better choice of parameters, the behaviour being observed falls out-

side of the behaviours described by the model, outside of $Z_{c,w}$, R and C, outside of P_{res} and P_{ex}, and thus outside of the RWA. So the question is, what causes the rise in pressure after the dicrotic notch? And why can it not be described by RWA? The answer to the former was covered in Section 2.5.3, it is caused by the reflected pressure waves arrival in late systole/early diastole, increasing pressure as observed by Murgo et al. (1980). The reason this rise cannot be described by the RWA is it assumes no wave behaviour during diastole, consistent with the limitations of the windkessel models on which it is based (Section 4.3.3). Thus, the ease of fitting P_{res} to P_{mea} is conditional on the measured diastolic decay being exponential (Segers et al., 2012). This limitation is possibly why Wang et al. (2003) chose to only use the last two-thirds of diastole when enforcing the condition of Equation 4.12.

The implications of the RWA internal inconsistencies have been covered well by others (Segers et al., 2012; Mynard et al., 2012; Mynard and Smolich, 2014a,b; Segers et al., 2015; Westerhof and Westerhof, 2015, 2017). For example, Segers et al. (2015) evaluated the assumption changes in P_{res} were proportional to changes in reservoir volume and showed during systole, P_{res} was lower than expected for the increase in volume (Segers et al., 2015). Mynard et al. (2012) showed by attributing all wave phenomena to P_{ex}, the RWA did not accurately represent wave travel in a system with known reflection sites and known impedance mismatches (Mynard et al., 2012; Mynard and Smolich, 2014a).

The fact P_{res} is a propagated disturbance and therefore not all wave behaviour can be attributed to P_{ex}, was later acknowledged by proponents of RWA (Tyberg et al., 2014). However, a significant amount of debate has continued to occur throughout the last decade about the validity of the approach (Aguado-Sierra et al., 2008; Alastruey, 2010; Borlotti and Khir, 2011; Mynard et al., 2012; Segers et al., 2012; Mynard and Smolich, 2014a,b; Tyberg et al., 2014; Mynard et al., 2015; Segers et al., 2015; Westerhof and Westerhof, 2015; Mynard and Smolich, 2017; Westerhof and Westerhof, 2017). The benefit of such debates is it has encouraged a re-examining of the different methods used for analysing arterial dy-

namics (Westerhof and Westerhof, 2017), and an addressing of conventional wave analysis methods shortcomings (Mynard and Smolich, 2014a, 2017).

4.6 Pressure Pulse Contour Derived Model Parameters

Wang et al. (2003) found P_{res} using a measured flow waveform. A flow waveform is a measurement usually confined to experiemental settings due to its invasiveness, as discussed in Chapter 3. Aguado-Sierra et al. (2008) implemented what they called the RWA in a manner that did not require Q_{in}. Although they acknowledged the three-element windkessel was an *"alternative way to express the reservoir component of the model"* they proposed, they also believed they were the first to hypothesis the electrical analogy as a description for the combined reservoir and wave components. However, the electrical circuit analogy had previously been shown in both Westerhof et al. (1971) and Wesseling et al. (1993). The only difference is these earlier studies did not interpret their models literally, as per the RWA.

Therefore, it should be clear from Section 4.3.2 and 4.4 that Aguado-Sierra et al. (2008) was not the first to describe a method of calculating P_{res} without Q_{in}, nor were they the first to imploy the electrical analogy. It is possible the lack of derived hydraulic equations relating to the electrical circuit in Wesseling et al. (1993) made Aguado-Sierra et al. (2008) believe their formulation of the equations was more novel than it was. Although this conclusion is speculatory, as the authors do not cite Wesseling et al. (1993), so it is possible they were unaware of the study. Nonetheless, despite different nomenclature for parameters in Aguado-Sierra et al. (2008), the resulting equations derive from the traditional three-element windkessel exactly, with parameters equivalent to $Z_{c,w}$, R and C.

What is slightly different is how Aguado-Sierra et al. (2008) calculates P_{res}. Instead of solving Equation 4.10 for P_{res} of the whole beat, giving Equation 4.11, they solved it separately for systole and diastole. The diastole part being the the same as Equation 4.16, except like Wang et al. (2003), P_{∞} was used in place of P_{cvp}. However, of the two analyses conducted in

Aguado-Sierra et al. (2008), one assumed P_∞ = 0, the other $P_\infty \approx$ mean P_{cvp} (Aguado-Sierra et al., 2008).

The author of this thesis assumes they used two different equations for P_{res} to simplify parameter identification. They identify their equivalent form of RC by fitting Equation 4.16 to measured data, similar to Wang et al. (2003) in Section 4.5. Their systolic equation for P_{res} depends on their equivalent forms of parameters RC and $Z_{c,w}C$. $Z_{c,w}C$ is found, along with P_{res} during systole, by enforcing (zeroth order) continuity with the diastolic equation. However, Figure 4.6 shows their resulting P_{res} can be first order discontinuous (discontinuous in its first and higher derivatives) in terms of continuity and thus physical and physiological relevance.

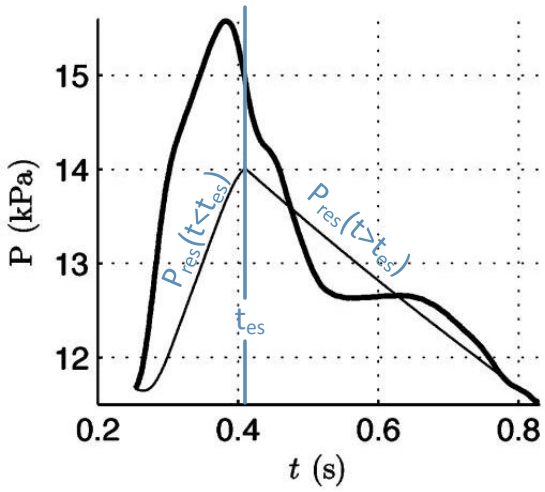

Figure 4.6: Example from Aguado-Sierra et al. (2008), showing the measured pressure waveform with P_{res}. Figure has been modified to show t_{es} and respective systolic and diastole P_{res}.

By solving P_{res} for a whole beat, as per Equation 4.11, Figures 4.3 and 4.4 show P_{res} should be continuously differentiable. Another interesting feature of Figure 4.6 is the measured diastolic pressure not being well described by the assumption of exponential decay. This limitation of the three-element windkessel was discussed in Section 4.5.1 and will be discussed further in Chapter 9.

Regardless, Aguado-Sierra et al. (2008) showed it was possible to estimate P_{res} from just the pressure waveform contour. The study did not rely on population demographic data

to estimate model parameters like Wesseling et al. (1993), in Section 4.4. However, this choice means parameters were only identified in their product forms, RC and $Z_{c,w}$C, and not individually. The advantages of calculating parameters in this way will be discussed further in Section 4.7.2.

4.7 Patient Specific Model Parameters

Sections 4.4 and 4.6 each included different approaches to windkessel model parameter identification. Firstly, Wesseling et al. (1993) (Section 4.4) calculated the model parameters individually. This had the advantage of knowing precisely how each lumped parameter would contribute to model behaviour. The first foreseeable disadvantage was $Z_{c,w}$ and C initially relied on population demographic data (Section 4.4.1), meaning the initial values were not *patient specific*. Estimating parameters, based on patient demographics, seems a reasonable approach for monitoring healthy, stable patients for whom the population data is likely representative. But Section 3.5.3 suggested the population demographic parameter identification may have contributed to FloTrac's poor performance when monitoring changes in SV (Hadian et al., 2010; Montenij et al., 2011; Marik, 2013).

4.7.1 Static Model Parameters

Wesseling et al. (1993) mitigated the potential issue of estimating parameters based on demographic data, by subsequently updating them with a CO calibration (Section 4.4.2). This ensured the parameters were patient specific *at the time of the calibration*. Thus, calibrated parameters can be considered *static* and are sufficient provided the patients state does not change, else re-calibration would be required. The need for PCA re-calibration was discussed for the PiCCO and LiDCO devices covered in Section 3.5.

4.7.2 Dynamic Model Parameters

Aguado-Sierra et al. (2008) (Section 4.6) calculated the parameters in their product form, $Z_{c,w}C$ and RC, as they appeared in Equation 4.11. This method had the disadvantage of not

knowing how each individual parameter was effecting the resulting P_{res}. However, the advantage was $Z_{c,w}C$ and RC are found beat-to-beat, specific to each beat's measured pressure waveform. Thus, the product forms of the parameters are *dynamic*, changing to reflect the current hemodynamic state. In this way, assuming perfect parameter identification, and valid model assumptions, P_{res} and P_{ex} would always be found satisfying Equation 4.3.

4.8 Summary

This chapter covered the development of arterial models from literature with the ability to relate measured pressure to $Q_{ao}/SV/CO$. This section was by no means exhaustive, with far more complex models, which are not readily identified at the bedside (Chase et al., 2018), not considered here (Smith et al., 2004, 2005; Pironet et al., 2013, 2016). Their exclusion is with regard to the goals of this thesis, a model must by dynamic enough to adequately capture changing patient hemodynamics, but simple enough to be implemented in a clinical environment. Thus, this section covers the necessary background literature informing the decisions for the model development and testing in this thesis.

This chapter gave particular focus to the arterial system modelled as a *windkessel*. When interpreted literally, as in the RWA, it vastly oversimplifies the complex wave propagation of the arterial tree. However, even those that spoke against the RWA, acknowledge the usefulness of the three-element windkessel (Segers et al., 2012, 2015; Mynard et al., 2015; Westerhof and Westerhof, 2017). After-all, 32 years passed between the three-element windkessels development, in Westerhof et al. (1971), and the RWA of Wang et al. (2003). The debates of the last decade were a re-evaluating of the windkessel limitations, covered extensively in Sections 4.3.3 and 4.5. To quote Nicolaas Westerhof, with who the three-element windkessel was credited, *"Windkessels model the arterial system but the arterial system is not a Windkessel."* Or George E. P. Box, a famous 20th century statistician, *"all models are wrong, but some are useful"*. The subsequent chapters will show the ways in which the windkessel model is wrong and in what ways it can still be useful.

CHAPTER 5

Experimental Data

5.1 Introduction

The previous chapters have covered the thesis goals and necessary background literature for a reader to understand the authors own work, which is covered in the remaining chapters. To begin with, this chapter details the experimental protocols for the three data sets used throughout this thesis (Balmer et al., 2017, 2018c,a,b). It also covers the initial signal processing common to all later analyses, enabling the more in-depth analysis presented in later chapters. These signal processing functions include filtering and discrete derivative implementations, as well as development of specific algorithms for peak, trough, and start-of-systole detection. End-systole detection was critical only in some analyses and is thus covered later in Chapters 8 and 10.

5.2 Porcine Trial Protocols

Data in this study was obtained from a prior series of pig experiments conducted at the Centre Hospitalier Universitaire de Liège, Belgium. Ethics approval for the experimental procedures, protocols and use of the data was provided by the Ethics Committee of the

University of Liège Medical Faculty, permit numbers 1452 & 14–1726, respectively. Their guidelines are consistent with the Guide for the Care and Use of Laboratory Animals published by the US National Institutes of Health (NIH Publication No. 85–23, revised 1996), as well as EU DIRECTIVE 2010/63/EU on the protection of animals used for scientific purposes.

15 pure pietrain pigs, weighting 18.5–29 kg, were used in the analysis across 3 protocols. Initial sedation and anaesthesia was achieved using Zoletil ($0.1\,\mathrm{ml\,kg^{-1}}$) and diazepam ($1\,\mathrm{mg\,kg^{-1}}$). Continuous infusion of sufentanil ($0.1\,\mathrm{ml\,kg^{-1}\,h^{-1}}$ at $5\,\mu\mathrm{g\,ml^{-1}}$), Thiobarbital ($0.1\,\mathrm{ml\,kg^{-1}\,h^{-1}}$) and Nimbex ($1\,\mathrm{ml\,kg^{-1}\,h^{-1}}$ at $2\,\mathrm{mg\,ml^{-1}}$) was delivered via a superior vena cava catheter to maintain sedation and anaesthesia. A GE Engstrom CareStation mechanical ventilator (GE Healthcare, Waukesha, US) was used via a tracheostomy with a baseline positive end-expiratory pressure (PEEP) of 5 $\mathrm{cmH_2O}$ and tidal volume of $10\,\mathrm{ml\,kg^{-1}}$. Blood pressure was measured in the aortic arch (P_{ao}) and either the abdominal aorta, iliac or femoral artery. For simplicity, the distal arterial pressure is referred to as P_{fem}. Pressure measurements used high fidelity pressure catheters (Transonic, Ithaca, NY, USA). Left ventricular pressure (P_{vent}) and volume (V_{vent}) were directly measured using 7F micromanometer-tipped admittance catheters (Transonic Ithaca, NY, USA) inserted into the ventricle through the right carotid artery. Some protocols had access to additional measures, including electrocardiogram (ECG), proximal aortic blood flow (Q_{ao}) and central venous pressure (P_{cvp}). These additional measures are discussed in the Sections 5.2.1, 5.2.2 and 5.2.3, and the implications for a protocol not having access to the additional measures are discussed Section 5.4.3, 5.4.4 and 12.2.1. A summary table of the relevant measures available from each protocol is included in Section 5.2.4 Table 5.1, after the protocol descriptions.

Once the pigs were sedated, anaesthetised and instrumentation was in place, a period of baseline/control data was recorded before any interventions. At the end of the protocol, euthanasia was performed via a bolus of pentobarbital ($30\,\mathrm{mg\,kg^{-1}}$) and sufentanil ($5\,\mu\mathrm{g\,kg^{-1}}$) causing respiratory arrest.

5.2.1 Protocol D, Dobutamine

Pigs D1–D5 are associated with the *dobutamine* protocol. In addition to the instrumentation covered in Section 5.2, this protocol included an *ECG* signal measurement. The experimental procedure was defined:

1. The first intervention was a ventilation recruitment manoeuvre (RM), where each pig underwent several step-wise changes in positive end-expiratory pressure (PEEP). RMs involved increasing PEEP with 5 cmH_2O steps to a maximum of 15 cmH_2O for Pig D5 and 20cmH_2O for Pigs D1–D4. Increases in PEEP can reduce systemic venous return to the right heart and increase pulmonary resistance, representing decreased preload and increased afterload, respectively (Luecke and Pelosi, 2005; Marik, 2010). Thus, if flow in and out of the right ventricle is impeded, flow into the left ventricle can also fall, decreasing left ventricular preload, ejected SV and arterial pressure (Wallace et al., 1963; Luecke and Pelosi, 2005; Marik, 2010).

2. Rapid fluid boluses were administered in 180 ml steps, up to a total of 900 ml for Pigs D1 –D4, and 720 ml for Pig D5. Fluid boluses are common therapies in intensive care, used to increase the blood volume in the hope of improving preload and stroke volume (*SV*) (Michard and Teboul, 2002; Reuter et al., 2002; Cecconi et al., 2015). However, the response to fluid administrations is clinically variable and depends on how the body distributes the introduced bolus (Michard and Teboul, 2002).

3. The protocols name is characterised by the use of a continuous dobutamine infusion. Pigs D3 and D4 were infused at a rate of 2.5 $\mu g\,kg^{-1}\,min^{-1}$ while Pigs D1, D2, and D5 were infused at 5 $\mu g\,kg^{-1}\,min^{-1}$. Dobutamine increases contractility of the heart and is commonly used to increase cardiac output (*CO*) in a clinical setting, but it can also act as a vasodilator (Ruffolo, 1987; Ellender and Skinner, 2008).

4. During the dobutamine infusion, a RM was performed in the same manner as described in 1.

5. In the transition between interventions, a vena cava occlusion (VCO) was first performed, using a Fogarty balloon. This technique allows changes in the contractile state of the heart to be assessed through the gradient of the end-systolic pressure volume relationship (ESPVR) (Sato et al., 1998).

5.2.2 Protocol S, Sepsis

Pigs S1–S6 are associated with the *sepsis* protocol. In addition to the instrumentation covered in Section 5.2, this protocol included an aortic flow probe (Transonic, Ithaca, NY, USA) and a pressure catheter in the superior vena cava P_{cvp}. A flow probe clamps around the aorta in a manner that does not constrict it. It was placed near the aortic valve to measure ventricular ejection, Q_{ao}. Probe placement was achieved via median sternotomy, after which the thorax was clamped closed for the remainder of the experiment. The experimental procedure was defined:

1. A RM like those in the dobutamine protocol, outlined in Section 5.2.1, is performed. Pig S4's RM maximum PEEP reached 15 cmH_2O, while the other sepsis pigs maximum PEEP was 20 cmH_2O.

2. A 500 ml infusion of saline solution, over a 30 min period. Fluid resuscitation therapy is one of the primary clinical interventions used for patients with severe sepsis, aiming to increase the circulatory volume, ventricular preload and *SV* (Michard and Teboul, 2002; Reuter et al., 2002; Cecconi et al., 2015).

3. E. Coli lipopolysaccharide (endotoxin) was infused over a 30 min period (0.5 $mg\,kg^{-1}$). This produces a septic shock like response: inflammation, capillary leakage, decreased afterload, hypovolemia, tissue hypoxia and eventual cardiac failure (Nguyen et al., 2006; Merx and Weber, 2010).

5.2.3 Protocol V, Vena Cava Occlusion (VCO)

Pigs V1–V4 are associated with a study involving extracorporeal support (Habran et al., 2018). However, aspects of interest from this protocol include the vena cava occlusions (VCO) preformed using a Fogarty balloon prior to extracorporeal support initiation. The VCO was a short term event designed to cause rapid reduction in preload, and thus *SV* per Section 2.4.2 and Figure 2.9 (McKay et al., 1986; Sato et al., 1998). This specific event, is the only data used from these experiments in this research.

5.2.4 Data Summary

Table 5.1 summarizes the measured data captured in each protocol.

Table 5.1: Summary of measurements available to each experimental protocol.

Protocol	ECG	P_{vent}	V_{vent}	P_{ao}	Q_{ao}	P_{fem}	P_{cvp}
D	✓	✓	✓	✓		✓	
S		✓	✓	✓	✓	✓	✓
V		✓	✓	✓		✓	✓

5.3 Data Selection

Each pig experiment was recorded as a single Notocord data file (Instem, Croissy-sur-Seine, France). Acquisition rates varied, with 1000Hz used for Protocol D, and 250Hz for Protocols S and V. As experiments lasted for several hours, data was subsequently separated into shorter distinct stages of the experimental protocol for analysis:

5.3.1 Protocol D Stages (Figure 5.1):

1. *Control:*

   Period of stable baseline measures, prior to hemodynamic interventions.

2. *High PEEP:*

   The highest PEEP of the RM following *Control*.

3. *High fluids:*

   The period following the pigs final 180 ml fluid administration, taking it to its highest fluid state.

4. *Dobutamine:*

   During continuous dobutamine admission.

5. *Dobutamine High PEEP:*

   The highest PEEP of the RM during continuous dobutamine admission.

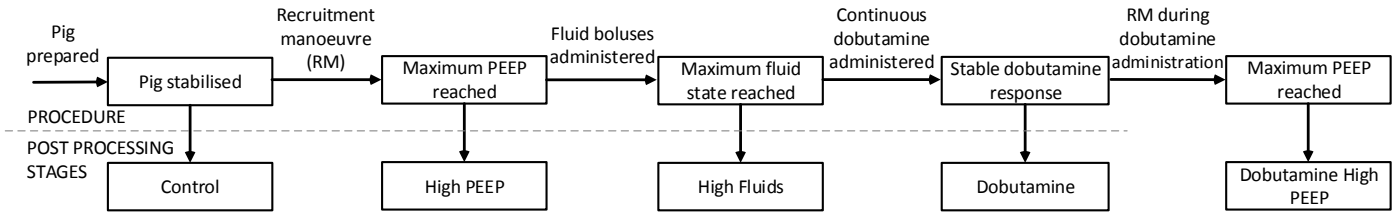

Figure 5.1: Dobutamine protocol experimental procedure and post processing stages. The experimental procedure was captured as a single data file, sampled at 1000 Hz.

5.3.2 Protocol S Stages (Figure 5.2):

1. *Control:*

   Period of stable baseline measures, prior to hemodynamic interventions.

2. *High PEEP:*

   The highest PEEP of the RM following *Control*.

3. *Before endo:*

   Data measured just prior to the start of endotoxin infusion and following 500 ml saline infusion.

4. *Start endo:*

   Data measured during the start of endotoxin infusion.

5. *End endo:*

   For Pigs S2, S3 and S5, this stage refers to beats just prior to the endotoxin infusion finishing. Pigs S1, S4 and S6 responded more dramatically to the endotoxin infusion and thus, various pressure measures dropped so low as to suggest cardiac/circulatory failure before the full 30 min was complete. Therefore, the End endo stage for Pigs

S1, S4 and S6 are during the late part of their rapid decline in hemodynamic stability.

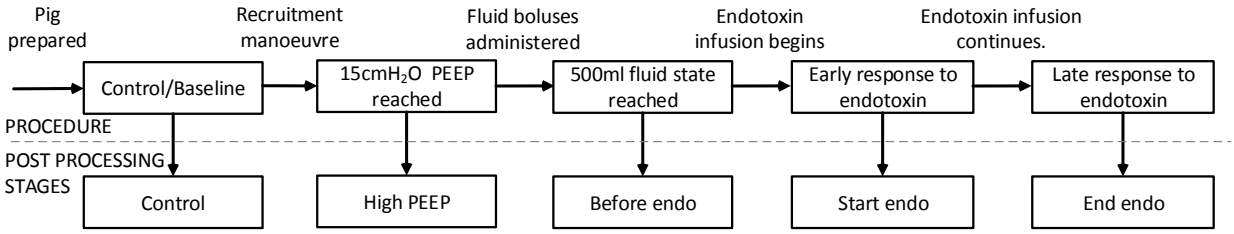

Figure 5.2: Sepsis protocol experimental procedure and post processing stages. The experimental procedure was captured as a single data file, sampled at 250 Hz.

5.3.3 Protocol V Stages

1. *Control:*

   Period of stable baseline measures, prior to hemodynamic interventions.

2. *VCO:*

   Data captured during Fogarty balloon inflation, causing vena cava occlusion, and subsequent recovery following balloon deflation.

Subsequent analysis chapters refer back to these protocols, and outline specifically which protocol(s) and pigs were used, as well as the number of heart beats. The number of beats used from each stage was analysis specific, since it depended on which pigs were used and the relevance of weighting/equal representation of pigs and stages to the analysis.

5.4 Initial Signal Processing

5.4.1 Discrete Derivatives

Some analyses in later chapters use the first ($\frac{dP}{dt}$) and/or second derivative of pressure with respect to time ($\frac{d^2P}{dt^2}$). As data from experiments are discrete, having been sampled digitally, these derivatives are calculated using central difference methods, whose general formula are defined:

$$\frac{df}{dx} = \frac{f(x+h) - f(x-h)}{2h} \tag{5.1}$$

$$\frac{d^2f}{dx^2} = \frac{f(x+h) - 2f(x) + f(x-h)}{h^2} \tag{5.2}$$

where h is the step size, in our case the sampling interval (*dt*). Unlike with a continuous signal, taking the derivative twice with Equation 5.1 results in a poorer second derivative approximation than applying Equation 5.2.

The exception to using Equations 5.1 and 5.2 are for the first (x_0) and last (x_f) points in a signal, where $x_0 - h$ and $x_f + h$ are undefined. Thus, for the first and last points of a signal being differentiated, the single sided difference approach is used, defined:

$$\frac{df(x_0)}{dx} = \frac{f(x_0+h) - f(x_0)}{h} \tag{5.3}$$

$$\frac{df(x_f)}{dx} = \frac{f(x_f) - f(x_f-h)}{h} \tag{5.4}$$

$$\frac{d^2f(x_0)}{dx^2} = \frac{f(x_0+2h) - 2f(x_0+h) + f(x_0)}{h^2} \tag{5.5}$$

$$\frac{d^2f(x_f)}{dx^2} = \frac{f(x_f) - 2f(x_f-h) + f(x_f-2h)}{h^2} \tag{5.6}$$

5.4.2 Filtering

Filtering Pressure Derivatives

Taking the derivative of a discrete signal amplifies noise. Thus, $\frac{dP}{dt}$ and $\frac{d^2P}{dt^2}$ were passed through a finite impulse response (FIR) Hamming low pass filter, with cutoff frequency (f_c) of 20Hz and transition band width (f_{tb}) of 5Hz. Figure 5.3 shows examples of P_{ao} and P_{fem}, and their unfiltered and filtered derivatives, using beats from Pig D4's Control stage. As can be seen, the higher order the derivative, the smaller the signal to noise ratio becomes.

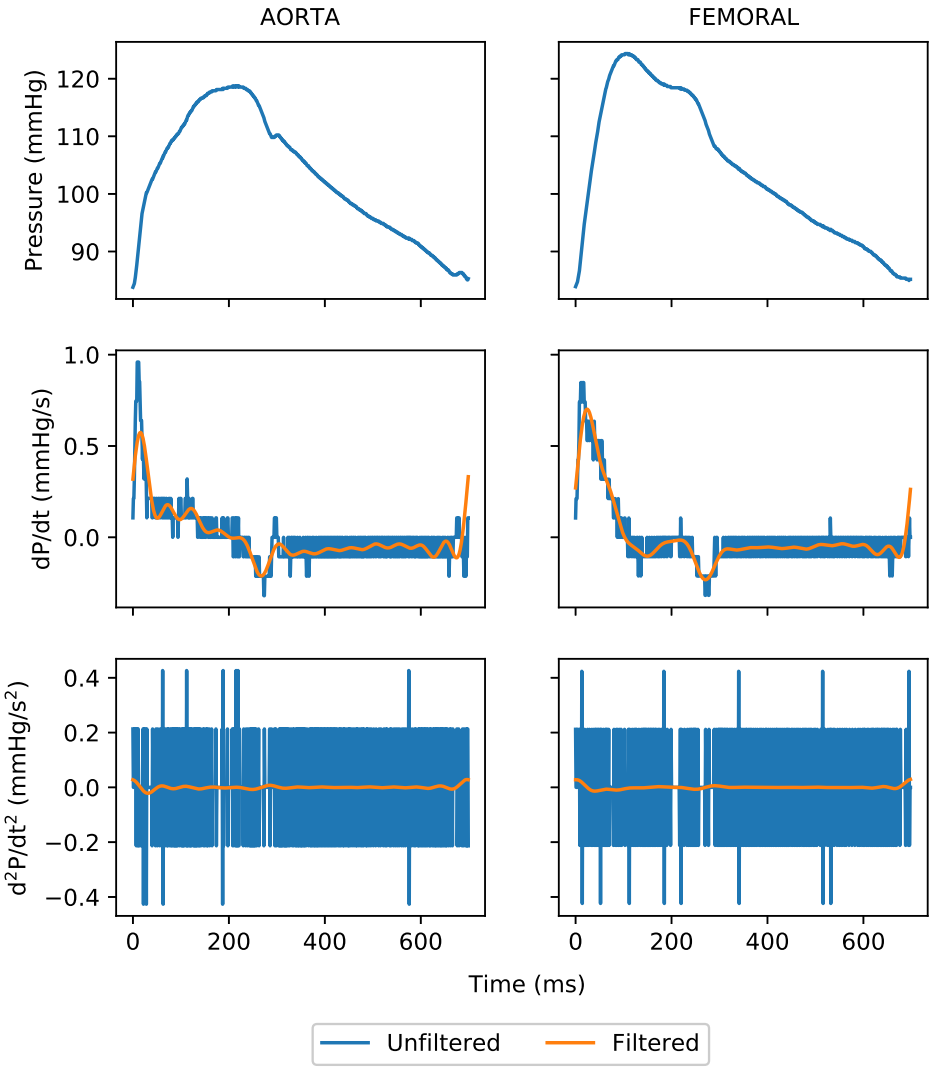

Figure 5.3: Example of unfiltered and filtered aortic arch and femoral pressure waveforms, using beats from Pig D4's Control stage.

Filtering Admittance Catheter Volume Signal

The ventricular admittance catheter data, V_{vent}, was also filtered to reduce noise, of which the majority was greater than 100Hz. Once again, a FIR Hamming low pass filter was used, with f_c = f_{tb} = 10Hz, sufficiently above expected heart rate. An example of the unfiltered and filtered V_{vent} is shown in Figure 5.4. It includes the filtered signal with a phase delay, whose removal is covered at the end of Section 5.4.2.

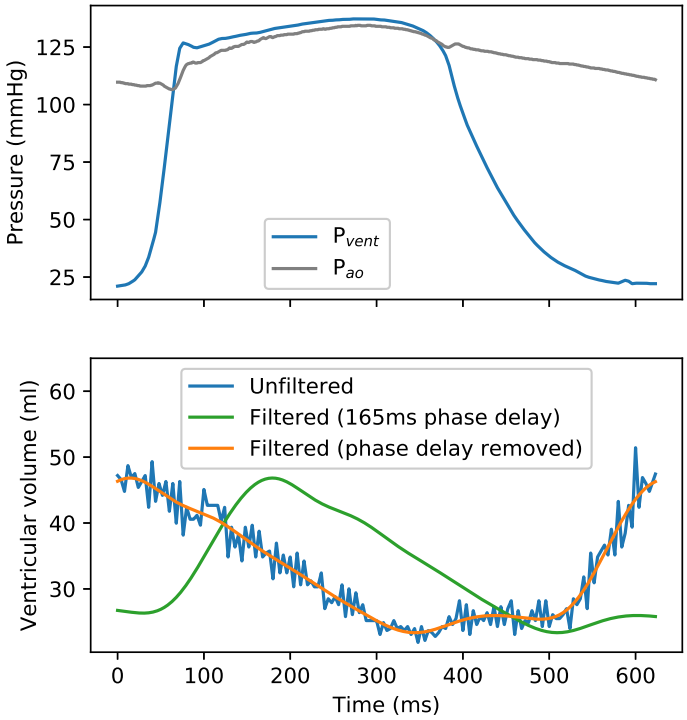

Figure 5.4: Example of unfiltered and filtered ventricle volume waveform, showing the effects of the phase delay as well as its correction and subsequent zero-phase with the unfiltered ventricle and aortic pressure using beats from Pig D4's Control stage.

Filtering Aortic Flow Probe Signal

Data from Pigs S3 and S4 have high frequency noise content of considerable magnitude during systole. This noise was attenuated by filtering with a f_c = 30Hz and f_{tb} = 10Hz. These values were chosen to preserve the *dicrotic notch*, the period of negative flow which causes aortic valve closure at end of systole (Hoeksel et al., 1997; Smith et al., 2004). While the other pigs of Protocol S had significantly less noise in their measured data, they too were passed through the filter for consistency. As can be seen in Figure 5.5, preserving the

dicrotic notch does result in noise less than f_c remaining in the signal. Since the flow probe is simply used as a reference measure during later analysis, the remaining noise content was tolerable.

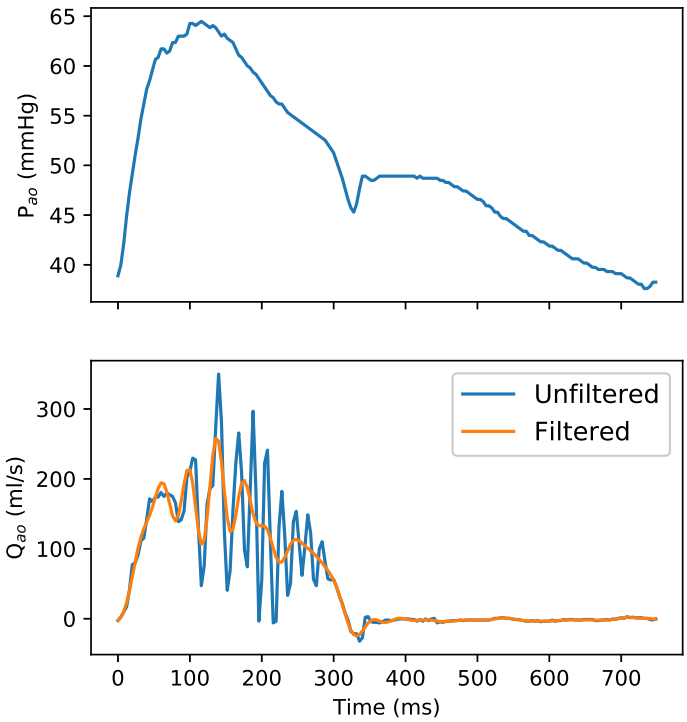

Figure 5.5: Example of unfiltered and filtered aortic flow, using a beat from Pig S4's Control stage as a worst case example. aortic arch/proximal aortic pressure (P_{ao}) shown for reference.

Filter Phase Delay and Edge Effects Correction

Aside from high frequency content removal, the FIR filter implementation also changes the output (filtered) signal relative to the input signal (unfiltered) in two other ways:

- A phase delay between the output signal relative to the input signal.
- The first $N_f - 1$ discrete samples in the filtered signal are not filtered to within f_c and f_{tb}, and therefore must be discarded.

The resulting phase delay must be removed, since many analyses in later chapters rely on *zero phase* delay between signals. Secondly, any sampled data points rendered unusable by filtering, must also be removed. The phase delay is found according to (Ifeachor and Jervis, 2001):

$$\Delta s = \frac{N_f - 1}{2} \quad \text{phase delay in number of samples} \tag{5.7}$$

$$\Delta t = \Delta s \; dt \quad \text{phase delay in seconds} \tag{5.8}$$

Where Δs is the phase delay each sampled data point experiences as it passes through the filter, calculated as a number of samples and is dependent on the filter length N_f. Δt is the phase delay expressed in units of time, based on the *dt*, and Δs. N_f for a Hamming FIR filter is determined by f_{tb} and *dt*, according to (Ifeachor and Jervis, 2001):

$$N_f = \frac{3.3}{f_{tb} dt} \tag{5.9}$$

Thus, removing the first Δs points in the filtered signal, removes the phase delay induced by filtering.

Equation 5.9 states a filter length of N_f is required to achieve the desired f_{tb}. Thus, filtering a data point to meet the desired specification requires the previous $N_f - 1$ data points. Hence, the first $N_f - 1$ data points are not filtered according to both f_c and f_{tb} and this *edge effect* needs to be removed before subsequent analysis. Since $\mathbf{\Delta} s$ points were already removed correcting the phase delay, only $(N_f - 1)/2$ unusable points remain to be removed.

However, after removing the first $N_f - 1$ points of the filtered signal, it is once again phase shifted, but now $(N_f - 1)/2$ earlier than other signals. It is also $N_f - 1$ points shorter in length. Thus, the non-filtered signals must have $(N_f - 1)/2$ points removed from the beginning and ends of their signals, such that they are in phase with the filtered signals and of the same length. Since $\frac{dP}{dt}$, $\frac{d^2P}{dt^2}$, V_{vent} and Q_{ao} have different f_{tb} and thus N_f, they will require different amounts of data trimming. Hence, in later chapters, after filtering, all filtered and unfiltered signals are trimmed so they are the same length as the filtered signal

with the largest N_f, and such that all signals have *zero phase* delay. Figure 5.4 includes an example of the filtered signal prior to the phase delay correction.

5.4.3 Start-Systole Detection

Many of the later chapters involve the calculation of beat-wise metrics, including the main focus of this thesis, *SV*. Therefore, to estimate these metrics, their dependent waveforms must first be separated into individual beats (single periods). As discussed in Section 2.3, each cardiac cycle begins with start of systole, t_0, marked by the *ECG* QRS complex, signalling ventricular depolarization causing contraction (Guyton and Hall, 2011; Newlin and Levenson, 1979). However, there is electro-mechanical delay between the QRS complex and the steep rise in P_{vent} due to ventricular contraction. Additionally, Section 2.5 discussed how once ventricular ejection begins, pressure and flow waveforms propagate along the arterial tree, meaning there is a delay between measuring the effects of systole at the ventricle verses a central or distal artery. In other words, t_0 can be relative to the measurement location and thus, remaining chapters refer to the following:

- $t_{0,ECG}$: absolute start of systole, the onset of ventricular depolarization, marked by the *ECG* Q-wave (Newlin and Levenson, 1979).
- $t_{0,P_{vent}}$: start of systole as measured by onset of ventricular contraction, the *foot* of the P_{vent} waveform.
- $t_{0,P_{ao}}$ / $t_{0,Q_{ao}}$: start of systole in the aorta corresponds with ventricular ejection, causing *feet* in P_{ao} and Q_{ao} waveforms.
- $t_{0,P_{fem}}$: start of systole in the femoral artery, marked by the pulse arrival causing a *foot* in the P_{fem} waveform.

Thus, in the remainder of this thesis, unless stated otherwise, the n^{th} period of a waveform, usually referred to as a beat, ranges $t_{0,n} \leq t < t_{0,n+1}$. For example, the n^{th} P_{ao} beat ranges $t_{0,P_{ao},n} \leq t < t_{0,P_{ao},n+1}$. However, when a beat is considered in isolation for beat-wise calculations, $t_{0,n}$ becomes t = 0 and time extends to T, the duration of the beat ($0 \leq t \leq T$).

Ventricular Depolarization — $t_{0,ECG}$

The ECG signal was covered in Section 2.3.1 with its ideal waveform shown in Figure 2.6. Figure 5.6 shows how the individual waves of the QRS complex were identified in real data. A threshold is constructed as an 81 ms *central moving mean* of the signal, with a vertical offset applied. The central moving means odd number ensures an even number of data points forward and backward of the current data point being averaged. In other words, point n is averaged using itself, along with points $n - 40$ to $n + 40$ inclusive. The window length choice of 81 ms, was simply because it *smoothed out* the high frequency QRS complex but retained the low frequency signal, such as the T-wave. As such, after applying the vertical offset, the R-wave still crosses above the threshold, but the moving mean ensures the T-wave does not, as seen in Figure 5.6.

The offset was adjusted based on the *peak prominence* of the R-wave, which is influenced by the *ECG* lead location (Guyton and Hall, 2011). Peaks are then identified as points above the threshold, whose immediate neighbouring points are of a lower value. Peaks are ignored if they have insufficient prominence or are too close to previous R-waves, as shown in Figure 5.6a. The S-wave can be found using the same methodology as finding the R-wave.

The Q-wave of each beat was found by shear-transforming a segment of the *ECG* signal, shown in Figure 5.6b. The shear line end point is the R-wave and the start point was 10% of the distance back toward the R-wave of the previous beat. The shear transform is calculated as the vertical difference between the *ECG* segment and the shear line. Thus, the Q-wave is the minima in the transformed *ECG* signal, or the point of maximum vertical displacement from the shear line in the *ECG* segment. In later analyses, and by the strictest of definitions, t_0 in the *ECG* signal ($t_{0,ECG}$) is the Q-wave (Talley et al., 1971; Newlin and Levenson, 1979; Balmer et al., 2018c), although some studies will use the R-wave since it is easier to detect (Payne et al., 2006; Pitson et al., 1994).

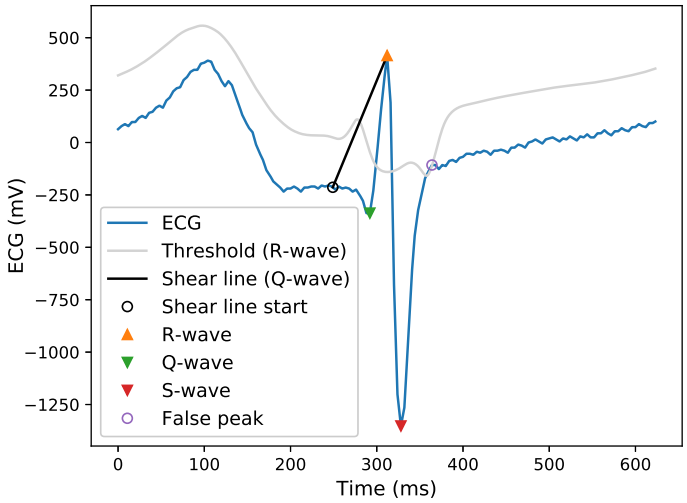

(a) Single cardiac cycle *ECG* signal

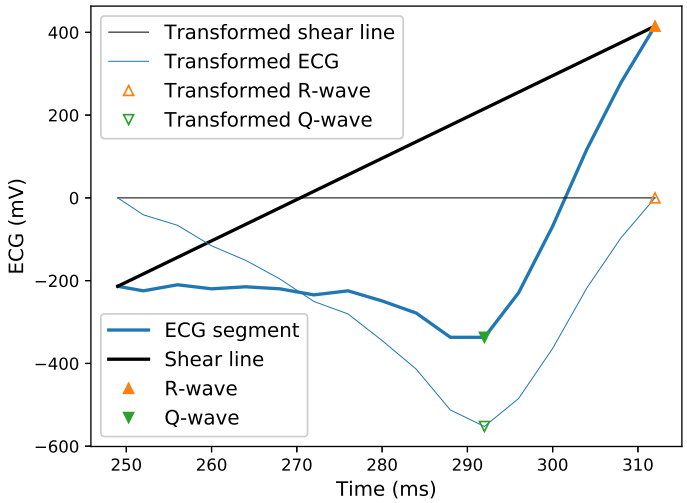

(b) ECG shear transform segment

Figure 5.6: (a) an ECG QRS complex, with the Q-wave, R-wave and S-wave identified. The threshold used to find the R-wave is shown, along with an ignored *false peak*. (b) the Q-wave is found as the minima in the shear transformed *ECG* segment. The example uses beats from Pig D3's Control stage.

Pressure Waveform Feet — $t_{0,P_{vent}}$, $t_{0,P_{ao}}$, $t_{0,P_{fem}}$

As shown in Table 5.1, *ECG* was not measured for Protocols S and V. For these protocols, the start of ventricular contraction ($t_{0,P_{vent}}$) is still clear on P_{vent} as a *foot*, formed by the sudden steep rise in pressure. This same foot feature is present in P_{ao} and P_{fem}, but is due to the pulse wavefront arrival at the respective pressure catheters, indicating $t_{0,P_{ao}}$ and $t_{0,P_{fem}}$ respectively. Once again, shear transforms are used to identify the feet as shown in Figure 5.7.

For P_{vent}, the shear line start point was the minimum pressure of the preceding beat ($P_{vent,\,min}$). Due to the difference between diastolic pressure relaxation in the ventricles versus the arteries, $P_{ao,\,min}$ and $P_{fem,\,min}$ often appear close to, or at the same time as, the foot in their respective waveforms, as shown in Figure 5.7. This similarity makes $P_{ao,\,min}$ and $P_{fem,\,min}$ inappropriate as shear line start points for their respective signals. Instead, their shear line start points are protocol dependent, Protocol D using *ECG* R-waves, while Protocols S and V use P_{vent} feet.

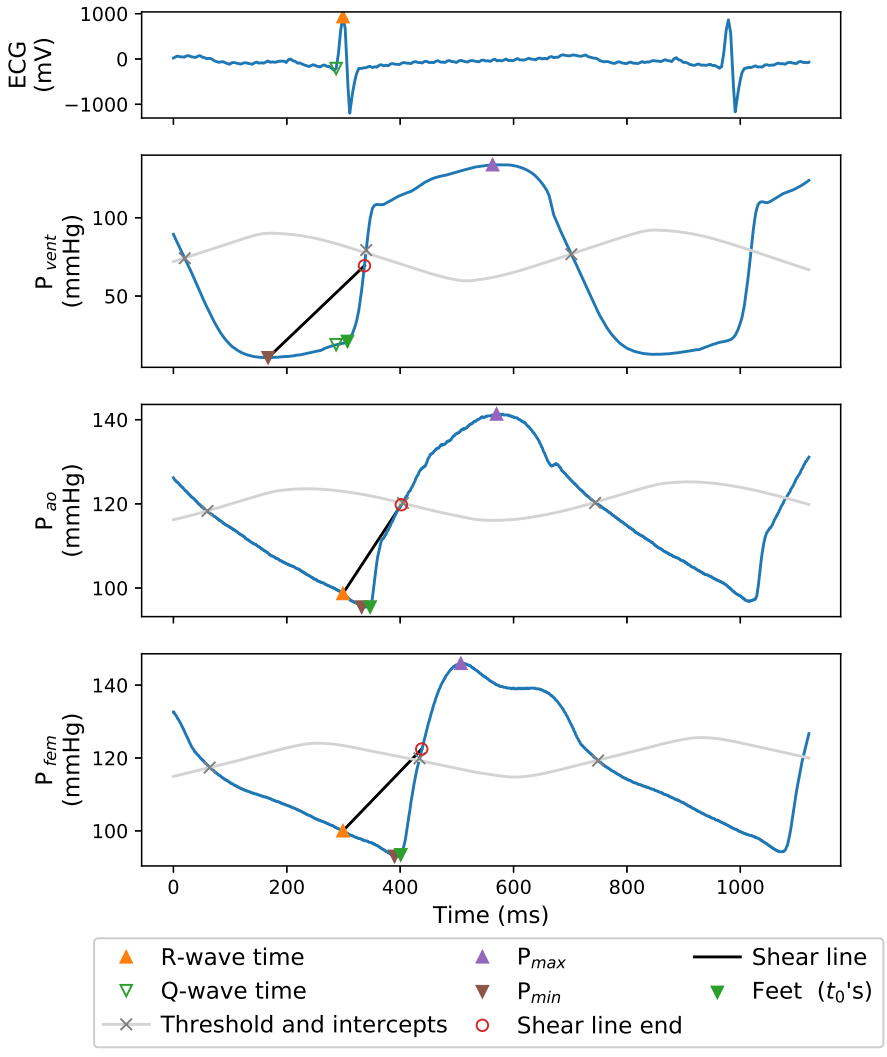

Figure 5.7: Example of how start-systole (t_0) for each pressure waveform beat is found as feet of the waveform. The example uses Pig D2, thus it includes the *ECG* R-wave, used as the shear line start point for arterial pressure foot detection. Protocols S and V used the time of P_{vent} feet in place of the R-waves, for arterial shear line start points. Additionally, the time of the *ECG* Q-wave is shown on the P_{vent} signal, indicating the electro-mechanical delay between $t_{0,ECG}$ and $t_{0,P_{vent}}$.

The shear line ends at a point where pressure is halfway between the pressure at shear line start and P_{max}. P_{max} in the ventricular and arterial signals lack the peak prominence necessary for the threshold algorithm used to detect *ECG* R-waves, shown in Figure 5.6a. Instead, a threshold is constructed from a central moving mean with window length of approximately 1 s (251 points in Protocols S and V, and 1001 points in Protocol D), and minima or maxima are found between the intercepts of the threshold with the pressure waveform. Finally, the shear transform is performed in the same manner as was shown with the *ECG* Q-wave, in Figure 5.6b.

t_0 and Cardiac Performance

Section 2.4.2 discussed how end-diastolic ventricular pressure (*EDVP*) and volume (*EDVV*) were surrogate measures of preload, as shown in Figure 2.9. Since start systole, t_0, is also the end of diastole, $P_{vent}(t_{0,P_{vent}})$ and $V_{vent}(t_{0,P_{vent}})$ represent *EDVP* and *EDVV* respectively.

Similarly, Section 2.4.3 discussed how end-diastolic aortic pressure (*EDAP*) is often used as a surrogate measure of afterload. *EDAP* is equally the aortic pressure at start of systole, $P_{ao}(t_{0,P_{ao}})$. Thus, by identifying the feet of the P_{vent} and P_{ao} waveforms, later analyses can monitor changes in preload and afterload respectively.

5.4.4 Stroke Volume Measurement

Admittance Catheter SV

Table 5.1 showed all protocols measured V_{vent} using an admittance catheter. *SV* for a beat can be calculated from V_{vent} as the difference between the maximum and minimum volume, as shown in Figure 5.8, and defined:

$$SV = V_{vent,max} - V_{vent,min} \tag{5.10}$$

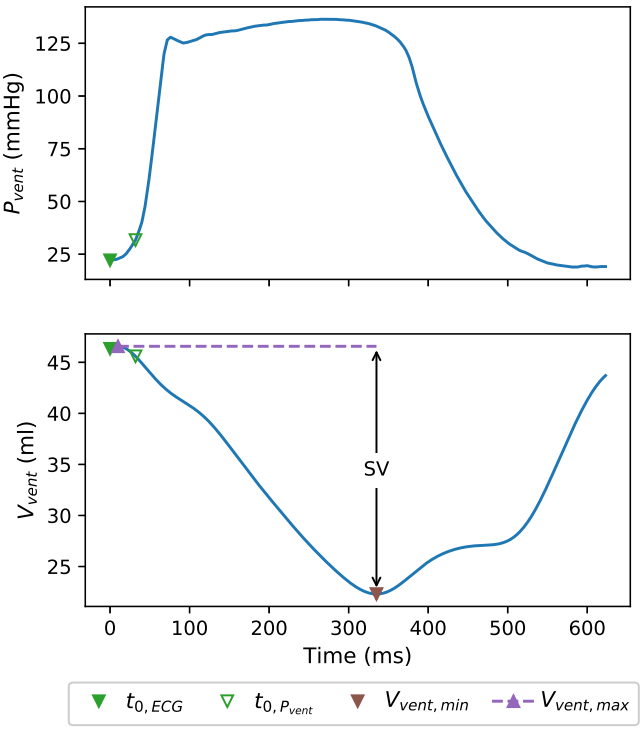

Figure 5.8: Example of how *SV* is calculated from the admittance catheters V_{vent} signal. This example uses Pig D3 Control stage, thus, $t_{0,ECG}$ is used for beat separation. $t_{0,P_{vent}}$ is shown for reference as Protocols S and V use it for beat separation, but this can lead to *slight* error in $V_{vent,max}$ identification.

Because the admittance catheter measured both V_{vent} and P_{vent}, $t_{0,P_{vent}}$ is applicable to both signals when separating beats in Protocols S and V. However, in Protocol D, $t_{0,ECG}$ was used to separate P_{vent} and V_{vent} into individual beats. This choice is because $V_{vent,max}$ can occur *slightly* before $t_{0,P_{vent}}$, as shown in Figure 5.8. Thus, using $t_{0,ECG}$ where possible means the electro-mechanical delay of ventricular depolarization and contraction improves $V_{vent,max}$ identification slightly, and subsequently measured SV.

It is also worth noting, although Protocols D and V did not record flow via an aortic flow probe, an estimate of the flow waveform can be derived from the admittance catheter:

$$Q_{V_{vent}}(t) = \begin{cases} \frac{dV_{vent}(t)}{dt} & : t_0 \leq t < t_{es} \\ 0 & : t \geq t_{es} \end{cases} \tag{5.11}$$

Where the derivative of V_{vent} can be computed with Equation 5.1.

Aortic Flow Probe SV

Protocol S also measured the rate of ventricular ejection (Q_{ao}), using an aortic flow probe located on the proximal aorta. Like the pressure waveforms, Q_{ao} has a foot feature enabling $t_{0,Q_{ao}}$ to be found via a shear transform. The shear line start point is one third the distance back from $Q_{ao,\,max}$ to the previous beats maximum point. The shear line end is a point whose flow is halfway between $Q_{ao,\,max}$ and the flow at shear line start. The shear line and $t_{0,Q_{ao}}$ detection is shown in Figure 5.9.

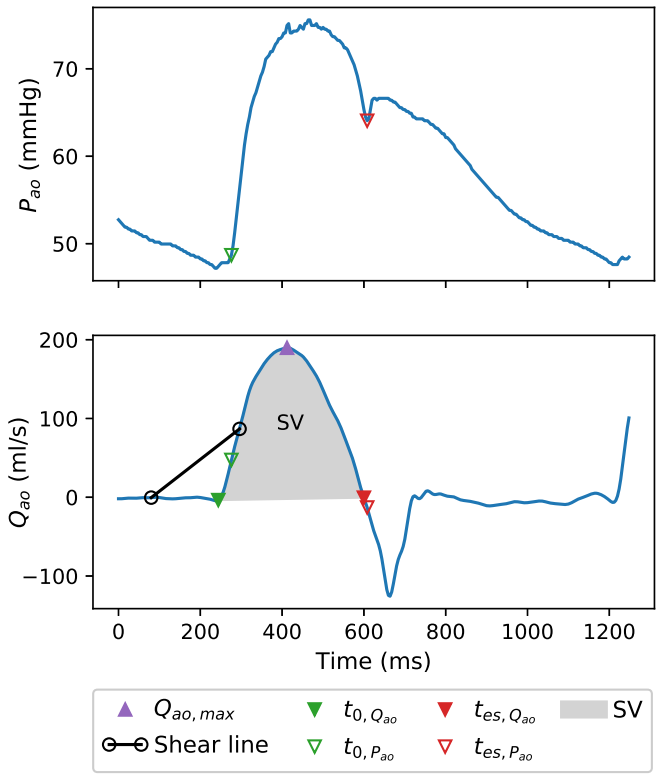

Figure 5.9: Example of how *SV* is calculated from the aortic flow probe Q_{ao} signal. This example uses Pig S1 Control stage, whose aortic flow probe was furthest from the aortic arch pressure catheter, representing the largest difference between $t_{0,P_{ao}}$ and $t_{0,Q_{ao}}$ points.

Once Q_{ao} beats are separated via $t_{0,Q_{ao}}$, SV can then be calculated as the integral of the flow over a beat:

$$SV = \int_{0}^{t_{es}} Q_{ao}(\tau)d\tau \tag{5.12}$$

Since, there is no ventricular ejection during diastole, the limits of integration need only cover systole, where time of end-systole in Q_{ao} ($t_{es,Q_{ao}}$) can be identified as the first zero crossing following a beats $Q_{ao,\,max}$. Figure 5.9 shows the Q_{ao} area integrated to give an SV measure.

Although the aortic flow probe was positioned near the pressure catheter in the aortic arch, no effort was made to perfectly match their positions, meaning $t_{0,P_{ao}}$ was often near, but not necessarily the same as, $t_{0,Q_{ao}}$. Simiarly, t_{es} for each signal could differ slightly. End-systole in P_{ao} was marked by a beats dicrotic notch, $t_{es,dic}$, as discussed in Section 2.3.1, and whose detection is covered in Chapter 8. The flow waveform also exhibits a dicrotic notch as negative flow for a brief period when $P_{ao} > P_{vent}$, leading to aortic valve closure (Hoeksel et al., 1997; Smith et al., 2004). However, if the dicrotic notch in Q_{ao} was used to obtain t_{es} in Equation 5.12, the negative flow would result in underestimation of SV.

Figure 5.9 illustrates the difference in systolic time intervals t_0 and t_{es} for the aortic signals. It uses data from Pig S1, whose $t_{0,Q_{ao}}$ had the largest disagreement when compared to $t_{0,P_{ao}}$. Finding t_0 and t_{es} separately for P_{ao} and Q_{ao} ensures the disagreement has no impact on later analyses.

5.5 Summary

This chapter covered aspects relevant to later chapters, included the experimental protocols, their hemodynamic interventions and data acquisition. It also covered the common initial data processing techniques, which enabled the later chapters analyses. Some of the processing used standard techniques, such as differentiating discrete signals and filtering. Other aspects were developed by the author specifically for this thesis, the algorithms for peak detection and waveform separation into individual beats. Finally, the two methods of measuring stroke volume, used in the thesis, were covered, one for the ventricular admittance catheter and the other for the aortic flow probe, respectively.

CHAPTER 6

Advantages and Limitations of the Kamoi model

6.1 Introduction

This chapter introduces a pulse contour analysis (PCA) stroke volume (*SV*) estimation model, whose development drew upon much of what was learned from the models covered in Chapter 4. Although many people were involved in the development of the model, including the author of this thesis, for simplicity it will be referred to as the *Kamoi model*, named after the lead developer (Kamoi, 2016; Kamoi et al., 2017). Having been apart of the Kamoi model's later stages of development, it became a benchmark and starting point for this thesis. Therefore, the chapter focuses on the successes and limitations of the Kamoi model and how they relate to the thesis goals (Section 1.4). The limitations identified subsequently enabled the improvements presented in later chapters.

6.2 The Kamoi method

The Kamoi model (Kamoi et al., 2017) was similar to Wesseling et al. (1993), using a three-element windkessel model to calculate *SV*. However, Kamoi et al. (2017) parameter identification was a hybrid between Westerhof et al. (1971), Wesseling et al. (1993) and Aguado-Sierra et al. (2008). Specifically, it would calculate *RC* in Equation 4.11 using PCA, as per Aguado-Sierra et al. (2008). However, Kamoi et al. (2017) factored in pulse wave velocity (*PWV*) to estimate reservoir pressure (P_{res}) and stroke volume (SV_{est}).

6.2.1 Incorporating PWV into the Three-Element Windkessel

Section 4.7 discussed the desire for parameters to be dynamic, reflecting the current hemodynamic state of a patient. Knowing two of the parameters of the windkessel model had previously been estimated using *PWV*, namely windkessel characteristic impedance ($Z_{c,w}$) and compliance (*C*), Kamoi et al. (2017) hypothesised continuously monitoring *PWV* could improve model performance.

Specifically, as per Sections 4.3.1, Westerhof et al. (1971) used the water hammer equation (Equation 2.7) to estimate $Z_{c,w}$. While Wesseling et al. (1993) estimated $Z_{c,w}$ from the combined water hammer and Bramwell-Hill equations (Section 4.4.1). Kamoi et al. (2017) utilized both approaches.

Redefining $Z_{c,w}C$ using *PWV*

Kamoi et al. (2017) combined the water hammer equation (Equation 2.7) and the volume form of the Bramwell-Hill equation (Equation 2.2), to estimate the parameter product $Z_{c,w}C$. Specifically, the product of Equation 2.7, in terms of $Z_{c,w}$, and Equation 2.2, in terms of (volumetric) compliance results in:

$$Z_{c,w}C = \frac{PWV\rho}{A} \times \frac{V}{\rho PWV^2} = \frac{L_c}{PWV} \tag{6.1}$$

This formulation allows Equation 4.11 to be rewritten using *PWV* and characteristic length (L_c):

$$P_{res}(t) = e^{-(\frac{PWV}{L_c}+\frac{1}{RC})t}\left(\int_0^t\left[e^{(\frac{PWV}{L_c}+\frac{1}{RC})\tau}\left(\frac{PWV}{L_c}P_{mea}(\tau)+\frac{P_{cvp}(\tau)}{RC}\right)\right]d\tau + P_{mea}(0)\right) \quad (6.2)$$

PWV for Dynamic $Z_{c,w}$

The identification of model parameters for Equation 6.2 will be discussed in Section 6.2.2, so for the moment, consider it possible to identify P_{res}. Aguado-Sierra et al. (2008) did not use P_{res} to solve for *SV*. Doing so would require $Z_{c,w}$ to be known separate from its product with compliance, as per Equation 4.17.

One way to identify $Z_{c,w}$ would be to use a calibration stroke volume measurement (SV_{cal}) and rearrange Equation 4.17, yielding:

$$Z_{c,cal} = \frac{1}{SV_{cal}}\int_0^t P_{ex}(\tau)d\tau \quad (6.3)$$

Where $Z_{c,cal}$ is the calibrated characteristic impedance, found from SV_{cal}. However, as per Section 4.7.1, using $Z_{c,cal}$ for $Z_{c,w}$ makes it a static parameter.

Since monitoring *PWV* was necessary for solving P_{res} according to Equation 6.2, Kamoi et al. (2017) decided to use the water hammer equation (Equation 2.7) to estimate $Z_{c,w}$, as Westerhof et al. (1971) had done at the inception of the three-element windkessel. The difference being, Kamoi et al. (2017) would monitor *PWV* continuously and thus update $Z_{c,w}$ every beat, making it a dynamic parameter.

However, the water hammer equation also requires cross-sectional area to be known. Kamoi et al. (2017) used the experimental data of Protocol D (Section 5.2.1), which did

not include measurement of the aortic area, but did have an admittance catheter for measuring left ventricular volume (V_{vent}). This measurement allowed stroke volume to be measured (SV_{mea}) throughout the experiment according to Equation 5.10. Thus, Kamoi et al. (2017) back calculated $Z_{c,cal}$ from Equation 6.3, and used this value with the water hammer equation to calibrate calibrated cross-sectional area (A_{cal}):

$$A_{cal} = \frac{PWV\rho}{Z_{c,cal}} \tag{6.4}$$

Kamoi et al. (2017) used the measured *SV* from multiple calibration beats to find an average $Z_{c,cal}$ and A_{cal}.

Kamoi et al. (2017) also assumed the relative change in aortic area throughout an experiment, would be inversely proportional to changes in systolic duration:

$$A = \frac{T_{sys,cal}}{T_{sys}} A_{cal} \tag{6.5}$$

Where A and T_{sys} represent the current beats cross-sectional area and systolic duration respectively. $T_{sys,cal}$ is the mean systolic duration during the calibration of A_{cal}.

T_{sys} was identified as the time between the times of start-systole (t_0) and end-systole (t_{es}). Start-systole was identified as $t_{0,P}$, the foot of the arterial pressure waveform, as discussed in Section 5.4.3, but used a different method than the authors shear-transform approach of Figure 5.7. A beat's point of maximum negative pressure gradient, $\frac{dP}{dt}\min$, was used to estimate end-systole. However, a generic weighting function was first applied to $\frac{dP}{dt}$, attenuating the signal the further it was from the centre of the beat. This weighted first derivative based estimate of the time of end-systole ($t_{es,dP/dt}$) will be discussed further in Chapters 8 and 10.

Finally, by measuring *PWV* via foot-to-foot pulse transit time (*PTT*), as shown in Figure 2.13, Kamoi et al. (2017) estimated $Z_{c,w}$ on a beat-to-beat bases using the water hammer

equation (Equation 2.7), modified with Equation 6.5, yielding:

$$Z_{c,w} = \frac{PWV\rho}{A_{cal}} \frac{T_{sys}}{T_{sys,cal}} \tag{6.6}$$

6.2.2 Kamoi Model P_{res} Calculation

L_c Calibration

The Kamoi model implementation requires L_c, as per Equation 6.2. Like Wesseling et al. (1993) (Section 4.4.1), Kamoi et al. (2017) treated L_c as a constant value representing the *"anatomical length"* of the aorta[1]. Thus, in the Kamoi model's case, Equation 6.1 essentially attributes changes in $Z_{c,w}C$ to PWV. However, instead of using an assumed aortic length like Wesseling et al. (1993), Kamoi et al. (2017) used a *grid search* technique to calibrate L_c.

The grid search involved iterating L_c over a range of potential values. Each iteration is referred to using the subscript ' i '. For each $L_{c,i}$, RC was also iterated over a range of values. For each pair of $L_{c,i}$ and RC_i, $P_{res,i}$ could be calculated according to Equation 6.2 for the whole beat. The error, $\mathcal{E}$, was then calculated over the diastolic part of the pressure waveform for each $P_{res,i}$, using the condition given in Equation 4.12. Specifically[2]:

$$\mathcal{E} = \sum \left(P_{mea}(t \geq t_{es}) - P_{res}(t \geq t_{es})\right)^2 \tag{6.7}$$

For every $L_{c,i}$, one of the RC_i values minimises $\mathcal{E}$ ($RC_{\min \mathcal{E}}$). P_{res} for each $L_{c,i}$ and $RC_{\min \mathcal{E}}$ pair is shown in Figure 6.1, referred to as $P_{res,min\ \mathcal{E}}$. Figure 6.1 shows $P_{res,min\ \mathcal{E}}(t \geq t_{es,dP/dt})$ can be very similar for different values of $L_{c,i}$. Thus, according to Kamoi et al. (2017), minimising the error according to Equation 6.7, was not enough to identify a *best fit* or *optimal* L_c value. Therefore, Kamoi et al. (2017) introduces a second condition:

[1] Kamoi et al. (2017) refers to this as L_{ao}, rather than a characteristic length.

[2] Kamoi et al. (2017) only states *"the discrepancy between Equation 10 and measured diastolic pressure decay was minimized"*, where Equation 10 in Kamoi et al. (2017) is Equation 6.2 in this thesis. Shun Kamoi's thesis (Kamoi, 2016) has a similar statement. Thus, although no explicit equation is given for the error minimisation, Equation 6.7 represents a common error minimisation approach known as the sum squared error.

$$P_{mea}(t_{es}) = P_{res}(t_{es}) \tag{6.8}$$

Where in Kamoi et al. (2017), end systole was $t_{es,dP/dt}$, as per Section 6.2.1. Thus, a calibration beat value for L_c was found as the value used in $P_{res,min\ \varepsilon}$ that satisfied, or came closest to the condition of Equation 6.8, which is referred to as $P_{res,cal}$ in Figure 6.1. Although Figure 6.1 shows only one beat used for identification of L_c, Kamoi et al. (2017) used an average L_c from the beats used when identifying $Z_{c,cal}$ (discussed in Section 6.2.1). This averaged L_c value was then fixed on the basis length will not change over time. Therefore, according to Equation 6.1, changes in $Z_{c,w}C$ are attributed to changes in PWV.

P_{res} Calculation Post L_c Identification

Unlike L_c, the value of RC was not fixed to the value used in calculating $P_{res,cal}$. $RC_{\min \varepsilon}$ was still found beat-wise by minimizing the error according to Equation 6.7, but applied to Equation 4.16 (Kamoi, 2016). It is unclear exactly how Kamoi et al. (2017) performed the error minimization, but the authors approach will be discussed later in Section 9.3.2. For now, an example of RC identification, post L_c calibration, is shown on the second beat of Figures 6.1a and 6.1b. Specifically, $P_{res,dia}$ refers to the exponential decay of Equation 4.16 according to the $RC_{\min \varepsilon}$. With L_c from the calibration and each beats $RC_{\min \varepsilon}$, P_{res} was then able to be calculated, with the measured PWV of the beat, according to Equation 6.2.

6.2.3 Kamoi Method Stroke Volume Estimation

With $Z_{c,w}$ identified per Section 6.2.1, and P_{res} found per Section 6.2.2, the Kamoi model then estimates stroke volume (SV_{est}) using the fundamental three-element windkessel model equations, of Section 4.3.2. Specifically, Equation 4.3 is used to find excess pressure (P_{ex}), and subsequently SV_{est} is found via Equation 4.17.

However, it is worth noting, the SV_{est} is actually calculated by integrating the estimated flow waveform of the model (Q_{est}), per Equation 4.17. Although Kamoi et al. (2017) ac-

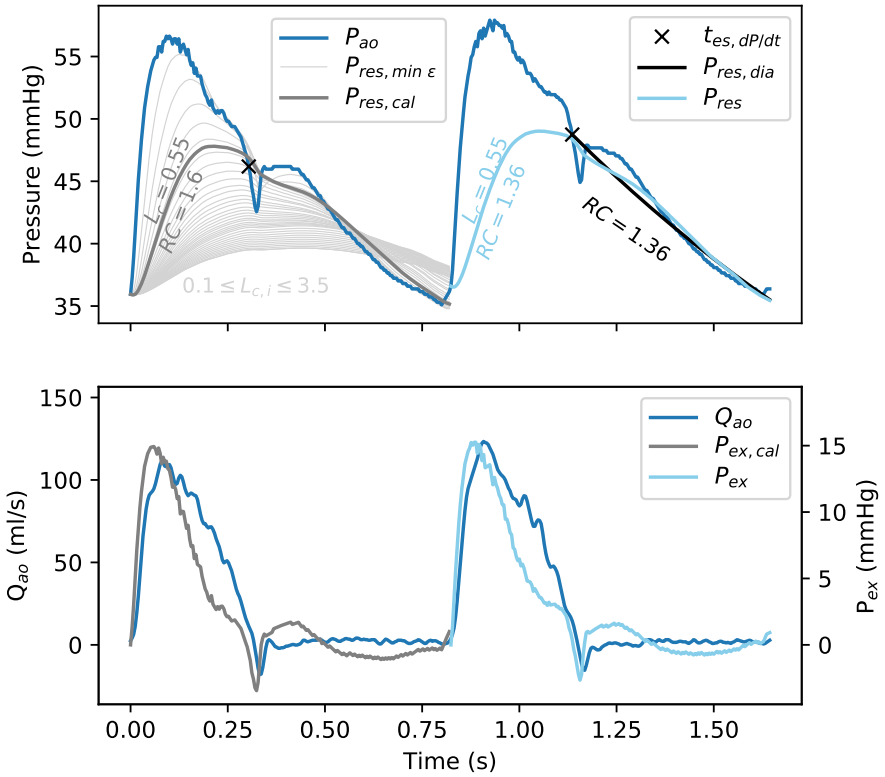

(a) Kamoi model method applied to aortic pressure waveform.

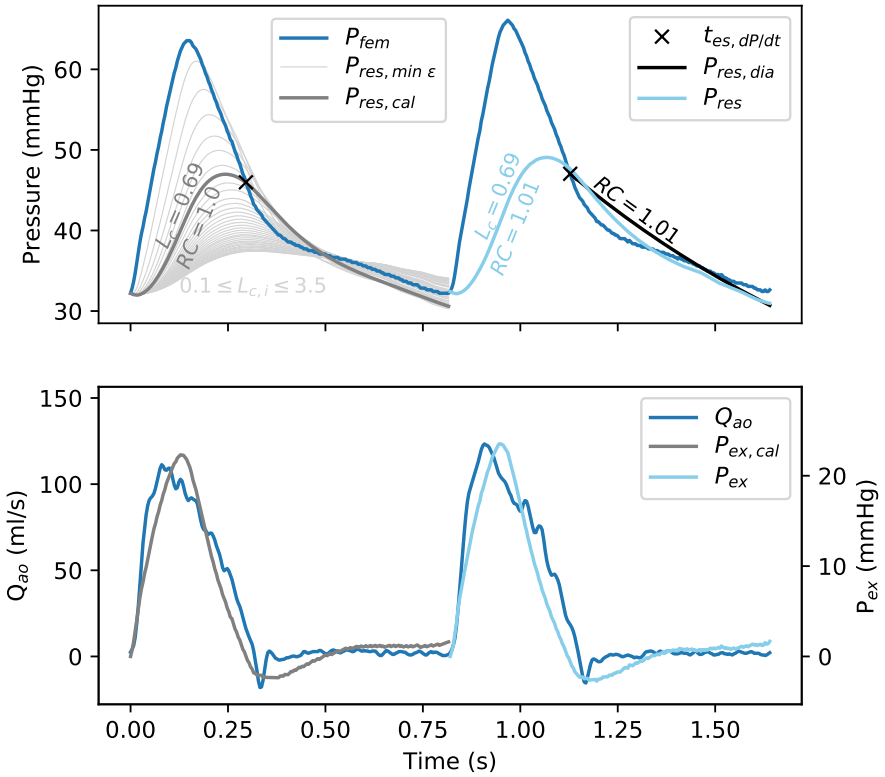

(b) Kamoi model method applied to femoral pressure waveform.

Figure 6.1: Kamoi model L_c calibration and subsequent beats RC and P_{res} calculation. (a) and (b) show the method applied to P_{ao} and P_{fem}, respectively. The grid search is applied to the first beat of each subplot, where $P_{res,min\,\varepsilon}$ minimised the error according to Equation 6.7. The grid search bounds were $0.01 \leq RC \leq 5$ and $0.1 \leq L_c \leq 3.5$, where $L_c \propto 1/P_{res}$. The phase delay has been removed from the femoral pressure signal relative to the flow probe, for easier comparison of the excess pressure and flow waveform shapes in (b). The beats analysed are from Pig S5's control stage.

knowledged the model's ability to predict flow, the results of the study focus on the more clinically relevant SV_{est}. The implications of presenting SV_{est}, but without presenting the mechanisms through which it is found, will be covered in Chapter 9.

6.2.4 Kamoi Method Implementation Summary

It should now be clear, using the Kamoi model implementations results in L_c as a static parameter, while parameters RC and $Z_{c,w}$ are dynamic. Additionally, the hybrid PWV and PCA approach developed has been shown, with L_c and RC being identified via PCA, but $Z_{c,w}C$ and $Z_{c,w}$ being found from PWV. Therefore, PWV will influence the shape of P_{res} and thus P_{ex} according to Equation 4.3. However, it also impacts the SV estimation more directly through changes in $Z_{c,w}$ according to Equation 6.6 and Equation 4.17.

6.3 Limitations of the Kamoi Method

The Kamoi model is essentially a three-element windkessel, with novel implementation, through the inclusion of PWV. Thus, Section 4.3.3, which covered the three-element windkessel limitations, is relevant to the Kamoi model. However, this section will cover the limitations specific to the Kamoi model implementation.

6.3.1 Clinical Applicability Challenges

The Kamoi method requires PWV, which can be measured in a clinical environment, but is not usually monitored continuously. For the model to meet the goals of this thesis (Section 1.4), a method of measuring PWV, using clinically available metrics, would need to be found. This issue will be discussed further in Chapter 7.

The second clinical limitation is cross-sectional area (A) must be known to estimate $Z_{c,w}$ from Equation 6.6. In a clinical environment, it is possible to measure the aortic cross-sectional area non-invasively, using trans-esophageal doppler ultrasound (Section 3.2.3). While measuring aortic area, trans-esophageal dopplier ultrasound could conveniently give you access to a calibration SV at the same time.

6.3.2 Signal Processing Limitations

The Kamoi method implementation is also sensitive to start and end-systole detection (t_0, t_{es}), through two mechanisms. First, t_0 to t_{es} defined systolic duration, T_{sys}. Beat-to-beat changes in systolic duration (ΔT_{sys}), relative to the calibrated value ($T_{sys,cal}$), are proportional to the value of $Z_{c,w}$ for a beat, through Equation 6.6. Subsequently, $\Delta Z_{c,w}$ will effect SV_{est} through Equation 4.17. Calibrating systolic duration ($T_{sys,cal}$), makes Equation 6.6 sensitive to t_{es} *precision* rather than *accuracy*. For example, consider Figure 6.2.

In Figure 6.2, dicrotic notches can be seen on the P_{ao} waveform, indicated by arrows. As discussed in Section 2.3.1, the dicrotic notch marks end-systole ($t_{es,dic}$) in P_{ao}. For these example P_{ao} waveforms, $t_{es,dP/dt}$ misidentifies $t_{es,dic}$, but in a manner which *consistently* overestimates $T_{sys,ao}$. Therefore, the aortic pressure $t_{es,dP/dt}$ values have low accuracy, but high precision, resulting in $\Delta T_{sys,ao} \approx 0$ and minimal $SV_{est,ao}$ error according to Figure 6.2.

In contrast, the central beat of P_{fem} in Figure 6.2, has a shorter T_{sys} than the other beats. This difference has little effect on $P_{res,fem}$ and $P_{ex,fem}$, because L_c has already been calibrated. However, due to the reduction in $\Delta T_{sys,fem}$, the modelled characteristic impedance ($Z_{c,w}$) from the femoral signal falls according to Equation 6.6, increasing the estimated flow ($Q_{est,fem}$) according to Equation 4.5. This overestimation of the flow leads to a significant spike in $SV_{est,fem}$ error for the beat.

The value of L_c is also largely dependent on end-systole detection, since L_c is found via the condition of Equation 6.8. The implications of this issue in end-systole detection will be explored in detail in Chapters 8, 9 and 10. However, for now, the impact of t_{es} identification can be seen through the comparison of Figure 6.1b with Figure 4.4. Figure 4.4 uses an improved end-systole detection method covered in Chapter 10. The improved t_{es} estimation contributes to Figure 4.4's lower error according to Equation 6.7, when compared with Figure 6.1b.

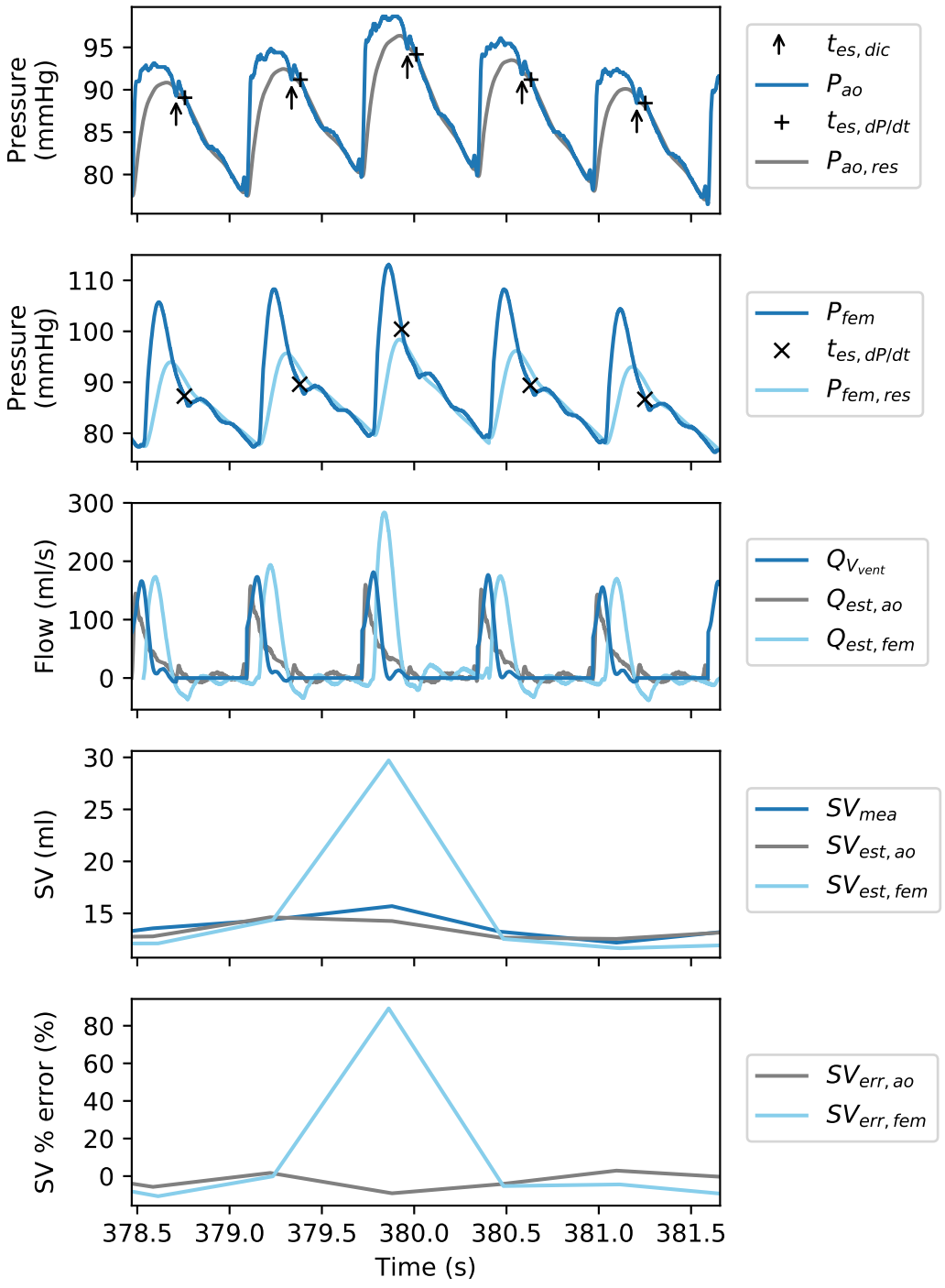

Figure 6.2: Example of how $t_{es,dP/dt}$ precision, rather than accuracy, influences SV_{est}. This example uses beats from Pig D3, high PEEP stage. Note that $Q_{V_{vent}}$ refers to the flow waveform estimated from Equation 5.11.

6.3.3 Stroke Volume Error and Clinical Accuracy

Kamoi et al. (2017) stated 95% of the estimated *SV* was within the ±30% criteria outlined by Critchley and Critchley (1999) (Section 3.5). However, it is worth noting, the criteria appears to be applied to each individual pig, rather than the sample of pig data as a whole (Kamoi, 2016; Kamoi et al., 2017). Furthermore, although it is not entirely clear[3], it appears the percentage error for each pig was calculated with respect to the mean SV_{mea} of the experiment ($\overline{SV_{mea}}$). If so, this approach leads to an under-representation of the error for beats whose $SV_{est} < \overline{SV_{mea}}$, but an over-representation for beats whose $SV_{est} > \overline{SV_{mea}}$. More accurately, stroke volume estimation error (SV_{err}) as a percentage ($SV_{\%err}$) should be calculated for each beat according to the estimated and measured *SV* for that beat:

$$SV_{err} = SV_{est} - SV_{mea} \tag{6.9}$$

$$SV_{\%err} = \frac{SV_{err}}{SV_{mea}} = \frac{SV_{est} - SV_{mea}}{SV_{mea}} \tag{6.10}$$

An exceptional case can be argued for beats with very low SV_{mea}. For example, consider SV_{mea} = 8 ml and SV_{est} = 5 ml, that is only SV_{err} = 3 ml, but the percentage error would be 37.5%. In this case it could be argued the percentage error over-represents what is actually very good absolute error.

6.4 Summary

This chapter outlined the Kamoi method, upon which this thesis is founded. The method combines the three-element windkessel model with continuous *PWV* monitoring. Specifically, the model used *PWV* to aid in parameter identification and subsequent P_{res} estima-

[3] Kamoi et al. (2017) states the "95% range was within ±10 ml (approximately 30%) for all pigs", consistent with each pigs $\overline{SV_{mea}} \approx 30$ ml. Additionally, the individual pig's Bland-Altman figures and summary table include the 2.5th-97.5th percentiles only in millilitres, but the caption states the "Precision is calculated as half the 95% range divided by mean *SV* for each pig".

tion. Although Kamoi et al. (2017) makes reference to the model's ability to estimate flow, the results do not include the modelled P_{res}, P_{ex} or Q_{est}, as in Figure 6.1 and 6.2. Instead, the results largely focus on estimating SV, which is more clinically relevant as per Chapter 1.

However, as discussed in Section 1.4, a physiologically accurate flow waveform shape acts as an indication of correct parameter identification, and may be useful when establishing whether the PCA method requires re-calibration. Essentially, Chapters 4 and 6 have demonstrated the potential of the three-element windkessel based models to estimate global physiology. The methods presented have drawn on the same theory, but their different implementations lead to different results. Thus, working towards the thesis goals of Section 1.4, the following chapters will attempt to overcome the limitations of the Kamoi model. Specifically, they will focus on improving the implementation of the method and its clinical relevance.

CHAPTER 7

Pre-ejection Period and Inadequate Pulse Transit Time Estimation

7.1 Introduction

Chapter 6 outlined the advantages and limitations of the Kamoi Model. One limitation was the model's reliance on pulse wave velocity (*PWV*), for its implementation of the three-element windkessel model. In a clinical environment, *PWV* is used as a surrogate measure of arterial stiffness, as discussed in Sections 2.5.1 and 2.5.3. However, it is not common to continuously monitor *PWV*, as required by the Kamoi model. This chapter presents and tests a non-additionally invasive method of beat-to-beat estimation of *PWV* suitable for a clinical environment.

7.2 *PWV* Clinical Relevance

Section 2.5.1 and Figure 2.11 covered pulse wave velocity and its physiological mechanisms in detail. In summary, *PWV* is the speed the blood pressure pulse travels through the arteries. As the pulse travels, vessel wall expansion stores energy from the wave front, reducing its speed. This relationship between *PWV* and compliance (*C*) is described by the Bramwell-Hill equation, Equations 2.2 and 2.3 (Bramwell and Hill, 1922).

Since *PWV* is easier to measure than arterial stiffness/compliance, *PWV* is often used clinically as a surrogate of arterial stiffness, which is itself a predictor for future cardiovascular dysfunction (Nye, 1964; Blacher et al., 1999a,b; Laurent et al., 2001; Cameron et al., 2003; Millasseau et al., 2005; Laurent et al., 2006; Nichols et al., 2011; Ben-Shlomo et al., 2014). Similarly, PWV is used in cardiovascular models to describe or capture the properties upon which it depends (Asmar et al., 1988; Pitson et al., 1994; Fung et al., 2004; Kamoi et al., 2015, 2017). This approach was the case in the Kamoi model of Chapter 6.

7.3 Clinical Methods for Measuring Pulse Transit Time (*PTT*) for *PWV*

PWV is usually measured as the *PTT* between two arterial sites a known distance apart, as per Figure 2.13 (Loukogeorgakis et al., 2002; Millasseau et al., 2005; Laurent et al., 2006; Payne et al., 2006; Dogui et al., 2011; Kamoi et al., 2015, 2017). Thus, *PWV* and *PTT* are inversely proportional, and dependent on the same underlying physiological factors. *PTT* can be measured locally, or more generally as an average over the length of the arterial system.

Local *PTT* can be found non-invasively using tonometry, magnetic resonance imaging (MRI) techniques and other separate medical devices (Yamashina et al., 2002; Rajzer et al., 2008; Townsend et al., 2015; Pereira et al., 2015; Joseph et al., 2016). The complexity and

cost of some of these techniques limits them to singular or short term measurements (Townsend et al., 2015).

A more general *PTT* can be estimated non-invasively and continuously using photoplethysmogram (*PPG*) signals (Loukogeorgakis et al., 2002; Fung et al., 2004; Payne et al., 2006; Muehlsteff et al., 2006; Lazaro et al., 2016). This method was discussed in Section 3.5.4, where it was used as part of the esCCO device (Nihon Kohden®). However, in a clinical setting, it is most relevant to measure local *PTT* along the aortic pathway as a surrogate for arterial stiffness (Blacher et al., 1999b; Laurent et al., 2006; Nichols et al., 2011; Townsend et al., 2015). This clinical relevance arises because the aorta is less stiff than the peripheral arteries, and shows a much larger change in stiffness over a human's lifetime (Nichols et al., 2011; Townsend et al., 2015), as discussed in Section 2.5.1. Thus, the 'gold standard' measure for arterial stiffness is a *PTT* from the pressure waveform foot of the common carotid artery to the femoral artery (Laurent et al., 2006; London and Pannier, 2010; Townsend et al., 2015), usually achieved by catheterisation of both sites (Laurent et al., 2006; Hanya, 2013). However, where applicable, such as when singular or short term measurements are desired, non-invasive methods can be used (Townsend et al., 2015). In this thesis, the target cohort are patients in critical or acute care environments, where catheterisation is more common, and thus more likely to be available for this type of measurement.

However, dual catheterisation represents an undesirable increase in clinical workload and patient burden over the typical single catheterisation of cardiovascular intensive care unit (ICU) patients. Therefore, for those ICU patients already (singly) catheterised, replacing one of the two required catheters with non-invasive pulse detection would enable non-additionally invasive, continuous estimation of *PTT* and arterial stiffness. Thus, there is a need for an accurate non-invasive surrogate measure from which to calculate *PTT*.

7.4 *ECG* based Non-Additionally Invasive *PTT* Surrogate

A popular non-invasive pulse detection surrogate is the *ECG* QRS complex (Figure 2.6), which is used in place of the centrally located pressure catheter (Katz et al., 2003; Chua and Heneghan, 2005; Liu et al., 2016). The advantages of an *ECG* signal are it is extremely common in medical care, non-invasive, and a central measurement. However, the QRS complex represents the electrochemical initiation of ventricular contraction, and not aortic valve opening (Guyton and Hall, 2011), as covered in Section 2.3.1. Thus, the QRS complex does not directly correspond to the actual onset of blood ejection from the ventricle.

The time interval between the Q-wave of the QRS complex and aortic valve opening is the pre-ejection period (*PEP*) (Talley et al., 1971; Newlin and Levenson, 1979). It is associated with the isovolumetric contraction of the heart overcoming upstream pressure in the aorta. Hence, the time between the Q-wave and the pulse arriving at a downstream site is not the true *PTT*, but is instead known as the pulse arrival time (*PAT*). *PAT* is the direct sum of *PEP* and the subsequent *PTT* from the aortic valve to the downstream detection site.

Despite this issue, many studies measure *PAT*, but incorrectly call it *PTT*, either without reference to *PEP* or by assuming *PEP* is negligible (Cameron et al., 2003; Fung et al., 2004; Chua and Heneghan, 2005; Kim et al., 2006; Liu et al., 2016). *PEP* has long been known to vary with cardiac performance metrics, such as contractility, preload and afterload (Section 2.4) (Harris et al., 1967; Newlin and Levenson, 1979). Thus, using *PAT* and assuming it is equivalent to *PTT* introduces the *PEP* as an error (Balmer et al., 2017, 2018c).

Several studies have already found neglecting *PEP* to be a poor assumption. For example, Payne et al. (2006) and Muehlsteff et al. (2006) found while changes in *PTT* can be used to non-invasively monitor blood pressure, *PAT* was less suitable. An advantage of these studies was the use of human subjects. However, this choice in turn, prevented the use of highly invasive ‘gold standard’ *PTT* and *PEP* measures or dramatic alteration of circulatory

system behaviour.

A similar study performed in dogs measured *PTT* between catheters in the ascending aorta and femoral artery (Zhang et al., 2011). However, the study does not identify the time of aortic valve opening, implying instead that *PEP* was overestimated as the time from the *ECG* Q-wave to the arrival of the pulse at the first catheter. Additionally, these studies generally used a 200–500Hz sampling rate, meaning a resolution of only 2ms–5ms was available.

Overall, there remains a need to accurately measure and quantify the variability and impact of *PEP* on *PTT*, and thus the level of variability, error and clinical utility of *PAT*. This study improves on previous studies by using a dual catheter aortic *PTT* measure, which is better than the clinical gold standard, and by using a ventricular catheter to detect aortic valve opening, providing highly accurate *PEP*. In addition, data was sampled at 1000Hz, at least double the measurement resolution available in previous studies, minimising inherent timing error.

The overall aim of this study is to use high resolution, gold standard measurements to investigate the relationship between *PAT*, *PEP* and *PTT* across several controlled clinical interventions commonly used to improve cardiac performance in a critical care environment. The results should determine the viability of using *PAT* as a surrogate for *PTT* across a range of cardiovascular conditions and behaviour commonly observed in a critical care environment. If *PAT* proves a reliable surrogate of *PTT*, it may be possible to estimate *PWV* in a clinically applicable manner for use with the Kamoi model of Chapter 6, dramatically improving the methods clinical applicability, one of the goals of this thesis (Section 1.4).

7.5 Method

7.5.1 Porcine Trials and Measurements

The data for this study comes from five pure Pietrain pigs, specifically Pigs D1–D5 of the dobutamine protocol, described in Section 5.2.1. Preparation of the pigs, including sedation and euthanasia, was covered in Section 5.2. The measurements available were summarised in Table 5.1.

7.5.2 Hemodynamic Modifications Effects on *PEP* & *PTT*

The hemodynamic modifications of Protocol D were covered in Section 5.2.1, and the subsequent data used in analyses, including this one, was given in Section 5.3.1 and Figure 5.1. The exception is the Dobutamine High PEEP stage, which was not used in this study. Thus, Figure 7.1 is a modified version of Figure 5.1, specific to this study.

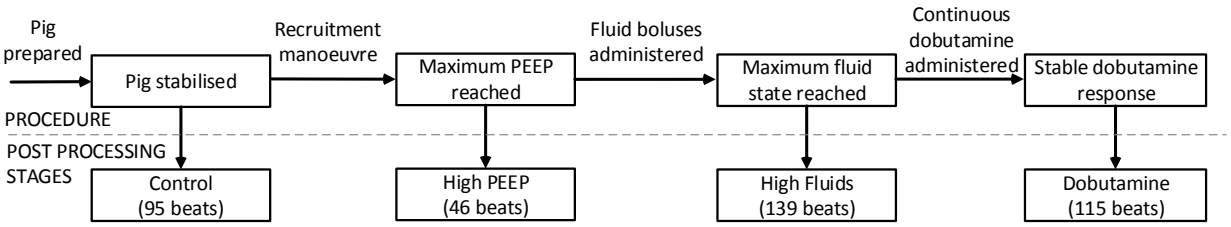

Figure 7.1: Dobutamine protocol experimental procedure, post processing stages and number of heart beats used from each stage, specific to this study. For full details on the protocol, refer to Section 5.2.1.

The remainder of this section summarises the interventions and predicts their effect on cardiac performance and the systolic time intervals of interest to the study. The degree to which each pig responds depends on its sensitivity to the specific intervention, as well as its state following prior interventions.

Recruitment Manoeuvre *High PEEP* Stage

The data analysed from the recruitment manoeuvre (RM), was captured during the duration of maximum positive end-expiratory pressure (PEEP), called the *high PEEP* stage. Per

Section 5.2.1, increases in PEEP can decrease preload and increase afterload (Luecke and Pelosi, 2005; Marik, 2010). In turn, the decreased left ventricular preload can increase *PEP* (Wallace et al., 1963). *PTT* changes during this modification are harder to predict, since the pressure in vessels lying outside the thorax are less effected by PEEP (Luecke and Pelosi, 2005).

Fluid Administration *High Fluids* Stage

The *high fluids* stage covers the time following each pig's final 180 ml fluid bolus administration, taking a pig to its highest fluid state. Section 5.2.1 explained fluids are administered in critical care to increase the blood volume in the hope of improving preload, and thus stroke volume (*SV*) through the Frank-Startling mechanism (Section 2.4.2) (Michard and Teboul, 2002; Cecconi et al., 2015). However, the aforementioned section highlighted response to fluid administrations is clinically variable and depends how the body distributes the introduced bolus (Michard and Teboul, 2002). Thus, it is possible little change in cardiac performance will occur for those pigs that are fluid unresponsive.

Dobutamine Administration

The final stage analysed is the continuous *dobutamine* infusion. Section 5.2.1 explained how the inotrope dobutamine is administered to increase contractility, and can lead to an increase in *SV*, as per Figure 2.8. Previous studies have shown *PEP* decreases with the increased velocity of muscle fibre shortening associated with increased contractility, provided other *PEP* influences remain unchanged (Harris et al., 1967; Newlin and Levenson, 1979).

Dobutamine can also act as a vasodilator. However, this effect is subject specific (Ruffolo, 1987; Ellender and Skinner, 2008). Significant vasodilation would increase *PTT* / reduce *PWV*, according to Equation 2.3 and 2.7.

Assessment of Contractile State

In the transition between interventions, a vena cava occlusion was performed. This technique allows changes in the contractile state of the heart to be assessed through the gradient of the end-systolic pressure volume relationship (ESPVR), as per Figure 2.8.

7.5.3 Identification of *PAT*, *PTT* and *PEP*

PTT calculation

In this study, *PTT* was directly measured using the *foot-to-foot* method of Figure 2.13. The feet of the aortic (P_{ao}) and femoral (P_{fem}) pressure waveforms, $t_{0,P_{ao}}$ and $t_{0,P_{fem}}$, were identified using the shear transform method shown in Figure 5.7. Figure 7.2 re-presents *PTT* detection, but also includes identification of *PEP*, pulse delay time (*PDT*) and *PAT*.

PEP calculation

PEP was measured as the time from absolute start of systole, $t_{0,ECG}$, to aortic valve opening. Identification of the *ECG* Q-wave as $t_{0,ECG}$ was discussed in Section 5.4.3 and shown in Figure 5.6. Aortic valve opening was identified as the time P_{vent} exceeded P_{ao}, as per Section 2.3.1 (Guyton and Hall, 2011), and is shown as a black '$\times$' on Figure 7.2.

PDT calculation

The time delay between the aortic valve opening and $t_{0,P_{ao}}$ represents the time it took for the pulse wave to reach the first catheter. This duration is shown on Figure 7.2, referred to as the pulse delay time (*PDT*), to distinguish it from *PTT*. Figure 7.2 specifically uses Pig D4, since it had the longest *PDT* of the cohort, with an average of 12 ms.

Some studies estimate *PEP* as the time from the *ECG* R-wave to $t_{0,P_{ao}}$ (Zhang et al., 2011). However, this time period includes *PDT* and therefore *PEP* estimated in this manner will be overestimated.

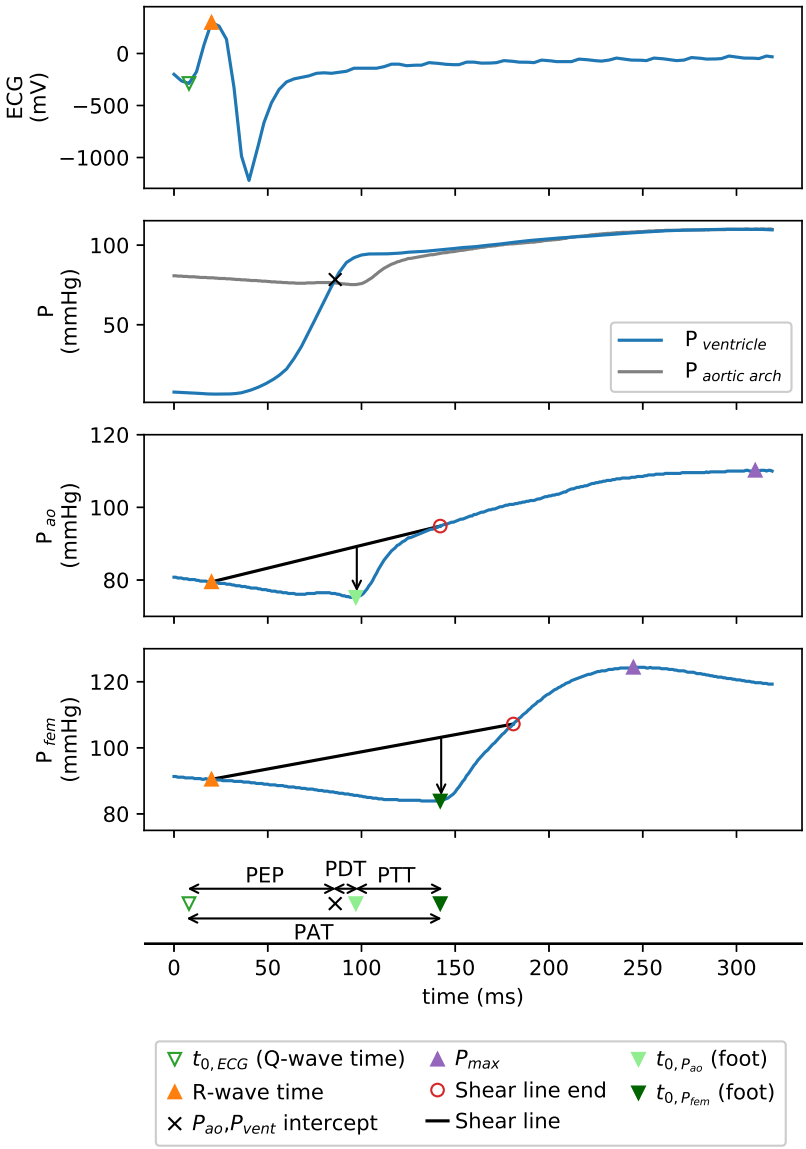

Figure 7.2: Example of how *PEP*, *PDT*, *PTT* and *PAT* were found for each beat. The example waveform comes from a control stage beat of Pig D4, which had the the longest *PDT* of the pigs in the study. The shear transform foot detection method shown, is the same as Figure 5.7.

PAT calculation

Finally, *PAT* was measured from the *ECG* Q-wave to the foot of P_{fem}, as shown in Figure 7.2. Thus, *PAT* is a sum of the other systolic time intervals mentioned, *PEP*, *PDT* and *PTT*, respectively. Each of the systolic time intervals are illustrated in Figure 7.3 to help distinguish between them.

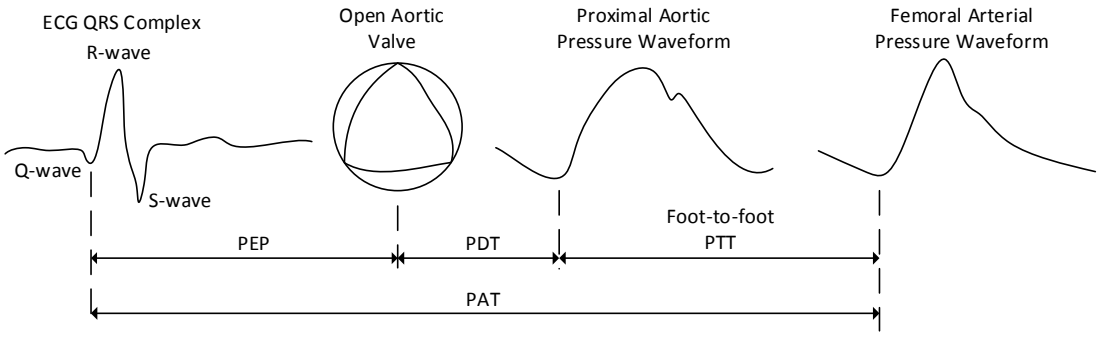

Figure 7.3: Qualitative representation of the systolic time intervals.

7.5.4 Estimation of Cardiac Performance Metrics

Sections 2.4.2 discussed how end-diastolic ventricular pressure (*EDVP*) and volume (*EDVV*) were ventricular preload surrogates. Similarly, Section 2.4.3 discussed how end-diastolic aortic pressure (*EDAP*) was a surrogate measure of ventricular afterload. As explained in Section 5.4.3, $P_{vent}(t_{0,P_{vent}})$, $V_{vent}(t_{0,P_{vent}})$ and $P_{ao}(t_{0,P_{ao}})$ are equivalent to *EDVP*, *EDVV* and *EDAP*, respectively. Thus, changes in ventricular preload and afterload were monitored using $P_{vent}(t_{0,P_{vent}})/V_{vent}(t_{0,P_{vent}})$ and $P_{ao}(t_{0,P_{ao}})$, respectively.

7.5.5 Data Analyses

A specific number of heart beats was used from each stage for data analysis, based on the pig with the fewest beats recorded for the stage. For example, Pig D4 had the shortest control stage with 95 beats before the recruitment manoeuvre began. Thus, the first 95 beats of the other pigs control stages were analysed and successive beats were ignored from the analysis. The remaining stages, high PEEP, high fluids and dobutamine, used 46, 139 and 115 beats respectively, as shown in Figure 7.1. This approach ensured each pig has equal representation in any comparisons.

Using the method in Figure 7.2, *PEP*, *PTT* and *PAT* were measured for each heart beat, and the mean and standard deviation calculated for each particular stage for each pig. The strength of relationship between *PAT* and *PTT* was evaluated for each stage using linear regression analysis and the coefficient of determination (r^2). The r^2 value represents the

fraction of the total observed variation in *PAT* due to the observed variation in *PTT*. Thus, $(\mathbf{1}-r^{\mathbf{2}}) \times \mathbf{100}$ is the percent of behaviour not captured by the linear model.

After individual stages were analysed for a particular pig, an overall analysis for that pig was conducted. The pig specific relationship of *PTT* and *PAT* are therefore accessed over the range of hemodynamic modifications. Finally, the inter-subject variability between pigs is evaluated. Comparing the overall analyses of each pig, differences in pig specific response to the hemodynamic modifications is observed, as well as the overall *PTT*, *PAT* relationship. Thus, similarities or inter-subject variability are highlighted.

7.6 Results

Table 7.1 presents the mean and standard deviation for *PEP*, *PTT* and *PAT* for each pig and each stage. Additionally, mean *PDT* was determined for each pig during the control stage and was found to range from $<$1 ms to 4 ms for Pigs D1, D2, D3 and D5, while Pig D4 had a mean *PDT* during control of 12 ms (results not shown). *PDT* was then re-measured during subsequent stages and did not change significantly, meaning the upstream catheter (measuring P_{ao}) moved little throughout the experiment.

Table 7.2 shows each stages mean change in preload ($\mathbf{\Delta}\overline{EDVV}$) and afterload ($\mathbf{\Delta}\overline{EDAP}$) measures, as well as mean changes in systolic time intervals. This result provides a more quantitative view of pig response to each stages intervention, which is referred to during the discussion.

Figure 7.4 shows the degree to which changes in *PEP* and *PTT* affected *PAT*, for each intervention. Coefficients of determination were also calculated for each pig individually, across all its stages, and were found to vary between r^2 = 0.05–0.60 (results not shown). In all cases, there is significant inter- and intra- pig variation and no strong relationship appears consistently between variables.

Table 7.1: Per pig, stage-specific statistics for pre-ejection period (*PEP*), pulse transit time (*PTT*) and pulse arrival time (*PAT*). Data is given as mean ± standard deviation in milliseconds (ms), with (percentage change) expressed for the hemodynamic modifications. For high PEEP and high fluids, percentage change is relative to the control stage, while for dobutamine it is relative to the high fluids stage.

Pig	Control			High PEEP			High Fluids			Dobutamine		
	PEP	PTT	PAT	PEP	PTT	PAT	PEP	PTT	PAT	PEP	PTT	PAT
D1	79.8 ± 2.5	62.9 ± 1.7	142.4 ± 3.2	84.0 ± 3.1 (+5%)	61.4 ± 1.9 (-2%)	144.1 ± 3.6 (+1%)	103.9 ± 2.3 (+30%)	62.3 ± 1.5 (-1%)	165.8 ± 3.1 (+16%)	57.7 ± 1.8 (-44%)	56.7 ± 1.3 (-9%)	114.1 ± 1.8) (-31%)
D2	57.6 ± 1.9	53.4 ± 1.4	114.3 ± 2.2	57.0 ± 1.8 (-1%)	53.9 ± 1.7 (+1%)	114.3 ± 2.2 (0%)	63.7 ± 1.6 (+11%)	55.4 ± 1.4 (+4%)	122.2 ± 1.9 (+7%)	66.0 ± 1.4 (+4%)	56.6 ± 1.5 (+2%)	124.9 ± 1.9 (+2%)
D3	85.1 ± 1.4	58.4 ± 1.3	141.9 ± 1.8	86.5 ± 3.1 (+2%)	64.3 ± 1.8 (+10%)	149.9 ± 3.8 (+6%)	95.5 ± 4.2 (+12%)	59.0 ± 1.6 (+1%)	154.2 ± 4.8 (+9%)	104.2 ± 3.2 (+9%)	62.5 ± 1.9 (+6%)	165.5 ± 4.0 (+7%)
D4	79.4 ± 3.8	44.9 ± 1.2	136.4 ± 3.6	87.5 ± 3.4 (+10%)	44.1 ± 1.5 (-2%)	137.5 ± 3.6 (+1%)	90.2 ± 1.9 (+14%)	42.3 ± 1.6 (-6%)	144.6 ± 2.7 (+6%)	81.8 ± 1.6 (-9%)	44.0 ± 1.4 (+4%)	137.3 ± 1.9 (-5%)
D5	52.7 ± 3.0	103.1 ± 2.0	157.7 ± 3.7	56.4 ± 3.0 (+7%)	113.3 ± 2.1 (+10%)	171.2 ± 3.2 (+9%)	58.5 ± 3.5 (+11%)	93.5 ± 2.1 (-9%)	155.6 ± 3.9 (-1%)	72.9 ± 3.4 (+25%)	86.0 ± 2.9 (-8%)	161.7 ± 4.8 (+4%)

Table 7.2: Mean change in afterload ($\Delta\overline{EDAP}$), preload ($\Delta\overline{EDVV}$), pre-ejection period ($\Delta\overline{PEP}$), pulse transit time ($\Delta\overline{PTT}$) and pulse arrival time ($\Delta\overline{PAT}$), between intervention stages.

	Pig				
	D1	**D2**	**D3**	**D4**	**D5**
	Control to High PEEP				
$\Delta\overline{EDAP}$	+2%	-12%	-26%	-5%	-15%
$\Delta\overline{EDVV}$	+8%	-20%	-49%	-38%	-17%
$\Delta\overline{PEP}$	+5%	-1%	+2%	+10%	+7%
$\Delta\overline{PTT}$	-2%	+1%	+10%	-2%	+10%
$\Delta\overline{PAT}$	+1%	0%	+6%	+1%	+9%
	Control to High Fluids				
$\Delta\overline{EDAP}$	+12%	-3%	+6%	+23%	+22%
$\Delta\overline{EDVV}$	+6%	+7%	+25%	+31%	+1%
$\Delta\overline{PEP}$	+30%	+11%	+12%	+14%	+11%
$\Delta\overline{PTT}$	-1%	+4%	+1%	-6%	-9%
$\Delta\overline{PAT}$	+16%	+7%	+9%	+6%	-1%
	High Fluids to Dobutamine				
$\Delta\overline{EDAP}$	-2%	-1%	-9%	-9%	0
$\Delta\overline{EDVV}$	-19%	-4%	-24%	-24%	-1%
$\Delta\overline{PEP}$	-44%	+4%	+9%	-9%	+25%
$\Delta\overline{PTT}$	-9%	+2%	+6%	+4%	-8%
$\Delta\overline{PAT}$	-31%	+2%	+7%	-5%	+4%

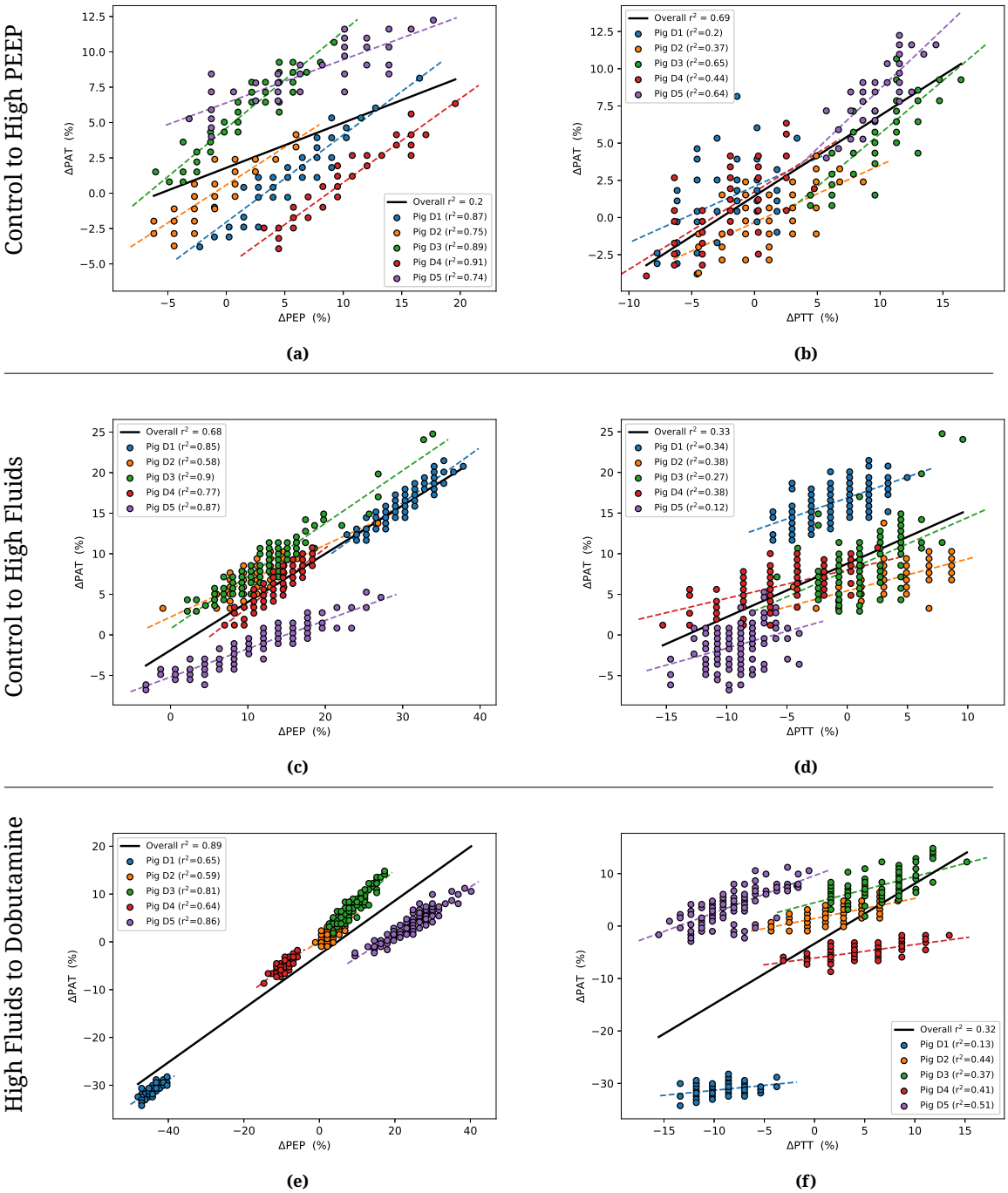

Figure 7.4: The percentage change (Δ) in each pig's systolic time interval with respect to control for the high PEEP and high fluids stages, and with respect to high fluids for the dobutamine stage.

7.7 Discussion

7.7.1 Response to Interventions

Response to High PEEP Stage

PEEP directly effects lung mechanics, rather than directly changing cardiac behaviour. Thus, *PEP* and *PTT* are indirectly effected by this intervention. PEEP caused significant reductions in preload (*EDVV*) and afterload (*EDAP*) in Pigs D2-D5, as seen in Table 7.2. Independently, a decrease in preload and afterload should have opposing effects on *PEP*, with preload being inversely proportional to *PEP*, while afterload is directly proportional (Weissler et al., 1968; Talley et al., 1971; Bendjelid et al., 2004). Preload appeared to dominate the response of Pigs D4 and D5 showing an increase in *PEP*, while Pigs D2 and D3 showed little change in *PEP* possibly due to the cancelling effect of their preload and afterload changes. Pig D3 and D5 also showed significant increases in *PTT*, coupled with the largest reductions in mean arterial pressure (*MAP*) (results not shown).

PAT increased in four of the five pigs, given its dependence on *PTT* and *PEP*. Under the relatively short term high PEEP stage, overall variation in *PAT* was largely explained by variation in *PTT* (r^2 = 0.69 in Figure 7.4b). However, the overall correlation is slightly misleading, since for any individual pig, variation in *PEP* correlated highly with *PAT*, explaining the lower individual correlation of *PAT* with *PTT*. Thus, the *PEP* increase would still cause an overestimate in the change (Δ) in *PAT* if it were to be used as a surrogate for ΔPTT.

Response to High Fluids Stage

The fluid administration caused significant increases in preload (*EDVV*) and afterload (*EDAP*), as seen in Table 7.2. However, it appears afterload dominated response in these cases, with increases in *PEP* of from 11%-30%. *PTT* was less effected, although it did show a notable reduction in Pigs D4 and D5. The lack of correlation between changes in *PAT* and

PTT (r^2 = 0.33) compared with changes in *PAT* and *PEP* (r^2 = 0.68), in Figures 7.4c and 7.4d, respectively, shows variation in *PAT* was dominated by changes in *PEP* during this stage. Thus, during this stage, the surrogate measure (*PAT*) performed poorly.

Response to Dobutamine Stage

The final intervention, dobutamine administration, successfully increased contractility for all pigs whose contractility was measured, namely Pigs D1, D3, D4 and D5, whose ESPVR slopes increased 104%, 16%, 55% and 79%, respectively (results not shown). Because dobutamine administration followed the high fluids stage, the effects of the dobutamine are compared with the hemodynamic state during the high fluids stage. This timing of the two therapies is a limitation of the study.

During dobutamine admission, significant pig specific changes in many of the measured hemodynamics was observed, as well as the largest intra- and inter- pig variation in *PEP*, *PTT* and *PAT*. Although *PEP* is known to change inversely to contractility (Harris et al., 1967; Newlin and Levenson, 1979), the relationship can be obscured by other factors, such as preload and afterload changes, which also were observed in this stage in Table 7.2. It is thus difficult to find consistent reasoning for the changes in *PEP* during this stage. However, this variability represents typical behaviour in a critical care environment, where patients have multiple contributing factors to any observed changes in hemodynamic behaviour.

For example, Pigs D1 and D5, show the largest contrasting changes in *PEP* of the study, with Pig D1 having a 44% mean reduction and Pig D5 having a 25% mean increase. Pig D1 went on to show the largest mean change in *PAT* of the study, falling 31%, significantly overestimating it's mean reduction in *PTT* of 9%. Pig D3 on the other hand showed a mean increase in *PAT* of 4%, driven by the *PEP* increase, despite *PTT* falling 8%. This stage then provides perhaps the best example of why *PAT* may be an inadequate surrogate of *PTT* under clinical conditions, with changes in *PTT* being both under and over estimated by reflected changes in *PAT*, according to Figure 7.4f.

7.7.2 Overall *PAT* and *PTT* relationship

Considering the effects of each stage individually and across pigs, the range of r^2 values (0.32-0.69, Figures 7.4b, 7.4d and 7.4d) and range of regression line slopes implies the relationship between *PAT* and *PTT*, is intervention specific. Additionally, the intra-pig *PTT* and *PAT* correlations for all stages were pig specific (r^2 = 0.05-0.60 results not shown). Thus, ΔPAT cannot be guaranteed to accurately reflect ΔPTT, even if an initial calibration of *PTT* occurs.

The low r^2 values show variation in *PTT* accounts for a small proportion of the variance in *PAT*. Since only a weak relationship exists between *PAT* and *PTT*, the results suggest *PAT* is an undesirable surrogate measure of *PTT*. Despite this evident variability and potential introduced error, *PAT* is still used as a surrogate for *PTT* in several studies (Pitson et al., 1994; Cameron et al., 2003; Katz et al., 2003; Chua and Heneghan, 2005; Kim et al., 2006; Liu et al., 2016).

However, given these results, the *PAT* surrogate should be used with caution. In a clinical environment where different therapies may be utilized across a wide range of patient disease states, and patient hemodynamic state can change unexpectedly, this study suggests using *PAT* as a surrogate to monitoring *PTT* is inappropriate.

7.7.3 Overall Effect of *PEP*

Looking at Table 7.1, mean *PEP* ranges from 53 ms (Pig D5 control) to 104 ms (Pig D3 dobutamine). The similar magnitudes of *PEP* and *PTT* explains why using *PAT* as a direct surrogate measure of *PTT* can result in a significant overestimate. It also explains why even a modest variation in *PEP*, independent of *PTT*, can cause poor correlations between *PAT* and *PTT*, as seen following two of the three clinical interventions. The results of this study suggest the variation in *PEP* is the main reason *PAT* is unsuitable as a surrogate for *PTT*, making it consistent with some other literature (Newlin and Levenson, 1979; Payne et al., 2006; Zhang et al., 2011).

In some studies, *PTT* is estimated by measuring *PAT* and subtracting an assumed constant *PEP* (Fung et al., 2004). However, variability between each pig's control stage *PEP* (Table 7.1) emphasises why a generic constant *PEP* assumption is problematic. Thus, it shows constant *PEP* would likely be incorrect for clinically unstable patients, where an accurate estimation is most needed.

For example, the two pigs with the least variability in *PEP*, Pigs D2 and D4, had mean values of 58 ms and 79 ms during the control stage, and 61 ms and 85 ms when averaged across all stages. Furthermore, Table 7.2 and Figure 7.4 show *PEP* is highly dependent on the hemodynamic state, which is itself also pig specific, rendering a constant *PEP* assumption even less valid if hemodynamic modifications are applied or the patient/subject is hemodynamically unstable.

Hence, in this study, *PEP* could not have been ignored or estimated from a population value to accurately capture changes in *PTT* using *PAT*. Therefore, the results also suggest any population based mean for *PEP* is not reliable for clinical analysis, evaluation or decision making.

7.7.4 Possible Solutions to *PEP* Bias

One solution to minimize bias due to *PEP* is to increase the distance over which the *PTT* portion of *PAT* is measured, for example measuring to a peripheral artery. This change would lead to *PEP* making up a smaller proportion of *PAT* relative to *PTT* and thus reduce the error in *PAT* as an estimate of *PTT* (Loukogeorgakis et al., 2002; Fung et al., 2004). However, a common clinical motivator for calculating *PTT* was the determination of arterial stiffness, specifically along the aortic pathway, as previously discussed in Section 7.3. Using the periphery for estimations of *PTT*, shifts the physiological area of interest to include a far greater part of circulation and thus leads to an overestimate in aortic arterial stiffness and incorrect diagnostic information.

The previous argument used the desire for a local/aortic stiffness as a reason *PAT* or *PTT*

from the heart to the periphery was undesirable. However, a more global *PTT* value is adequate for other uses, such as monitoring changes in blood pressure (Geddes et al., 1981) and a more averaged measure of *PWV* from heart to periphery. A global measure of *PAT* could also be fully non-invasive, as discussed in Section 7.1. Unfortunately, *PAT* measured to the periphery has still been shown to correlate poorly with other physiological metrics known to have strong relationships with *PTT* (Geddes et al., 1981), suggesting *PEP* duration and variability is still significant and must be directly accounted for. For example Pitson et al. (1994) measured *PAT* in humans from the ECG R-wave to a *PPG* signal from a finger pulse oximeter, and found it to be *"approximately 250 ms"*, while *PEP* was found to be *"approximately 160 ms"*, meaning *PEP* still contributed over 60% to *PAT*. In another study using humans and similar methods, Payne et al. (2006) showed *PAT* values similar to Pitson et al. (1994) while mean baseline *PEP* was found to be approximately 95 ms, meaning *PEP* could still realistically contribute 30%-40% of *PAT* (Payne et al., 2006). Thus, *PEP* is significant and highly variable, and use of PTT without this value could be significantly misleading.

Despite these issues, in more recent years, non-invasive measures of *PAT* have still been used as a measure for *PTT* and as a marker for blood pressure changes and arterial stiffness in several studies (Pitson et al., 1994; Bulpitt et al., 1999; Cameron et al., 2003; Katz et al., 2003; Chua and Heneghan, 2005; Kim et al., 2006; Liu et al., 2016). Once again, the evidences suggests assuming *PEP* is negligible or constant, is invalid, even over the longer pulse distance.

Furthermore, using the same analysis as in Figure 7.4, no relationship was seen between change in *PEP* and change in *PTT* ($r^2 < 0.1$, results not shown). It is thus unlikely a calibration measure of *PEP* would enable *PAT* to act as a *PTT* surrogate. Hence, unless an accurate measure or estimate of *PEP* is obtained per beat, *PAT* is an unreliable surrogate for a *PTT* measurement in a clinical environment or cardiovascular model.

7.8 Limitations

The study was motivated by a desire to investigate the suitability of *PAT* as a surrogate measure of *PTT* in an ICU environment. Therefore, the experimental protocol used in this study reflected the common therapies in a critical care setting. It is possible that in an outpatient or community health application, where patients typically present more stable hemodynamics, less variability in *PEP* may be present, and as such, *PAT* may be an applicable *PTT* substitute. However, confirming this possibility would require additional investigation.

7.9 Summary

This study showed changes in pulse arrival time from the *ECG* Q-wave to a downstream arterial site (*PAT*), cannot be assumed to reflect changes in pulse transit time (*PTT*) in patients with unstable hemodynamics or who are given therapies altering hemodynamic state. The weak relationship between *PAT* and *PTT* within pigs and across interventions (r^2 = 0.32-0.69), and changes in *PAT* and *PTT* across pigs (r^2 = 0.05-0.60), was shown to be due to variability in *PEP*, independent of changes in *PTT*. *PEP* appeared to be pig specific and changed inconsistently across intervention stages, with means of the stages ranging from 53 ms to 104 ms. Therefore, *PEP* had a similar magnitude to *PTT*, but with significant variability, meaning its contribution to *PAT* could not be neglected.

In a clinical setting where patients can have multiple disease states and be receiving multiple treatments simultaneously, prediction of *PEP* response may be more difficult. Hence, under these circumstances, this study concludes *PAT* is an inappropriate surrogate for *PTT* if an accurate estimate of *PEP* cannot be found. This conclusion holds regardless of whether the downstream pulse detection is in a proximal or peripheral artery.

This research has extended initial results in this area. They confirm the conclusions hold over a range of therapies common in the critical care cohorts that were the focus of this

study and which alter hemodynamic state. It is thus a fully general result in these clinical relevant patient populations.

Finally, these conclusions strongly suggest using *PAT* to monitor changing central *PWV* beat-to-beat, is inadvisable. The reason for monitoring *PWV* beat-to-beat was for its use in the Kamoi model. Chapter 6 highlighted the potential for the Kamoi model to continuously monitor *SV*, which has significant use in clinical management of circulatory and cardiac shock (Cecconi et al., 2014). However, one of the limitations was the Kamoi model required continuously monitored *PWV* to do so. Thus, the Kamoi model represented an experimental, rather than clinically applicable model, until a method of monitoring *PWV* in a convenient manner could be found. Since unstable patients are those that stand to benefit most from continuous *SV* monitoring, as per Section 1.3.1, *PAT* appears to be an inappropriate surrogate measure for *PTT* and thus *PWV*.

CHAPTER 8

Dicrotic Notch Detection

8.1 Introduction

Chapter 6 discussed how the Kamoi method identified end systole using a weighted first derivative method ($t_{es,dP/dt}$). Section 6.3.2 and Figure 6.2 highlighted the method's inability to accurately detect the *dicrotic notches* marking end-systole in proximal aortic pressure waveforms ($t_{es,dic}$). It also showed the resulting poor precision in $t_{es,dP/dt}$ caused subsequent error in both the Kamoi method's estimated flow waveform (Q_{est}) and stroke volume (SV_{est}).

This chapter develops a more robust method of dicrotic notch detection, for the purpose of end-systole detection. Specifically, the new method is an adaptive shear transform algorithm, which accounts for changes in the pressure waveform shape due to intervention and/or disease progression. A more robust method of identifying the time of end-systole (t_{es}), may contribute to improving the Kamoi method parameter identification and subsequent flow waveform estimation. This outcome would achieve one of the thesis goals in Section 1.4.

8.2 Dicrotic Notch as End-Systole

The dicrotic notch is a distinct stationary point in proximal arterial (often aortic) pressure signals, following a beat's maximum pressure (P_{max}). It may be a point of *inflection* with (approximately) zero gradient, or a combination of two turning points with respective local minimum and maximum, resulting in a *trough* type notch. An example of each type is shown in Figure 8.1. Figure 8.1a also illustrates how end-systole is marked by the dicrotic notch, but the onset of diastolic pressure decay begins from the local maximum after the notch.

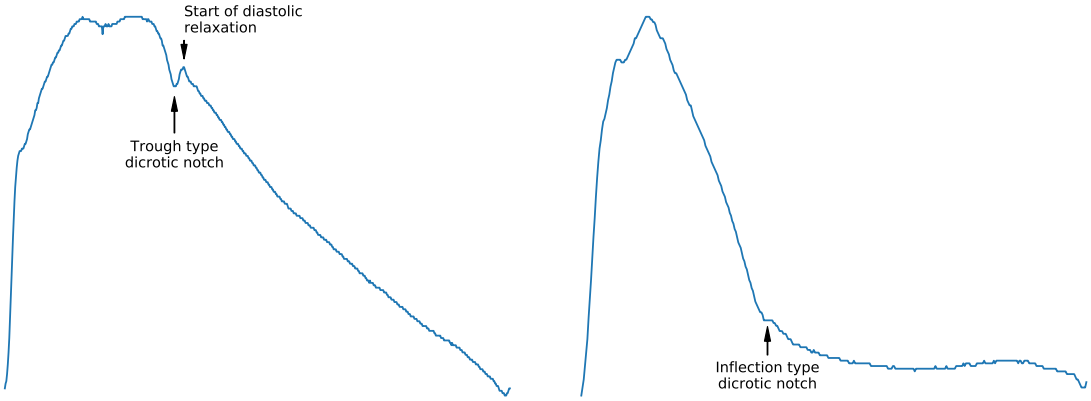

(a) Trough type dicrotic notch example, from Pig D2's control stage. Note, start of diastolic relaxtion is delayed briefly by the dicrotic notch, beginning at the local maximum.

(b) Inflection type dicrotic notch example, from Pig D5's dobutamine high PEEP stage.

Figure 8.1: Examples of the the two types of dicrotic notch shape in P_{ao}. The trough type (a) is clearest in proximal pressure signals, but can be attenuated, either partly (b), or fully, when measured at distances further from the heart or due to abnormal cardiovascular behaviour.

Section 2.3.1 explained the dicrotic notch is formed by wave reflection off of the aortic valve, following valve closure (Lewis, 1906). Thus, it is clearest in proximal pressure signals and crucial for determining transition from systole to diastole in aortic pressure waveforms (Oppenheim and Sittig, 1995). Specifically, aortic systolic duration ($T_{sys,\mathrm{ao}}$), associated with left ventricular ejection, lasts from the *foot* of the aortic pressure waveform, marking start systole ($t_{0,P_{ao}}$), as per Section 5.4.3, to the time of the dicrotic notch, marking end systole ($t_{es,dic}$) (Talley et al., 1971; Payne et al., 2006; Marik, 2013). Diastolic duration, associated with aortic relaxation, is the remaining time from the dicrotic notch to the next pressure waveform foot, signifying start-systole of the next beat.

Given the notch's physical significance as a systolic/diastolic time reference, it has been used in numerous applications, including pulse wave velocity (*PWV*) calculations (Hermeling et al., 2009), models estimating cardiovascular function (Stevenson et al., 2010, 2012b; Balmer et al., 2018b)), and the previously stated left ventricular ejection time ($T_{sys,\text{ao}}$). Therefore, there are many different algorithms applying different signal processing methods to dicrotic notch detection (Oppenheim and Sittig, 1995; Takazawa et al., 1995; Hoeksel et al., 1997; Stevenson et al., 2012a; Balmer et al., 2018a).

To simplify t_{es} estimation, some studies have assumed it is located at the point of maximum negative pressure gradient with respect to time ($\frac{\boldsymbol{dP}}{\boldsymbol{dt}}\text{min}$) (Abel, 1981; Aguado-Sierra et al., 2008; Kamoi et al., 2014, 2017), typically occurring between the maximum pressure of a beat and before the start of diastolic relaxation. This simplification underestimates T_{sys} and overestimates duration of diastole (Balmer et al., 2018a). However, it provides consistent predictable performance in signals with and without dicrotic notches.

8.3 Kamoi's Weighted First Derivative Dicrotic Notch Detection

An example first derivative based end-systole method was briefly described in Chapter 6. Specifically, Kamoi et al. (2017) applied a *"generic"* weighting function to the beat's first derivative, before identifying end-systole as the point of minimum pressure gradient ($\frac{\boldsymbol{dP}}{\boldsymbol{dt}}\text{min}$), referred to as $t_{es,dP/dt}$. The method of finding $t_{es,dP/dt}$ is shown in Figure 8.2, using the same beats shown in Figure 8.1. The first derivative was calculated using Equations 5.1, 5.3 & 5.4, and subsequently filtered using the method outlined in Section 5.4.2. The weighting is calculated and applied to each beat's $\frac{\boldsymbol{dP}}{\boldsymbol{dt}}$ signal individually, considering the start of each beat ($t_{0,P_{ao}}$) to be time zero:

$$w(t) = \frac{\left(0.5 - \left|0.5 - \frac{t}{T}\right|\right)^2}{0.25} \quad where \quad 0 \leq t \leq T \tag{8.1}$$

Where w is the weighting and T is the duration of the entire beat. The author of this thesis also added the 0.25 denominator to normalized the function ($0 \leq w(t) \leq 1$).

The main limitation of identifying $t_{es,dic}$ as $t_{es,dP/dt}$, is the dicrotic notch, being a turning point, has a gradient $\frac{dP}{dt}$ = 0, not the resulting minimum gradient of the weighted signal. The second limitation is the weighting is centred at the middle of the beat, as shown in Figure 8.2. This generic weighting function often results in attenuation of the first derivative around the dicrotic notch, counter to the intention of the method.

Figure 8.2 also includes the estimated time of end-systole based on the minimum of a shear transform ($t_{es,shear}$) (Balmer et al., 2018a). The method used to identify $t_{es,shear}$ is the focus of this chapter, and is only shown here for comparison and motivation.

8.4 Methods

8.4.1 Porcine Trials and Measurements

The data for this study comes from Pigs D1, D2, D4 and D5 of the dobutamine protocol, covered in Section 5.2.1. Preparation of the pigs, including sedation and euthanasia, was covered in Section 5.2. The measurements available were also covered in the aforementioned sections, and summarised in Table 5.1. Specifically, since this study is focused on dicrotic notch detection, the primary measurement of interest is the proximal aortic pressure (P_{ao}).

8.4.2 Hemodynamic Modification

The original purpose of Protocol D was to assess the accuracy of a stroke volume (SV) model under induced hemodynamic modifications outlined in Section 5.2.1 (Kamoi et al., 2015, 2017). However, this study is not concerned about the hemodynamic interventions effect on SV. Instead, the protocol simply provided a variety of pressure waveform shapes to test an improved dicrotic notch detection algorithm.

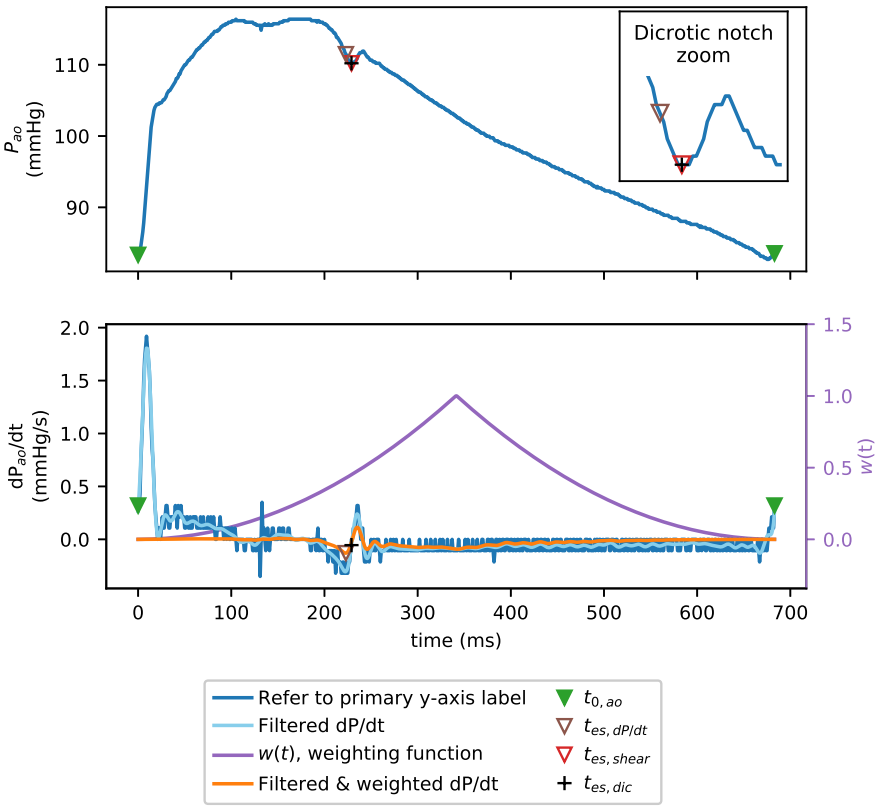

(a) Kamoi et al. (2017) end-systole detection method applied to Pig D2.

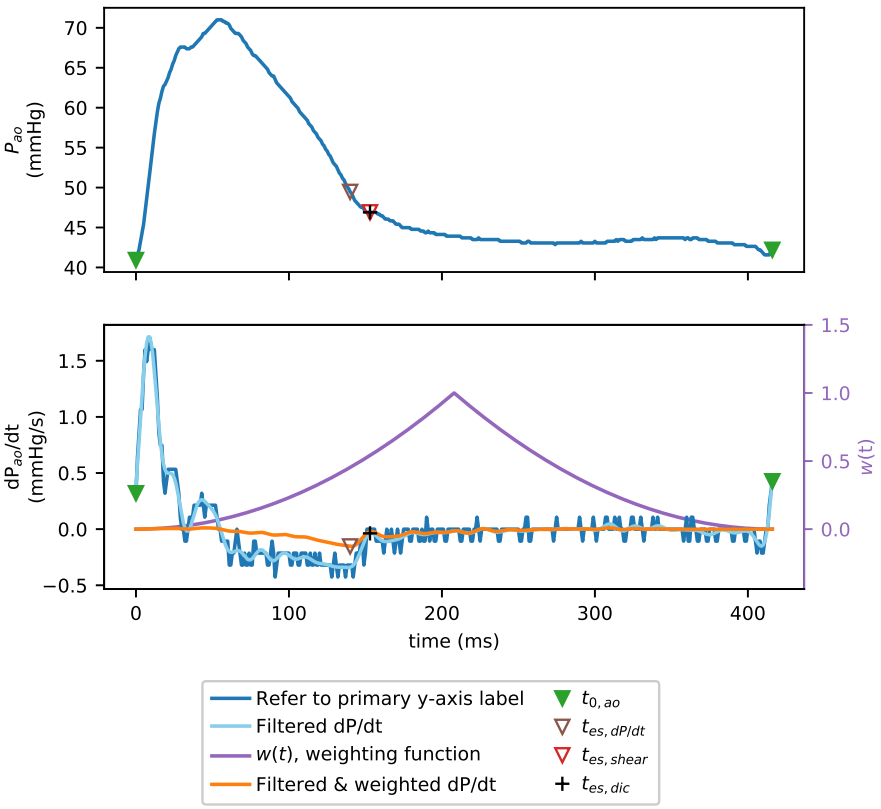

(b) Kamoi et al. (2017) end-systole detection method applied to Pig D5.

Figure 8.2: Kamoi et al. (2017) end-systole detection method ($t_{es,dP/dt}$) applied to the beats shown in Figure 8.1. The figures also included as a reference $t_{es,dic}$ and $t_{es,shear}$, the definitive dicrotic notch location from Figure 8.1, and the improved method of dicrotic notch detection developed in this chapter, respectively.

8.4.3 Data Selection Summary

The data used to test the dicrotic notch detection algorithm is taken from two distinct sections of the experiment: the baseline *control* and *dobutamine high PEEP* stages. The control stage was when a pig was at rest following anaesthesia, but before any hemodynamic modifications were applied. Dobutamine high PEEP data was captured during the highest PEEP level of the recruitment manoeuvre (RM) during dobutamine admission, per Figure 5.1. For each pig, from each stage, 10 heart beats were used, leading to a total of 80 beats for the analysis. These two stages were chosen as they represented contrasting hemodynamic states, causing significant change in the aortic pressure waveform analysed.

8.4.4 Beat Separation and Manual Dicrotic Notch Identification

Before dicrotic notch identification began, the P_{ao} signal for each pig and stage was separated into the 10 individual beats, using start-systole ($t_{0,P_{ao}}$). Once again, $t_{0,P_{ao}}$ was identified as the foot of each waveform, using the established algorithm discussed in Section 5.4.3 and shown in Figure 5.7 (Balmer et al., 2018c).

To measure the accuracy of a dicrotic notch detection algorithm, the definitive dicrotic notch locations must be known. Since there is no gold standard algorithm, the best comparison is to locations chosen by trained eye, from the discrete aortic pressure signal. Therefore, points were found manually prior to the algorithm estimates. To aid in selection, the left ventricular pressure (P_{vent}) waveform could be plotted with the P_{ao} signal, since after aortic valve closure, different ventricular and aortic relaxation rates lead to the divergence of the two pressure signals, as seen in Figures 2.5, 4.3 and 5.4. This divergence served only as a secondary reference for manual notch location. The primary identifier being the turning point or point of inflection in the signal, following a beats P_{max}.

8.4.5 Adaptive Shear Transform Algorithm Implementation for Dicrotic Notch & Start of Diastolic Relaxation Identification

The dicrotic notch detection algorithm utilizes a shear transform, applied to each beat in a similar manner to time of start-systole (t_0) in the electrocardiogram (*ECG*) and pressure signals in Section 5.4.3. The shear line start (*SP*) and end points (*EP*), and hence gradient, are adaptive and dependent on waveform shape.

Both the *SP* and *EP* have separate rationales for being iterable. The aim for *SP* is for it to reside in the region of consistent negative pressure gradient, following the maximum pressure, but prior to the dicrotic notch. *EP* on the other hand, is used to ensure the shear line is *quasi-parallel* to the pressure over the region the dicrotic notch is expected to reside.

The process is defined in three sections (A, B, C) comprising a total of 10 steps:

A. Shear Line Start Point (SP) Calculation

1. Identify the maximum pressure in a beat, P_{max}. For this data, P_{max} was actually found prior as part of $t_{0,P_{ao}}$ identification, as per Section 5.4.3.

2. In the region from P_{max} and up to a 1/3 of the remaining time toward the end of the beat, identify the beat's point of minimum gradient ($P_{min\ dP/dt}$). $\frac{dP}{dt}$ is calculated and filtered as per Sections 5.4.1 and 5.4.2.

3. Identify the point *where pressure* is halfway between P_{max} and $P_{min\ dP/dt}$, as the shear line start point (*SP*).

4. Identify an initial shear line end point (*EP*), being a certain time between *SP* and the end of the current beat, based on P_{max}:

    - If $P_{max} < 100$ mmHg: initial *EP* is 3/4 of the way from *SP* to end of beat.

    - If 100 mmHg $< P_{max} <$ 140 mmHg: initial *EP* is 1/2 of the way from *SP* to end of beat.

- If $P_{max} > 140$ mmHg: initial *EP* is 1/3 of the way from *SP* to end of beat.

EP initial location being later in time for beats with low P_{max} values, is simply based on observation of later and lower pressure dicrotic notches (relative to P_{max}) in low pressure signals.

5. Construct the shear line over the section of pressure signal between *SP* and *EP*. Calculate the shear transform, from the section of pressure signal to the shear line, the calculation process is the same as performed for t_0 in Section 5.4.3. Check the resulting shear transform:

   - If more than 50% of the shear transform is greater than zero, i.e. if more than 50% of the shear line is below the corresponding pressure section, assume the shear line start point was poorly identified. This may be due to unexpected physiological behaviour, or simply signal noise. Return to step 2, using the next most minimum gradient point to find a new *SP*. An example of this situation is shown in Figure 8.3.

   - Else, assume *SP* has been correctly identified and move on to check and possibly update the initial *EP*.

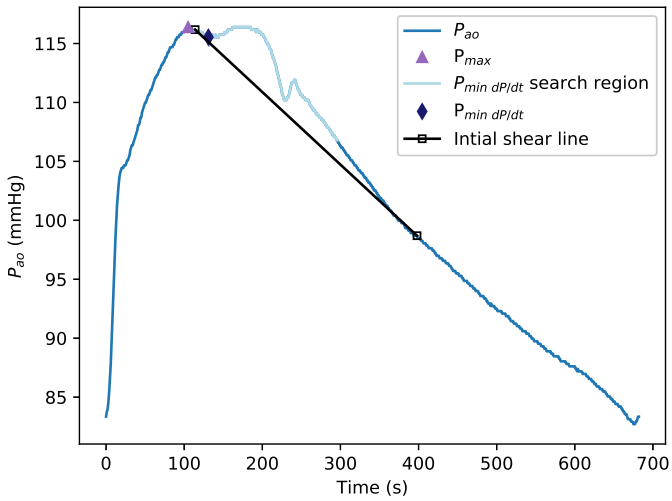

(a) More than 50% of the shear lines length is under the pressure signal, failing the condition outlined in Step 5.

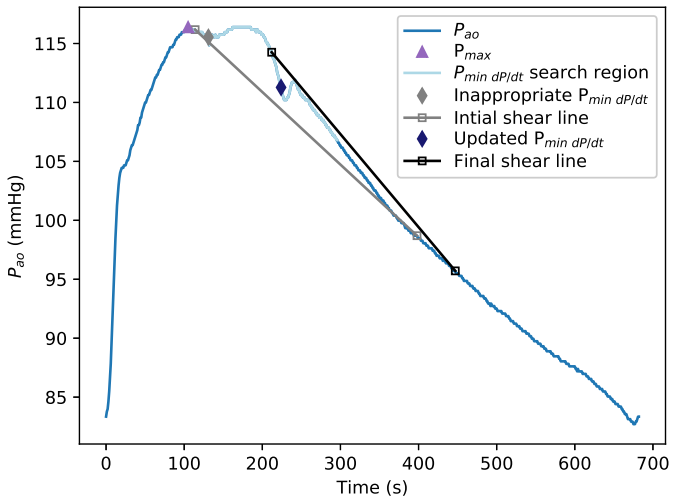

(b) Iterated $P_{min\ \mathrm{dP/dt}}$ until Step 5 condition is met.

Figure 8.3: Example of how incorrect choice of $P_{min\ \mathrm{dP/dt}}$ can lead to a shear line start point (*SP*) that results in the shear line passing under the pressure signal (a). This is resolved by iterating $P_{min\ \mathrm{dP/dt}}$, using the next most minimum gradient point to find a new *SP* (b).

B. Shear Line End Point (EP) Calculation

EP condition is based on the orthogonal distance from points on the shear line to points on the pressure waveform:

6. Normalize the shear line and the section of pressure associated with the shear line, in both time and pressure, so that it is scale invariant.

7. For each point on the normalized shear line, calculate the orthogonal distance to a point on the normalized pressure signal. If any point's orthogonal distance $>$ a tolerance of 0.3, shift *EP* closer to *SP* until orthogonal distance ≤ 0.3, at which point assume *EP* location is adequate[1]. An example of this process is shown in Figure 8.4.

C. Identifying the Dicrotic Notch and Start of Diastolic Relaxation

8. Re-calculate the shear transform from the section of pressure signal, between the finalised *SP* and *EP* points, to the shear line. The calculation process is the same as performed for t_0 in Section 5.4.3. The point of most negative shear ($P_{min,shear}$) is initially

[1] If *EP* needs to be updated, the root-finding *bisection method* is used to solve for *EP* that satisfies the orthogonal distance condition, since it is more efficient than an iterative approach.

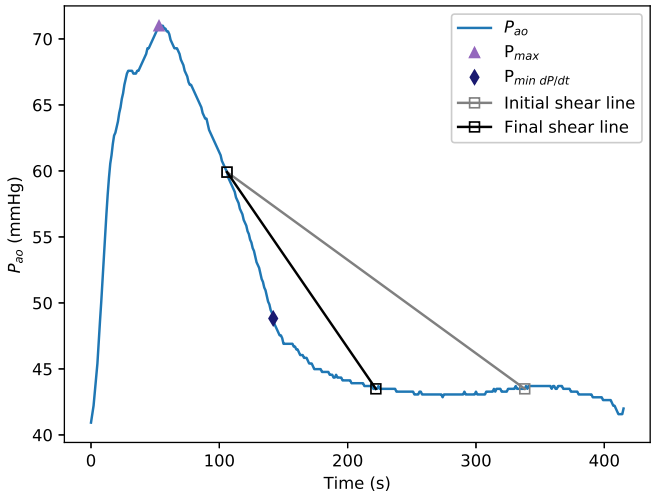

(a) Example initial and final shear lines, where the initial shear lines gradient was too low *in magnitude* relative to the signals gradient in the region of expected $t_{es,dic}$. The shear line is then updated via Step 7, illustrated in Figure 8.4b.

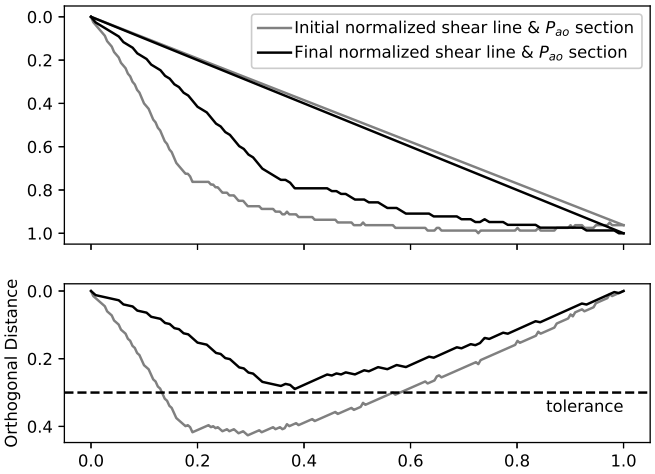

(b) Upper panel shows the initial and final shear lines of Figure 8.4a and their corresponding pressure signals, after normalization. The lower panel shows the orthogonal distance from each normalized shear line to the normalized pressure signal, as well as the orthogonal distance tolerance of 0.3.

Figure 8.4: Example of how the end point (*EP*) is shifted until the resulting shear line is considered *quasi-parallel* with the pressure waveform in the region of $t_{es,dic}$.

assumed to be a point *within* the trough of a dicrotic notch. However, it is possible the $P_{min,shear}$ is not the lowest point of a trough type dicrotic notch. Furthermore, the dicrotic notch may not be a notch at all, it could simply be the inflection type of Figure 8.1b. Thus, additional steps address theses possibilities.

9. Find the start of diastolic relaxation/decay (t_{dr}), as the point of maximum pressure between the point $P_{min,shear}$ and the end of the beat. If the dicrotic notch is a trough,

this will find the local maximum turning point following the trough and is assumed the start of diastolic relaxation (t_{dr}), as per Figure 8.1a.

10. Search from $P_{min,shear}$ (inclusive) to t_{dr} for any points lower than $P_{min,shear}$. The lowest of these point is the estimated dicrotic notch and end-systole, $t_{es,shear}$, based on the adaptive shear transform. If there are multiple points with equal lowest values, take the middle of the lowest points as the dicrotic notch.

Shear Transform Algorithm Summary

The algorithm outlined may initially appear complex due to the number of steps, but each step individually is simple and the intention for the final shear line is conceptually easy to understand. Specifically, the steps aimed to construct a shear line whose gradient is similar to the average gradient of the pressure signal below the shear line. The shear transform itself is simply the vertical distance between each point on the pressure waveform, and the corresponding point in time on the shear line. The expectation is as the pressure falls rapidly in late systole, leading into the local minimum of a dicrotic notch, the vertical displacement from the shear line will be greatest. Figure 8.5 shows the overall method applied to each type of dicrotic notch shown in Figure 8.1, including the final $t_{es,shear}$ and t_{dr} points.

8.4.6 Analyses

Rather than directly comparing the difference between the algorithmically estimated dicrotic notch location ($t_{es,shear}$) and its location by eye ($t_{es,dic}$), the systolic duration resulting from each is compared, $T_{sys,shear}$ & $T_{sys,mea}$ respectively. This approach is because, as discussed in Section 8.2, the dicrotic notch is often used to determine systolic and diastolic time intervals (Talley et al., 1971; Payne et al., 2006; Marik, 2013). In addition, the shear transform method $T_{sys,shear}$, is compared with the systolic duration measured to $t_{es,dP/dt}$ ($T_{sys,dP/dt}$), the systolic duration used in Kamoi et al. (2017), as outlined in Chapter 6.

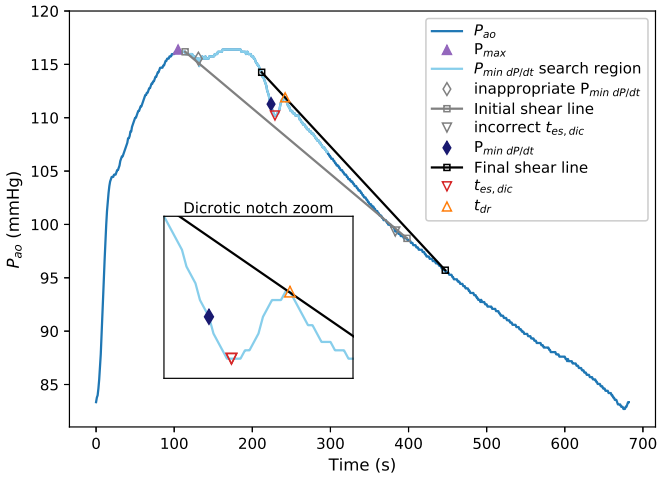

(a) The grey shear line misidentifies the dicrotic notch, due to $P_{min\ dP/dt}$ being too close to P_{max}. The black shear line shows the iteration of $P_{min\ dP/dt}$, which led to a satisfactory *SP* and subsequent dicrotic notch detection.

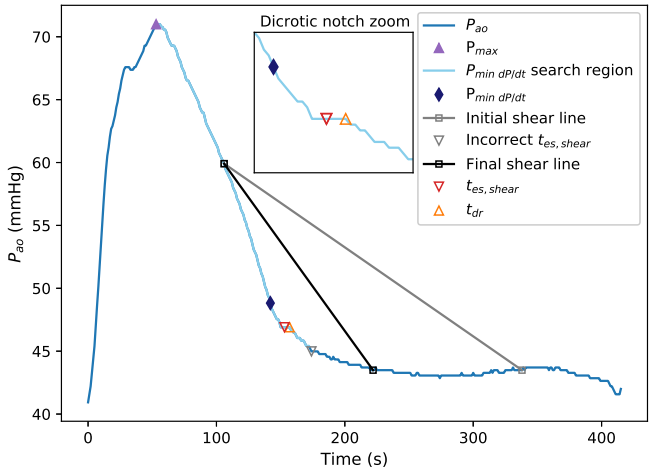

(b) The grey shear line has too greater orthogonal distance from the pressure waveform, misidentifying the dicrotic notch. The black shear line shows the iteration of *EP* using the orthogonality condition, and subsequent dicrotic notch detection.

Figure 8.5: Complete algorithm process for identifying $t_{es,shear}$ and t_{dr} on the two types of dicrotic notches originally shown in Figure 8.1. Each subfigure also includes its initial shear line and the dicrotic notch estimate which would have resulted if it were not for the adaptive approach of the shear line start and end points.

The accuracy of the two algorithmic dicrotic notch detection methods ($t_{es,shear}$ and $t_{es,dP/dt}$) were analysed using their respective T_{sys} values in two formats. First, regression analysis and coefficients of determination (r^2), both overall and for individual pigs and stages. The coefficient of determination, r^2, represents the fraction of the total observed variation in the algorithmically *estimated systolic duration* ($T_{sys,shear}$ or $T_{sys,dP/dt}$) due to the observed variation in the *measured systolic time* ($T_{sys,mea}$). The closer r^2 is to 1.0, the better the ability of the algorithm to track changes in $T_{sys,mea}$.

Table 8.1: Coefficient of determination (r^2) for each T_{sys} estimate ($T_{sys,shear}$ & $T_{sys,dP/dt}$) vs $T_{sys,mea}$, for each stage.

	Pig			
	D1	**D2**	**D4**	**D5**
	Control			
$T_{sys,shear}$	1.0	1.0	1.0	1.0
$T_{sys,dP/dt}$	0.83	0.69	0.89	0.82
	Dobutamine High PEEP			
$T_{sys,shear}$	0.99	1.0	1.0	0.21
$T_{sys,dP/dt}$	0.97	0.01	0.68	0.01

However, correlation does not imply agreement or causality in the absolute sense (Bland and Altman, 1986). Therefore, Bland-Altman analysis was used to assess the agreement between the estimated and measured systolic time, and hence agreement between estimated and measured dicrotic notches locations.

8.5 Results & Discussion

Figure 8.6 shows the regression analyses and overall coefficients of determination. Individual pig stages r^2 are shown in Table 8.1. Bland-Altman plots are seen in Figure 8.7. Overall, the plots show improved trending and agreement for the shear transform algorithms over Kamoi's method.

8.5.1 Correlation Outcomes

Figures 8.6a & 8.6b show excellent overall correlations outcomes. However, the overall result alone is misleading, due the clustering of each pig's individual stage data (Bewick et al., 2003). The difference between the two algorithmic methods ability to track changes in systolic time becomes clearer when comparing the coefficients of determination (r^2) for the individual pigs and stages, referring to Table 8.1. In all pigs and stages, the shear transform method of dicrotic notch detection performs better than the Kamoi method, resulting in individual pig stage r^2 values closer to 1.0.

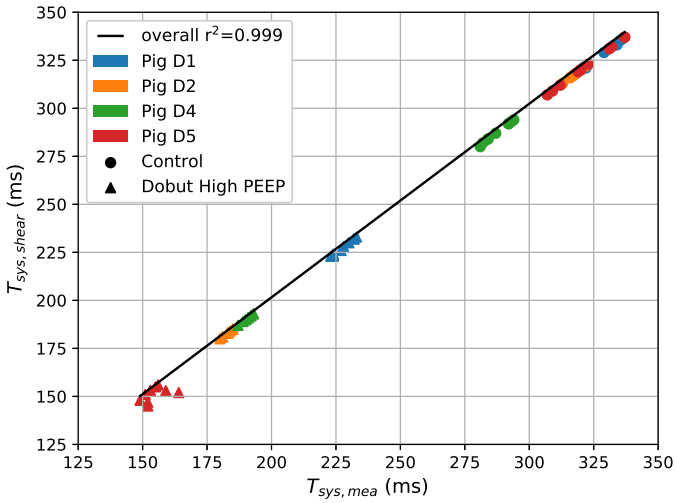

(a) Overall regression analysis between $T_{sys,shear}$ (estimated from $t_{es,shear}$) and $T_{sys,mea}$

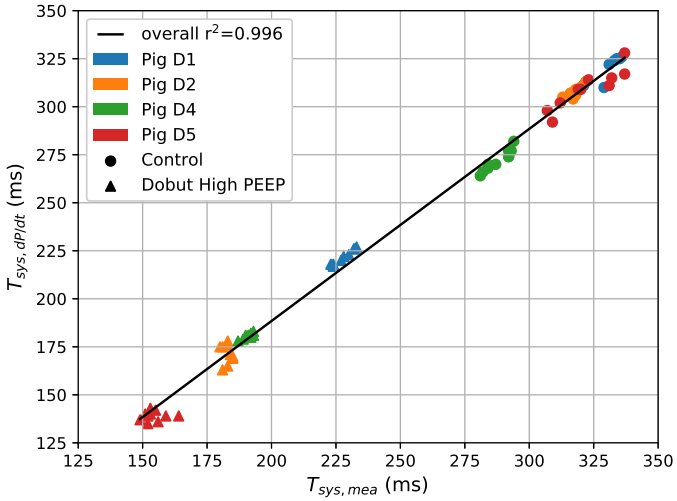

(b) Overall regression analysis between $T_{sys,dP/dt}$ (estimated from $t_{es,dP/dt}$) and $T_{sys,mea}$

Figure 8.6: Regression Analysis: (a) and (b) show the overall and individual regression analyses for the pigs, for both the shear line estimated systolic time and Kamoi method estimated systolic time, respectively. Coefficients of determination in the legend were rounded to three decimal places and dobut high PEEP refers to the dobutamine high PEEP data.

In addition, the Kamoi method's ability to track variation in systolic time decreased following hemodynamic modification, from baseline to the dobutamine high PEEP state, which is coupled with a reduction in systolic time. This result is evident in the reduced coefficients of determination during dobutamine high PEEP stages. With the exception of Pig D5, the shear transform method showed no significant change in performance between hemodynamic states.

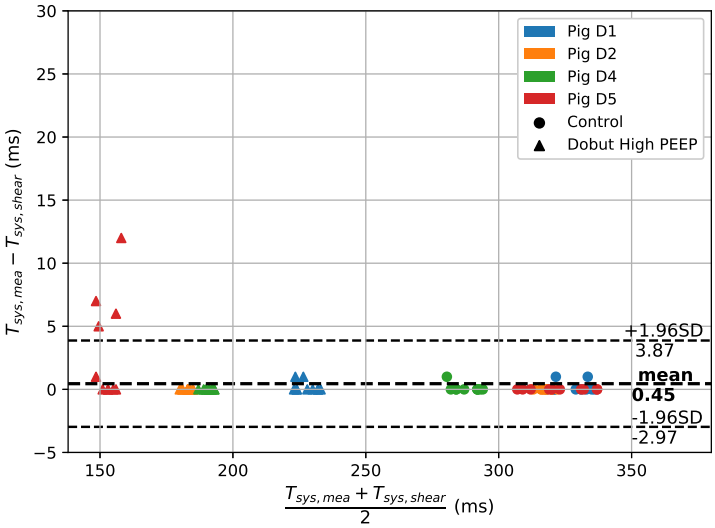

(a) Agreement between $T_{sys,shear}$ (estimated from $t_{es,shear}$) and $T_{sys,mea}$

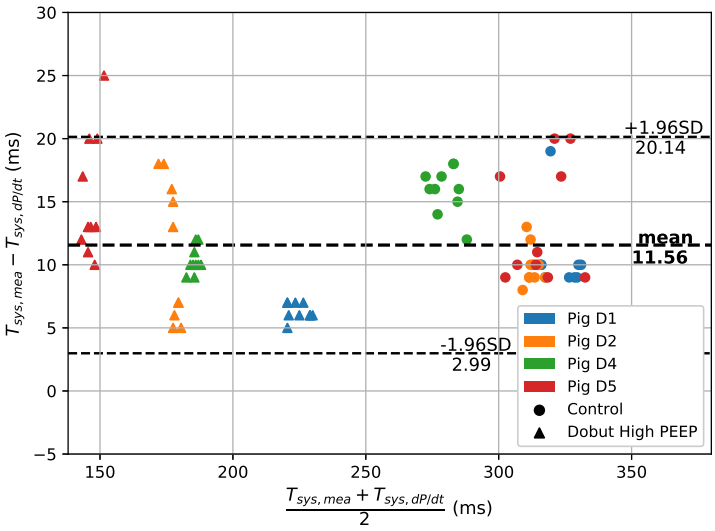

(b) Agreement between $T_{sys,dP/dt}$ (estimated from $t_{es,dP/dt}$) and $T_{sys,mea}$

Figure 8.7: Bland Altman analysis: Bland Altman plots show the degree of agreement between the estimated and measured systolic times. The mean bias between the measured and estimated systolic times are shown ($\bar{d}$), as well as the limits of agreement ($\bar{d} \pm 1.96 \times SD$) to indicate the expected variation between measure and estimate. Note, dobut h PEEP label is an abbreviation of dobutamine high PEEP.

The reason for the lower performance of the Kamoi method following the hemodynamic modifications, and for the shear method in Pig D5's case, appears due to changes in the dicrotic notch shape. Taking Pigs D2 and D5 as examples, Pig's D2 dicrotic notches, in general became wider during dobutamine high PEEP ($\approx$ 28 ms), compared with the baseline stage ($\approx$ 8 ms), when manual measurements were made from the waveform plots between the widest points of the dicrotic notches. This change results in more points forming the dicrotic notch shape, increasing the possibility the algorithm finds a point different from

that chosen manually. This issue is discussed further in Section 8.5.3. In contrast, Pig D5 showed an almost disappearing of its dicrotic notch during dobutamine high PEEP compared to baseline, as seen in the example Figures 8.1b and 8.5b. Naturally, when the dicrotic notch is difficult to detect by eye, a human observer's ability to accurately identify it is reduced. This makes it more difficult to say with certainty which dicrotic notch represents aortic valve closure best, the point identified by the algorithm or chosen manually. Hence, in Pig D5's dobutamine high PEEP stage, poorer correlation outcomes were unsurprising.

In summary, inter-pig and stage correlation analysis results suggest both algorithmic methods track significant changes in systolic time well. However, the tracking of the shear transform method is superior to the Kamoi method in all cases.

8.5.2 Bland Altman Outcomes

The contrasting systemic error of the Kamoi method relative to the shear transform method, as shown by the mean differences of $\overline{d_{dP/dt}}$ = 11.6 ms verses $\overline{d_{shear}}$ = 0.5 ms respectively, is the most obvious result of Figure 8.7. This much lower $\overline{d_{shear}}$ value represents the higher *accuracy* of $t_{es,shear}$, verse $t_{es,dP/dt}$. Additionally, Figure 8.7b shows the limits of agreement ($\bar{d} \pm \mathbf{1.96} \times \boldsymbol{SD}$) are wider for the $T_{sys,dP/dt}$ estimate, with 17.1 ms vs 6.8 ms of $T_{sys,shear}$. The wider limits of agreement of $T_{sys,dP/dt}$ indicate the lower *precision* of $t_{es,dP/dt}$. Given the measured systolic times ranged from 149 ms to 337 ms, both estimates limits of agreement may prove satisfactory. However, this conclusion would depend on the specific use of the systolic duration estimate. For example, if the systolic duration is a particularly sensitive parameter in a model, as in Equation 6.6 of the Kamoi model, the accuracy and precision of estimation will be an important consideration.

Another interesting and obvious result, evident in both Figures 8.7a & 8.7b, is the bias leading to the lack of negative difference values. In the weighted first derivative method's case, this issue is easily explained. Because points just prior to the dicrotic notch tend to have a

more negative gradient than points associated with diastolic relaxation, $t_{es,dP/dt}$ is usually found just prior to the dicrotic notch, as in Figures 8.2a and 8.2b. The approach of using the point of most negative gradient for t_{es} detection, may not make sense when a dicrotic notch is present. However, for waveforms with difficult to identify or even non-existent dicrotic notch features, $t_{es,dP/dt}$ offers a consistent and predictable method of estimating its location, as stated in Section 8.2, despite the early onset of diastole bias. This issue is clinically relevant given the distinct dicrotic notch shape is known to deteriorate with age (Dawber et al., 1973).

In contrast, the shear transform method is developed specifically to identify turning and inflection points of the dicrotic notch. It also never over estimated the duration of systole. A positive bias indicates the dicrotic notches identified by the shear transform method, occurred before the location found by eye, and is a result of the shear transform bias discussed in the limitations section below.

8.5.3 Shear Transform Algorithm Limitations

The correlation analysis in Section 8.5.1 revealed an increase in variation between the shear transform identified dicrotic notches and those found by eye, when a distinct turning point was not present. Second, the Bland-Altman analysis of Section 8.5.2, showed the shear transform algorithm consistently predicted a dicrotic notch location earlier or equal too those found by eye, but never later. The reason for both of these observations is evident in the way the algorithm is implemented.

The first and most obvious limitation is if the dicrotic notch depth is small or even simply flat, as it was for Pig D5's dobutamine high PEEP waveforms (Figure 8.2b), it becomes difficult to identify the notch's exact location. This difficulty occurs because the shear transform will have a similar shape to the signal from which it is derived. Thus, if no trough type notch is present in the pressure signal, none will be evident in its shear transform either.

The second less obvious impact of the dicrotic notch shape is the shear transform algorithm's bias. When the shear transform is applied in algorithm Step 8, points just left of the true dicrotic notch minimum will have a sheared value that is more negative than points just right of the minimum. In this sense, Step 8 favours points left of the minimum to be the dicrotic notch, more than the points right of the minimum. This bias arises because of the shear line negative gradient, leading to a lower value with each time step, meaning, the vertical distance from the shear line to the dicrotic notch (the shear transform) is greatest for the points tending down into the trough of the dicrotic notch, compared to a point of equal pressure but whose rising out of the trough. The same is true for cases where the dicrotic notch is in fact a flat section, or point of inflection, where points left of the inflection point are favoured more than those to the right.

The impact of this bias is most evident when algorithm Steps 9 & 10 are ignored and a pressure signal with wide dicrotic notches is analysed. As previously discussed, Pig D2's dicrotic notches, became wider during dobutamine high PEEP ($\approx$ 28 ms), compared with the baseline stage ($\approx$ 8 ms). The wide dicrotic notches often had minimums with multiple points of equal pressure. Step 8 of the algorithm would find the left-most point of the minimum, while the human observer is likely to choose the middle of the multi-point minimum. Ignoring Steps 9 & 10 would result in a consistent mean difference, for Pig D2's dobutamine high PEEP stage, of 3 ms and range of 1 ms to 7 ms (results not shown). While the addition of Steps 9 & 10, result in perfect dicrotic notch detection by the algorithm, with respect to those found manually by eye.

Thus, the accuracy of the algorithm without the final two steps is still an improvement over the Kamoi method, and may be sufficient depending on the application. However, the final steps are crucial for identifying the true dicrotic notch minimum, thus minimising the positive bias and maximising accuracy. Additionally, the final steps identify the true start of diastolic relaxation, which will be of subsequent value in Chapter 9.

A final limitation of the study is its limited data and single location from which the pressure

waveform was drawn. In the study, only 80 beats were used from two hemodynamic states and all from aortic pressure recorded in the aortic arch of pigs. While this proved adequate as a proof of concept, Chapter 10 will discuss its reduced performance on pressure signals common in a clinical setting, such as a femoral artery pressure waveform. If clinical data was used, it is also likely Step 4's pressure conditions would need to be adapted to reflect hypo- and hyper- tension cases in humans.

8.6 Summary

This chapter presented a new method of dicrotic notch detection, utilizing adaptive shear transforms whose transform region was optimized to favour detection of turning points associated with the dicrotic notch. While Section 8.2 highlighted the physiological relevance and uses of dicrotic notch detection, the motivation of this study was for improved physiological flow waveform prediction and more robust *SV* estimation from the Kamoi model, as per Section 8.1. Thus, the method was tested against the original, weighted first derivative based end-systole detection method, presented with the Kamoi model in Chapter 6 (Kamoi et al., 2017). The shear transform method was shown to be superior to weighted first derivative method of end-systole detection, when compared with dicrotic notches identified manually by eye. In addition, the shear transform method included steps enabling it to identify *the start of diastolic relaxation*, showing the dicrotic notch causes a delay in the onset of diastolic pressure exponential decay. Chapter 9 will apply this new adaptive shear transform end-systole method to the Kamoi model and assess how it impacts both estimated flow and stroke volume performance.

CHAPTER 9

The Dicrotic Notch and The Kamoi Model

9.1 Introduction

Chapter 8 developed an improved method for identifying the time of the dicrotic notch ($t_{es,dic}$), which marks end-systole in a proximal aortic pressure waveform (P_{ao}). Specifically, the method used an adaptive shear transforms algorithm to identify the dicrotic notch and was denoted $t_{es,shear}$. The results discussed in Section 8.5.2, highlighted the superior accuracy and precision of $t_{es,shear}$ over the original end-systole detection method used in the Kamoi model, $t_{es,dP/dt}$. Thus, the expectation was using $t_{es,shear}$ in the Kamoi model would reduce the limitations associated with poor $t_{es,dic}$ detection, covered in Section 6.3.2. Specifically, the hypothesis was using $t_{es,shear}$ would improving the Kamoi model parameter identification and subsequent estimation of flow (Q_{est}) and stoke volume (SV_{est}). If the hypothesis were correct, one of the thesis goals laid out in Section 1.4, would have been achieved. However, Chapter 8 did not include analysis or discussion of the impact of $t_{es,shear}$ on the Kamoi method estimate of stroke volume (SV), as the method was presented to be

independent of any specific model or application.

Therefore, this chapter assess the impact of dicrotic notch detection on the Kamoi model. It is also worth noting, as outlined Section 6.3, the Kamoi model is an implementation of the three-element windkessel model covered in Section 4.3. Thus, the analysis in this chapter is relevant to other implementations of the three-element windkessel, particularly those using pulse contour analysis (PCA) as part of the parameter identification process.

9.2 Flow and Stroke Volume Estimation Recapitulation

It is first worth re-summarising the mechanisms through which accurate estimation of flow (Q_{est}) and stroke volume (SV_{est}) are achieved. This recapping is for two reasons. First, the mechanisms inform how the figures in this section are presented. Second, Chapter 6 focused on the implementation of the Kamoi model and how it was used to estimate SV, but little emphasis was given to the estimated flow waveform.

Calculating Q_{est} and SV_{est} with the three-element windkessel model, was covered in detail in Section 4.3.2. The fundamental theory was no different for the Kamoi model in Chapter 6, the only difference being the parameter product $Z_{c,w}C$, in the reservoir pressure (P_{res}) Equation 4.11, was replaced by pulse wave velocity (PWV) and characteristic length (L_c) as per Section 6.2.1 and Equation 6.2.

9.2.1 Model Parameter Identification Relationship with Profiles of Excess Pressure (P_{ex}) and Proximal Aortic Blood Flow (Q_{ao})

Regardless of the method/implementation by which P_{res} is found, the Equation for calculating P_{ex} is the same, using Equation 4.3. The shape of P_{ex} is then the shape of Q_{est}, according to Equation 4.5. Therefore, identification of $Z_{c,w}$ is not necessary for indicating whether the parameter identification led to a physiological flow waveform shape, instead this is possible by simply comparing the measured flow waveform (Q_{ao}) in conjunction with P_{ex}. This approach of plotting P_{ex} and Q_{ao} was also utilized in Figures 4.3, 4.4 and 6.1.

9.2.2 Accurate Estimated Stroke Volume (SV_{est}), from an Unphysiological Estimated Flow Waveform (Q_{est})

Using the approach in Section 9.2.1, if the shape of P_{ex} is found to be substantially different from Q_{ao}, this does not necessarily guarantee error between SV_{est} and measured stroke volume (SV_{mea}). Equations 4.17 and 5.12 are used to calculated SV_{est} and SV_{mea}, respectively. Equating these two equations, assuming $SV_{est} = SV_{mea}$, yields:

$$SV_{mea} = \int_0^{t_{es}} Q_{ao}(\tau)d\tau = \int_0^{t} Q_{in}(\tau)d\tau = \frac{1}{Z_{c,w}} \int_0^{t} P_{ex}(\tau)d\tau = SV_{est} \tag{9.1}$$

Where $Q_{in} \equiv Q_{est}$, the former being the nomenclature used in Section 4.3 to signify the models estimated flow *into* the windkessel/reservoir. Equation 9.1 shows $Z_{c,w}$ can scale P_{ex} so the integrated flow Q_{in}/Q_{est} is equivalent to the integrated measured flow, Q_{ao}. Thus, it is still possible to achieve perfect SV_{est}, even if the resulting Q_{est} of Equation 4.5 is unphysiological. Section 4.2 discussed how the *Corrected Characteristic Impedance* method was able to estimate *SV* in this manner, from potentially unphysiological flow waveforms. Furthermore, Section 3.6 alluded to this possibility, and stated this chapter would show examples of unphysiological flow waveforms predicting accurate *SV*.

9.3 Improved Dicrotic Notch Detection and the Kamoi Model

9.3.1 Impact of $t_{es,shear}$ on Characteristic Length L_c Calibration

Section 6.2.2 discussed the Kamoi method of identifying L_c, via the condition in Equation 6.8. With the detection of the dicrotic notch now significantly improved, its impact on the subsequent L_c calibration can be assessed. Figure 9.1 shows the updated L_c calibration using $t_{es,shear}$ for end-systole, using the same beats originally used in Figure 6.1a.

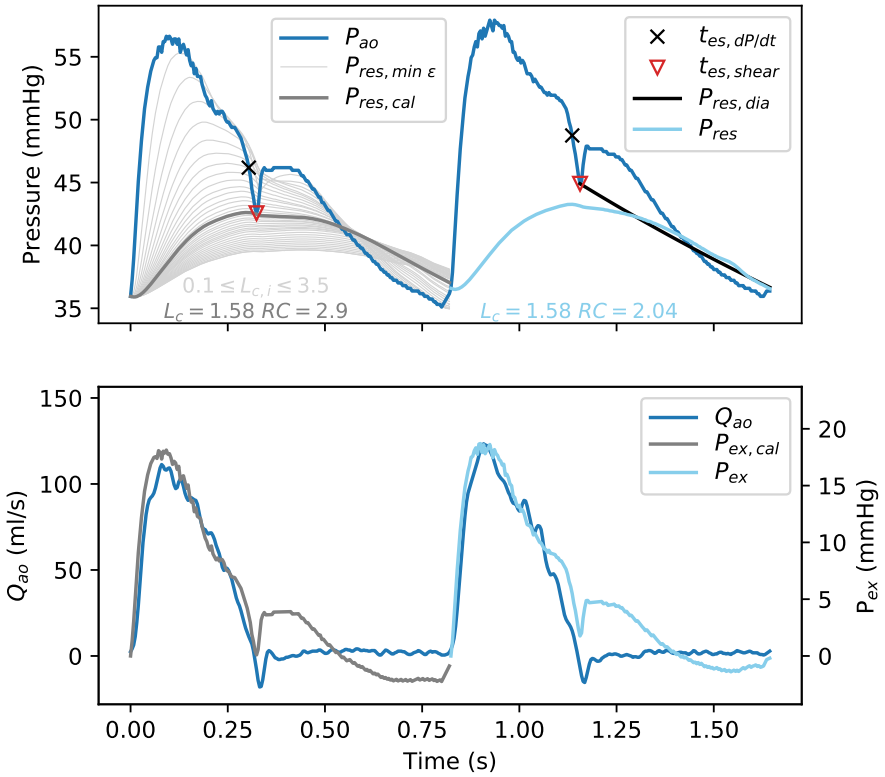

Figure 9.1: Kamoi model method (Chapter 6) applied to the same aortic pressure waveform as in Figure 6.1a (Pig S5's control stage), but using improved dicrotic notch detection, $t_{es,shear}$.

Typical Trough Type Dicrotic Notch Example

Comparing the systolic portions of Figures 9.1 and 6.1a, the P_{ex} resulting from using $t_{es,shear}$ for L_c calibration, more closely predicts the measure flow waveform shape (Q_{ao}). However, during diastole, the opposite is true, P_{res} calculated from L_c (Equation 6.2) using $t_{es,shear}$, deviates further from the measured P_{ao} during diastole. This deviation results in a larger non-zero P_{ex} during diastole according to Equation 4.3, rather than the desired $P_{ex} = Q_{ao} = 0$. In other words, even during calibration of the Kamoi model, when accuracy is expected to be highest, using $t_{es,shear}$ results in positive flow prediction during the first half of diastole, and then negative flow, representing the direction back toward the ventricle, during the second half of diastole.

Section 4.3.2 discussed the example shown in Figure 9.1, where imperfect parameter identification leads to non-zero P_{ex} during diastole. It stated that by using systole only for

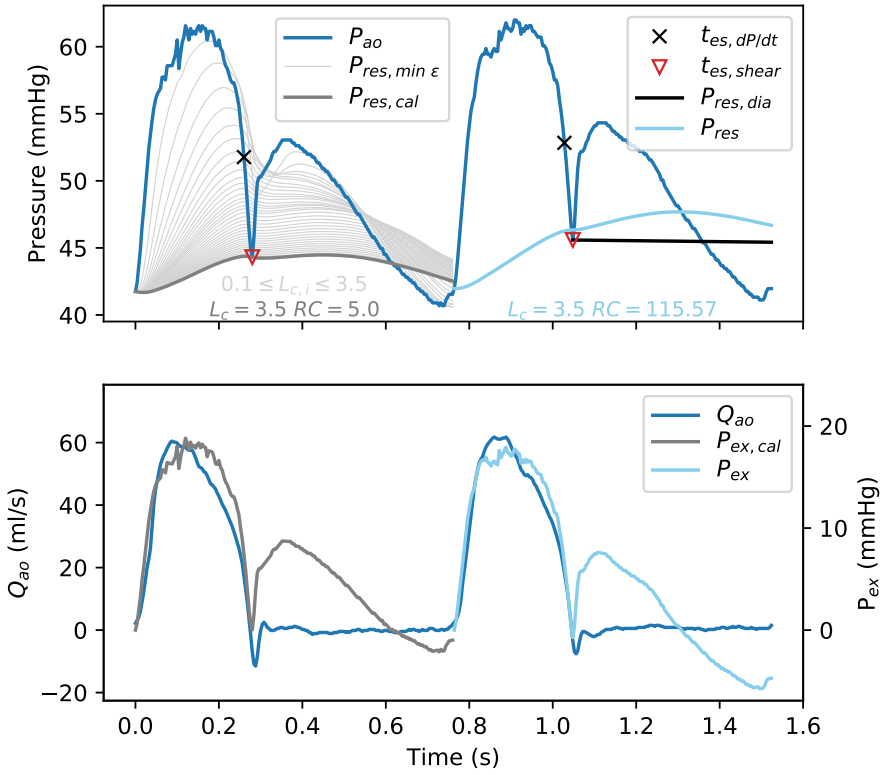

Figure 9.2: Kamoi model method (Chapter 6) applied Pig S6's control stage beats, using improved dicrotic notch detection, $t_{es,shear}$.

the integration limits of Equation 4.17, it would be possible to accurately estimate stroke volume SV_{est}. However, doing so is contrary to the goal of this thesis, which is for the developed model to estimate SV from physiologically sound flow waveforms.

Large Trough Type Dicrotic Notch Example

The reduction in model performance, inadvertently caused by $t_{es,shear}$, is even more pronounced with larger dicrotic notches. Figure 9.2 shows the large dicrotic notches of Pig S6's control stage. In this case, the upper bounds of $L_{c,i}$ and RC_i for the grid search, were chosen to ensure the condition in Equation 6.8 was met using $t_{es,shear}$. Specifically, the bounds used were $0.01 \leq RC_i \leq 5$ and $0.1 \leq L_{c,i} \leq 3.5$.

The resulting P_{res} calculation led to systolic P_{ex} closely matching systolic Q_{ao}, satisfying Equation 4.5. However, the larger dicrotic notches exacerbate the diastolic error according to Equation 6.7, and subsequently P_{ex}(t>$t_{es,shear}$) causes the model to estimate flow dur-

ing diastole according to Equation 4.5. Thus, calculation of the P_{res} during systole has improved using $t_{es,shear}$ in place of $t_{es,dP/dt}$. However, the error during diastole, as per Equation 6.7, has increased.

Impact of Assumed Anatomical L_c

Contrary to the bounds used in Figures 6.1, 9.1 and 9.2, Section 6.2.2 stated Kamoi et al. (2017) treated L_c as the *"anatomical length"* of the aorta. This assumption is reflected in the grid search bounds used in Kamoi et al. (2017), specifically, $0.5 \leq L_{c,i} \leq 1.5$.

However, it is worth noting, as per Section 4.4.1, L_c describes the volumetric compliance of the *model* and therefore is not necessarily representitive of a true physiological or anatomical value. This was also covered in Sections 4.3.3, which cautioned treating three-element windkessel parameters as representative of local physiology. Had the bounds of L_c been restricted to anatomical values, it would have been impossible to meet the condition in Equation 6.8, for Figure 9.2. Thus, the narrower bounds imposed in Kamoi et al. (2017) limited insight into the implications of different L_c values impact on the predicted flow waveform shape, Q_{est}.

Section 1.3.1 outlined the target cohort that stands to benefit most from *SV* monitoring is critical care patients. It is possible these patients may present periods of abnormal or less common physiological behaviour, including the variety of dicrotic notches shapes (Dawber et al., 1973). Therefore, it is critically important the behaviour presented in Figure 9.2, is factored in model development, rather than simply considering it an outlying case.

9.3.2 Impact of $t_{es,shear}$ on *RC* Identification

Accurate dicrotic notch detection has not only adversley impacted L_c calibration, but also *RC* identification in subsequent beats. As a reminder, Section 6.2.2 explained Kamoi et al. (2017) identified $RC_{\min \mathcal{E}}$, for non-calibration beats, by minimising the error between the measured diastolic aortic pressure ($P_{ao}(t \geq t_{es})$) and the calculated diastolic reservoir pressure ($P_{res}(t \geq t_{es})$), according to Equation 6.7. $P_{res}(t \geq t_{es})$ was calculated using Equation

4.16 (Kamoi, 2016), which assumes $P_{ao}(t \geq t_{es})$ follows an exponential decay. The rationale for this approach was covered in Section 4.3.2, where the three-element windkessel model estimated diastolic pressure as the exponential pressure decay of an emptying reservoir, according to the *time constant RC* (Equations 4.15 and 4.16).

It is unclear how Kamoi et al. (2017) performed the error minimisation to identify each non-calibration beat's $RC_{\min \mathcal{E}}$. However, the author of this thesis does so by using linear regression, on a linearised[1] Equation 4.16. The linearisation (in the statistical sense) is achieved by taking the natural log of the equation, which can subsequently and conveniently be re-arranging into to the form $y = mx + c$, making it also a linear function:

$$ln(P_{ao}(t) - P_{cvp}) = \frac{t_{es} - t}{RC} + ln(P_{ao}(t_{es}) - P_{cvp}) \quad where \quad t \geq t_{es} \tag{9.2}$$

A reminder, when measuring P_{ao} and assuming a constant value for central venous pressure (P_{cvp}), the only unknown in Equation 9.2, is *RC*, the parameter to be identified. The author used Equation 9.2 and *linear least squares* regression (programmed in Python 3.7.2), to identify $RC_{\min \mathcal{E}}$ for non-calibration beats, including the the second beats of Figures 6.1a, 6.1b, 9.1 and 9.2. Finding *RC* in this manner means it is no longer bound as it was in the grid search, allowing it to take on the much larger value than the calibration beat.

Regardless, the second beat in Figure 9.2 shows Equation 4.16, cannot adequately describe the diastolic pressure when it is taken to be $P_{ao}(t \geq t_{es,shear})$. This outcome is no surprise, since measured $P_{ao}(t \geq t_{es,shear})$ is clearly in violation of the approaches main assumption. Specifically, in this case, $P_{ao}(t \geq t_{es,shear})$ no longer resembles simple exponential decay in diastole. Thus, it is not possible for $RC_{\min \mathcal{E}}$ and Equation 4.16, to predict a $P_{res}(t \geq t_{es,shear}) \approx P_{ao}(t \geq t_{es,shear})$.

[1] Linearisation in the context of statistical linear models, is different from linear functions in calculus. However, in this case, the *linear model* (Equation 9.2) is also a linear function.

9.3.3 The Dicrotic Notch and The Three-Element Windkessel

Figure 9.2 illustrates the impact of *"imperfect [parameter] identification"*, discussed in Section 4.3.2. However, interestingly, in this context, parameter identification of L_c has been improved, by improved end-systole detection, but at the expense of *RC* identification, and the violation of the foundational model assumption governed by Equation 4.12. Thus, the behaviour seen in Figures 9.1 and 9.2 is not strictly a poor parameter identification, but rather a re-surfacing of the three-element windkessel limitations.

Specifically, Sections 4.3.1, 4.3.2 and 4.3.3 exhaustively stated the three-element windkessel model cannot describe wave phenomena. Furthermore, Section 8.2 explained the dicrotic notch is caused by *wave phenomena*. Moreover, Section 4.5.1 highlighted the difficulty of fitting P_{res} to P_{ao} during early diastole, due to reflected wave behaviour, as part of the critique of the reservoir wave approach (RWA). So, in hindsight, it is unsurprising that relatively large dicrotic notches, as in Figures 9.1 and 9.2, lead to model implementation issues.

Interestingly, the poor flow waveform prediction in this section, has essentially been due to model parameter identification via PCA. Recalling Section 4.4, Wesseling et al. (1993) successfully estimated physiological flow waveforms from both the aortic and radial pressure waveforms. Reflected waves often cause a turning point that appears similar to a dicrotic notch in the radial artery pressure signal, but do not correspond to end systole (Oppenheim and Sittig, 1995; Hoeksel et al., 1997). The natural question, in light of the issues highlighted in the chapter, is how did Wesseling et al. (1993) overcome the issue of reflected waves? The author thinks the answer likely lies in the method Wesseling et al. (1993) used to identify the model parameters. Specifically, parameters were not based on PCA, not in the sense of *fitting* parameters to the pressure waveform shape as in the Kamoi model. Instead, parameters were calculated individually using patient demographic data and empirical equations. Section 4.7 highlighted the limitations of non-patient specific parameter identification. However, in this section, a potential advantage is identified. Specif-

ically, Wesseling et al. (1993) parameter identification was not subject to the three-element windkessel model's inherent limitations.

9.4 Start of Diastolic Relaxation and the Kamoi Model

Section 9.3 showed identifying end-systole as the dicrotic notch ($t_{es,dic}$), with $t_{es,shear}$, and using it for Equation 6.7 and the condition in Equation 6.8, led to significant error according to Equation 6.7. However, more importantly, it showed this undesirable behaviour of the Kamoi model was due to the measured diastolic pressure ($P_{ao}(t \geq t_{es,shear})$) not resembling exponential decay, as the model assumes. Therefore, the reduced performance was not *explicitly* caused by improved end-systole detection, but nonetheless needs to be addressed.

The final two steps of the shear transform method, in Section 8.4.5, identified the *start of diastolic relaxation* t_{dr}. The rational for defining and identifying t_{dr}, was the recognition pressure rises out of the dicrotic notch, prior to diastole resembling exponential decay. Thus, a hypothesis was made that treating end-systole (t_{es}) as t_{dr}, in Equations 6.7 and 6.8, would improve model performance. In other words, as far as the model would be concerned, measured diastolic pressure is treated as $P_{ao}(t \geq t_{dr})$. Figure 9.3 shows the Kamoi method outlined in Section 6.2.2, but applied treating t_{dr} as end-systole.

Impact of t_{dr} on Reservoir and Excess Pressure Calculations

Comparing Figures 9.1 & 9.2 to Figures 9.3a & 9.3b, respectively, it is clear using t_{dr} has led to the opposite behaviour of $t_{es,shear}$. Specifically, t_{dr} led to the L_c calibration approaching the lower bounds of the grid search, subsequently improving fitting of P_{res} according to the model assumption of Equation 4.12. However, it also reduced the model's ability to predict P_{ex} with a similar shape to Q_{ao} during systole. Additionally, what is not immediately clear, due to the different scaling of the excess pressure axes of Figures 9.1 & 9.2 compared with Figures 9.3a & 9.3b, is the excess pressure for the t_{dr} cases, is significantly smaller.

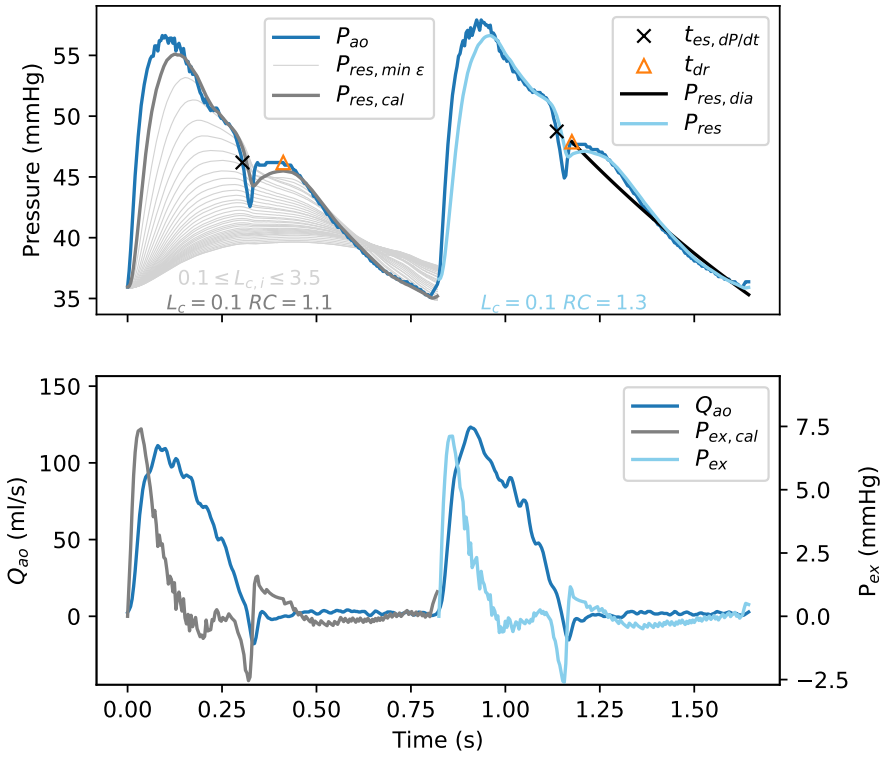

(a) Kamoi model method (Chapter 6) applied to the same aortic pressure waveform as in Figure 6.1a and Figure 9.1 (Pig S5's control stage), but using t_{dr} to define the start of the diastolic pressure decay.

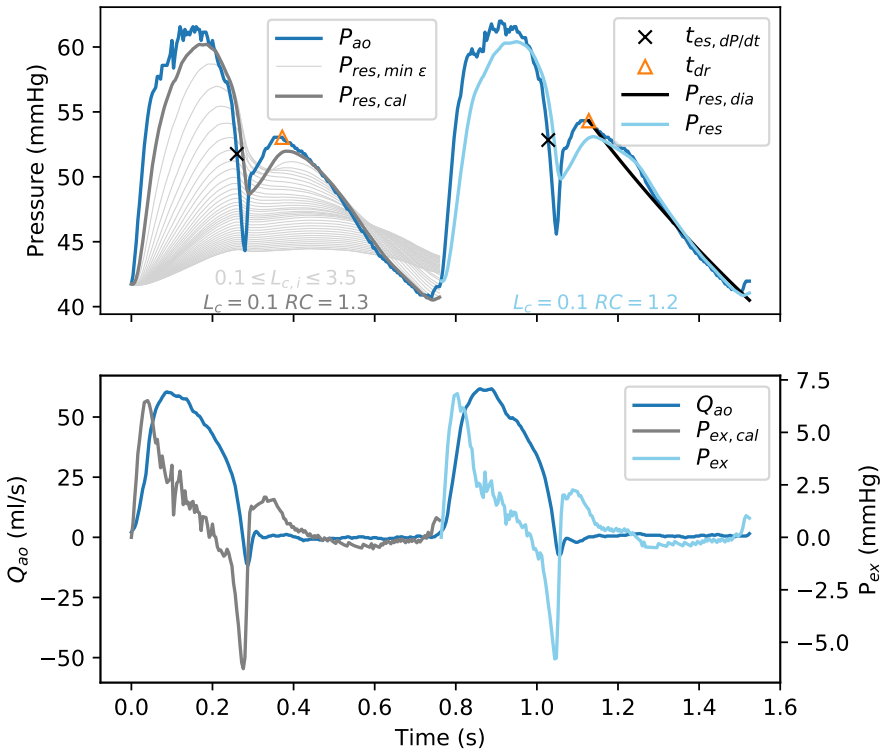

(b) Kamoi model method (Chapter 6) applied the same beats as shown in Figure 9.2 (Pig S6's control stage), but using t_{dr} to define the start of the diastolic pressure decay.

Figure 9.3: Illustrating the effect of assuming measured diastolic pressure lasts from t_{dr} to the end of the beat, $P_{ao}(t \geq t_{dr})$, on resulting Kamoi model parameter identification and subsequent P_{res} and P_{ex} prediction.

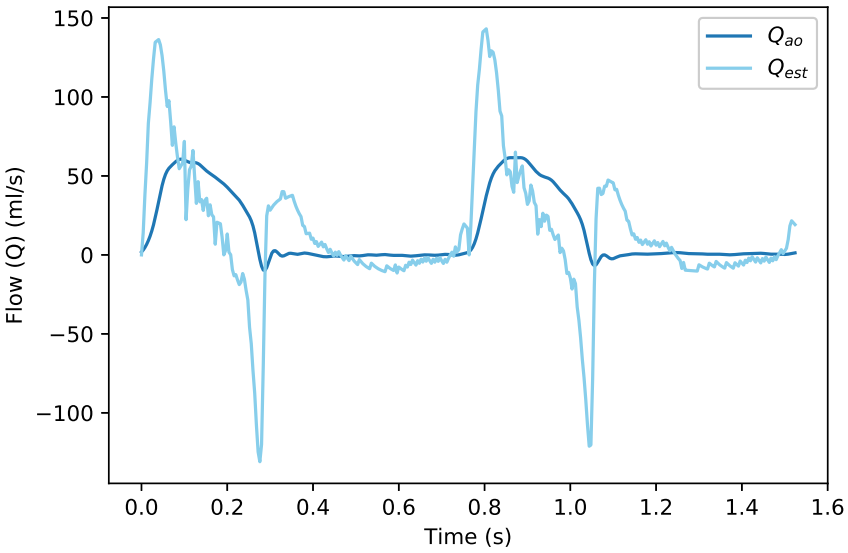

Figure 9.4: Q_{est} from the two beats in Figure 9.3b.

Impact of t_{dr} on Estimated Q_{est} and SV_{est}

It is still possible to predict an accurate stroke volume using P_{ex} for the beats in Figure 9.3, as outlined in Section 9.2.2. First, $Z_{c,w}$ needs to be found, relating P_{ex} to Q_{est}, per Equation 4.5. Section 6.2.1 explained Kamoi et al. (2017) used calibrating stroke volume measurements to calibrate $Z_{c,w}$, according to Equation 6.3. The same approach was used for the beats shown in Figure 9.3b, where Protocol S's aortic flow probe enabled SV_{mea} for every beat, according to the process outlined in Section 5.4.4. Figure 9.4 shows the resulting Q_{est} that satisfies Equation 9.1.

Figure 9.4 shows, despite the equivalent SV from the flow probe and model, the estimated flow waveform predicts more than double the peak measured flow. Additionally, Q_{est} from mid to late systole falls rapidly, to an equally significant negative flow value. This negative value would represent flow back towards the ventricle of the heart, and in a healthy patient, cause abrupt aortic valve closure, as per Section 2.3.1. It is also worth noting, accurate SV_{est} still requires precise end-systole detection, since it is sensitive to systolic duration (T_{sys}), as covered in Section 6.3.2. Chapter 8 showed $t_{es,shear}$ improved both accuracy and precision of end-systole detection, over the Kamoi models original $t_{es,dP/dt}$. Thus, SV_{est} is more reliable using $t_{es,shear}$, thanks to improved tracking of ΔT_{sys}.

9.5 Implications of Unphysiological Flow Estimation in a Clinical Environment

Sections 9.3 and 9.4 showed the Kamoi model parameter identification process was highly sensitive to the relative size of a dicrotic notch in the pressure waveform. For each assumed end-systole point, $t_{es,shear}$ and t_{dr} respectively, very different Q_{est} shapes were produced. If either of the approaches were implemented in a clinical setting, clinicians provided with Q_{est} may attribute the flow waveforms unconventional shape to disease, rather than recognising it as a product of the parameter identification process.

Nonetheless, Sections 9.2.2 and 9.4 showed it is still possible to have reasonable SV_{est}, from poor Q_{est} prediction. Poor flow prediction may be why many of the PCA methods, including the Corrected Characteristic Impedance Method (Section 4.2), the Kamoi model (Chapter 6) and many of the commercial devices (Section 3.5), provide only a SV_{est}, excluding Q_{est}, as alluded to in Sections 3.6, 4.2 and 6.2.3. Importantly, accurately capturing Q_{est}, as well as SV_{est}, would provide greater clinical insight and greater confidence in the SV_{est} value.

However, although SV_{est} is correct for the calibration beats and those soon after, this accuracy is only due to the calibration of $Z_{c,w}$ to a measured stroke volume. In reality, the underlying model parameters L_c and RC, led to a P_{res} and P_{ex} that failed to accurately represent the dynamics of aortic ejection. Moreover, a fixed and incorrect L_c will restrict the model's ability to accurately reflect changes in patient state through the Q_{est} waveform. It would still be possible to monitor patient state through changes in SV_{est}, provided any changes are adequately captured by the dynamic parameters, PWV and T_{sys} (updating $Z_{c,w}$ through Equation 6.6), and RC, as per Section 6.2.4. However, Figure 9.2 shows significant changes in RC beat-to-beat, have less influence on the final P_{res} and subsequent P_{ex} profiles, compared with the L_c parameter.

In summary, the P_{res} and P_{ex}/Q_{est} profiles, provide a qualitative and quantitative measure

of the parameter identification quality. Without the expected P_{res} shape, the model can still predict and track changes in SV. However, these SV_{est} values would be from model behaviour which is, in reality, far from the three-element windkessel theory, as is the case in Figure 9.4.

9.6 Parameter Identification via Diastolic Best Fit

After the learnings in the earlier sections of this chapter, a natural question is, is there a better way to identify the parameter L_c? Preferably one which lessens the effects of the dicrotic notch in the pressure waveform. To answer this question, consider how the condition of Equation 6.8 arose. Section 6.2.2 explained how Kamoi et al. (2017) used a grid search to identify an array of potential parameter pairs, ($L_{c,i}$ & RC_i), each resulting in some amount of error between P_{res} and measured pressure (P_{mea}) during diastole, per Equation 6.7. This approach was aligned with the windkessel assumption in Equation 4.12, that P_{ex} = 0 during diastole. However, rather than just use the pair of parameters giving the *minimum* error for diastole, Kamoi et al. (2017) placed the final emphasis on the L_c, RC pair which yielded a P_{res} waveform that passed through a single point, t_{es}, a condition enforced with Equation 6.8. The approach was used since many of the grid search $L_{c,i}$ iterations have very similar $P_{res,min\ \mathcal{E}}(t \geq t_{es})$, as discussed in Section 6.2.2 and seen in Figure 6.1a. However, the repercussion of the approach is, the choice of end-systole, $t_{es,dP/dt}$, $t_{es,shear}$ or t_{dr}, dramatically effects the L_c value chosen, and subsequently the systolic ratio of P_{res} to P_{ex} as seen in Figures 9.1 – 9.3.

However, as covered in Section 4.5, Wang et al. (2003) identified windkessel parameters with a least squared error algorithm applied to the final two-thirds of diastole. This approach is equivalent to the grid search parameters that minimised the diastolic error according to Equation 6.7, but using only the last two-thirds of diastole has the advantage of ignoring the transient effects of the dicrotic notch.

Thus, attempting a similar approach, diastole is treated as t $\geq t_{dr}$, ignoring the effects of

the diacrotic notch ($t_{es,dic} < t_{dr}$), which led to better diastolic fitting of P_{res} to P_{ao}, in Section 9.4. Furthermore, using only the final two-thirds of diastole for the error minimisation, excludes the pressure rise associated with the *distinct* reflected pressure wave of late-systole/early-diastole in P_{ao} waveforms, as covered in Sections 9.3.3 and 4.5.1.

The optimisation/error minimisation used SciPy's (v1.3.0) non-linear least squares trust region reflective algorithm[2] (implemented in Python 3.7.2), to identify the parameters L_c and RC, for the calibration beat, shown in Figure 9.5. Specifically, the optimisation function calculates P_{res} using Equation 6.2, for the whole beat, for iterations of the parameters L_c and RC. However, the error minimisation within the function uses Equation 6.7, *but only the final two-thirds of diastole*, where $t_{2/3}$ marks the start of this final two-thirds. This process is also far more efficient than employing the grid search approach.

As can be seen from Figure 9.5, both the dicrotic notch, and the rise in pressure before diastolic exponential decay, still lead to an imperfect fit of P_{res} to P_{mea} during all of diastole. However, while not being ideal, the approach strikes a balance between achieving a reasonably close physiological match of P_{ex} to Q_{ao}, without causing too significant non-zero P_{ex}, and thus Q_{est}, during diastole.

9.7 Ideal Parameter Identification from Aortic Flow

Access to the aortic flow probe signal Q_{ao}, in the Protocol S pigs, makes it possible to back-calculate the *ideal* parameters. Ideal parameters are the combination L_c, RC and $Z_{c,w}$, used in Equation 6.2 and 4.11, which result in the closest possible match between Q_{est} and measured Q_{ao}. To identify the ideal parameters, non-linear least squares fitting of Q_{est} to Q_{ao} is performed. This process is similar to using non-linear least squares fitting applied to P_{res}(t $\geq t_{2/3}$) and P_{ao}(t $\geq t_{2/3}$) in Section 9.6, except, in the flow case, it calculates the error for the entire flow waveform, not just systole or diastole. Figure 9.6 shows the approach, using the same beats shown in Figure 9.5.

[2] SciPy is a open source software library, compatabile with the Python programming language.

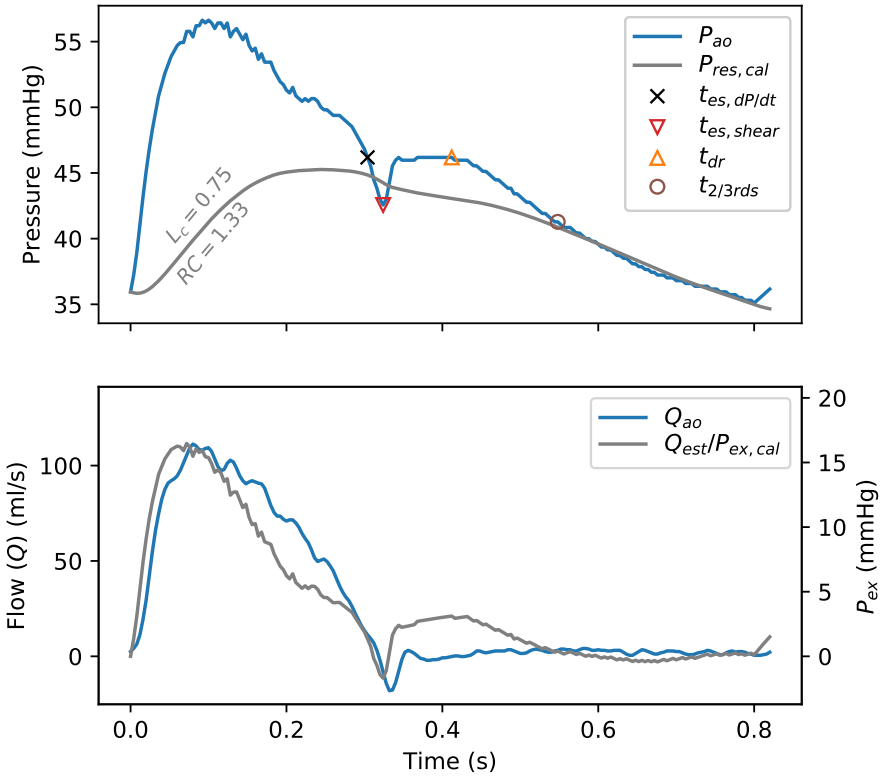

(a) Example beat from Pig S5 control stage, showing the P_{res} and P_{ex} waveforms from non-linear least squares parameter identification.

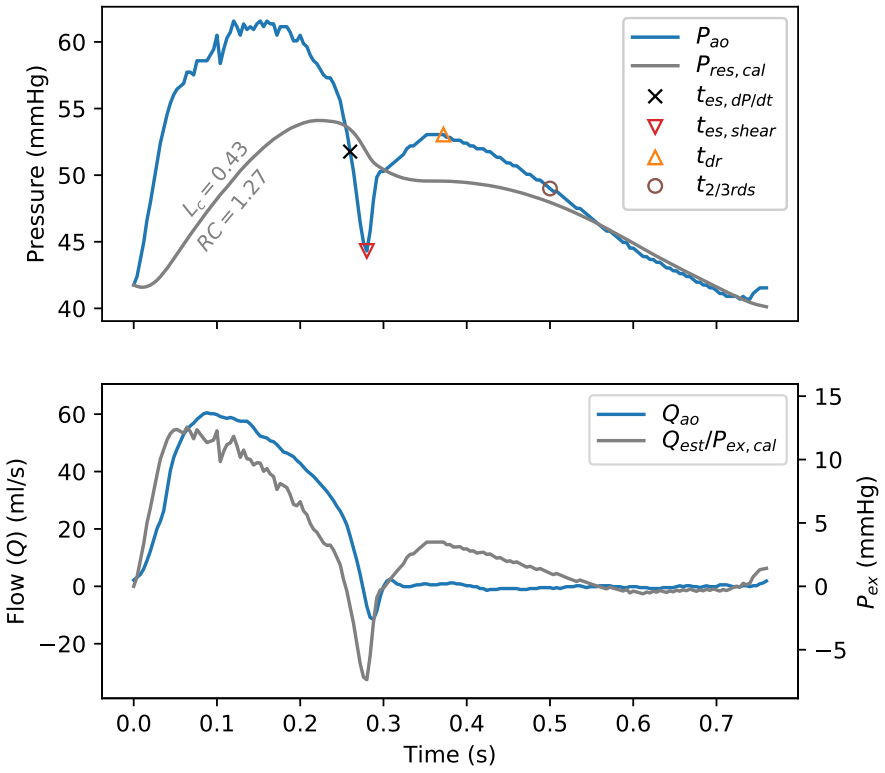

(b) Example beat from Pig S6 control stage, showing the P_{res} and P_{ex} waveforms from non-linear least squares parameter identification.

Figure 9.5: Calculating P_{res} using parameters identified from non-linear least squared error fitting of P_{res} to P_{mea}, during the final two-thirds of diastole. The beats shown in (a) and (b) are the calibration beats used in Figures 9.1, 9.2 and 9.3, for consistency.

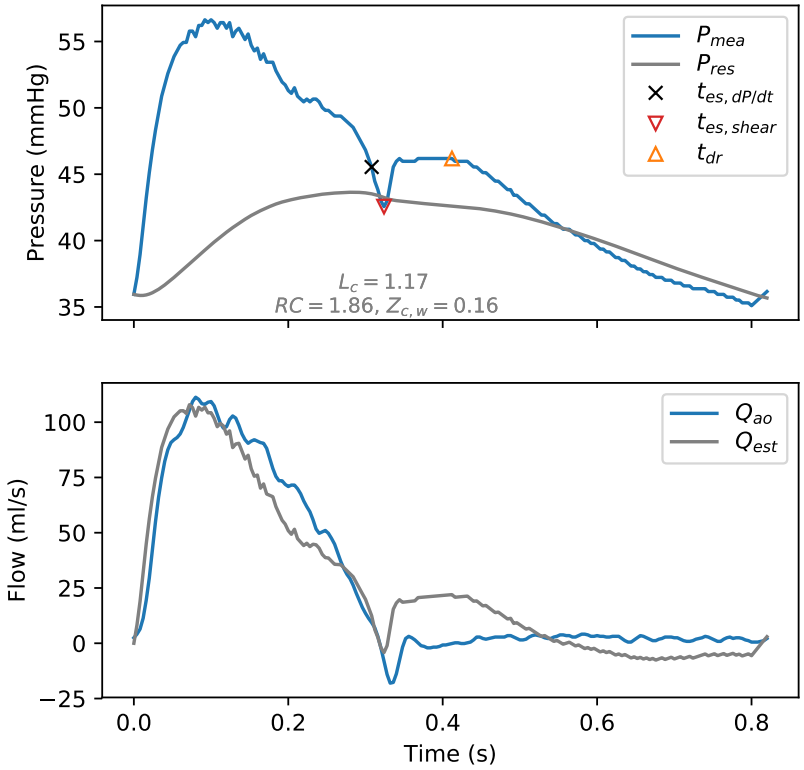

(a) Example beat from Pig S5 control stage, showing the closest possible fit of Q_{est} to Q_{ao}, and back calculated paramaters, which in conjunction with P_{ao} would return the P_{res} and P_{ex}, leading to Q_{est}.

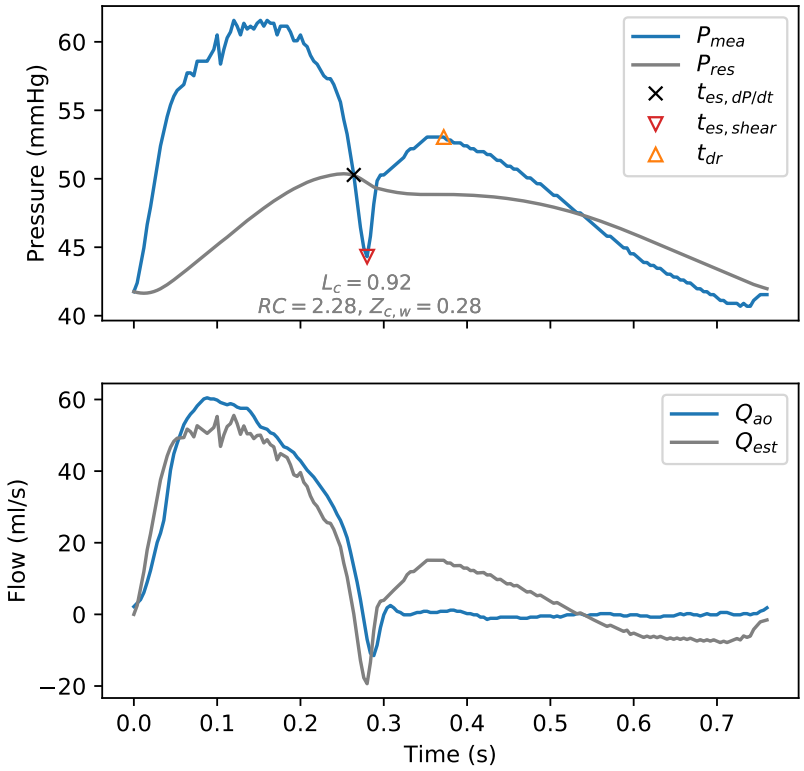

(b) Example beat from Pig S5 control stage, showing the closest possible fit of Q_{est} to Q_{ao}, and back calculated paramaters, which in conjunction with P_{ao} would return the P_{res} and P_{ex}, leading to Q_{est}.

Figure 9.6: Calculating P_{res} using parameters identified from non-linear least squared error fitting of Q_{est} to Q_{ao}, for the entire beat. The beats shown in (a) and (b) are the same beats as in Figure 9.5, for comparison of the P_{res} with the pressure based non-linear parameter fitting.

Figure 9.6 is further evidence to the fact the three-element windkessel, as described in Section 4.3, cannot describe the phenomina of the dicrotic notch, or any significant rise in pressure following it, prior to the start of diastolic exponential pressure decay. Thus, this result confirms what was already stated in Sections 9.3.3. However, by comparing Figures 9.6 and 9.5, it is clear the parameter identification approach described in Section 9.6 provides Q_{est} close to the ideal model behaviour.

9.8 Summary

This chapter assessed the impact of improved dicrotic notch detection on the Kamoi model. Section 6.3.2 identified two mechanisms through which the Kamoi model was negatively impacted by poor end-systole identification (t_{es}). Specifically, these where through estimation of systolic duration (T_{sys}) and calibration of the parameter L_c. The dicrotic notch ($t_{es,dic}$) provided a definitive t_{es} marker in P_{ao} signals, and an improved detection method, $t_{es,shear}$, was developed in Chapter 8. Robust detection of the notch immediately resolved the limitations associated with poor T_{sys} precision. However, L_c identification, being dependent on PCA, was shown to be highly sensitive to the profile of the dicrotic notch. In fact, when the notch was relatively large, the improved dicrotic notch detection led to L_c, and subsequent P_{res} and P_{ex}, which estimated an unphysiological flow waveform.

In an attempt to overcome the negative effects of the dicrotic notch on parameter identification, t_{dr} was treated as end-systole. The point t_{dr} was identified as part of the improved end-systole detection in Chapter 8. It is the time point when the pressure has risen out of the dicrotic notch, and thus better marks the start of diastolic exponential pressure decay. However, using t_{dr} revealed a limitation of the Kamoi model's implementation. Specifically, attempting to force $P_{res} = P_{ao}$ at the start of diastole, could lead to very small systolic P_{ex} and additionally unphysiological Q_{est} profiles.

Instead, a more reasonable approach for parameter identification was to simply minimise the error according to Equation 6.7. This approach is aligned with the three-element wind-

kessel model assumption of Equation 4.12, on which the Kamoi model is based. Once more, transient pressure effects caused by the dicrotic notch, and possible influence of distinct reflected wave behaviour during early diastole, was mitigated by using the last two-thirds of diastole, when start of diastole was treated as t_{dr}. The resulting parameter identification, and flow waveform profile estimation from the non-linear least squares diastolic pressure error minimisation, was shown to be similar to ideal parameters back-calculated from the measure flow waveform Q_{ao}.

Therefore, a key conclusion of this chapter is although t_{es} is easily identified using dicrotic notches in a P_{ao} waveform, parameter identification via PCA is made more difficult by the transient dicrotic notch behaviour and possibly distinct reflected waves. Moreover, no combination of three-element windkessel/Kamoi model parameters were able to describe wave propagation phenomena. This limitation of the three-element model had been discussed in Sections 4.3.1 – 4.3.3. However, this analysis, illustrates the issues numerically and conclusively for the first time in literature, as far as the author is aware.

Finally, although the aorta represents a significant amount of the arterial tree's compliance, and thus seemed suitable for modelling the lumped windkessel/reservoir behaviour of the arterial system, these advantages in favour of P_{ao}, appear to be outweighed by the presence of dicrotic notches. Considering the acquisition of the aortic pressure waveform requires a much higher level of invasion, compared with the more clinically common femoral artery pressure (Cousins and O'Donnell, 2004), it may in fact be advantageous to develop a three-element windkessel model implementation that does not require the presence of dicrotic notches to facilitate robust end-systole detection.

More succinctly, in cardiovascular modelling it has often been assumed the dicrotic notch is "your friend", delineating elements of the cardiac cycle. This chapter analytically demonstrates this assumption is not always the case.

CHAPTER 10

Dicrotic Notch-less End-Sytole Detection

10.1 Introduction

Chapter 6 highlighted the Kamoi-model-identified end-systole (t_{es}) time point, using a weighted first derivative method ($t_{es,dP/dt}$), which was subsequently illustrated in Figure 8.2. Section 6.3.2 outlined the sensitivity of the method's stroke volume (SV) estimate to end-systole detection, which became the focus of Chapter 9. Chapter 9 concluded some of the limitations were specific to the Kamoi model, in particular the process by which Kamoi et al. (2017) had identified the parameter characteristic length (L_c). However, Chapter 9 also showed dicrotic notch and other reflected wave behaviour impacted three-element windkessel models more generally.

Despite the difficulties produced by the presence of a dicrotic notch, Section 9.4 showed it was still possible to estimate SV from the proximal aortic (P_{ao}) signal, regardless of the estimated flow waveform (Q_{est}) shape. However, to achieve a reasonably physiological Q_{est} from pulse contour analysis (PCA), robust end-systole detection was required. This end-

systole point was subsequently used to identify the end of transient pressure behaviour, which is followed by exponential pressure decay.

The main reason for the focus on P_{ao} in Chapters 8 and 9, were the ease of identification and validation, of the end-systole point via the dicrotic notch. In addition, physiological values associated with the aorta, had previously been used to estimate windkessel parameters. Specifically, Westerhof et al. (1971) showed the aortic characteristic impedance ($Z_{c,ao}$), was a reasonable value to use for the three-element windkessel model characteristic impedance, $Z_{c,w}$, as discussed in Section 4.3.1. Moreover, Section 4.4.1 covered how Wesseling et al. (1993) calculated windkessel (volumetric) compliance (C) using an aortic area compliance and length, per Equation 4.19. The methods employed by Westerhof et al. (1971) and Wesseling et al. (1993) did not utilize PCA in conjunction with *fitting* techniques as in Chapter 9, thereby mitigating the effects of the dicrotic notch on the parameter identification process.

However, Sections 4.6 and 4.7 highlighted a potential advantage of parameter identification via PCA. Specifically, beat-to-beat PCA allowed parameters to be patient specific and represent the current hemodynamic state. However, the parameter identification difficulties caused by the dicrotic notch, covered in Chapter 9, can outweigh the advantages of the easily identified end-systole, on which the parameter identification process relies. Finally, in a clinical environment, it is not common to monitor central arterial pressure via a catheter in the proximal aorta (Cousins and O'Donnell, 2004; Watson and Wilkinson, 2012).

Considering these limitations, identified over Chapters 6 – 9, an ideal alternative arterial pressure waveform to P_{ao}, for use with the three-element model, would have the following traits:

- Limited/relatively small distinct reflected wave behaviour contributing to the waveform during diastole.
- The typical measured diastolic pressure would have exponential decay, improving

compatibility with windkessel model assumptions, as a result of the first requirement.

- Non-additionally invasive measurement location, in-line with the thesis goals in Section 1.4.

Pressure measured in the femoral artery, seen in Figure 2.4, has these traits. Being downstream of the aortic-iliac branch, it is less effected by the distinct reflection site identified by in Murgo et al. (1980), discussed in Section 2.5.3. Its distance from the aortic valve means the dicrotic notch is attenuated, sometimes to a notch-less point of inflection or simply a slight change in curvature (Oppenheim and Sittig, 1995; Watson and Wilkinson, 2012). Exacerbating the attenuation is the reduced compliance associated with aging (Dawber et al., 1973), covered in Section 2.4.4. Moreover, the femoral artery is a more common clinical catheterisation site, considered a suitable surrogate for the more invasive aortic pressure measurement (Cousins and O'Donnell, 2004; Watson and Wilkinson, 2012).

However, the attenuation of the dicrotic notch makes t_{es} more difficult to identify in distal pressure waveforms (Oppenheim and Sittig, 1995). This difficulty is a severe limitation when finding the estimated end-systole time based on the minimum of a shear transform ($t_{es,shear}$), developed in Chapter 8. The $t_{es,shear}$ method assumed distinct dicrotic notches were present in the signal, and as stated in Section 8.5.3, if there is no clear dicrotic notch in the pressure waveform, there will be none in the shear transformed signal either. Thus, this method is less appropriate for the more clinically relevant arterial pressure waveforms without dicrotic notches.

The potential lack of any dicrotic notch in arterial signals highlights an advantage of assuming t_{es} at the point of maximum negative pressure gradient with respect to time ($\frac{dP}{dt}_{\min}$) (Aguado-Sierra et al., 2008; Kamoi et al., 2014, 2017). Specifically, as stated in Section 8.2, the method provides consistent predictable performance, since it does not actually attempt to identify a dicrotic notch per se. However, this simplification underestimates systolic duration (T_{sys}) and overestimates diastole (Balmer et al., 2018a), as shown in Figure 8.7b.

In a previous study by the author, the iliac pressure was found to return similar estimated stroke volume (SV_{est}) performance to a P_{ao} signal when using the Kamoi model (Balmer et al., 2018b). However, the study had assumed end-systole occurs at the start of diastolic relaxation/decay (t_{dr}), as per Section 9.4. This study, although not part of the published results, contributed to Section 9.4, where the resulting estimated flow could be unphysiological. Moreover, the accuracy of end-systole detection using $t_{es,shear}$ of Chapter 8, in the dicrotic notch-less iliac pressure waveforms, was found to be no better than the original $t_{es,dP/dt}$ method described in Section 8.3. Thus, the study's end-systole detection was plagued by the same issues described in Section 6.3.2, where the shear transform end-systole detection has low accuracy, but high precision in signals without dicrotic notches.

Finally, to achieve both accurate SV_{est} and Q_{est} using the femoral pressure (P_{fem}) or similar arterial pressure, an accurate method of end-systole detection needs to be found. This method is the focus of this chapter, to develop yet another method for end-systole detection, but this time with particular focus on t_{es} in signals without dicrotic notches. In addition, the method should be robust enough to also identify t_{es} in signals with dicrotic notches, since, as already stated, in a clinical setting it is still possible for the dicrotic notch to propogate to the femoral artery, albeit in an attenuated state.

10.2 End-Systole in Arterial Pressure Signals

Chapter 8 focused on the dicrotic notch as delineating end-systole with respect to the aorta and left ventricle, provided P_{ao} was measured proximal to the aortic valve, as discussed in Sections 2.3.1 and 8.2. However, it is worth considering end-systole and its effect on the arterial pressure waveform more generally, doing so will make the fundamental theory behind the new t_{es} detection method and its validation clearer.

10.2.1 End-Systole Propagation and Pulse Transit Time

Like start-systole, there is a time delay between the effects of absolute end-systole, the time of aortic valve closure, and its effect being experienced in different parts of the arterial tree. Section 5.4.3 defined absolute start of systole, as the time of the electrocardiogram (*ECG*) Q-wave ($t_{0,ECG}$), but the effects of systole were experienced later in the arteries ($t_{0,P_{ao}}$ & $t_{0,P_{fem}}$). The aforementioned section explained the absolute and relative nature of start-systole being due to the delay between start of ventricular contraction and ejection, as well as the propagated nature of the pulse wave. The time delay associated with the pulse wave travelling between different locations in the arterial tree, was defined in Section 2.5.1 as the pulse transit time (*PTT*). Later, in Chapter 7, the other time delays were formally defined (*PEP*, *PDT* and *PAT*).

Figures 2.13 and 7.2 showed *PTT* was the delay between start-systole as experienced in the aortic ($t_{0,P_{ao}}$) and femoral arteries ($t_{0,P_{fem}}$). Similarly, there is a delay in the effects of aortic valve closure propagating along the arterial tree. Section 2.3 discussed how during diastole, the passive contraction of the arteries, particularly the aorta, helps sustain blood pressure and flow to the periphery. At absolute end-systole/start diastole, diastolic pressure decay can also be described as wave propagation, with valve closure causing a *forward travelling expansion wave*, reducing pressure as it travels along the arterial tree (Mynard and Smolich, 2014b, 2017). It is important to note, *expansion* here refers to the pressure reducing aspect of this wave, not expansion of the arteries. The expansion wave simply describes the decay in pressure originating in the proximal aorta, and, as the aorta passively contracts, it delays the passive relaxation and pressure decay of downstream arteries.

The implication of recognising the effects of absolute end-systole as a propagation, means the time delay between the relative end-systole experienced at two different sites, should be the same as the time it took the pulse wave to propagate the distance between the two sites. In other words, *PTT* should predict the time delay between the start of diastolic decay

at different pressure measurement locations, just as it did for the relative start-systole (t_0) of different arterial sites. Figure 10.1 shows this phenomina of *PTT* predicting the propagation of end-systole[1].

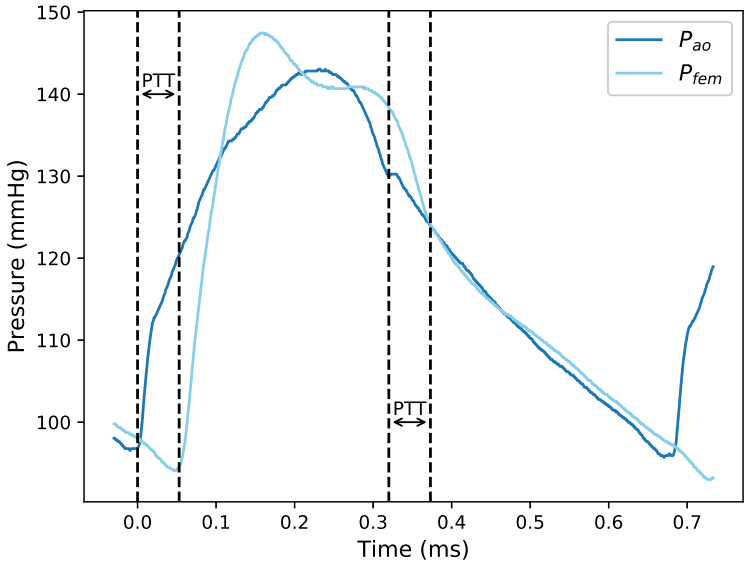

Figure 10.1: Simultaneously measured aortic arch and femoral pressures from Pig D2 control stage. This shows the *foot-to-foot PTT* detection in the same manner as Figure 2.13. However, this figure also shows, forward projecting the *PTT* from the dicrotic notch of a proximal aortic signal, strongly predicts the beginning of diastolic relaxation in the downstream pressure measurement.

However, it is worth noting the end-systole point predicted in the downstream signal ($t_{es,PTT}$), is *not* definitive, since the approach negates the effects of the changing waveform shape as it travels along the arterial tree (Westerhof et al., 2010c; Guyton and Hall, 2011), discussed in Sections 2.2.2 and 2.5.4. Additionally, $t_{es,PTT}$ requires two pressure measurement sites, one with a distinct identifiable t_{es} point, such as the dicrotic notch of P_{ao}. Two arterial pressure measurements are not common in a clinical setting, as covered in Section 7.3. Thus, the method is not viable in a clinical setting. However, it still provides a means of validating the end-systole point in a dicrotic notch-less signal in an experimental setting.

[1] An aside, *PTT* can also be used to forward project the start of diastolic relaxation/decay (t_{dr}) point, but the need to do so is outside the scope of this particular analysis

10.2.2 End-Systole, Attenuated Dicrotic Notches and Measures of Curvature

Section 8.3, stated the dicrotic notch has a gradient $\frac{dP}{dt} = 0$, not $\frac{dP}{dt}_{min}$, as predicted by $t_{es,dP/dt}$ (Kamoi, 2016; Kamoi et al., 2017). Attenuated dicrotic notches transition to points of inflection or simply just a change in curvature, where the latter is seen in P_{fem} of Figure 10.1, where $t_{es,PTT}$ marked the transition from a steep negative gradient in late systole, to a less negative gradient in exponential decay. Thus, end-systole in a dicrotic notch-less signal resembles a point of *downward concavity*, a point of distinct change in curvature.

Moreover, the curvature or concavity of the pressure signal corresponds to its *second* derivative, $\frac{d^2P}{dt^2}$. Specifically, the local change in curvature at end-systole is measured as a peak in $\frac{d^2P}{dt^2}$, as illustrated in Figure 10.2. The larger the change in curvature, the less attenuated the dicrotic notch, and the more prominent the $\frac{d^2P}{dt^2}$ peak. Thus, the hypothesis is $\frac{d^2P}{dt^2}$ provides a more appropriate signal for t_{es} detection than $\frac{dP}{dt}$.

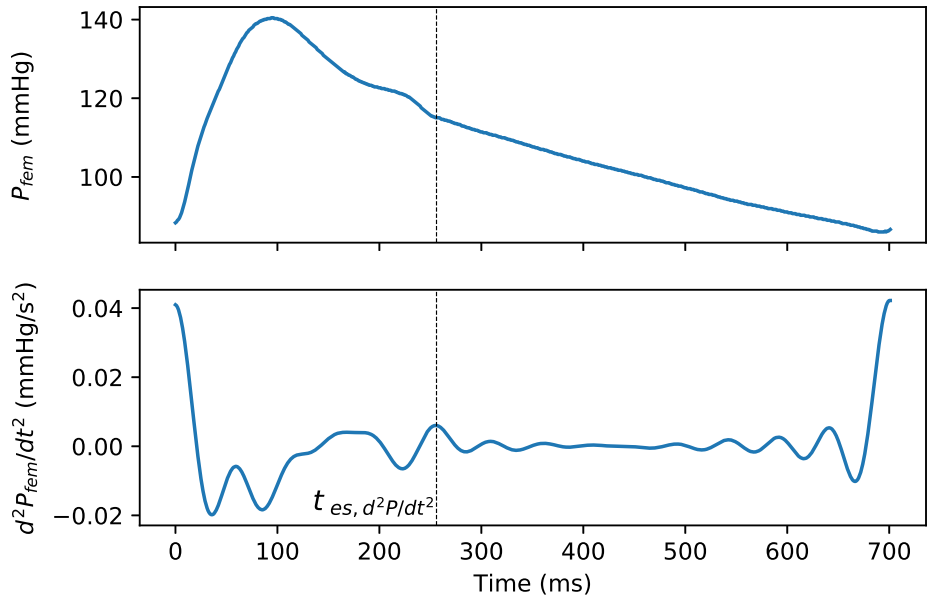

Figure 10.2: The rationale for identifying end systole as a prominent peak in the filtered second derivative ($t_{es,d^2P/dt^2}$), corresponding to the transition to start of diastole. This beat is taken from Pig D2's high PEEP stage.

However, since the arterial pressure waveform has other regions of changing curvature, such as the t_0 or the maximum pressure of a beat (P_{max}), identification of the correct peak associated with t_{es} is made more difficult. To overcome this issue, the aim was to weight $\frac{d^2P}{dt^2}$, so the resulting peak corresponds to the local maximum curvature in the region of downward concavity, making it appropriate for signals with and without dicrotic notches. End-systole identified with the weighted $\frac{d^2P}{dt^2}$ is referred to in this thesis as $t_{es,d^2P/dt^2}$, to distinguish it from the other end-systole detection methods covered in this thesis.

The remaining sections of this chapter cover the development of the $t_{es,d^2P/dt^2}$ method, and test its performance. Specifically, the accuracy and robustness of the new method is tested on the more difficult, dicrotic notch-less signals, increasing its clinical applicability as per Section 10.1. It is also compared to $t_{es,dP/dt}$, since as per Sections 8.2 and 10.1, an advantage of $t_{es,dP/dt}$ was its consistency in signals with and without dicrotic notches, as well as it being the method of choice for other implementations of three-element windkessel based models[2] (Aguado-Sierra et al., 2008; Alastruey, 2010; Kamoi et al., 2017)

10.3 Methods

10.3.1 Porcine Trial and Measurements

The data for this study comes from Protocols D and S. Specifically, it uses data from Pigs D1, D2, D4 and D5 of the dobutamine protocol, covered in Section 5.2.1, and Pigs S1– S6 of the sepsis protocol, covered in Section 5.2.2. Preparation of the pigs was covered in Section 5.2, and available measurements summarised in Table 5.1. Since this study is focused on dicrotic notch-less end-systole detection, the primary measurement of interest is the femoral pressure (P_{fem}), although P_{ao} is used as part of the validation process, covered in Section 10.3.5.

[2]Aguado-Sierra et al. (2008) states end-systole is *"the time of the first zero crossing of the second derivative"*, which is equivalent to a minimum in the first derivative. Alastruey (2010) does not outline their algorithm for end-systole detection, but Figure 11 of the publication strongly suggests the point of maximum negative gradient, with the dicrotic notch clearly attributed to early diastole.

10.3.2 Hemodynamic Modification

The hemodynamic modifications of Protocols D and S were originally used to assess different cardiac performance metrics, such as *SV* and PV-loops (Kamoi et al., 2015; Kamoi, 2016; Kamoi et al., 2017; Davidson et al., 2018). However, similar to Section 8.4.2, this study is not concerned with the hemodynamic interventions effects per se. Instead, the protocols simply provide a variety of pressure waveform shapes to test an improved end-systole detection algorithm.

10.3.3 Data Selection Summary

The data used in the analysis is taken from distinct *stages* of the two experimental protocols. All the stages of each protocol were shown in Figures 5.1 and 5.2, respectively. However, not all stages and beats were used in this analysis, thus, this section summaries those that were used.

Specifically, 30 heart beats are used for each stage to ensure equal representation in statistical comparisons. The *control* stage was when a pig was at rest following anaesthesia, before any hemodynamic modifications were applied. Both protocols included recruitment manoeuvres (RM). However, some pigs maximum PEEP during the RM reached 15 cmH_2O, while others reached 20 cmH_2O. For consistency, the *high PEEP* stage in this study used data associated with a PEEP level of 15 cmH_2O, for all pigs. Pigs associated with Protocol D have the *dobutamine* stage, where the 30 beats are during the continuous dobutamine infusion. Protocol S's final stage is *end endo*, which for Pigs S2, S3 and S5 refers to 30 beats just prior to the cessation of the endotoxin infusion. Pigs S1, S4 and S6 responded more dramatically to the endotoxin infusion causing cardiac/circulatory failure before the full 30 min was complete. Therefore, the *end endo* stage for these pigs is during the late part of their rapid decline in hemodynamic stability.

10.3.4 Weighted Second Derivative Algorithm Implementation

Summarising Section 10.2.2, end-systole in P_{fem} occurs in the region of downward concavity leading into diastolic decay. Concavity can be measured using the second derivative with respect to time ($\frac{d^2P}{dt^2}$). End systole ($t_{es,d^2P/dt^2}$) corresponds to a prominent peak in $\frac{d^2P}{dt^2}$, in the region after the peak pressure, as shown in Figure 10.2.

However, as covered in Section 5.4.2, noise is amplified when calculating discrete data's derivatives, making $\frac{d^2P}{dt^2}$ peak detection more difficult. Although filtering $\frac{d^2P}{dt^2}$ removes most of the noise, noise at a similar frequency to the peak associated with $t_{es,d^2P/dt^2}$ cannot be removed, as seen in Figure 10.2. Therefore, a weighting function, $w(t)$, is applied to attenuate $\frac{d^2P}{dt^2}$ peaks based on their distance from the region in which t_{es} is expected to occur. The weighting is based on a normalized beta distribution probability density function (Johnson et al., 1994), so its magnitude ranges from 0 to 1. The algorithm implementation is as follows:

1. $\frac{d^2P}{dt^2}$ is calculated as per Section 5.4.1, using Equations 5.2, 5.5 and 5.6. It is subsequently passed through a zero phase delay Hamming low pass filter, with a cutoff frequency (f_c) of 20 Hz and transition band width (f_{tb}) of 5 Hz, per Section 5.4.2 and Figure 5.3.

2. Time of start of systole for each beat ($t_{0,fem}$) is identified as the feet in the pressure waveform, along with the time of each beats peak pressure ($t_{P_{max}}$). The algorithm used is outlined in Section 5.4.3 and illustrated in Figure 5.7 (Balmer et al., 2018a,c).

3. The weighting is calculated and applied to each beat individually according to the following steps:

   (a) The n^{th} beat ($t_{0,fem,n} \leq t \leq t_{0,fem,n+1}$) is considered in isolation, so time is with respect to the start of the beat, ranging $0 \leq t \leq T$, where T is the duration of the beat.

(b) The weighting function $w(t)$ is calculated:

$$w(t) = \begin{cases} 0 & : t \leq t_{P_{max}} \\ \tau^{\alpha-1}(1-\tau)^{\beta-1} & : t > t_{P_{max}} \quad \text{where} \quad \tau(t) = \frac{t - t_{P_{max}}}{T - t_{P_{max}}} \end{cases} \tag{10.1}$$

Where for $t > t_{P_{max}}$, $w(t)$ becomes a beta distribution probability density function, distributed over the remainder of the beat. With $0 \leq \tau \leq 1$ and $\beta = 5$, the basic shape of $w(t)$ is defined. The α value allows control over the final shape by shifting its peak, as shown in Figure 10.3.

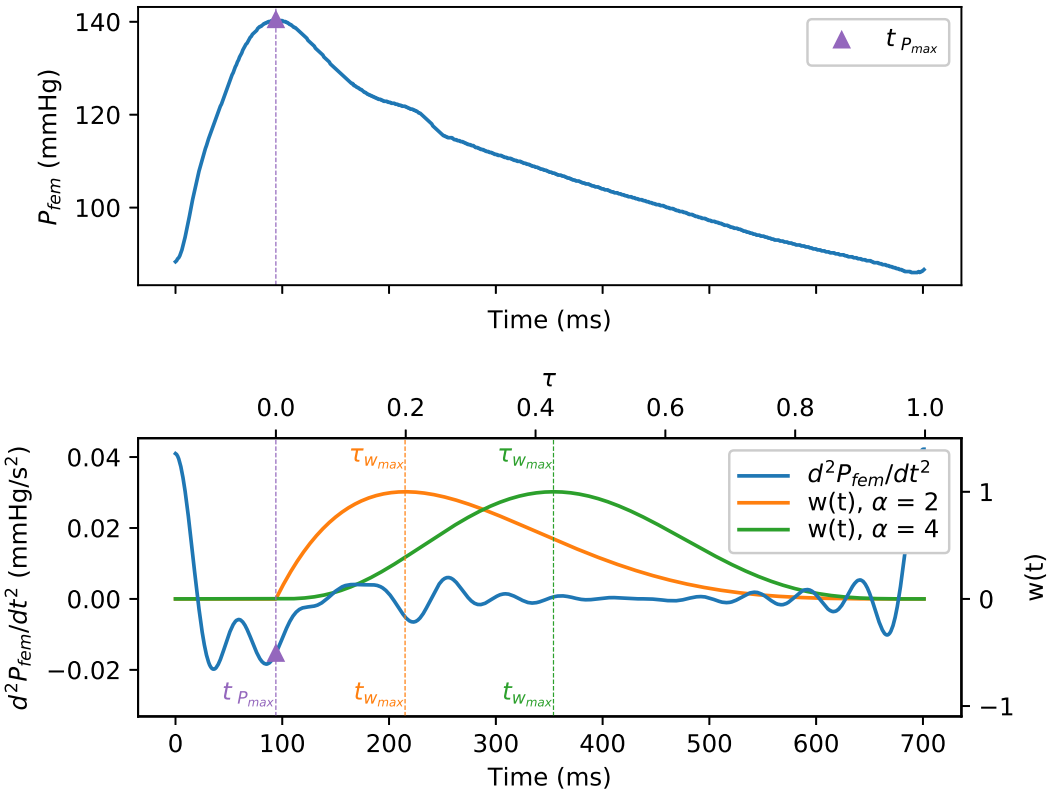

Figure 10.3: Two different possible weighting functions are shown, illustrating the effect of α on the weightings peak location, $t_{w_{max}}$ and $\tau_{w_{max}}$ respectively. The example uses the same beat as for Figure 10.2.

More specifically, α ensures an adaptive beat specific weighting, that places the $w(t)$ peak ($t_{w_{max}}$) in the expected vicinity of t_{es}. The value of α is calculated:

$$\alpha = \frac{\beta\tau_{w_{max}} - 2\tau_{w_{max}} + 1}{1 - \tau_{w_{max}}} \quad \text{where} \quad \tau_{w_{max}} = \frac{t_{w_{max}} - t_{P_{max}}}{T - t_{P_{max}}} \tag{10.2}$$

Equation 10.2 is derived from recognition $\tau_{w_{\max}}$ comes from $\frac{dw(t>t_{P_{max}})}{dt} = 0$. Thus, all that is necessary is to define $t_{w_{max}}$ in the location of the expected end systole point (t_{es}) for the n^{th} beat according to the following:

i. If $n \leq 3$, an empirical relationship gives an estimate of systolic duration based on heart rate ($T_{sys,HR}$), where heart rate (HR) is in beats per second (Gemignani et al., 2008):

$$t_{w_{max}} = T_{sys,HR} = -0.1HR + 0.45 \tag{10.3}$$

where $T_{sys,HR}$ is used to define $t_{w_{max}}$ with respect to the start of the beat.

ii. If $n > 3$, $t_{w_{max}}$ is the mean systolic duration ($\overline{T_{sys}}$) from the previous three beats identified $t_{es,d^2P/dt^2}$ points:

$$t_{w_{max}} = \overline{T_{sys}} = \frac{1}{3}\sum_{i=1}^{3} T_{sys,n-i} \tag{10.4}$$

The value of α is also constrained between 1.5 and 4.5, ensuring $t_{w_{max}}$ is not placed too early in systole, or too late in diastole.

4. With $w(t)$ calculated using Equation 10.1, $t_{es,d^2P/dt^2}$ is found as the time of the most prominent peak in the product $w(t)\frac{d^2P}{dt^2}$, the weighted second derivative. The culmination of all steps is shown in Figure 10.4, using the third and fourth beats of Pig D2's high PEEP stage. This way, both steps 3(b)i and 3(b)ii, for $t_{w_{max}}$ determination, are illustrated in this figures choice of heart beats.

5. *This final step is only necessary for dicrotic notches and subsequent identification of* t_{dr}.

Thus, while not necessary for this dicrotic notch-less analysis, the step is outlined here for completeness. As stated in Section 10.2.2, $t_{es,d^2P/dt^2}$ identification is easier when applied to proximal pressure signals, because the second derivative peak associated with a dicrotic notch has much more prominence. However, filtering the second derivative in Step 1 will shift the $t_{es,d^2P/dt^2}$ peak due to the removal of some frequency content. To account for this, Steps 9 and 10 from the dicrotic notch detection algorithm in Section 8.4.5, can also be implemented here. Specifically, check whether a local maximum in pressure occurs following $t_{es,d^2P/dt^2}$, if so this point is identified as t_{dr}. Subsequently, update $t_{es,d^2P/dt^2}$ to the minimum that resides between the initial $t_{es,d^2P/dt^2}$ and t_{dr}. An example of the $t_{es,d^2P/dt^2}$ method applied to P_{ao}, including these additional steps, is shown in Figure 10.5.

The main purpose of Figure 10.4 is to illustrate the $t_{es,d^2P/dt^2}$ method. However, it also includes the $t_{es,dP/dt}$ and $t_{es,PTT}$ methods, for comparison. The $t_{es,dP/dt}$ algorithm was covered in Section 8.3, but only illustrated for waveforms with dicrotic notches in Figure 8.2. Since $t_{es,dP/dt}$ performance will be compared to $t_{es,d^2P/dt^2}$ in the subsequent analysis, $t_{es,dP/dt}$ is shown here applied to the dicrotic notch-less case. The method for identifying $t_{es,PTT}$ was illustrated in Figure 10.1, and is used as a validation reference method, to quantify the performance of the two derivative based approaches ($t_{es,dP/dt}$ and $t_{es,d^2P/dt^2}$), discussed further in Section 10.3.5.

10.3.5 Validation of Time of End-Systole Point

Since, by eye, there is no definitive t_{es} location in a dicrotic notch-less arterial pressure waveform, validation of $t_{es,d^2P/dt^2}$ for notch-less waveforms is difficult. However, as covered in Section 10.2.1, *PTT* can be used to forward project the dicrotic notch location from P_{ao} onto the the P_{fem} signal. Despite the lack of a definitive end-systole point in P_{fem}, forward projected $t_{es,PTT}$ provides a physiologically based estimate of t_{es}, as shown in Figure 10.1. Thus, $t_{es,PTT}$ is considered the reference end-systole point in P_{fem} for the analysis, to which, $t_{es,dP/dt}$ and $t_{es,d^2P/dt^2}$ can be compared to assess their performance.

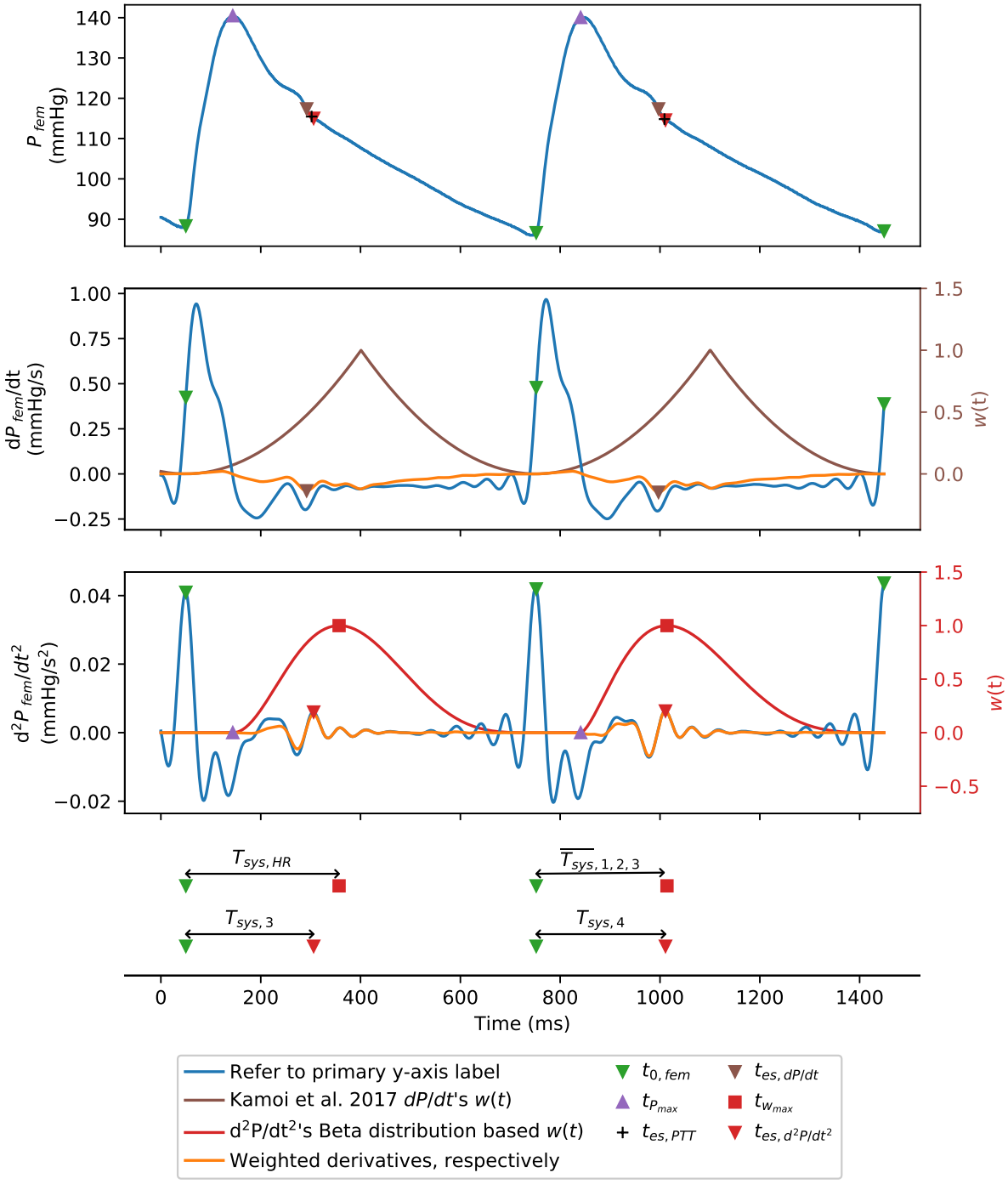

Figure 10.4: Example $t_{es,d^2P/dt^2}$ end systole detection, using the 3rd and 4th beats of Pig D2's high PEEP stage. Note, beats 1-3 use Equation 10.3 to define $t_{w_{max}}$ location. Subsequent beats move $t_{w_{max}}$ using the mean systolic duration of the previous three beats, per Equation 10.4, thus, beat four uses the mean of beats 1-3, $\overline{T_{sys,1,2,3}}$. Additionally, the comparison method $t_{es,dP/dt}$ is shown, identified via the first derivative, and $t_{es,PTT}$ the reference/validation end-systole point. Finally, the derivatives shown are post filtering.

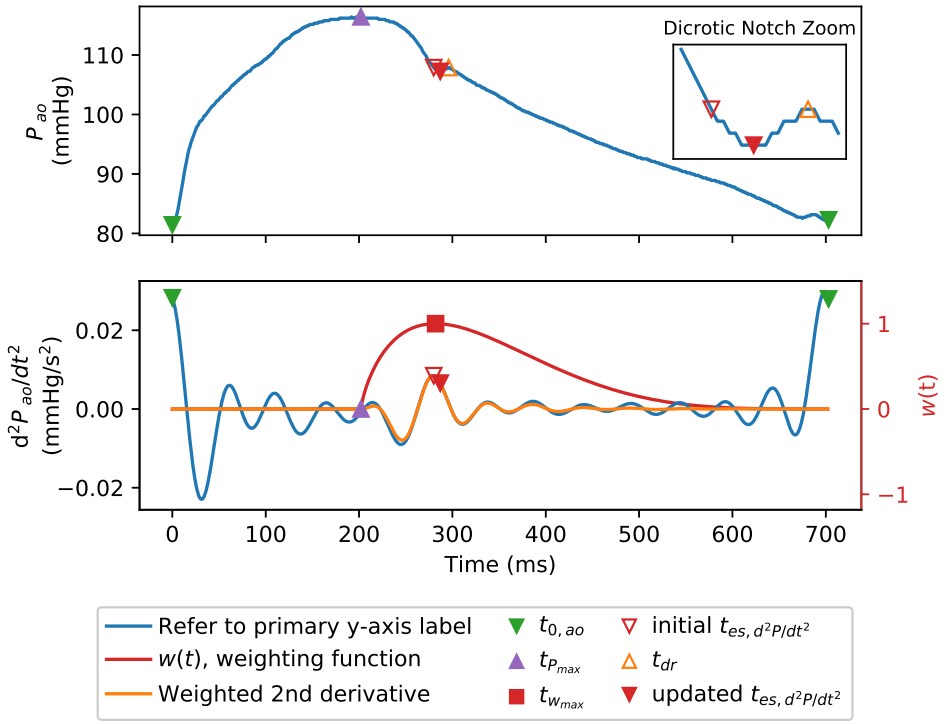

Figure 10.5: Example of $t_{es,d^2P/dt^2}$ detection in a pressure waveform with a dicrotic notch. The example uses a proximal pressure waveform from Pig D4's control stage.

Per Table 5.2.4, P_{ao} was measured for both protocols in this study. Thus, dicrotic notch detection ($t_{es,dic}$) in P_{ao} was performed using the adaptive shear transform method developed in Chapter 8, $t_{es,shear}$.

10.3.6 Analyses

Rather than directly comparing the difference between the derivative based end systole estimates ($t_{es,dP/dt}$ & $t_{es,d^2P/dt^2}$) and $t_{es,PTT}$, their resulting systolic durations are compared. The three systolic durations are shown in Figure 10.6 and summarized below, with their respective end-systole estimates:

- $T_{sys,PTT}$, where end-systole is $t_{es,PTT}$
- $T_{sys,dP/dt}$, where end-systole is $t_{es,dP/dt}$
- $T_{sys,d^2P/dt^2}$, where end-systole is $t_{es,d^2P/dt^2}$

The reason for using T_{sys} to assess each methods end-systole performance, is the same as

when assessing $t_{es,shear}$ in Chapter 8. Specifically, Section 8.2 outlined how the end-systole time point is often found to determine systolic and diastolic time intervals (Talley et al., 1971; Payne et al., 2006; Marik, 2013), as in Kamoi et al. (2017).

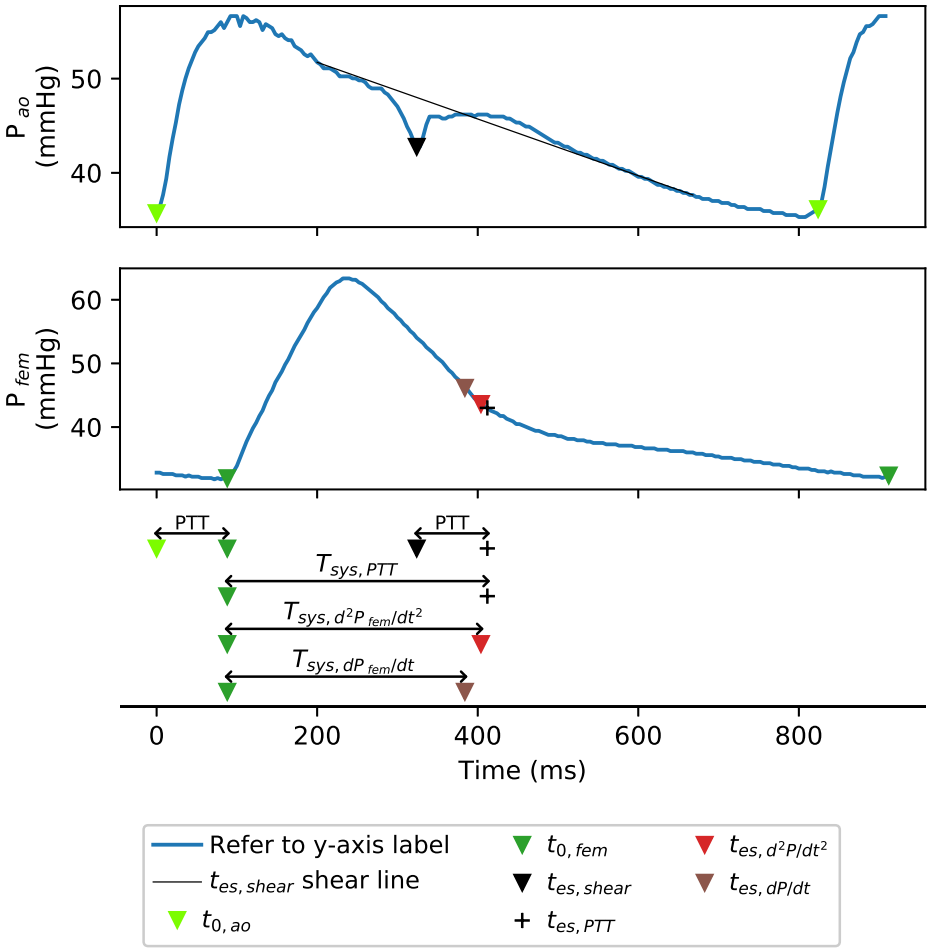

Figure 10.6: Example of how pulse transit time (*PTT*) was used to compare the t_{es} algorithms using T_{sys} estimates. The example uses pressure waveforms from Pig S5's control stage.

The accuracy of $T_{sys,dP/dt}$ and $T_{sys,d^2P/dt^2}$ compared with $T_{sys,PTT}$, are analysed using two formats. First, regression analysis and coefficients of determination (r^2), both overall and for individual pigs. The coefficient of determination, r^2, represents the fraction of the total observed variation in $T_{sys,d^2P/dt^2}$ or $T_{sys,dP/dt}$, due to the observed variation in $T_{sys,PTT}$. However, correlation does not imply agreement (Bland and Altman, 1986) and therefore Bland-Altman analysis is also used.

10.4 Results & Discussion

10.4.1 Correlation Outcomes

Overall correlations are shown in Figure 10.7, with r^2 = 0.77 verses 0.87, for $T_{sys,dP/dt}$ and $T_{sys,d^2P/dt^2}$ respectively. The results suggest more of the variability in $T_{sys,d^2P/dt^2}$ is explained by $T_{sys,PTT}$, compared with $T_{sys,dP/dt}$. However, Table 10.1 shows the individual r^2 for Pigs S1 and S4 was higher for $T_{sys,dP/dt}$ than $T_{sys,d^2P/dt^2}$. These two higher individual pig r^2 values can be misleading if used to assess agreement (Bland and Altman, 1986), since for Pig S1, $t_{es,d^2P/dt^2}$ was closest to $t_{es,PTT}$ for 87 of its 90 beats, with only 3 beats during end endo where $t_{es,dP/dt}$ was closer to $t_{es,PTT}$. Similarly $t_{es,d^2P/dt^2}$ was the better estimate in 17 of 30 beats in Pig S4 end endo.

As stated in Section 10.3.3, inadequate pulse pressures led to circulatory failure prior to the full 30 min of endotoxin infusion in Pigs S1 and S4. This circulatory failure is to blame for the reduction in end-systole detection accuracy and outliers in Figures 10.7 and 10.8. Specifically, Pig S4's femoral pressure fell to a mean value of 24 mmHg, with a pulse pressure of only a few millimetres of mercury, at which point the near non-pulsatile signal makes end-systole detection difficult for any algorithm. Since P_{ao} was maintained longer than P_{fem} during the end endo stage, a dicrotic notch still enabled reasonable $t_{es,PTT}$ estimation.

Table 10.1: Coefficient of determination (r^2) for each T_{sys} estimate ($T_{sys,dP/dt}$ & $T_{sys,d^2P/dt^2}$) vs $T_{sys,PTT}$, for each individual pig (rounded to 2 d.p.).

	Pig									
	D1	**D2**	**D4**	**D5**	**S1**	**S2**	**S3**	**S4**	**S5**	**S6**
$T_{sys,dP/dt}$	1.0	1.0	0.99	0.83	0.59	0.93	0.98	0.44	0.98	0.87
$T_{sys,d^2P/dt^2}$	1.0	1.0	0.99	0.83	0.01	0.94	0.97	0.0	0.98	0.87

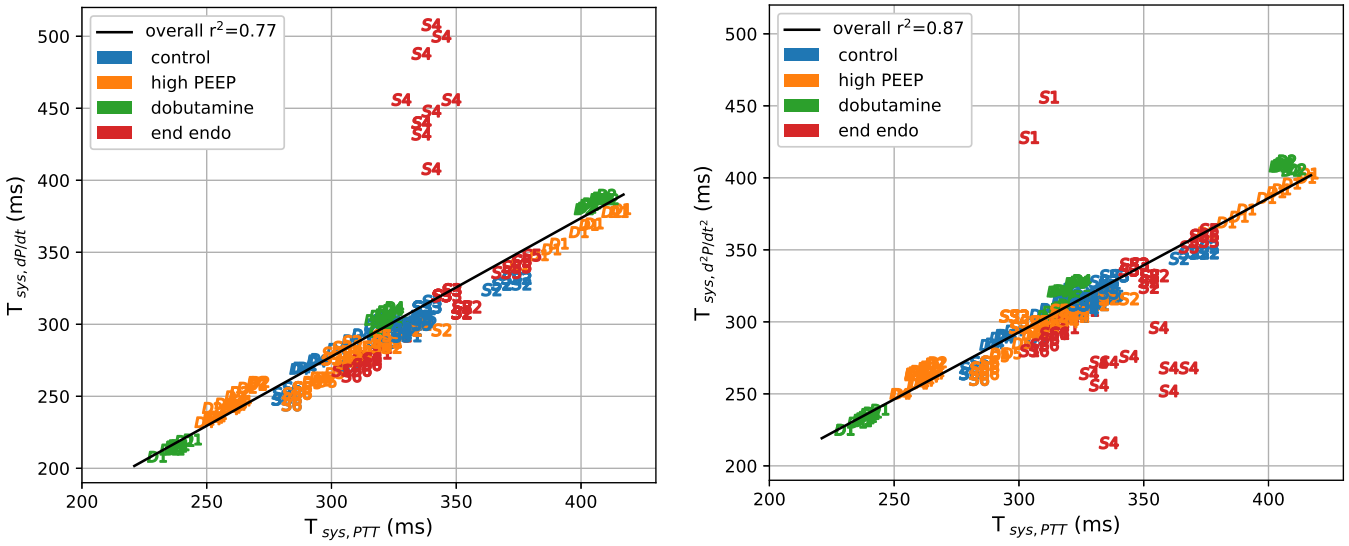

(a) Variation in $T_{sys,dP/dt}$ described by $T_{sys,PTT}$

(b) Variation in $T_{sys,d^2P/dt^2}$ described by $T_{sys,PTT}$

Figure 10.7: Regression analysis: (a) and (b) show the overall coefficient of determination (round to 2 d.p.), for both $T_{sys,dP/dt}$ and $T_{sys,d^2P/dt^2}$ estimation methods. Pig markers are according to their label, and while all beats contribute to the overall r^2, the 10 beats of highest error are shown for each pigs stage, to improve clarity.

10.4.2 Bland Altman Outcomes

Figures 10.8 shows the mean systematic error of the weighted second derivative method ($t_{es,d^2P/dt^2}/T_{sys,d^2P/dt^2}$) was lower than its weighted first derivative counterpart ($t_{es,dP/dt}/T_{sys,dP/dt}$), −8.7 ms versus −23.2 ms respectively. Additionally, the new algorithm has narrower limits of agreement (mean ± 1.96 standard deviations), of ±26.6 ms verses ±37.7 ms, confirming across all pigs and stages its superiority over the old algorithm.

Notably, ignoring Pig S4's end endo stage outliers, explained in Section 10.4.1, $t_{es,dP/dt}$ consistently underestimates systolic duration, with all data points in Figure 10.8a being less than zero, ensuring negative mean bias. This limitation is expected, since a trough in the first derivative describes a local point of maximum negative gradient, as opposed to a stationary point. Figure 10.4 shows this max negative gradient lies between $t_{P_{max}}$ and $t_{es,PTT}$, with the magnitude of the gradient reducing through $t_{es,PTT}$ and into diastole. This behaviour is mirrored in the results of Section 8.5.2, where $t_{es,dP/dt}$ consistently underestimated T_{sys} in

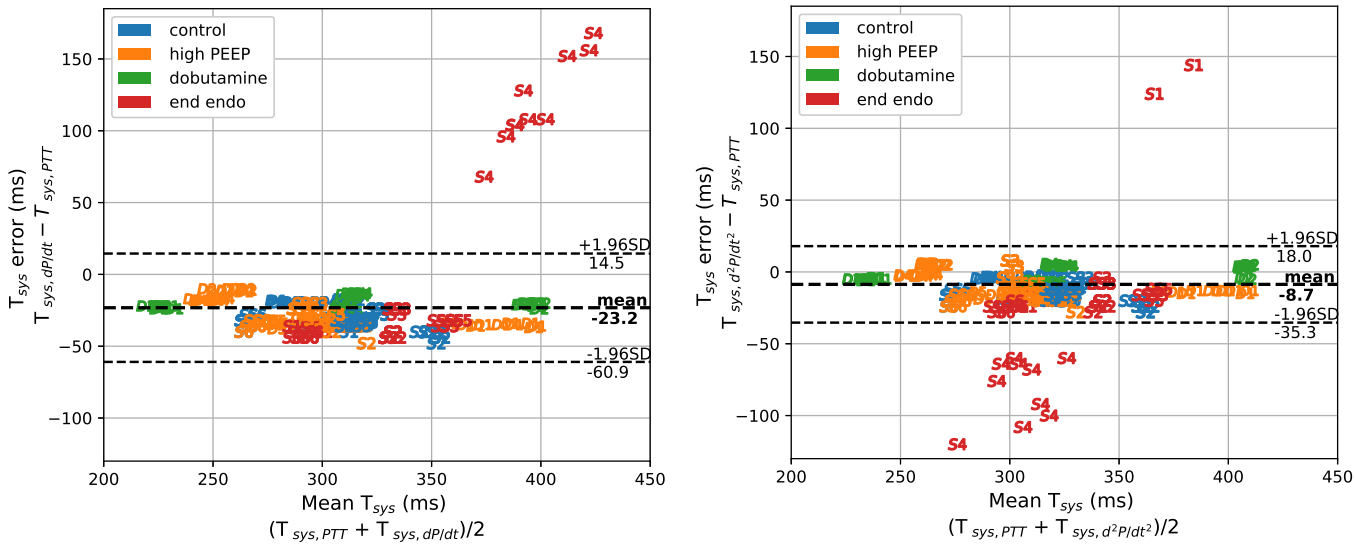

(a) Agreement between $T_{sys,dP/dt}$ and $T_{sys,PTT}$

(b) Agreement between $T_{sys,d^2P/dt^2}$ and $T_{sys,PTT}$

Figure 10.8: Bland Altman analysis: the mean bias between $T_{sys,PTT}$ and the derivative based T_{sys} estimates are shown as well as the limits of agreement. Pig markers are according to their label, and while all beats contribute to the mean bias and limits of agreement, the 10 beats of highest error are shown for each pigs stage, to improve clarity.

P_{ao} with dicrotic notches[3] (Balmer et al., 2018a).

In contrast, the weighting in $t_{es,d^2P/dt^2}$ is developed specifically to estimate the location of an attenuated dicrotic notch. The results indicate, despite no dicrotic notch being present, physiologically based end-systole detection is still possible, without having to compromise accuracy using the first derivative method. More importantly, the approach significantly improves the clinical applicability of other algorithms and methods requiring end systole detection as an input.

10.4.3 End Systole Detection Limitations

The study is generalizable to human arterial signals measured from the proximal aorta to the femoral artery, shown in Figure 2.4. However, a reduction in performance may occur in even more peripheral arterial signals, where reflected waves can cause turning points that appear similar to a dicrotic notch, but do not correspond to end systole. Such signals are found, for example, in the radial artery (Oppenheim and Sittig, 1995; Hoeksel

[3]Figure 8.7b error was calculated as $T_{sys,mea}$ - $T_{sys,dP/dt}$, i.e. reference T_{sys} - estimated T_{sys}. Figure 10.8a calculated error as $T_{sys,dP/dt}$ - $T_{sys,PTT}$, i.e. estimated T_{sys} - reference T_{sys}. Thus, the positive error in Chapter 8's analysis, represents equivalent behaviour as the negative error in this chapter.

et al., 1997), as stated in Section 9.3.3. The algorithm has not yet been tested on such peripheral signals, as this study extends only as far as the femoral artery, which as per the desired traits in Section 10.1, is readily accessible in intensive care and similar clinical situations (Cousins and O'Donnell, 2004; Watson and Wilkinson, 2012), and is less prone to wave reflection induced distortions (Westerhof et al., 2010c). However, methods do exist to approximate a central arterial pressure waveform from the likes of a measured radial waveform, which may help to extend clinical applicability further (Gao et al., 2016).

This study used a range of hemodynamic states found in an intensive care setting, including recruitment manoeuvres, dobutamine admission and septic shock like response. While this diversity ensured both stable and unstable hemodynamics were tested, it is possible other behaviour not tested could cause issues. For example, cardiac arrhythmia can significantly alter expected pressure waveform shape beat-to-beat. It is likely the algorithm presented in this study would suffer reduced performance under these conditions. However, in a clinical setting, severe cardiac arrhythmia would not be left unresolved and end systole detection under such conditions is unlikely of immediate clinical need or interest.

10.5 Summary

The study developed a simple end-systole detection algorithm for use in arterial pressure waveforms, with or without dicrotic notches. The analysis was conducted on the more difficult dicrotic notch-less case, and results showed improved end-systole detection over an existing method. Specifically, the novel adaptively weighted second derivative method, $t_{es,d^2P/dt^2}$, was better able to monitor systolic duration, with less bias and narrower limits of agreement, when compared with the existing $t_{es,dP/dt}$ method (-8.7 ± 26.6 ms verses -23.2 ± 37.7 ms).

While end-systole detection is a useful tool, which can be used for many purposes, the authors motivation for developing $t_{es,d^2P/dt^2}$ was to overcome the limitations summarised in Section 9.8. Specifically, the hypothesis was, with limited effect of distinct reflected wave

phenomena in the femoral pressure waveform, the three-element windkessel parameter identification via PCA might be improved, subsequently improving the aortic flow and *SV* estimation. However, before this hypothesis could be assessed, a robust method of end-systole detection in femoral pressure waveforms needed to be developed, which was the goal achieved in this chapter.

CHAPTER 11

Clinically Applicable, Physiologically Accurate, Model Based Flow Estimation

11.1 Introduction

Chapters 6 introduced the Kamoi model, a unique hybrid implementation, of the three-element windkessel (Section 4.3) with pulse wave velocity (*PWV*). Section 6.1 stated it was a benchmark and starting point for this thesis. Thus, Chapter 6 was particularly focused on the limitations of the model, discussed in Section 6.3. Subsequently, Chapters 7 – 10 focused on addressing each of the limitations associated with the Kamoi model. The learnings from the previous chapters will be summaries with respect to the intent of this chapter.

Chapter 7 tested pulse arrival time (*PAT*) as a surrogate for pulse transit time (*PTT*). As explained in Section 7.3, aortic *PWV* is usually measured by measuring *PTT*. In Kamoi et al. (2017), *PTT* was measured via dual arterial catheterisation, which is not common clinically and contradicts this thesis's goals of developing a clinically applicable method

for flow and stroke volume (*SV*) estimation, per Section 1.4. *PAT* represented a potential clinical surrogate for *PTT*, but was shown to be inappropriate due to variability in the pre-ejection period (*PEP*). Thus, an accurate clinically applicable method of monitoring *PWV*, in a critical care environment, was not found.

Chapter 8 focused on improving end-systole (t_{es}) detection in proximal aortic pressure waveforms (P_{ao}). Section 8.1 summaries how the end-systole method employed in Kamoi et al. (2017), $t_{es,dP/dt}$, had low accuracy, and hypothesised an improved t_{es} detection method would improve the flow and *SV* estimation accuracy of the Kamoi model. As shown in Section 8.5, the newly developed dicrotic notch detection method, $t_{es,shear}$, was a significant improvement over $t_{es,dP/dt}$. However, Chapter 9 showed, despite improved detection using $t_{es,shear}$, the transient behaviour of the dicrotic notch made the Kamoi model's method of parameter identification more difficult.

The erroneous effect of the transient dicrotic notch behaviour was minimised in Section 9.6, by using a more efficient method for model parameter identification than Kamoi et al. (2017), in conjunction with t_{dr}. Importantly, t_{dr} is defined as the start of *diastolic relaxation*, a point after the transient dicrotic notch behaviour, marking the approximate start of diastolic exponential pressure decay. However, Section 9.8 ultimately concluded the advantages of easy end-systole detection, via the dicrotic notch and $t_{es,shear}$, were outweighed by the mechanisms responsible for the dicrotic notch being in conflict with the core assumptions and limitation of the three-element windkessel model. Additionally, the invasiveness of a P_{ao} measurement made it uncommon in a clinical setting and therefore at odds with the thesis goals of Section 1.4.

In Chapter 10, the decision was made to use the clinically more acceptable femoral arterial pressure waveform (P_{fem}) to test an implementation of the three-element windkessel model. Section 10.1, explained P_{fem} was less impacted by dicrotic notch and distinct reflected wave behaviour, and was a common clinical pressure measurement. Thus, the hypothesis was P_{fem} would not present the same limitations as P_{ao} in Chapter 9. However,

the obvious repercussion was end-systole would be more difficult to identify in P_{fem}, having negligible dicrotic notch behaviour.

Chapter 10 developed an improved end-systole detection method, $t_{es,d^2P/dt^2}$, which did not rely on leveraging the contour of a dicrotic notch per se, as $t_{es,shear}$ had done. Instead, $t_{es,d^2P/dt^2}$ used an adaptive weighted second derivative ($\frac{d^2P}{dt^2}$), to identified end-systole as a local point of maximum changing curvature. This approach made $t_{es,d^2P/dt^2}$ appropriate for pressure waveforms, with or without dicrotic notches.

While Section 4.3 discussed windkessel theory and limitations, in practice, actually implementing a model gave greater clarity as to windkessel behaviour. Considering Chapters 7 – 10 in aggregate, the three-element windkessel model is now better understood, with much of the analysis illustrated, not having been found elsewhere in the existing literature. Thus, this chapter applies all that has been learnt so far, and attempts to implement a three-element model which meets all the goals outlined in Section 1.4.

11.2 Methods

11.2.1 Porcine Trial and Measurements

The data for this study comes from Protocol S, outlined in Section 5.2.2. Specifically, it uses Pigs S1, S2 and S4 – S6. Pig S3 was ignored due to suspected issues with the instrumentation and/or data acquisition from the aortic flow probe and aortic pressure catheter. First, the aortic flow probe data, Q_{ao}, had significant noise throughout the entire cardiac cycle, much more than the other pigs in the cohort. Second, its P_{ao} signal also had significant noise, but confined only to early systole. Moreover, during early systole, P_{ao} was much lower than left ventricular pressure (P_{vent}), rather than the physiologically expected tracking outlined in Section 2.3.1 and Figure 2.5. The erroneous P_{ao} signal being limited to early systole of each beat, meant it was still usable for the analysis of Chapter 10.

Since this study plans to use P_{fem} for the measured pressure input to the model, P_{ao} acqui-

sition issues would not directly matter. However, the unreliable P_{ao} and Q_{ao} signals cast enough doubt over the acquisition of the remaining experimental data, so the decision was made to simply exclude the pig from this chapters analysis.

Preparation of the pigs, including sedation and euthanasia, was covered in Section 5.2. The measurements available were also covered in the aforementioned sections, and summarised in Table 5.1. Specifically, since this study is focused on estimating aortic flow (Q_{est}) and stroke volume (SV_{est}) via P_{fem}, the two primary measurement of interest are P_{fem} and Q_{ao}, where the latter enables validation of excess pressure (P_{ex}) shape, explained in Section 9.2.1, and calculation of measured stroke volume (SV_{mea}) via Equation 5.12.

11.2.2 Hemodynamic Modification

The hemodynamic modifications of Protocol S were covered in detail in Section 5.2.2 and included expected effects on cardiac performance. Specifically, Q_{ao} and SV_{mea} will change in response to changes in cardiac preload, afterload and contractility, as noted in Section 2.4. In this section, a summary of the interventions is provided:

1. The first intervention was an recruitment manoeuvre (RM), where the increase in positive end-expiratory pressure (PEEP) can reduce left ventricular preload and thus SV, per Figure 2.9 (Wallace et al., 1963; Luecke and Pelosi, 2005; Marik, 2010). However, the interventions effectiveness may be limited by the opening of the chest to place the aortic flow probe. Specifically, as per Section 5.2.2, the chest was closed with clamps after placing the probe, but the clamps do not provide a perfect seal.

2. The 500 ml fluid infusion can increase preload through the increased circulatory volume (Michard and Teboul, 2002; Reuter et al., 2002; Cecconi et al., 2015). Thus, it can increase SV per Figure 2.9.

3. The E. Coli lipopolysaccharide (endotoxin) infusion produces a septic shock like response, after which the protocol is named. The endotoxin infusion represents the main hemodynamic intervention of interest in this analysis. As per Section 5.2.2, it

can cause inflammation, capillary leakage, decreased afterload, hypovolemia, tissue hypoxia and eventual cardiac failure (Nguyen et al., 2006; Merx and Weber, 2010). Thus, it represents a severe life threatening case, which can occur clinically, providing a *worst case scenario* test of the developed three-element windkessel model.

The degree to which each pig responds depends on its sensitivity to the specific intervention, as well as its state following prior interventions.

11.2.3 Data Selection Summary

As per the previous analyses in this thesis, the experimental data was separated into stages. The stages of Protocol S were detailed in Section 5.3.2, and all stages shown in Figure 5.2 were used in this analysis. Specifically, 30 heart beats were extracted from each stage, making a total of 750 heart beats used in the analysis. An equal number of beats was used per stage for equal representation in any statistical analyses. As a reminder, recall the *end endo* stage was characterised by either the end of the 30 min endotoxin infusion (Pigs S2 and S5), or being in the later stages of circulatory failure (Pigs S1, S4 and S6).

11.2.4 The Three-Elements Windkessel Implementation

Many different implementations of three-element windkessel models have been presented and discussed throughout this thesis. However, this section outlines the implementation used by the author, and its rationale, in light of what has been learned in the preceding chapters, and aligning the method with the original thesis goals. For convenience, Figure 11.1 summarises the implementation process, including references to key sections within the thesis, key equations as they are used in this chapter, and key signals used in this chapter.

The Return to $Z_{c,w}C$

The most important difference between the Kamoi model of Section 6.2, and the three-element windkessel model used in this chapter, is the returning to a standard three-element model, describing reservoir pressure via Equation 4.11. Specifically, this choice means *PWV* and characteristic length (L_c) are *not* incorporated into this model. Thus, Equation 6.1 is ignored and reservoir pressure (P_{res}) is once more described by the parameter products $Z_{c,w}C$ and RC.

There are two main reasons for not using *PWV* and L_c in the model. First, as stated in Section 11.1, no clinically feasible means of monitoring *PWV* was found in Chapter 7. Without the ability to monitor *PWV*, the Kamoi model could not be implemented clinically. Second, and more importantly, Section 9.5 discussed how treating L_c as a fixed anatomical length hindered the Kamoi model's ability to predict physiologically relevant flow (Q_{est}). On the contrary, allowing $Z_{c,w}C$ to vary per beat will ensure P_{res} is always found minimising the error in Equation 6.7, thus reflecting the assumed model behaviour in Equation 4.12.

Therefore, the hypothesis in this chapter is using $Z_{c,w}C$, as a dynamic parameter, identified beat-to-beat, will enable improved P_{ex} shape prediction and lead to physiologically accurate Q_{est} and subsequent *SV* values. With the improved end-systole detection provided by $t_{es,d^2P/dt^2}$, it would be possible to use a femoral pressure waveform (P_{fem}) as the measured pressure input to Equation 4.11, as originally shown in Figure 4.4.

Reservoir and Excess Pressure Calculation

The parameters product forms in Equation 4.11, $Z_{c,w}C$ and RC, would need to be identified for each beat to estimate model P_{res}. Section 9.6 showed the most effective approach thus far in the thesis, identifying parameters via pulse contour analysis (PCA) and SciPy's (v1.3.0) non-linear least squares error minimisation function. Section 9.6, achieved the best fit of P_{res} to P_{ao}, according to Equation 6.7, by minimising the error for the final two-thirds of diastole, $t_{2/3}$, mitigating the effect of the dicrotic notch on parameter identifica-

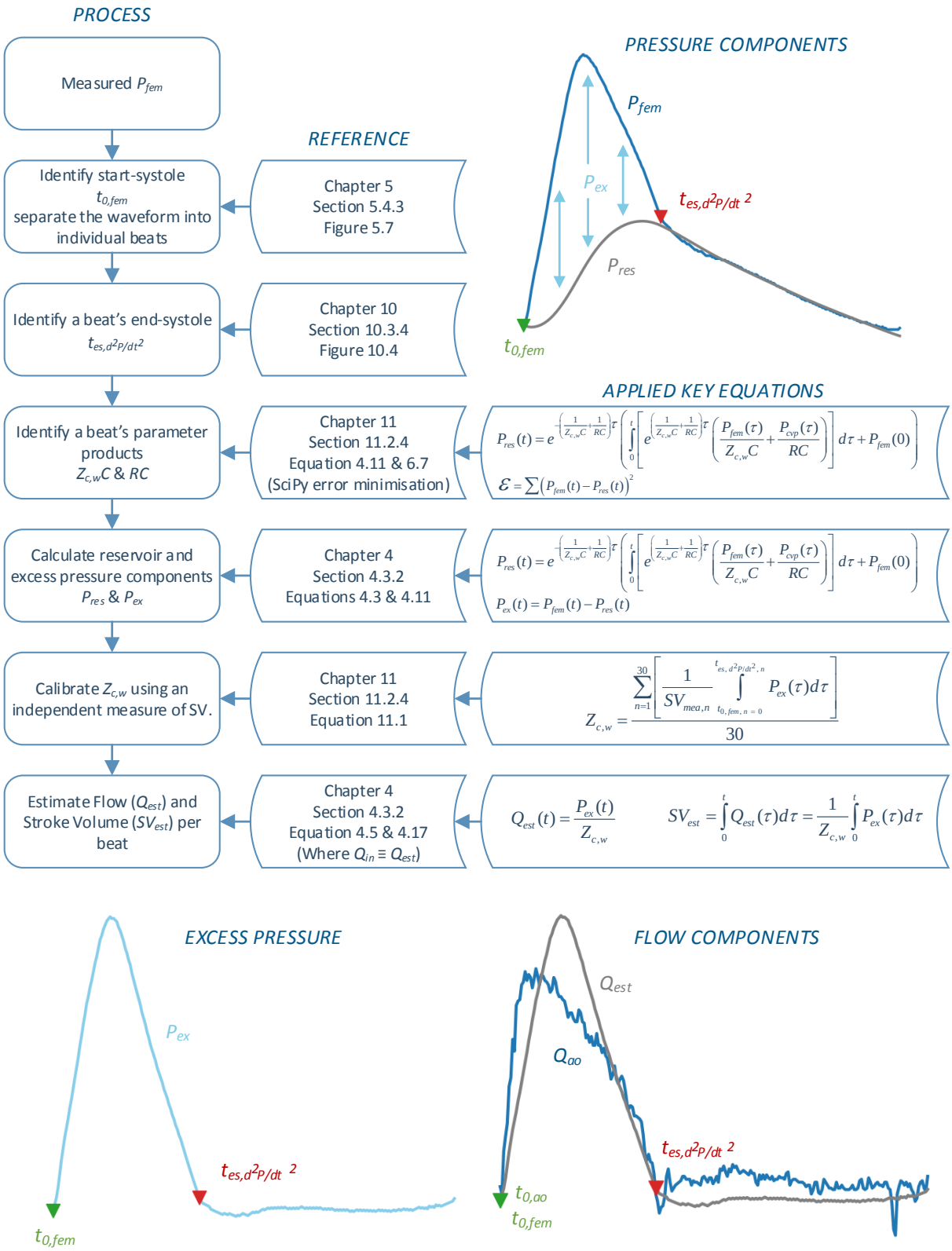

Figure 11.1: Model implementation summary, including reference to the chapter, section and figure/equation that explains each step in detail. For convenience, the referenced equations are also shown in their form applied in this analysis.

tion. Since in this analysis, it was known *a priori* that dicrotic notch behaviour in P_{fem} was negligible, using $t_{2/3}$ was not necessary. Moreover, the lack of dicrotic notches also implies $t_{es,d^2P/dt^2} \approx t_{dr}$, when identifying $t_{es,d^2P/dt^2}$ and subsequently t_{dr}.

Therefore, in this analysis, the optimisation calculates P_{res} using Equation 4.11, for the whole beat, for iterations of the parameter products $Z_{c,w}C$ and RC. However, the error minimisation within the function uses Equation 6.7, where $t_{es} = t_{es,d^2P/dt^2}$. In a clinical environment, or situation where dicrotic notch-less waveforms cannot be guaranteed, using $t_{2/3}$ to define end-systole/start-diastole in Equation 6.7 for the parameter identification processes, is advisable.

Finally, for transparency, since central venous pressure (P_{cvp}) was measured in the experiment, it was treated as a variable in Equation 4.11. However, as stated in Section 4.3.2, and shown later in Section 11.4.2, assuming a constant P_{cvp} for the model leads to similar results.

Windkessel Model Characteristic Impedance Calculation and Subsequent Flow and Stroke Volume Estimation

Once again, as in all previous three-element model implementations discussed in this thesis, P_{ex} and Q_{est} were calculated via Equations 4.3 and 4.5, respectively. Thus, in order to calculate Q_{est}, $Z_{c,w}$ would need to be found, separately from its product with windkessel compliance, $Z_{c,w}C$. This same situation arose in Section 6.2.1, where $Z_{c,w}$ was identified as $Z_{c,cal}$, using a calibrating stroke volume measurement, SV_{cal}, and Equation 6.3. Thanks to the aortic flow probe measurement providing SV_{mea}, this same approach can be applied to the control stage of this analysis, according to the following equation:

$$Z_{c,w} = Z_{c,cal} = \frac{\sum_{n=1}^{30}\left[\frac{1}{SV_{mea,n}}\int_{t_{0,fem,n}=0}^{t_{es,d^2P/dt^2,n}} P_{ex}(\tau)d\tau\right]}{30} \tag{11.1}$$

Where subscript ' n ' indicates the variable is associated with the n^{th} heart beat. Thus, Equation 11.1 simply states $Z_{c,w}$ is the mean of all 30 *control stage* beats individually calculated $Z_{c,cal}$ values, from each beats respective SV_{mea} and P_{ex}. It is also worth noting, the integral of P_{ex} is performed beat-wise considering the start of the beat, start-systole (t_0), as time zero, and lasting the duration of systole $T_{sys,d^2P/dt^2}$, identified by $t_{es,d^2P/dt^2}$. As discussed in Section 4.3.2, integrating P_{ex} only over systole reflects the expectation $P_{ex}(t > t_{es,d^2P/dt^2}) \approx 0$, requiring P_{res} to have been calculated satisfying the condition in Equation 4.12. Since during the control stage, the pigs are stable with waveforms unaltered by interventions, Equation 4.12 is more easily met. In a clinical environment, calibrating the model to an already unstable patient would potentially present more of a challenge, as will be discussed in Section 11.4.5.

Once $Z_{c,w}$ was found during the control stage, it was treated as a constant value for each successive stage of the analysis. Their were two reasons for fixing $Z_{c,w}$, the first was necessity, as the analysis was not using PWV and therefore could not use the water hammer or Bramwell-Hill equations as in Kamoi et al. (2017). Second, it was hypothesised that *any and all* changes to hemodynamic state could be captured through P_{fem} and the parameters products $Z_{c,w}C$ and RC, i.e. through P_{res} and subsequent P_{ex}. In other words, the hypothesis was using PCA with P_{fem}, in conjunction with the now improved end-systole detection $t_{es,d^2P/dt^2}$, would capture any changing hemodynamics, after $Z_{c,w}$ calibration. Assuming the hypothesis was correct, $Z_{c,w}$ would always provide a reasonable scaling of P_{ex} to correctly estimate flow Q_{est} and SV_{est} via Equations 4.5 and 4.17, respectively.

Importantly, in contrast to Equation 11.1, the integration limits for Equation 4.17 used the entire beat when calculating SV_{est}. This difference is because, unlike during the $Z_{c,w}$ calibration, following the hemodynamic modification of later stages, no assumption is made that $P_{ex}(t > t_{es,d^2P/dt^2}) \approx 0$. Of course, $P_{ex}(t > t_{es,d^2P/dt^2}) \approx 0$ for all pigs and stages is the desired outcome of the analysis. However, it is important to let any non-zero diastolic P_{ex} contribute to SV_{est}, rather than conveniently disregard this form of error.

11.2.5 Data Analysis

Bland-Altman analysis is used to assess the beat-to-beat error in *SV* (SV_{err}) and thus the overall agreement between SV_{est} (from Equation 4.17) and SV_{mea} (from Equation 5.12). Intra-pig *SV* error across the different stages enables identification of times of high or low *SV* accuracy. However, this analysis does not quantify how well changes in *SV* are tracked by the estimation method (Marik, 2013). Change in *SV* ($\boldsymbol{\Delta}SV$) due to the interventions is not a beat-wise metric like SV_{mea}, SV_{est} or SV_{err}, it is the difference between the mean *SV* ($\overline{SV}$) of consecutive stages, calculated as follows:

$$\Delta SV_{s\rightarrow s+1} = \overline{SV}_{s+1} - \overline{SV}_{s} \tag{11.2}$$

Where s and $s+1$ are a stage (s) and its consecutive stage ($s+1$) as depicted in Figure 5.2, for example, from the control stage to the high PEEP stage. In this manner, $\boldsymbol{\Delta}SV_{mea}$ and $\boldsymbol{\Delta}SV_{est}$ can be calculated between stages.

Thus, the error in the estimation methods ability to track changes in SV ($\boldsymbol{\Delta}SV_{err}$) is defined:

$$\Delta SV_{err,s\rightarrow s+1} = \Delta SV_{est,s\rightarrow s+1} - \Delta SV_{mea,s\rightarrow s+1} \tag{11.3}$$

$$\Delta SV_{err,s\rightarrow s+1}(\%) = \frac{\Delta SV_{err,s\rightarrow s+1}}{\overline{SV}_{mea,s+1}} \tag{11.4}$$

Where Equation 11.4 represents the error as a percentage with respect to stage $s+1$'s mean measured stroke volume ($\overline{SV}_{mea,s+1}$).

There are two limitations when calculating $\boldsymbol{\Delta}SV$ in the above manner, first using $\overline{SV}$ of each stage means the variability *within* a particular stage is not captured. Second, it dramatically reduces the number of measures when compared to the Bland-Altman beat-to-

beat analysis. Specifically, 5 pigs and 5 stages (4 interventions) gives 20 ΔSV_{err} data points. Thus, it becomes more appropriate to assess the tracking performance of the method across the cohort of 5 pigs using cumulative distribution functions (CDF), quantifying the proportion of ΔSV_{err} falling within a particular range. However, ΔSV_{err} is still reported for each individual pig and intervention, to rationalise times of high tracking error.

Finally, the strength with which P_{ex} estimates the shape of the measured flow waveform (Q_{ao}), is assessed using linear regression and the coefficient of determination, r^2. In other words, the validity of Equation 4.5 is assessed. Additionally, comparing r^2 of the control stage to the other stages, also allows Section 11.2.4's constant $Z_{c,w}$ assumption (Equation 11.1) to be checked.

11.3 Results

Figure 11.2 shows each pig's measured pressure (P_{fem}), flow (Q_{ao}) and stroke volume (SV_{mea}), as well as modelled reservoir pressure (P_{res}), estimated flow (Q_{est}) and stroke volume (SV_{est}). The final five pressure and flow waveforms of each stage are shown for clarity, but all 30 beats measured and estimated SV are shown. Hence, the different time axis limits for the pressure/flow rows verses the stroke volume row.

Bland-Altman analysis compares beat-wise SV_{est} to SV_{mea}. Figure 11.3 shows the error (SV_{err}) in millilitres (ml) and percentage error respectively. Figure 11.3b does not include the *end endo* stage of Pig S4, due to its measured SV being very low, as seen in Figure 11.3a. This low SV_{mea} causes the percentage error to be very high, despite comparatively low error in millilitres, as discussed further in Section 11.4.2. Mean SV_{err} for each pig and stage is also shown in Table 11.1.

Table 11.2 quantifies ΔSV_{err} for each pig, expressed in millilitres as per Equation 11.3 and percentage as per Equation 11.4. This table was then used to assess the overall ΔSV_{err} across the cohort of pigs in the CDF's of Figure 11.4.

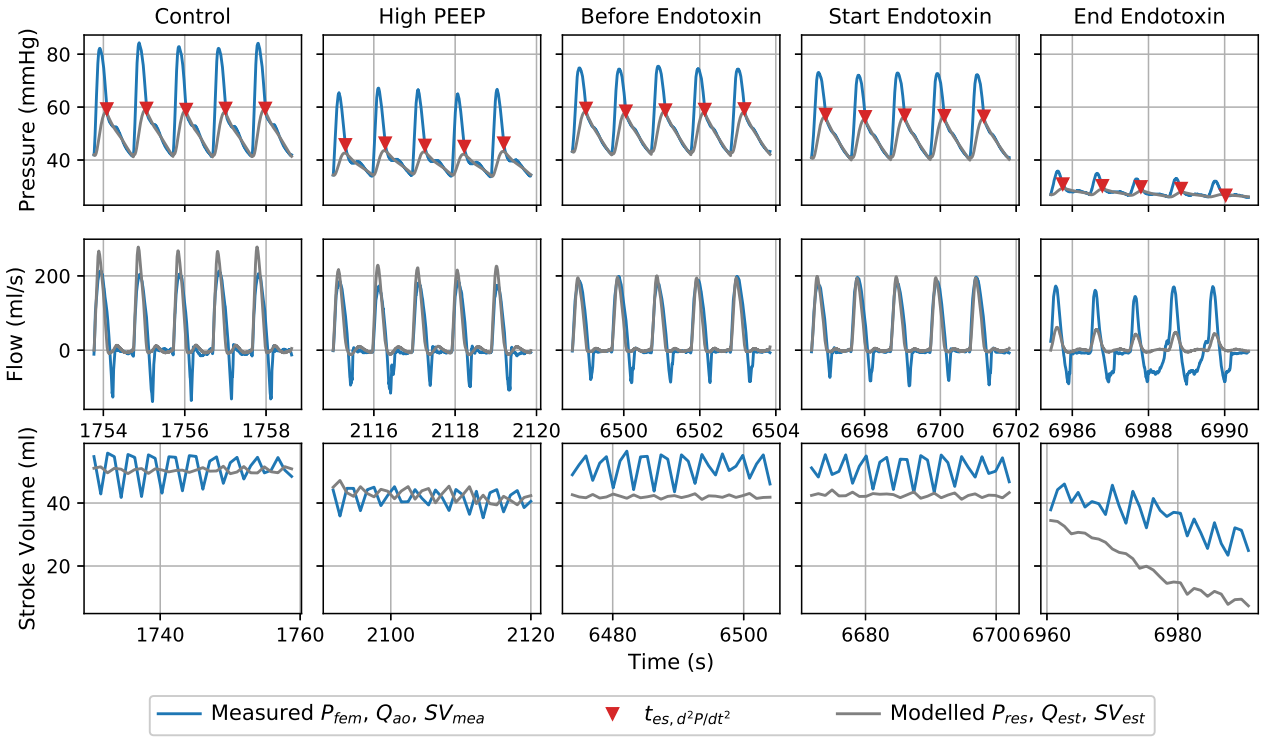

(a) Pig S1 pressure, flow and stroke volume waveforms for each stage.

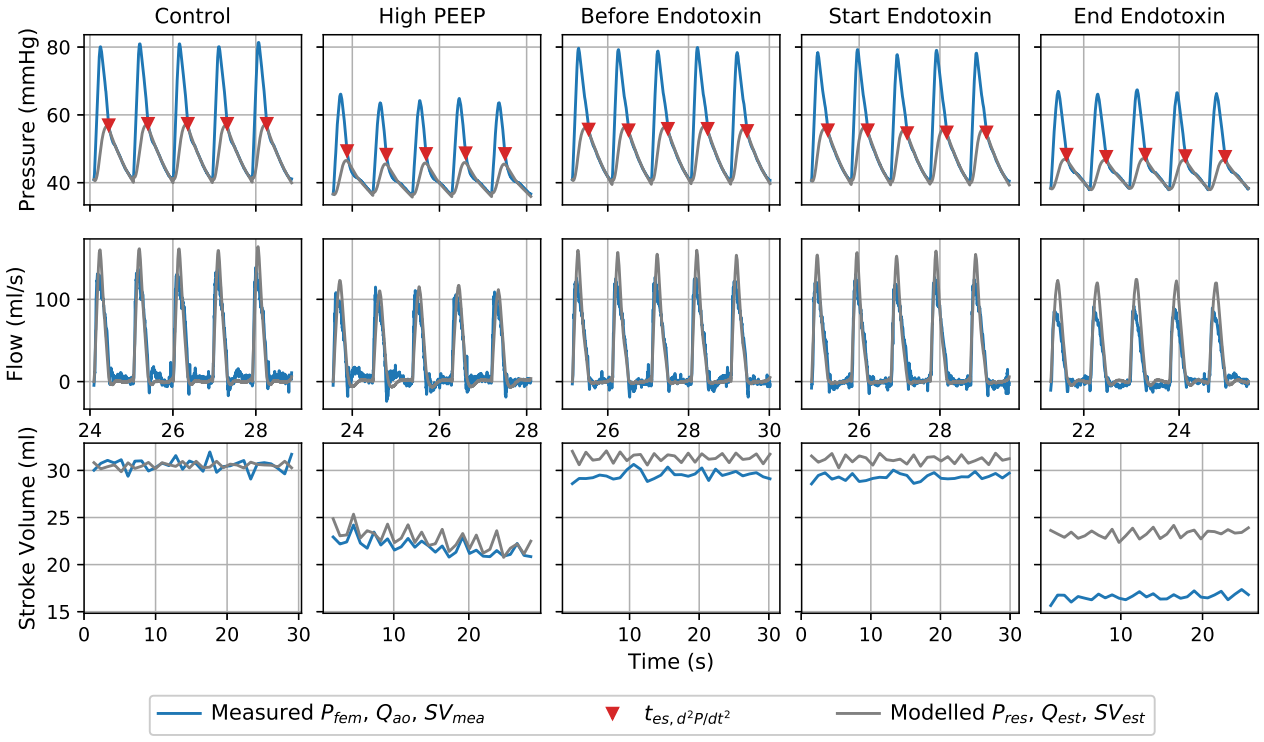

(b) Pig S2 pressure, flow and stroke volume waveforms for each stage.

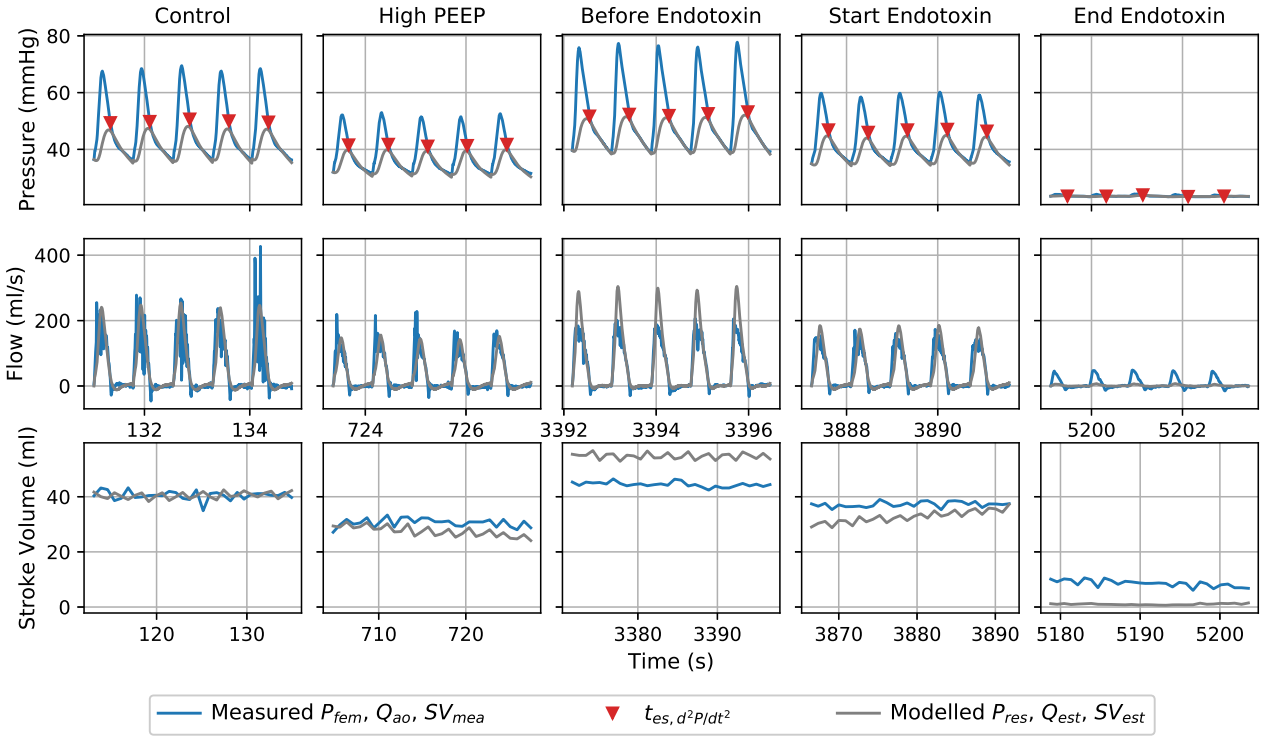

(c) Pig S4 pressure, flow and stroke volume waveforms for each stage.

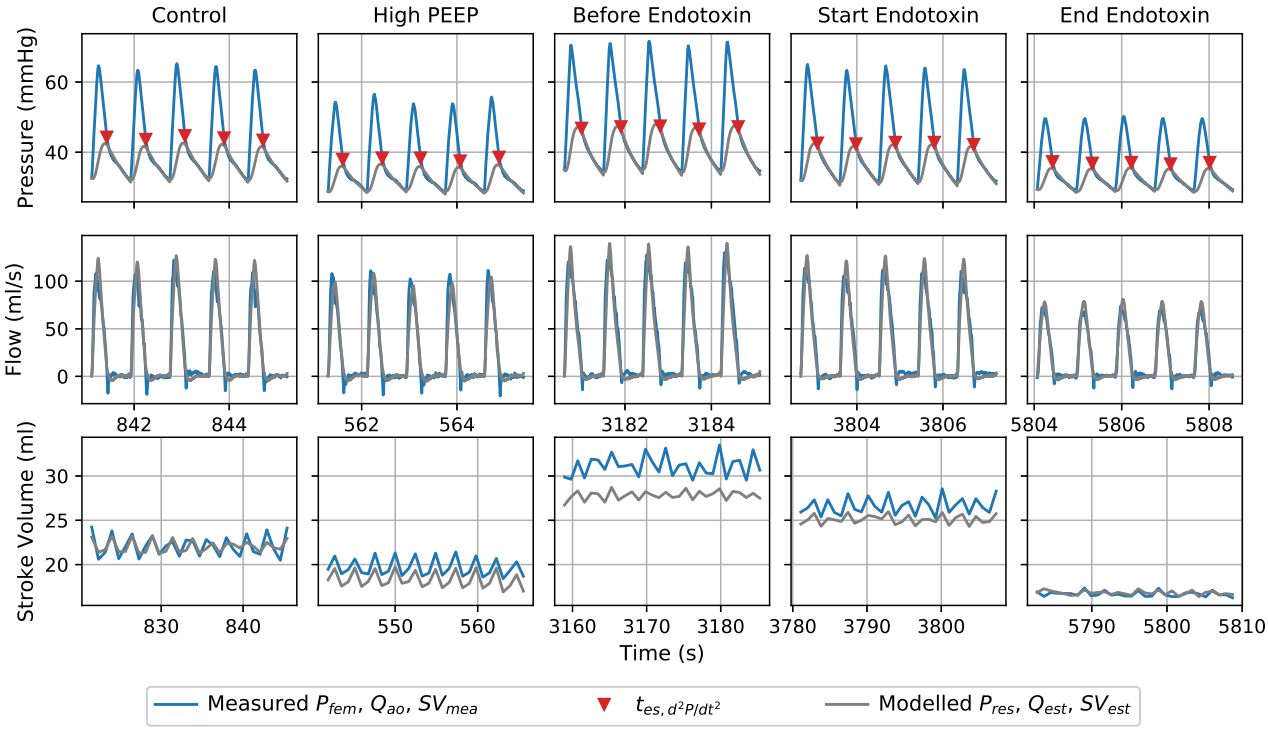

(d) Pig S5 pressure, flow and stroke volume waveforms for each stage.

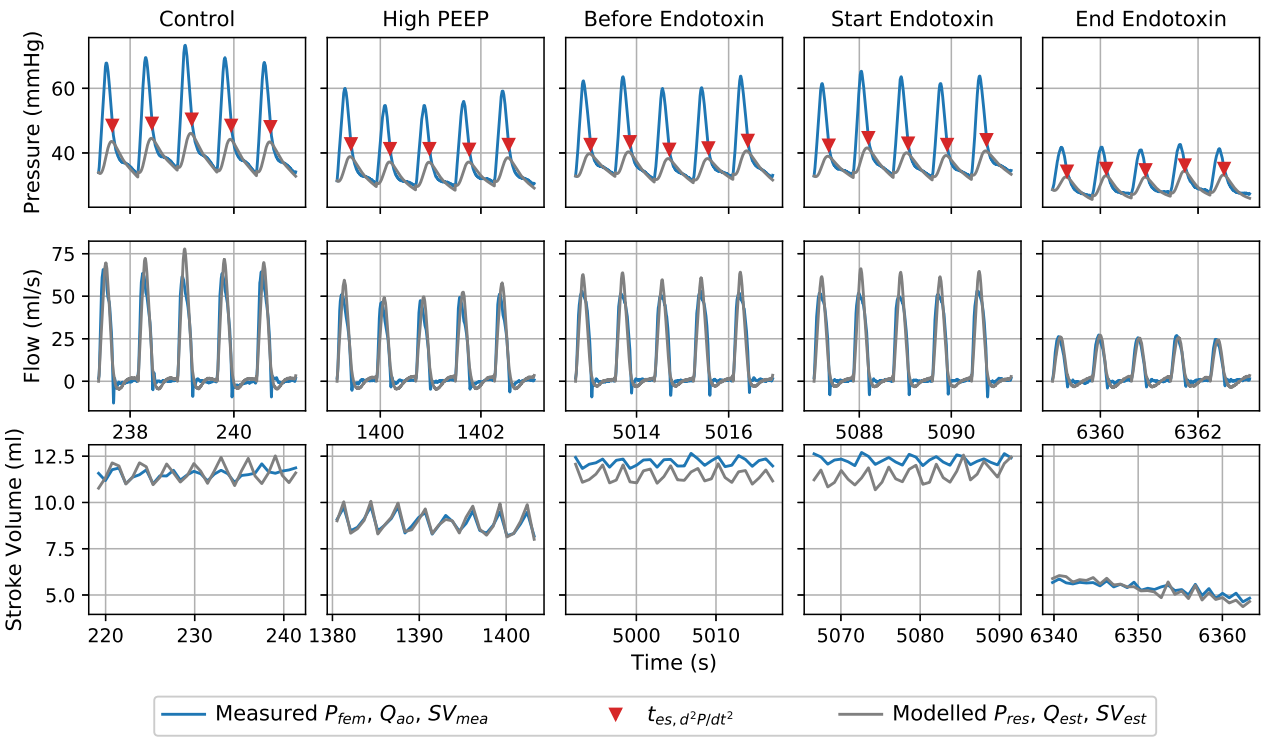

(e) Pig S6 pressure, flow and stroke volume waveforms for each stage.

Figure 11.2: Each Pig's pressure, flow and stroke volume waveforms for each stage. The first two rows show the last five beats of the stage to enhance clarity. The final row shows stroke volume for all 30 beats of each stage.

Lastly, the assumption that $Z_{c,w}$ remains constant and Equation 4.5 holds, is assessed using a simple linear regression and coefficient of determination (r^2). The r^2 in this analysis, represents the percentage of variation in P_{ex} reflected in the variation in Q_{ao}. Figure 11.5 shows the analysis for each pig, notably with some hysteresis behaviour. Thus, Section 11.4.4, along with Figure 11.6, consider the hysteresis behaviour in further detail.

Table 11.1: Pigs stroke volume estimation percentage error (%): presented as mean (± standard deviation).

Pig	Control	High PEEP	Before endo	Start endo	End endo
S1	-0.2 (± 10.9)	3.7 (± 11.7)	-17.5 (± 7.6)	-15.7 (± 8.0)	-46.5 (± 17.7)
S2	-0.1 (± 2.8)	3.9 (± 2.9)	6.3 (± 2.2)	6.4 (± 2.2)	40.2 (± 3.8)
S4	0.2 (± 6.1)	-10.0 (± 5.8)	23.3 (± 3.9)	-12.1 (± 5.4)	-87.5 (± 3.2)
S5	-0.1 (± 3.3)	-7.0 (± 1.2)	-10.6 (± 2.4)	-5.7 (± 2.0)	0.8 (± 1.6)
S6	0.5 (± 3.8)	0.5 (± 2.0)	-6.0 (± 1.9)	-6.4 (± 3.1)	-0.9 (± 4.0)

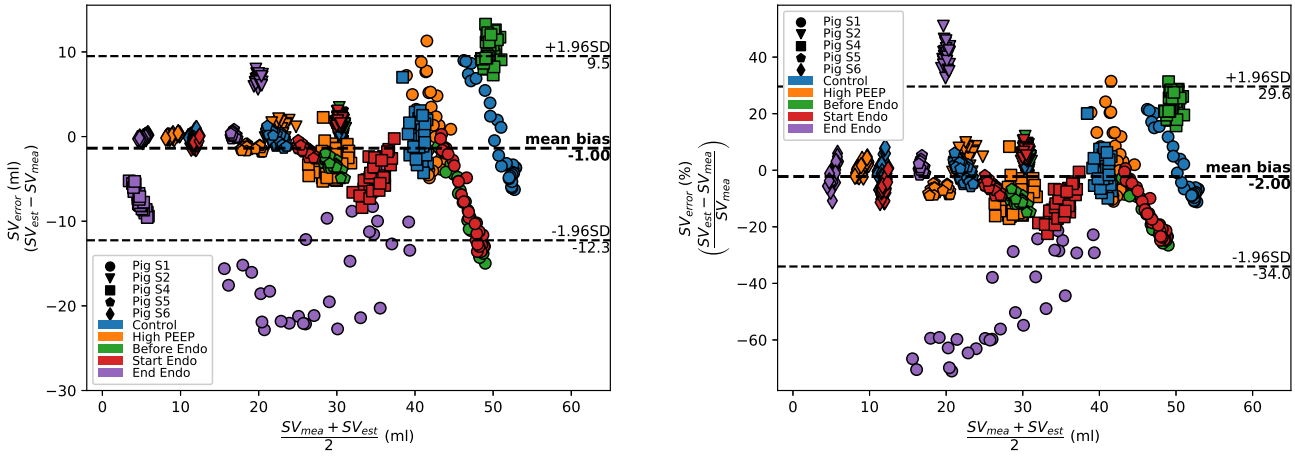

(a) SV error in millilitres.

(b) SV error as a percentage.

Figure 11.3: Bland Altman analysis. The mean bias between the measured and estimated SV are shown, as well as the limits of agreement ($\pm$ 1.96 standard deviations) to indicate the expected variation.

Table 11.2: Stroke volume tracking error between interventions (ΔSV_{err}), expressed in millilitres and (absolute percentage) for each pig intervention.

Pig	Control → High PEEP	High PEEP → Before endo	Before endo → Start endo	Start endo → End endo
S1	1.8 (4.3%)	-10.5 (20.4%)	1.0 (2.0%)	-7.9 (22.0%)
S2	0.9 (4.1%)	1.0 (3.4%)	0.02 (0.06%)	4.8 (28.9%)
S4	-3.1 (10.1%)	13.4 (30.2%)	-14.8 (39.7%)	-3.1 (36.3%)
S5	-1.3 (6.8%)	-1.9 (6.2%)	1.8 (6.7%)	1.7 (9.9%)
S6	0.01 (0.1%)	-0.8 (6.3%)	-0.1 (0.6%)	0.7 (13.7%)

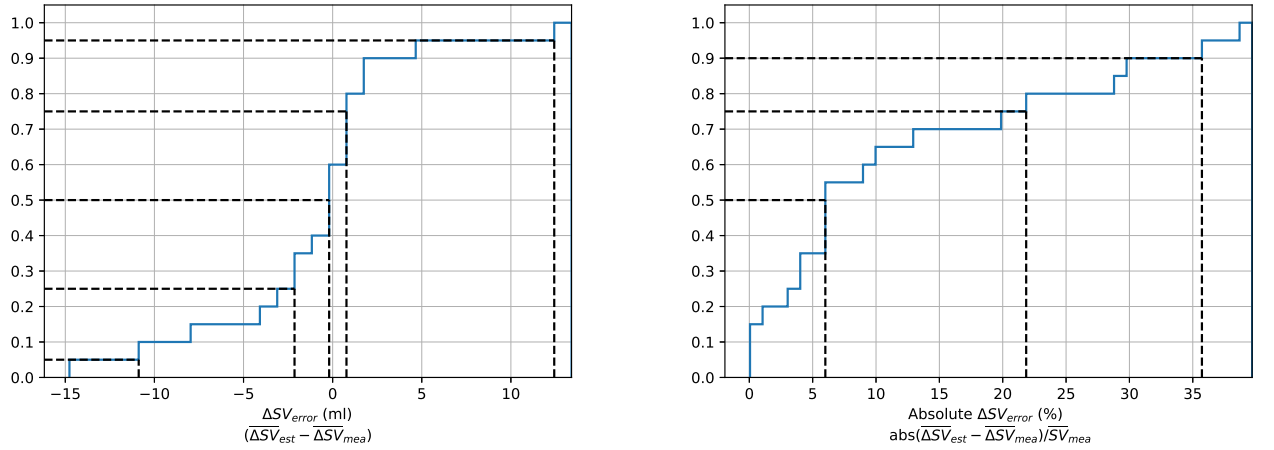

(a) ΔSV_{err} in millilitres.

(b) Absolute ΔSV_{err} as a percentage of the mean measured SV.

Figure 11.4: Cumulative distribution function for the error in the model estimated changes in SV (ΔSV_{err}). Percentage error is relative to the mean measured SV of a particular stage.

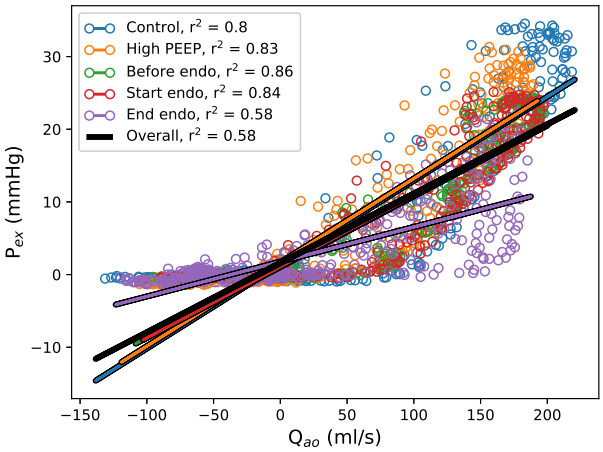

(a) Pig S1

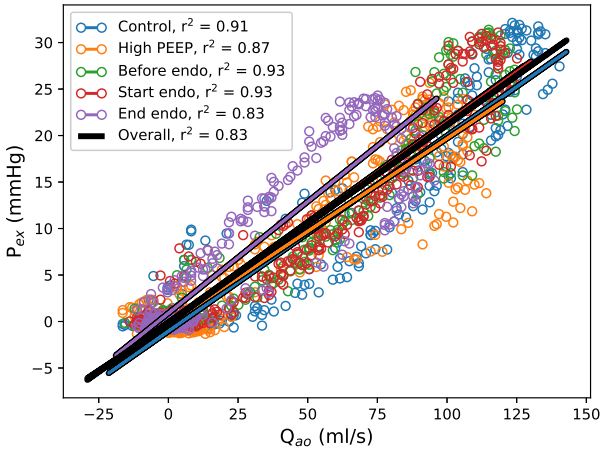

(b) Pig S2

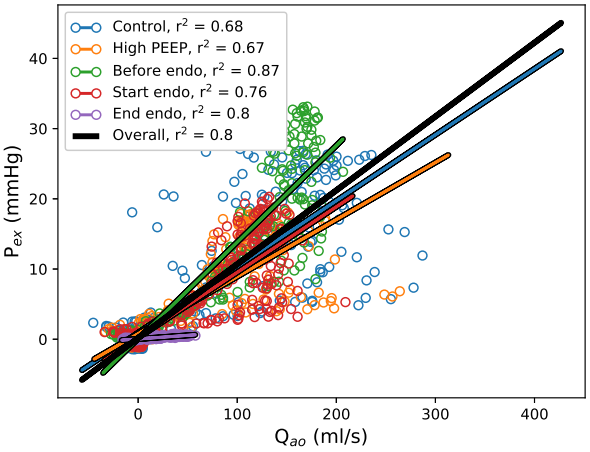

(c) Pig S4

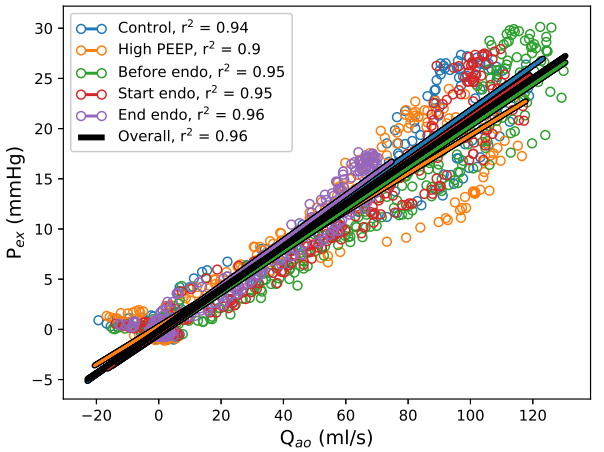

(d) Pig S5

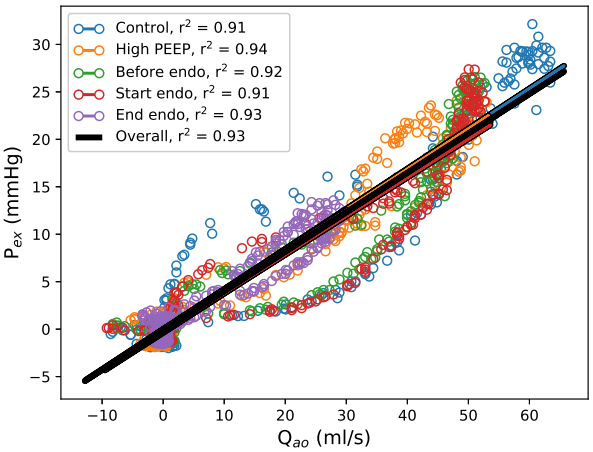

(e) Pig S6

Figure 11.5: Linear regression analysis on excess pressure and measured flow for each pig. Note, the gradient of each linear fit represents the $Z_{c,w}$, that in conjunction with modelled P_{ex}, best describes the measured flow (Q_{ao}) according to Equation 4.5.

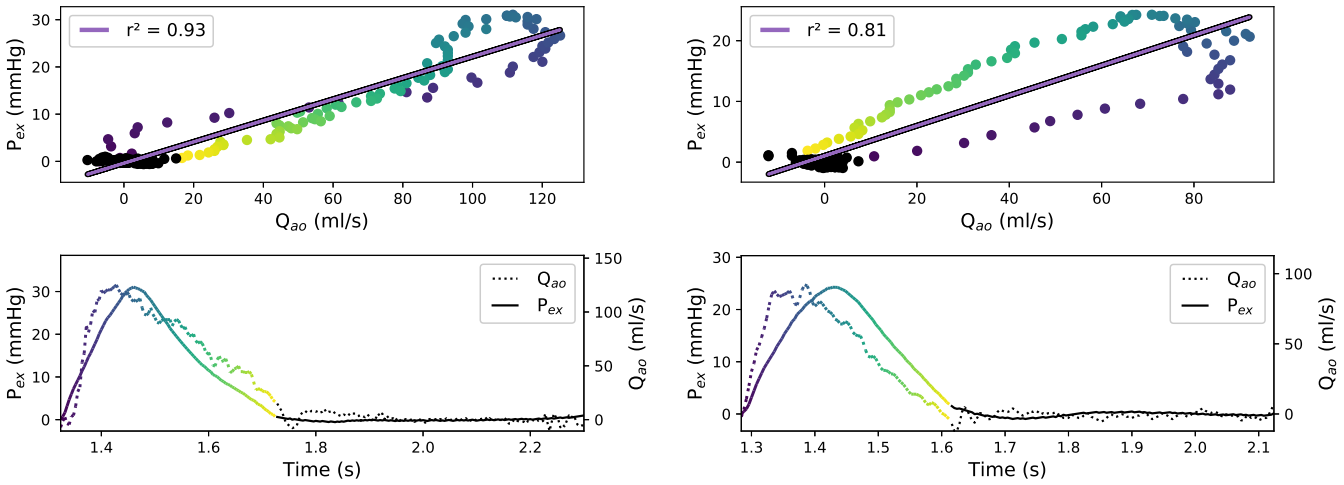

(a) Start endo stage beat.

(b) End endo stage beat.

Figure 11.6: Hysteresis example beats using Pig S2. The colour-time relationship is shown in the lower (waveform) panels of each subfigure.

11.4 Discussion

11.4.1 Response to Interventions

With the exception of the fluids admission, Figure 11.2 shows the desired variation in SV_{mea}, due to the interventions discussed in Section 11.2.2, was achieved across all pigs and stages, particularly during both the high PEEP and end endotoxin stages. Fluids administration, which finished just prior to the before endo stage, per Figure 5.2, appeared to only impact S5, with an $\approx$ 40% increase in SV_{mea} relative to its control stage value. However, this lack of *fluid responsiveness* is also common in a critical care environment and therefore not entirely surprising (Michard and Teboul, 2002).

Sections 5.3.2 and 11.2.3 stated Pigs S2 and S5 were more resilient to the endotoxin infusion than the other pigs, remaining stable throughout the 30 min. This resiliance is now illustrated in Figures 11.2b and 11.2d. In contrast Pigs S1, S4 and S6 succumbed to the effect of the endotoxin infusion faster, with marked falls in P_{fem} and SV_{mea}, to inadequate levels, as seen in Figures 11.2a, 11.2c and 11.2e, respectively. As a result, the experimental protocol provided a suitably severe range of hemodynamic states to test the model.

11.4.2 Absolute Stroke Volume Estimation Performance

The Bland-Altman plots in Figure 11.3 differ in the exclusion of Pig S4's end endo stage from the analysis on the percentage error. During this stage, seen in Figure 11.2c, P_{fem} fell to a mean value of 24 mmHg with a pulse pressure of only a few millimetres of mercury. The resulting negligible P_{ex}, caused the model to estimate *SV*'s of between 0–2 ml. The flow probe also measured a small mean *SV* of 8.6 ml, indicating the approaching death of Pig S4. Despite the mean error of the stage being only −7.5 ml, the percentage error is -87.5%, as seen in Table 11.1. Thus, when dealing with very small measured values tending to zero, the percentage error can over represent what is actually acceptable absolute error, previously discussed in Section 6.3.3. Hence, the Pig S4 end endo stage is excluded from Fig 11.3b.

As first discussed in Section 3.5, Critchley and Critchley (1999) stated new cardiac output (*CO*) techniques should have $\pm$30% limits of agreement when compared to an existing technique (Critchley and Critchley, 1999). The limits of agreement for the data shown in Figure 11.3b, are +29.6% and -34.0% respectively, thus adjusting for the -2% bias, these limits represent $\pm$32%. Thus, the method falls just outside the criteria. Importantly however, Protocol S end endo, causing the errors $>$30%, represents rapid hemodynamic decline from a health state, in excess of what is expected in a typical clinical environment. Moreover, with the exception of Pigs' S1, S2 and S4 end endo stages, all other pigs and stages had mean beat-to-beat error $<$24%, according to Table 11.1. Thus, while this result does not meet the $\pm$30% criteria of Critchley and Critchley (1999), the model performance is promising given the severity of the interventions tested. Furthermore, by using non-parameteric median and the 5th to 95th percentiles of this non-normally distributed data, 90% of the data falls within -24.2% and +27.9%. The beat-to-beat *SV* estimates could also be filtered/averaged the to reduce the random error shown in Fig 11.3.

The error in Figure 11.3 is similar to those listed in Kamoi et al. (2017). However, as discussed in Section 6.3.3, it appears Kamoi et al. (2017) calculated the limits of agreement

on a per pig basis, biasing narrower limits relative to a cohort based assessment. Thus, the similarly valued limits in this analysis, but for the whole cohort of pigs, represents measurable improvement over the Kamoi model implementation.

Pig S1's end endotoxin stage contributes the most towards the SV error in Figure 11.3b. Figure 11.2a shows while there is a significant offset between SV_{mea} and SV_{est} during this stage, the model accurately predicts a significant decrease. So although the model failed to accurately track the absolute value of SV_{mea} during this stage, the ability to capture the dramatic fall is clinically useful. Thus, ignoring this stage, the traditional limits of agreement improve to $\pm$25% (results not shown).

Finally, as stated in Section 11.2.4, this implementation of a three-element model treated P_{cvp} as time variable, using the data measured during the experiment. However, the aforementioned section, along with Section 4.3.2, stated similar model performance can be achieved assuming a constant P_{cvp}. Assuming P_{cvp} = 8.7 mmHg (Hannon et al., 1990), all else unchanged, the Bland-Altman mean bias remains at -2% and the limits of agreement change negligibly from the values in Figure 11.3b, to +30.0% and -33.0% (results not shown).

11.4.3 Stroke Volume Tracking Performance

In a clinical situation, accurately estimating the change in SV, following either a clinical or patient based change in hemodynamic state, is of value, independent of the absolute accuracy in SV_{est} (Marik, 2013). Thus, ΔSV_{err} is quantified using Equations 11.3 and 11.4, and displayed using CDF's shown in Figure 11.4. Figure 11.4a shows a narrow interquartile range of −2 to 1 ml. Fig 11.4b shows 85% of ΔSV_{err} fell below 30%. Table 11.2 shows Pig S4 is responsible for $\Delta SV_{err} > 30\%$. The 36.3% error in $\Delta SV_{err,\ start\ endo \rightarrow end\ endo}$ is largely as a result of $\overline{SV}_{mea,\ end\ endo}$ being very small, at 8.6 ml, with the ΔSV_{err} in millilitres of only −3.1 ml. Thus, despite the 36.3% error, the method did in fact accurately estimate the dramatic fall in SV to a very low level as the endotoxin led to eventual circulatory failure.

The high PEEP to before endo, and before endo to start endo transitions also had ΔSV_{err} of more than 30%. While this magnitude is higher than desirable, Figure 11.2c shows SV_{est} throughout the experimental protocol still provides the correct directions of change, with reasonable absolute SV estimation, and is thus still of clinical value.

11.4.4 Linear Relationship between P_{ex} and Q_{ao}

Figure 4.2a and Equation 4.5 result in the flow into the aorta (Q_{in}) being modelled as linearly dependent on P_{ex} and $Z_{c,w}$. The coefficients of determination seen in Figure 11.5, suggest strong linear relation within each stage between P_{ex} and Q_{ao}. This outcome is a significant improvement on the issues highlighted in Chapter 6, where the Kamoi model had similar SV monitoring, but could estimate unphysiological flow waveform shapes.

However, Figure 11.5 still contains some interesting nonlinear behaviour worth explaining. At end-systole, as both P_{ex} and Q_{ao} should be tending to zero, Q_{ao} often momentarily measures negatively, leading to its dicrotic notch behaviour discussed in Section 5.4.4 and seen very clearly in Figure 5.9. This behaviour is also evident in Figures 11.6 and 11.2 of this chapter's analysis. Because the excess pressure is derived from dicrotic notch-less P_{fem}, the magnitude of negative values at end-systole in P_{ex}, and thus Q_{est}, are negligible.

The linear regression analysis also tests whether characteristic impedance, $Z_{c,w}$, is relatively constant for each pig throughout the experiment, as assumed in Section 11.2.4. Unlike parameter products $Z_{c,w}C$ and RC, $Z_{c,w}$ was calibrated during the control stage, per Equation 11.1. Section 11.2.4 hypothesised variation in flow after the baseline control stage, would be accounted for by changes in P_{ex}, which, as exhaustively shown throughout the thesis, relies on correct identification of $Z_{c,w}C$ and RC. If characteristic impedance were indeed constant for a pig, the lines of best fit for stages with hemodynamic modifications, would share the control stage gradient. Thus, the relatively consistent gradients associated with Pigs S2, S5 and S6 (Figures 11.5b, 11.5d and 11.5e, respectively), strongly support the constant $Z_{c,w}$ approach. However, Pigs S1 and S4, in Figures 11.5a and 11.5c, showed

variability in the characteristic impedance (gradient) that best fit each stage. Unsurprisingly, Table 11.1 shows Pigs S1 and S4 had higher percentage error (SV_{err}) as a result. Pig S2 still shows the impact of invalidly assuming a constant $Z_{c,w}$, where Fig 11.5b shows the end endotoxin stage best fit gradient, and thus $Z_{c,w}$ value, has deviated from the calibrated $Z_{c,w}$ from control and Equation 11.1. As a result, Table 11.1 and Figure 11.2b show end endotoxin SV being overestimated.

Another interesting feature is the hysteresis behaviour. Figures 11.6a and 11.6b illustrate this phenomena using single beats from Pig S2's start and end endotoxin stages, respectively. Colour mapping most of the systolic points on the scatter plot enables them to be located on the waveform. From this plot, it is clear hysteresis is caused by the modifying of the femoral pressure and thus excess pressure shape, relative to the flow measurement further upstream. These effects of changing arterial properties and wave behaviour, on measured waveforms, was covered in Sections 2.2.2 and 2.5.3. Since P_{ex} defines the shape of Q_{est} via Equation 4.5, the difference in P_{ex} shape and Q_{ao} also contribute to the difference in measured and estimated SV.

With the region of nonlinear behaviour at end-systole, due to the dicrotic notch in Q_{ao}, and the hysteresis behaviour accounted for, it is clear strong linearity exists. This result is in line with the linearity reported by Wang et al. (2003) and discussed in Section 4.5 (Wang et al., 2003; Tyberg et al., 2014). However, the difference is, Wang et al. (2003) used Q_{ao} to derive P_{res} via Equation 4.22 and subsequently P_{ex} via Equation 4.23. In contrast and importantly, this study modelled the same behaviour using only clinically available P_{fem} measures[1].

11.4.5 Implementation Limitations

One of the constraints in development of the method, was it needed to be clinically applicable and not additionally invasive, in line with the thesis goals in Section 1.4. The result is

[1]The common clinical measure P_{cvp} was used, but as per Section 11.4.2, treating this as a constant rather than a measured variable, has negligible impact on model performance.

a relatively simple and identifiable model (Chase et al., 2018) capable of accurately tracking flow and *SV*. However, as discussed in Section 4.3.3, the simplicity of three-element windkessel based models, means the parameters do not necessarily represent physiological values and should only be viewed from within the model framework (Westerhof et al., 2009; Westerhof and Westerhof, 2017; Segers et al., 2015). Thus, while it is possible for values to be similar to physiology, it is not guaranteed and should not be assumed, particularly when applied to unstable patient dynamics, as seen in the end endo stages here.

On the topic of unstable patients, this analysis calibrated the model during a period of stable hemodynamics, and required an independent *SV* measurement to do so. While Section 11.4.4 showed each pig's calibrated $Z_{c,w}$ value remained relatively constant, despite the hemodynamic interventions, trying to calibrate the value during unstable behaviour in a clinical environment may prove difficult. This issue may present a significant limitation, since as per Section 1.3.1, it is unstable patients who stand to benefit most from continuous monitoring.

In this study, the femoral pressure was used as the measured pressure input to the model (P_{mea}). It would be clinically even more desirable to use a peripheral pressure measurement. However, peripheral arterial signals are more prone to reflected waves causing turning points that appear similar to a dicrotic notch, but do not correspond to end-systole. These notches may cause two issues, both previously discussed.

First, reflected waves in a peripheral arterial pressure waveform, may make end-systole detection more difficult, since the turning points due to reflected waves could lead to *false positive* $t_{es,d^2P/dt^2}$. This issue was alluded to in Section 10.4.3. While Chapter 9.1 focused on the dicrotic notch, more generally, it illustrated the importance of accurate and precise t_{es} identification for correctly estimating the the proportions of P_{res} and P_{ex} that make up P_{mea} according to Equation 4.3.

Second, as discussed in Sections 4.3.1, 4.3.2, 4.3.3 and 9.3.3 the three-element windkessel model cannot describe wave propagation phenomena. Again, although Chapter 9 focused

on the dicrotic notch, more generally in Sections 9.6 and 9.7, it illustrated the impact of reflected wave behaviour on PCA based windkessel parameter identification. Specifically, when the measured diastolic pressure (P_{mea}(t $>t_{es}$)) varied from the model expected exponential decay, the variation led to non-zero P_{ex} during diastole and subsequent unphysiological aortic flow profile prediction during diastole. The limitations caused by reflected waves were mitigated specifically by using a more distal waveform like P_{fem}, where Section 10.1 outlined the traits that made it desirable for use with the model.

Another possible issue with a peripheral arterial pressure waveform, would be relative changes in how the ejected SV distributes within the arterial tree. In smaller, more peripheral arteries, the distribution of blood may vary more dramatically in response to patient state, than the larger central arteries. This behaviour could contribute to model SV_{err}.

Finally, the study tested only a few hemodynamic interventions, namely the recruitment manoeuvre, fluid admission (before endo stage) and endotoxin. While the assumption of a constant characteristic impedance ($Z_{c,w}$) proved sufficient under these conditions, it may not necessarily hold in other hemodynamic events. Therefore, there is room for further investigation and potential improvement by introducing a more dynamic calibration method, rather than fixing a parameter constant (Kamoi et al., 2017).

11.5 Summary

This chapter implemented the three-element windkessel model in a non-additionally invasive manner, increasing the utility of already available clinical measures. Specifically, the model used a femoral artery pressure waveform to derive parameters via pulse contour analysis (PCA), for estimating physiologically accurate flow waveforms and subsequent SV.

Thus, this implementation overcame the limitations identified in other three-element windkessel based models, covered in this thesis. First, parameters were identified in a patient

specific manner, where P_{res}/P_{ex} were calculated per beat, always reflecting current patient state, as portrayed via P_{fem}. Second, and more importantly, P_{ex} described a physiologically accurate flow profile, in line with model theory. In contrast, other implementations have focused mainly on *SV*, where parameters may have been identified in a beat-to-beat manner, but subsequently relied on the calibrating $Z_{c,w}$ to correct for any poor model implementation causing unphysiological flow, per Section 9.2.2.

While the *correcting quality* of the $Z_{c,w}$ calibration represents useful redundancy, the author would argue it should not be the main mechanism by which model implementation is *forced* to succeed. The aim should still be to implement the model in a manner that reflects the theory and assumptions that went into its development. Afterall, a model's theory is only as good as its implementation. In the case of the three-element windkessel, its theory was outlined in Section 4.3.2.

Thus, in this thesis, one of the main avenues of improved implementation was the end-systole detection. As hypothesised in Section 6.3.2, accurate end-systole detection was shown to improve calculation of P_{res}/P_{ex} according to the model expectations, particularly Equations 4.5 and 4.12, for P_{ao} in Chapter 9. Subsequently, in this chapter, robust, accurate and precise end-systole detection has also improved P_{res}/P_{ex} calculation from the more clinically applicable P_{fem}. Thus, although it is difficult to compare results of different model implementations across different study protocols, it appears adhering to the foundational windkessel model assumptions has resulted in similar, if not better performance, than more complex implementations.

The overall *SV* error had a mean bias of -2% and 90% of errors fell within -24.2% and +27.9%. Moreover, 4 of the 5 pigs error in change in *SV*, following interventions, was $<$ 30%. However, there are still two shortcomings associated with this analysis. First, the limits of agreement (95% of errors) were greater than the $\pm$30% acceptable criteria outlined by Critchley and Critchley (1999). Specifically, adjusting for the bias, the limits of agreement in Figure 11.3 were $\pm$32%. Failing this criteria was partly due to the analysis

including near death cardiovascular behaviour. Thus, the ability to achieve this criteria is heavily dependent on the severity of the hemodynamic changes within the experimental data. If the model were tested in an observational clinical trial and retrospectively validated, the expectation is the model errors would be much lower on the less severe hemodynamic changes. However, a more typical, less *worst case* data set has not yet been analysed.

The other issue still to be resolved is the handling of the parameter $Z_{c,w}$. In this analysis, the model implementation still required calibration via a *SV* measurement, similar to many of the commercial PCA devices covered in Section 3.5. The calibration in this analysis scaled the excess pressure (P_{ex}) to an estimated flow (Q_{est}) of the same magnitude as the measured flow (Q_{ao}). The hypothesis was that $Z_{c,w}$ would remain constant throughout the experiment and changes in hemodynamic state would simply be reflected in the proportions of P_{res} and P_{ex} that described P_{fem}, according to Equation 4.3. The results showed the hypothesis of a constant $Z_{c,w}$ was largely correct, with 4 of the 5 pigs having overall coefficients of determination $r^2 \geq 0.8$ for variation in P_{ex} reflected in Q_{ao}, supportive evidence for the validity of Equation 4.5. This result represents significant improvement over other commercial PCA methods covered in Section 3.5, which required re-calibration following significant hemodynamic changes. However, there were times, particular during the most severe hemodynamic changes, where an updated $Z_{c,w}$ value would have improved model performance. Rather than require re-calibration, it may be possible to update the $Z_{c,w}$ parameter in a dynamic manner, as attempted in Kamoi et al. (2017) covered in Section 6.2.1.

Regardless, the overall thesis goals of Section 1.4 have been achieved. The implemented model no longer relies on *PWV*. The model now predicts accurate flow profiles. Finally, the windkessel limitations regarding dicrotic notches and reflected waves suggest the femoral arterial pressure, or similar waveform, is most appropriate for the measured pressure input to the model.

CHAPTER 12

Re-accessing the use of Pulse Wave Velocity in the Model

12.1 Introduction

Chapter 11 used a three-element windkessel model to estimate physiologically accurate flow profiles and subsequently estimate stroke volume (SV). Considering the severity of the interventions, causing circulatory failure, the method showed a reasonable level of accuracy. The strengths of the implementation lay in the novel end-systole detection methods ($t_{es,shear}$ and $t_{es,d^2P/dt^2}$) and subsequent insight they provided in regard to parameter identification. Ultimately, $t_{es,d^2P/dt^2}$, end-systole detection via an adaptive weighted second derivative algorithm, enabled windkessel model parameters to be identified via pulse contour analysis (PCA) in the dicrotic notch-less femoral pressure (P_{fem}). Thus, the clinically applicable P_{fem} signal became a robust choice for estimating physiological flow profiles and SV using the three-element windkessel model, achieving the goals of Section 1.4.

The implementation in Chapter 11 differed from the Kamoi model in Chapter 6, returning to the *standard* three-element windkessel model described in Section 4.3.2. Essentially,

Chapter 11 improved performance by simply ensuring the implementation reflected the foundational/fundamental windkessel model theory, before introducing further complexity, like pulse wave velocity (*PWV*). However, now the foundations of the model have been well tested and are better understood, the potential of *PWV* to improve model performance can be better assessed. Thus, re-introducing *PWV* into the model implementation is the focus of this chapter.

High accuracy and precision in the end-systole detection using $t_{es,d^2P/dt^2}$, led to robust identification of the resevoir (P_{res}) and excess (P_{ex}) windkessel model pressure components in Chapter 11. Thus, contrary to Kamoi et al. (2017), Chapter 11's results suggest it is unnecessary to use *PWV* to estimate P_{res} via Equation 6.2. Doing so could possibly be detrimental, since ΔPWV, post L_c calibration, could make satisfying the measured pressure (P_{mea}) and P_{res} relationship in Equation 4.12 more difficult. Thus, it seems most appropriate to simply identify $Z_{c,w}C$ and RC via PCA from P_{mea}.

However, one of the limitations in Sections 11.4.4 and 11.4.5, was the assumption $Z_{c,w}$ remained constant throughout the experiment. While this assumption was generally true for most pigs and interventions in the analysis, the results suggested treating $Z_{c,w}$ as a dynamic, patient specific parameter could improve performance further. Advantages and disadvantages of dynamic versus static model parameters were covered in Section 4.7. This chapter will assess two potential methods of updating $Z_{c,w}$ after calibration, both using *PWV*, and compare model performance with the constant calibrated $Z_{c,w}$ approach of Chapter 11.

12.1.1 Two Avenues for Dynamic $Z_{c,w}$ Parameter Identification

Section 2.5.2 showed how (general) characteristic impedance (Z_c) is related to *PWV* in the water hammer equation (Equation 2.7). Modified water hammer equations were used by both Wesseling et al. (1993) (Section 4.4.1) and Kamoi et al. (2017) (Section 6.2.1) to identify $Z_{c,w}$. Thus, using the water hammer equation will be the first of two methods tested for

dynamically identifying/updating $Z_{c,w}$ post calibration.

The second method assumes $Z_{c,w}$ could be identified or updated from changes in the $Z_{c,w}C$ parameter, identified via PCA. In Chapter 11, $Z_{c,w}C$ and RC were calculated on a beat-to-beat basis, adapting to the each beat's waveform per Section 11.2.4, ensuring Equation 4.12 was met. The windkessel compliance, C in $Z_{c,w}C$, is a volumetric compliance as explained in Section 4.3.1 and Equation 4.8. Change (Δ) in volumetric compliance (ΔC) could also be described by ΔPWV via the Bramwell-Hill equation, per Section 2.5.1 and Equation 2.2. Thus, ΔC could subsequently be used to update $Z_{c,w}$ on a per beat basis. The exact process by which the updating of $Z_{c,w}$ occurs is elaborated on in detail in Section 12.2.4, here, only the rationale of each method was explained.

12.2 Method

12.2.1 Porcine Trial and Measurements

The data for this study uses all three protocols outlined in Section 5.2. All pigs from each protocol are used, with the exception of Pig S3, which is excluded due to data acquisition issues explained in Section 11.2.1.

The measurements available to each protocol were outlined in Table 5.1 and shows central venous pressure (P_{cvp}) was not available in Protocol D. However, calculation of P_{res} via Equation 4.11 requires P_{cvp}, but, as explained in Section 4.3.2, it can be treated as a constant. Additionally, Section 11.4.2 showed assuming a constant value of P_{cvp} = 8.7 mmHg, for the Protocol S pig analysis, made little difference to the model performance. Thus, for consistancy, in this analysis, P_{cvp} is treated a constant for all protocols, with the value of P_{cvp} = 8.7 mmHg (Hannon et al., 1990).

Chapter 11 focused on assessing the accuracy of model estimated aortic flow (Q_{est}) and left ventricular ejected stroke volume (SV_{est}), and used the aortic flow probe measurement available in Protocol S for validation. The same approach is used once more for Protocol

S pigs, where measured stroke volume (SV_{mea}) is found via Equation 5.12. However, Protocols D and V only have access to the left ventricular volume (V_{vent}), via the ventricular admittance catheter, per Table 5.1. Thus, for Protocols D and V, SV_{mea} is calculated via Equation 5.10. However, an approximation of the equivalent aortic flow can still be calculated from V_{vent} and Equation 5.11, defined $Q_{V_{vent}}$ to signify it is not the true measured aortic flow.

Finally, it is also worth noting the different data acquisition sampling rates outlined in Section 5.3. Specifically Protocol D was sampled at 1000 Hz, while Protocols S and V were sampled at 250 Hz. While Protocol D could be downsampled so the sampling rate is consistent in the analysis, the decision was made not to do so, on the basis high sampling rates lead to better resolution of changes in pulse transit time (*PTT*) and thus *PWV*, which is crucial in this analysis.

12.2.2 Hemodynamic Modification

The interventions associated with each protocol were covered in Sections 5.2.1 – 5.2.3. Since Protocol V has not been used in a prior chapters analysis, a brief summary is given here. The vena cava occlusion (VCO) associated with Pigs V1–V4 is a short term event designed to cause rapid reduction in preload and thus *SV*, according to Section 2.4.2 and Figure 2.9. Similar to the induced septic shock in Protocol S, the VCO in Protocol V represents a dramatic change in hemodynamics, more rapid than would typically be expected clinically. Thus, across all three protocols, a vast range of hemodynamic conditions can be assessed.

12.2.3 Data Selection Summary

Per the previous analyses in this thesis, the experimental data was separated into stages. The stages of each protocol were detailed in Sections 5.3.1 – 5.3.3. Specifically, 30 heart beats were extracted from each stage, making a total of 1,590 heart beats across the 14 pigs used in the analysis. As in previous chapters, the reason for using an equal number

of beats per stage is for equal representation of each pig and stage in statistical analyses. As a reminder, recall the *end endo* stage was characterised by either the end of the 30 min endotoxin infusion (Pigs S2 and S5), or being in the later stages of circulatory failure (Pigs S1, S4 and S6).

12.2.4 The Three-Elements Windkessel Model Implementation

The implementation in this chapter is identical to Chapter 11, which was covered in detail in Section 11.2.4. The exception is, unlike the single $Z_{c,w}$ identification method used in Chapter 11 ($Z_{c,cal}$ from Equation 11.1), this chapters analysis will test two *additional* methods of $Z_{c,w}$ identification, where both additional methods require beat-to-beat *PTT*. Thus, the two methods requiring continuous *PTT* monitoring are not clinically applicable, as explained in Sections 6.3.1 and 11.2.4. However, since *PTT* is available in the porcine trials via dual arterial catheterisation and the foot-to-foot method shown in Figure 2.13, it is still worth exploring whether *PTT* could improve model performance.

To re-iterate, this chapter tests a total of three $Z_{c,w}$ identification methods. Therefore, to clearly distinguish between the different $Z_{c,w}$ identification methods, three different labels will be used. First, $Z_{c,cal}$, which refers to the constant control calibration approach used in Chapter 11 (Equation 11.1). The two additional *PTT* based methods for calculating $Z_{c,w}$, are labelled $Z_{wh,cal}$ and $Z_{bh,cal}$. All three methods are detailed:

Static Control Calibration, $Z_{c,cal}$

The first method, $Z_{c,cal}$, is the static control stage calibration used in Chapter 11, covered in Section 11.2.4 and Equation 11.1. The static calibration acts as the reference method, on which the dynamic methods could improve. A reminder, Equation 11.1 also used the general windkessel characteristic impedance subscripts $Z_{c,w}$, since no other methods for calculating $Z_{c,w}$ were tested in Chapter 11. However, as explained above, to distinguish the *static control calibration based* $Z_{c,w}$ from the other two dynamic methods tested in this chapter, it is labelled $Z_{c,cal}$.

Dynamic Water hammer based $Z_{wh,cal}$

The second method will use the water hammer equation to *update* the value of $Z_{c,w}$ on a per beat basis, post calibration. In other words, $Z_{wh,cal}$ is the updating of $Z_{c,cal}$, defined:

$$Z_{wh,cal,n} = Z_{c,cal} \times \frac{Z_{wh,n}}{\overline{Z_{wh,control}}} \tag{12.1}$$

Where Z_{wh} is the Z_c found from the water hammer equation (Equation 2.7) and the subscript 'n' signifies it is calculated on a per beat basis, making $Z_{wh,cal}$ a dynamic beat-to-beat variable. $\overline{Z_{wh,control}}$ is the mean Z_{wh} value from the 30 beats of a pigs baseline control stage:

$$\overline{Z_{wh,control}} = \left(\frac{\sum_{n=1}^{30} Z_{wh,n}}{30} \right)_{control} = \left(\frac{\sum_{n=1}^{30} \frac{\rho PWV_n}{A}}{30} \right)_{control} = \left(\frac{\sum_{n=1}^{30} \frac{\rho d}{A\ PTT_n}}{30} \right)_{control} \tag{12.2}$$

The final form of the equations uses the substitution of Equation 2.6 to express $\overline{Z_{wh,control}}$ in terms of PTT. Blood density (ρ), cross-sectional area (A) and the distance over which PWV is measured (d) are treated as constants. Thus, the only variables are PWV or PTT, enabling simplification of Equation 12.1 by substituting Equation 2.7 for Z_{wh}, and Equation 12.2 for $\overline{Z_{wh,control}}$:

$$Z_{wh,cal,n} = Z_{c,cal} \times \frac{\overline{\frac{1}{PTT_n}}}{\overline{\left(\frac{1}{PTT}\right)}_{control}} \tag{12.3}$$

Where again, the subscript 'n' represents the value for a particular beat, and, importantly, the denominator is the mean value of the 30 control stage beats *reciprocal* PTT values. The remainder of this chapter refers to $Z_{wh,cal}$ as the *water hammer based $Z_{c,w}$ method*.

Dynamic Bramwell-Hill based $Z_{bh,cal}$

The final method of determining $Z_{c,w}$ uses a combination of PCA and the Bramwell-Hill equation (Equation 2.2), as alluded to in Section 12.1.1. Specifically, $Z_{c,w}C$ is identified via PCA as part of calculating P_{res} for a particular beat, pre Section 11.2.4. Bramwell-Hill provides a method of calculating volumetric compliance using PWV and Equation 2.2, enabling the separation of a beats $Z_{c,w}C$ parameter product:

$$Z_{c,w,n} = \frac{(Z_{c,w}C)_n}{C_{bh,n}} = (Z_{c,w}C)_n \times \frac{\rho PWV_n^2}{V} = (Z_{c,w}C)_n \times \frac{\rho d^2}{VPTT_n^2} \tag{12.4}$$

Where once more, the subscript ' n ' indicates the beat-wise variables and the final form of the Equation 12.4 used the substitution of Equation 2.6 to express it in terms of PTT. Furthermore, the subscript ' bh ' in C_{bh} is to indicate it is the compliance calculated via the Bramwell-Hill equation (Equation 2.2), assumed to be equivalent to the compliance C in the PCA parameter product $Z_{c,w}C$.

However, to actually calculate $Z_{c,w}$ per beat via Equation 12.4, a value for the volume would be required. As outlined in Section 4.4.1, Wesseling et al. (1993) calculated volume using aortic cross-sectional area via an empirical equation (Langewouters et al., 1984), and assumed an aortic length of 80 cm. Similarly, Sections 6.2.1 and 6.2.2 explained how Kamoi et al. (2017) calibrated cross-sectional area per Equation 6.4 and found an "*anatomical length*" using a parameter grid search. This analysis uses a different approach, not needing to justify a *particular* volume used with the three-element windkessel. Instead, Equation 12.4 is used to *update* $Z_{c,cal}$ beat-to-beat, rather than calculate $Z_{c,w}$ directly:

$$Z_{bh,cal,n} = Z_{c,cal} \times \frac{\frac{(Z_{c,w}C)_n}{C_{bh,n}}}{\left(\frac{Z_{c,w}C}{C_{bh}}\right)_{control}} = Z_{c,cal} \times \frac{\frac{(Z_{c,w}C)_n \rho d^2}{VPTT_n^2}}{\left(\frac{1}{30}\sum_{n=1}^{30}\frac{(Z_{c,w}C)_n \rho d^2}{VPTT_n^2}\right)_{control}} \tag{12.5}$$

Where, the subscripts of $Z_{bh,cal}$ indicate it is the calibrated characterisitic impedance updated via changes in PCA found $Z_{c,w}C$, but facilitated by the Bramwell-Hill Equation. Similar to the formulation of Equation 12.3, assuming ρ, d and V are constants means Equation 12.5 can be simplified to:

$$Z_{bh,cal,n} = Z_{c,cal} \times \frac{\frac{(Z_{c,w}C)_n}{PTT_n^2}}{\left(\frac{1}{30}\sum_{n=1}^{30}\frac{(Z_{c,w}C)_n}{PTT_n^2}\right)_{control}} = Z_{c,cal} \times \frac{\frac{(Z_{c,w}C)_n}{PTT_n^2}}{\left(\frac{Z_{c,w}C}{PTT^2}\right)_{control}} \tag{12.6}$$

Thus, any particular beat's $Z_{c,w}$ value can be approximated by $Z_{bh,cal}$ from Equation 12.6, provided *PTT* is monitored. The remainder of this chapter refers to $Z_{bh,cal}$ as the *PCA-Bramwell-Hill based $Z_{c,w}$ method.*

It is also worth noting the similarities and differences between the PCA-Bramwell-Hill based $Z_{c,w}$ method and the Kamoi model outlined in Section 6.2.1. Specifically, both the Kamoi model and the $Z_{bh,cal}$ method are hybrid PCA and *PTT*/*PWV* approaches to parameter identification. However, the Kamoi model used *PWV* to identify P_{res}, and Chapter 11 showed this approach added unnecessary complexity for accurate P_{res}/P_{ex} estimation, as explained in Section 12.1. Thus, this chapter's hybrid approach differs from Kamoi et al. (2017), opting to identify $Z_{c,w}$ from PCA and *PTT*.

Flow and Stroke Volume Estimation

In this analysis, each methods of calculating $Z_{c,w}$, leads to a different Q_{est} and SV_{est} per Equations 4.5 and 4.17. Specifically, each estimated flow (Q_{est}) and stroke volume (SV_{est}) share the subscript of the $Z_{c,w}$ method from which they are derived:

- $Z_{c,cal}$ estimated flow $Q_{est,c}$, stroke volume $SV_{est,c}$, and stroke volume error $SV_{err,c}$
- $Z_{wh,cal}$ estimated flow $Q_{est,wh}$, stroke volume $SV_{est,wh}$, and stroke volume error $SV_{err,wh}$

- $Z_{bh,cal}$ estimated flow $Q_{est,bh}$, stroke volume $SV_{est,bh}$, and stroke volume error $SV_{err,bh}$

Implementation Summary Flow Chart

For clarity and convenience, the process flow chart first shown in Figure 11.1 is included here, but with changed/additional boxes specific to this chapter's analysis shown in bold. Specifically $Z_{c,w}$ can be calculated as either $Z_{c,cal}$ (the same method used in Chapter 11) or via the additional step using $Z_{wh,cal}$ and $Z_{bh,cal}$.

12.2.5 Data Analysis

Bland-Altman analysis is used to assess each $Z_{c,w}$ methods ($Z_{c,cal}$, $Z_{wh,cal}$, $Z_{bh,cal}$) beat-to-beat error in SV ($SV_{err,c}$, $SV_{err,wh}$, $SV_{err,bh}$) and thus the overall agreement between each methods SV_{est} and SV_{mea}.

Since Protocols D and V do not have an aortic flow probe measurement (Q_{ao}) the linear relationship between P_{ex} and Q_{ao} is not assessed in the same way it was in Section 11.4.4 of Chapter 11. Instead, linear regression between each $Z_{c,w}$ estimation method ($Z_{c,cal}$, $Z_{wh,cal}$ and $Z_{bh,cal}$), and the *ideal* $Z_{c,w}$ ($Z_{c,ideal}$) is performed. $Z_{c,ideal}$ is not dissimilar from a calibration of $Z_{c,w}$ using SV_{mea} and P_{ex}, like Equations 6.3 and 11.1. However, unlike the control calibration, it is calculated for every beat using each beat's unique SV_{mea} and P_{ex}:

$$Z_{c,ideal} = \frac{1}{SV_{mea}} \int_0^t P_{ex}(\tau) d\tau \tag{12.7}$$

Of course $Z_{c,ideal}$ is only correct provided P_{ex} is well identified. However, Chapter 11 confirmed the implementation in Figure 12.1 does robustly identify P_{ex}. Furthermore, P_{ex} has no effect on the $Z_{c,w}$ identification methods comparison, since all methods ($Z_{c,cal}$, $Z_{wh,cal}$, $Z_{bh,cal}$ and $Z_{c,ideal}$) use the same P_{ex}.

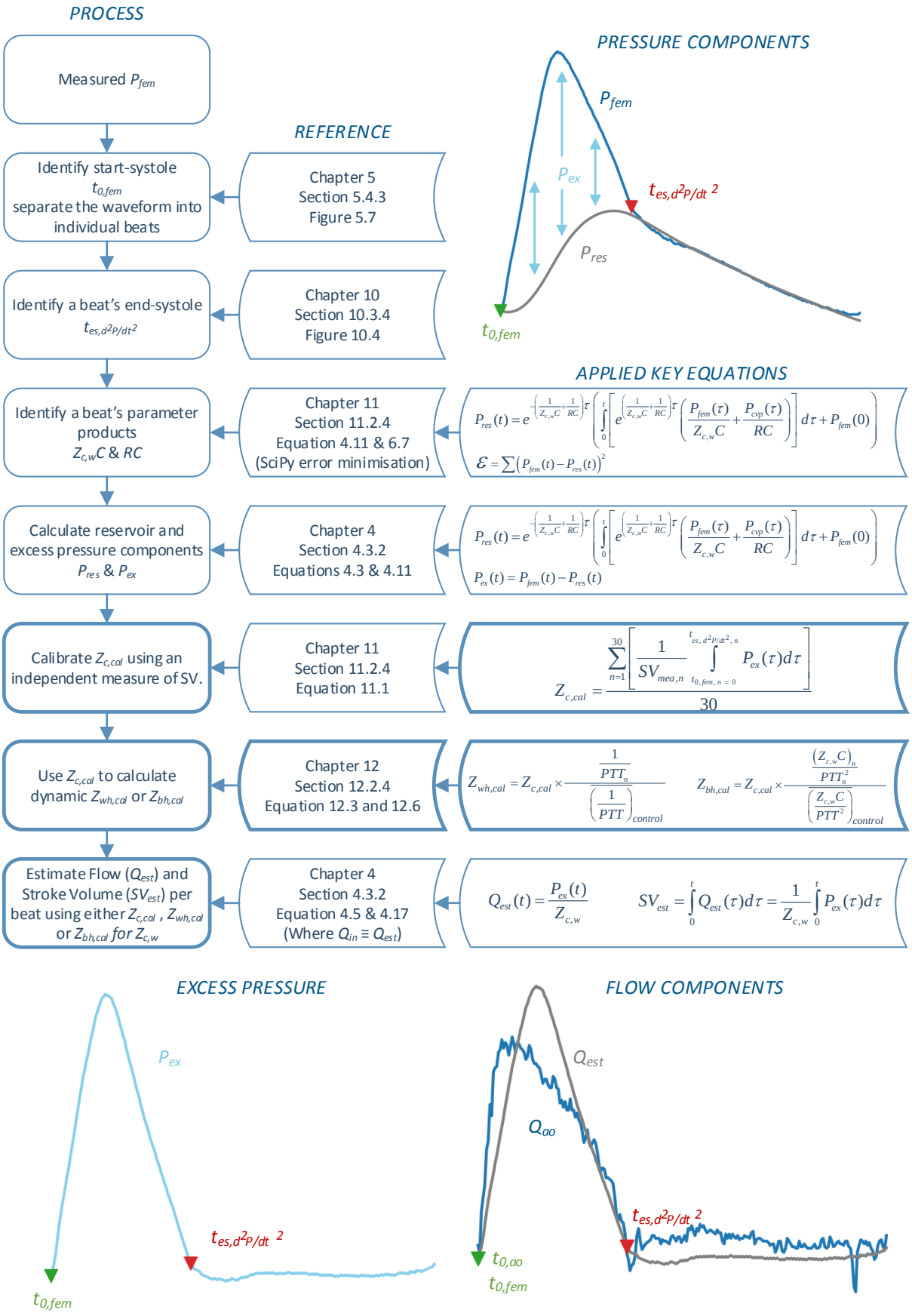

Figure 12.1: Model implementation summary, specific to this chapter. At each step, reference to the chapter, section and figure/equation is included for more detail. For convenience, the referenced equations are also shown in their form applied in this analysis. The flow chart is very similar to Figure 11.1, but includes the two additional methods methods of calculating $Z_{c,w}$ this chapter.

12.3 Results

Figures 12.2 – 12.4 show each pig's measured pressure (P_{fem}), flow (Q_{ao}), stroke volume (SV_{mea}) and reciprocal PTT, as well as modelled reservoir pressure (P_{res}), and estimated flow (Q_{est}) and stroke volume (SV_{est}) for each $Z_{c,w}$ method. The final five pressure and flow waveforms of each stage are shown for clarity, but all 30 beats measured and estimated SV are shown, and reciprocal PTT. Hence, the different time axis limits for the pressure/flow rows versus the stroke volume row.

Bland-Altman analysis in Figure 12.5 compares each $Z_{c,w}$ method ($Z_{c,cal}$, $Z_{wh,cal}$, $Z_{bh,cal}$) beat-wise SV_{est} ($SV_{est,c}$, $SV_{est,wh}$, $SV_{est,bh}$) to SV_{mea}, where the error is represented as a percentage. Since this chapter is interested in the comparison of the three $Z_{c,w}$ prediction methods, the presentation of the Bland-Altmans plots differs slightly from those shown previously in the thesis. Specifically, the Bland-Altman plots use non-parametric median bias and 5th and 95th percentiles, better reflecting the non-normal distribution of the methods errors (Motulsky, 2010).

Furthermore, the control stage is shown in Figure 12.5, but is not included in the calculation of median bias and percentiles. The quasi-steady state dynamics of the control stage means $Z_{wh,cal}$ and $Z_{bh,cal}$ do not change significantly from the $Z_{c,cal}$, according to Equation 12.3 and 12.6, respectively. Thus, including the stage in the Bland-Altman analysis would be clinically relevant, and indeed narrow the percentiles considerably. However, by not doing so, the percentiles better reflect only the periods of high hemodynamic change, for better method comparison, the focus of this study.

Finally, unlike in Section 11.3, no pig's stages are excluded from the Bland-Altman analysis. Given the number of pigs and stages, it can be difficult to determine the error of individual pig's stages in Figure 12.5. Thus, Table 12.1 presents the individual pig and stage stroke volume estimation error (SV_{err}) for each of the $Z_{c,w}$ methods.

Figure 12.6 compares how much variation in each of the stroke volume estimates ($SV_{est,c}$, $SV_{est,wh}$, $SV_{est,bh}$) is reflected in the measured stroke volume (SV_{mea}), using an overall coefficient of determination (r^2). Additionally, Figure 12.7 assesses each $Z_{c,w}$ identification method more directly, comparing it with the calculated $Z_{c,ideal}$. Figure 12.7 only shows the overall r^2 for each $Z_{c,w}$ identification method compared to $Z_{c,ideal}$. However Table 12.2 shows the individual pig r^2 values for the dynamic methods ($Z_{wh,cal}$ and $Z_{bh,cal}$) versus $Z_{c,ideal}$.

Table 12.1: Stroke volume estimation percentage error (%) for each individual pigs and stages, presented as mean $SV_{err,c}$, $SV_{err,wh}$ and $SV_{err,bh}$, respectively. The value(s) of minimum error for a particular pig and stage are shown in bold. Additionally, 1 decimal place is included where $SV_{err} < 10\%$.

Protocol D				
Pig	**Control**	**High PEEP**	**High fluids**	**Dobutamine**
D1	3.0, **2.9**, 6.1	11, 12, **9.0**	107, 105, **7.9**	**8.4**, 11, 34
D2	7.8, **7.4**, 8.9	43, 42, **24**	26, 31, **10**	32, 41, **24**
D3	**3.2**, 3.3, 4.3	29, 22, **4.2**	22, 24, **9.9**	**20**, 29, 25
D4	**4.6**, 5.0, 5.4	39, 40, **37**	33, **25**, 37	123, 119, **82**
D5	**5.3**, 5.9, 9.3	22, 15, **8.6**	34, **21**, 23	31, **11**, 21

Protocol S					
Pig	**Control**	**High PEEP**	**Before endo**	**Start endo**	**End endo**
S1	**9.8**, **9.8**, 10	**10**, 16, 15	17, 13, **10**	15, **11**, 12	46, **34**, 44
S2	**2.1**, 5.8, 9.9	**3.8**, 9.4, 11	**7.4**, 8.2, 10	7.5, **6.7**, 8.4	39, 48, **21**
S4	4.7, **4.2**, 5.5	10, **7.2**, 8.4	24, 24, **6.4**	11, **4.0**, 14	87, 82, **69**
S5	**2.9**, 3.2, 4.4	6.6, **4.5**, 15	6.2, **4.8**, 6.0	3.8, **2.6**, 3.0	**1.4**, 10, 8.4
S6	2.9, **2.7**, 5.1	**1.8**, 7.2, 6.5	**5.2**, 6.5, 20	**5.9**, 7.4, 21	**3.8**, 29, 87

Protocol V		
Pig	**Control**	**VCO**
V1	4.6, **4.4**, 6.1	41, **35**, 44
V2	**3.9**, 5.7, 10	46, 41, **31**
V3	**11**, **11**, 12	30, **25**, 54
V4	3.7, **3.1**, 5.2	10, **4.9**, 19

Table 12.2: Coefficient of determination (r^2) for each dynamic $Z_{c,w}$ estimate ($Z_{wh,cal}$ & $Z_{bh,cal}$) vs $Z_{c,ideal}$, for each individual pig (rounded to 2 d.p.). $Z_{c,cal}$ is not included, as it is a constant for each pig and therefore individual pig r^2 values would be meaningless.

	Pig													
	D1	**D2**	**D3**	**D4**	**D5**	**S1**	**S2**	**S4**	**S5**	**S6**	**V1**	**V2**	**V3**	**V4**
$Z_{wh,cal}$	0.06	0.17	0.18	0.0	0.72	0.41	0.12	0.74	0.02	0.01	0.63	0.74	0.4	0.63
$Z_{bh,cal}$	0.71	0.73	0.57	0.06	0.60	0.04	0.15	0.53	0.01	0.27	0.24	0.56	0.57	0.18

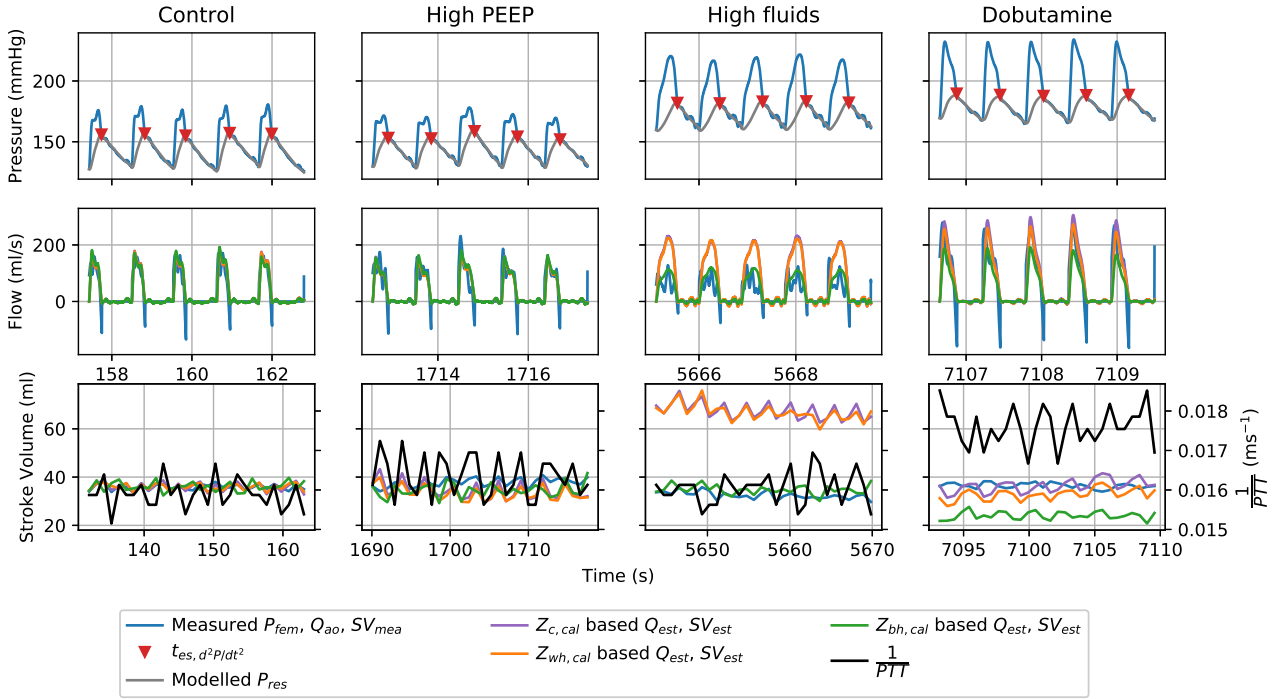

(a) Pig D1 pressure, flow and stroke volume and reciprocal *PTT* waveforms for each stage.

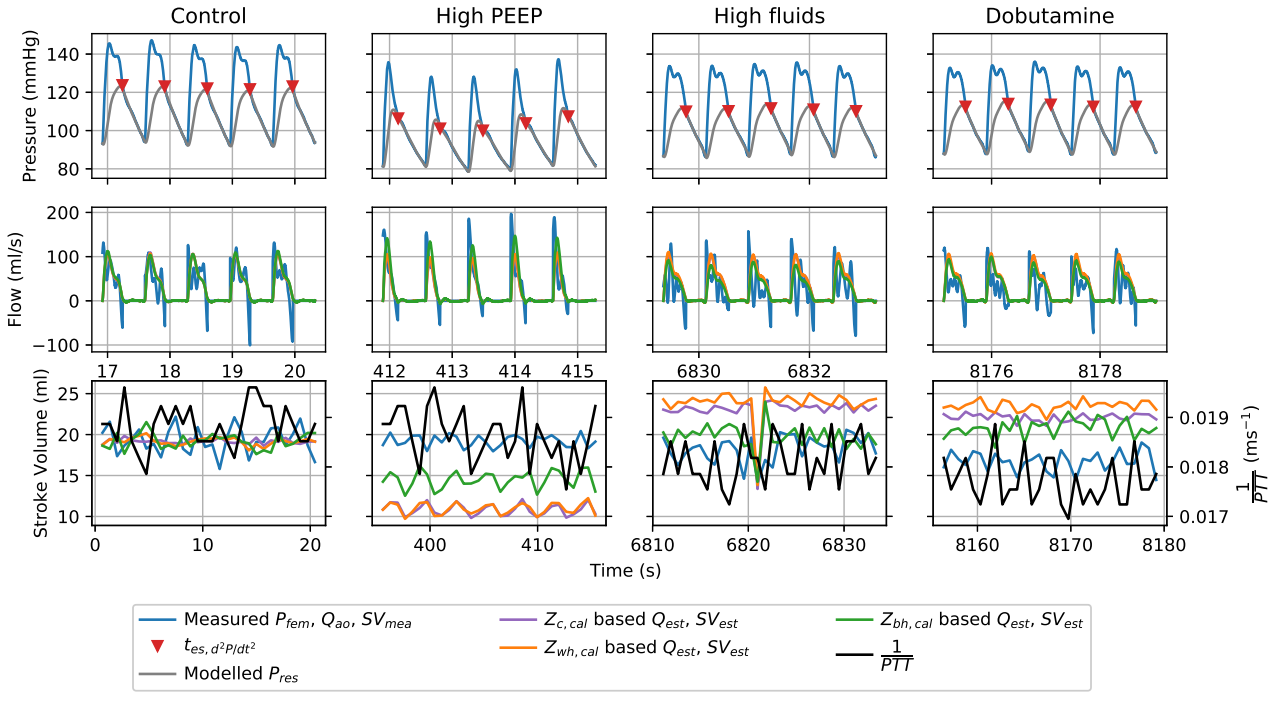

(b) Pig D2 pressure, flow and stroke volume and reciprocal *PTT* waveforms for each stage.

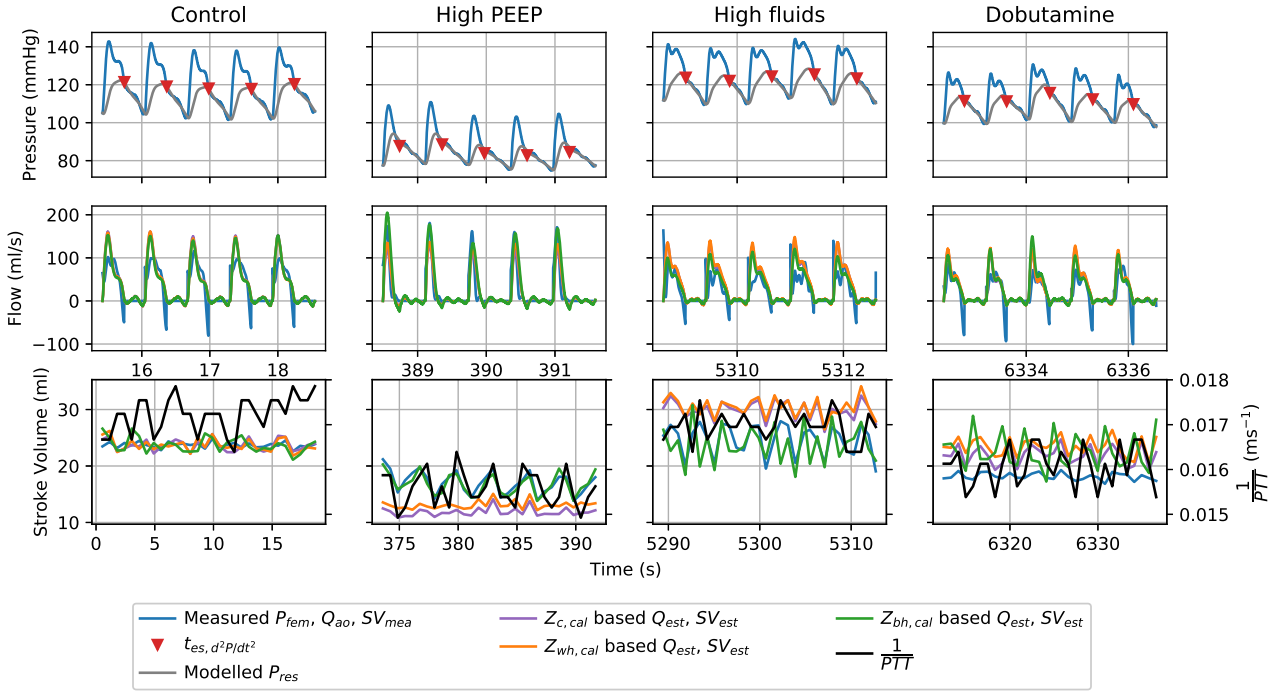

(c) Pig D3 pressure, flow and stroke volume and reciprocal *PTT* waveforms for each stage.

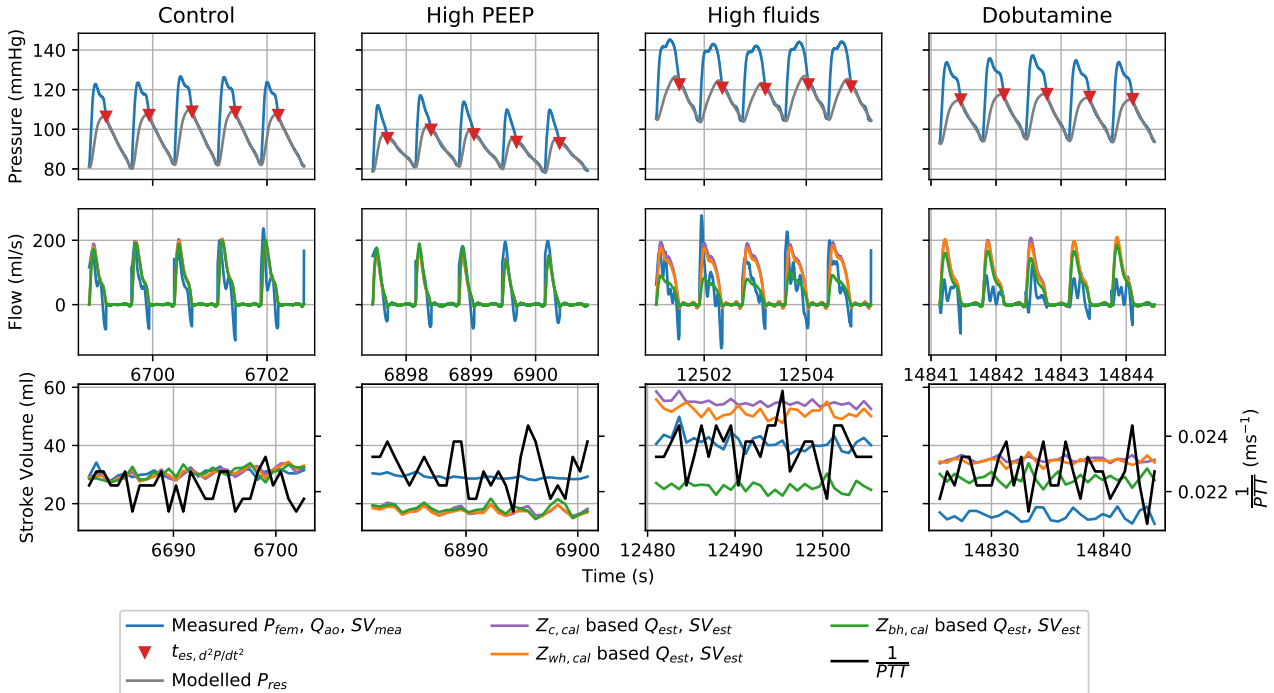

(d) Pig D4 pressure, flow and stroke volume and reciprocal *PTT* waveforms for each stage.

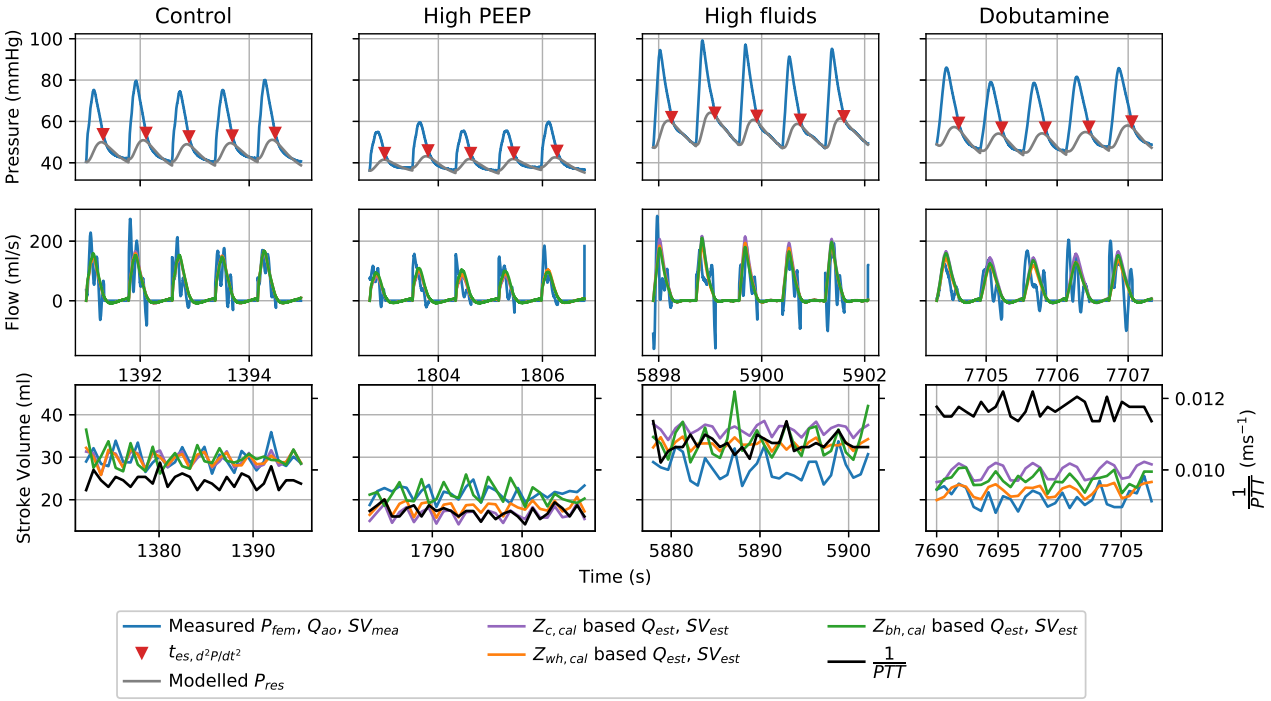

(e) Pig D5 pressure, flow and stroke volume and reciprocal *PTT* waveforms for each stage.

Figure 12.2: Each Protocol D Pig's pressure, flow, stroke volume and reciprocal *PTT* waveform for each stage. The first two rows show the last five beats of the stage to enhance clarity. The final row shows stroke volume for all 30 beats of each stage.

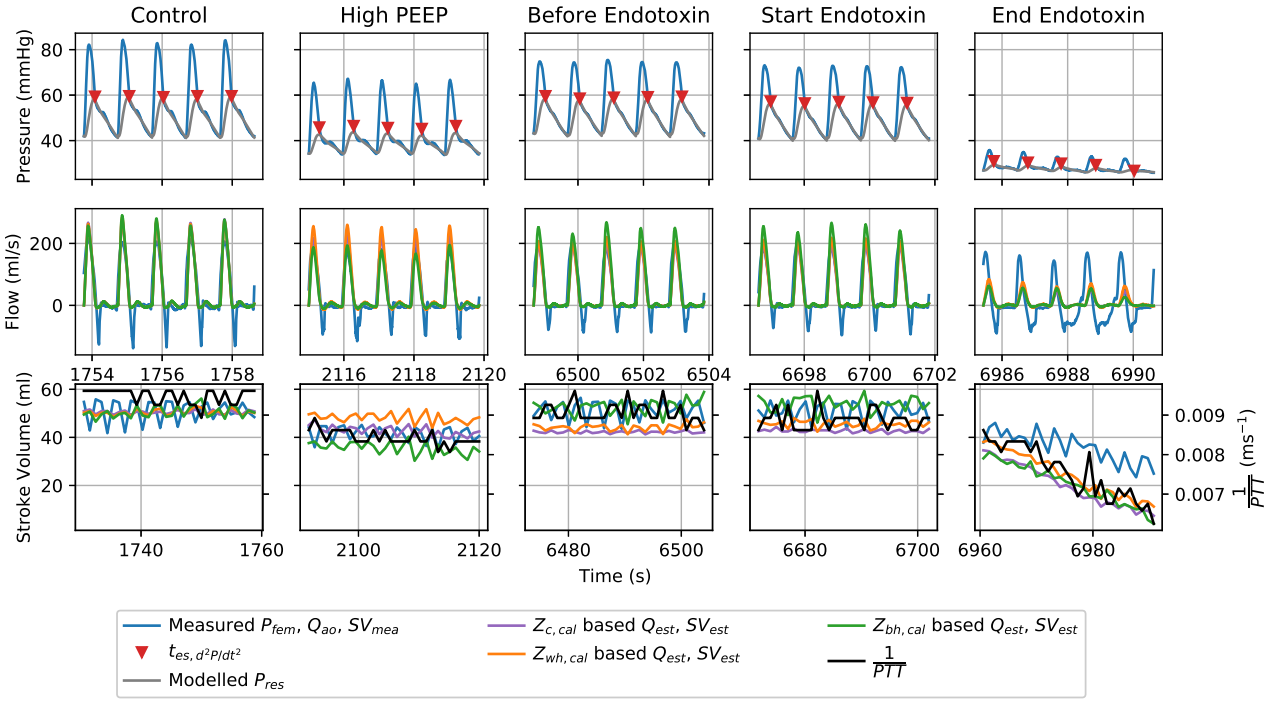

(a) Pig S1 pressure, flow and stroke volume and reciprocal *PTT* waveforms for each stage.

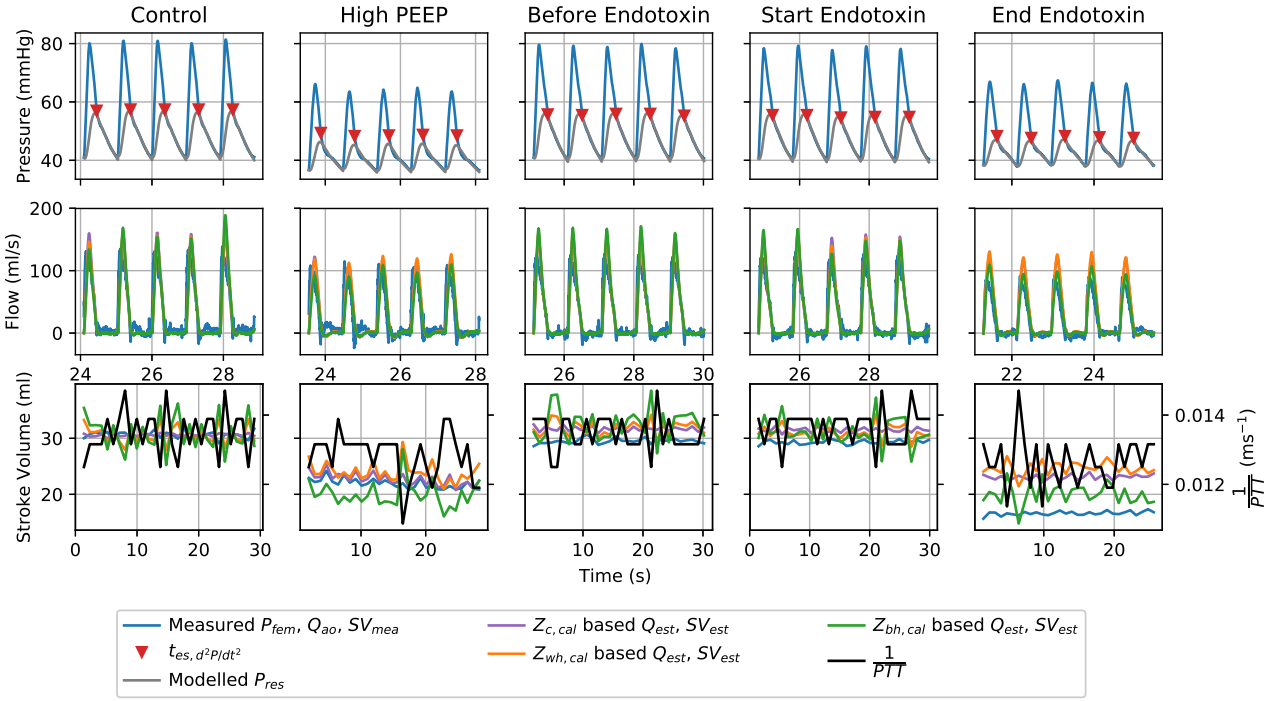

(b) Pig S2 pressure, flow and stroke volume and reciprocal *PTT* waveforms for each stage.

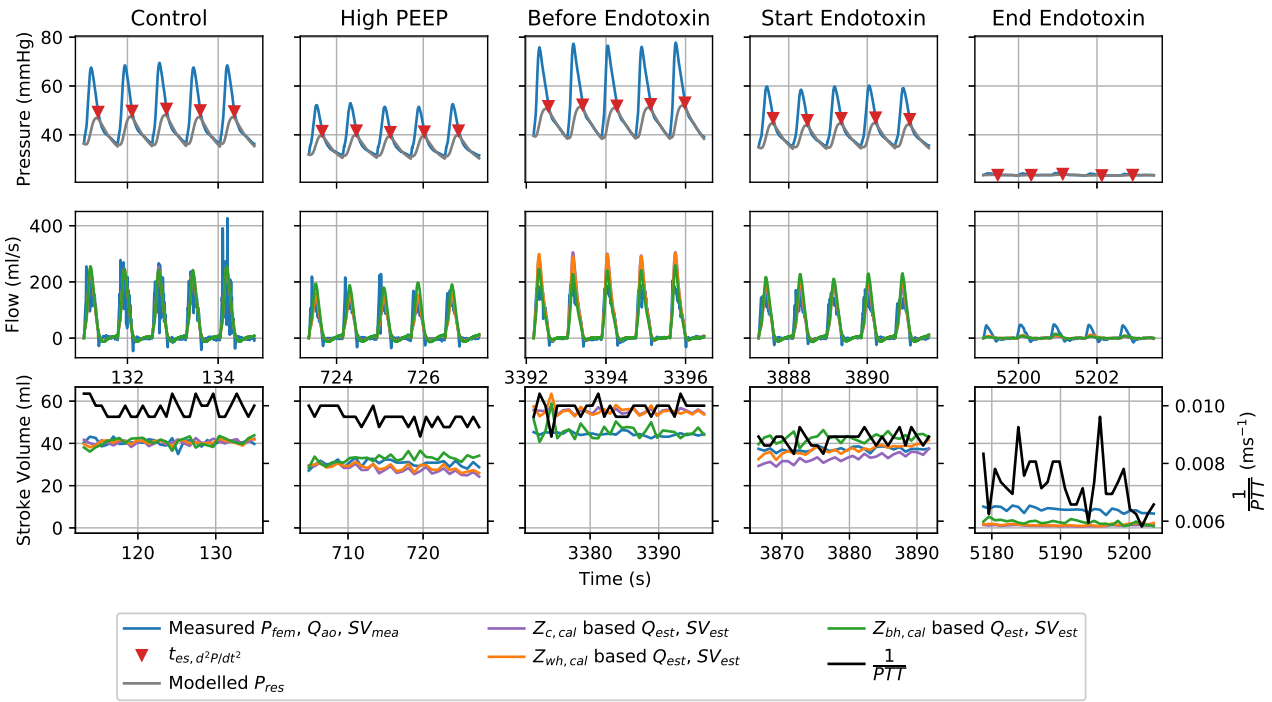

(c) Pig S4 pressure, flow and stroke volume and reciprocal *PTT* waveforms for each stage.

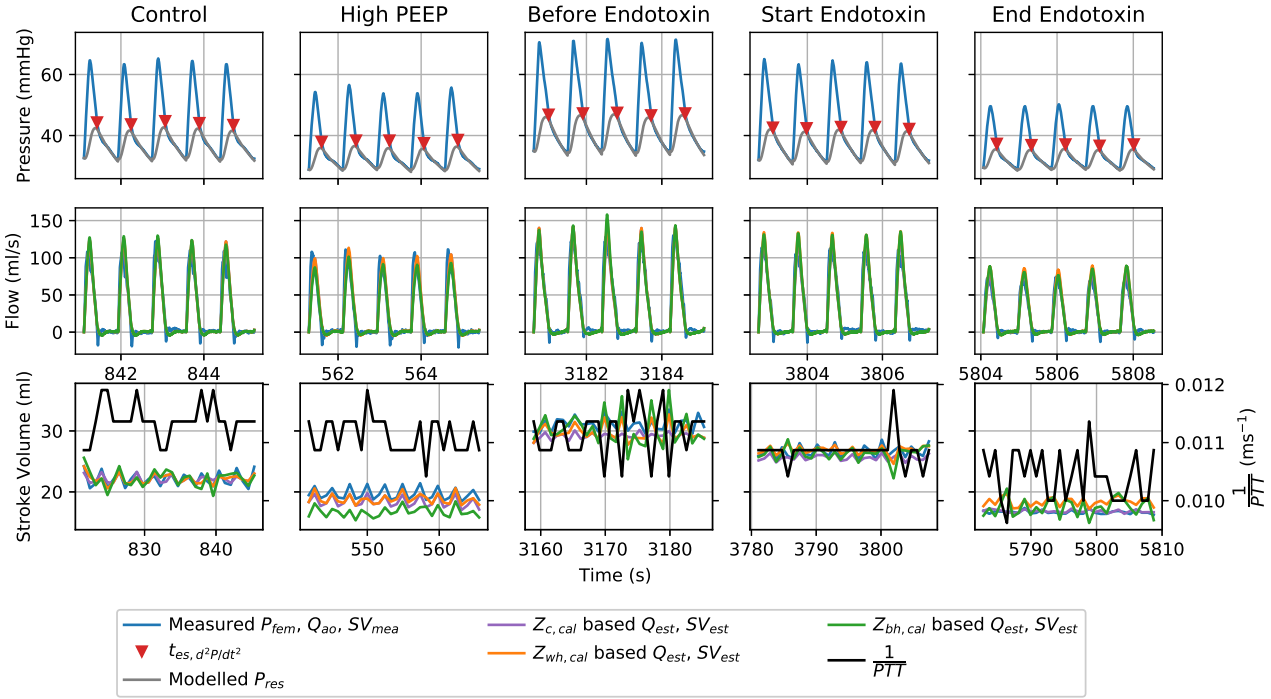

(d) Pig S5 pressure, flow and stroke volume and reciprocal *PTT* waveforms for each stage.

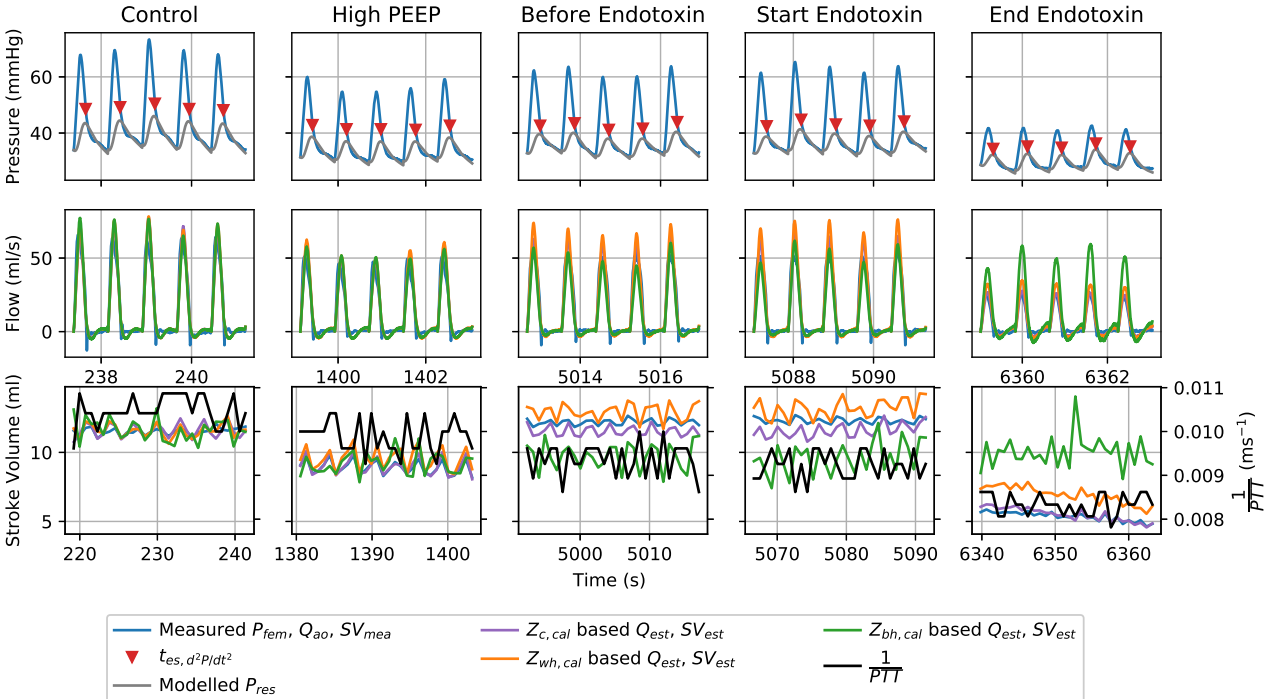

(e) Pig S6 pressure, flow and stroke volume and reciprocal *PTT* waveforms for each stage.

Figure 12.3: Each Protocol S Pig's pressure, flow, stroke volume and reciprocal *PTT* waveform for each stage. The first two rows show the last five beats of the stage to enhance clarity. The final row shows stroke volume for all 30 beats of each stage.

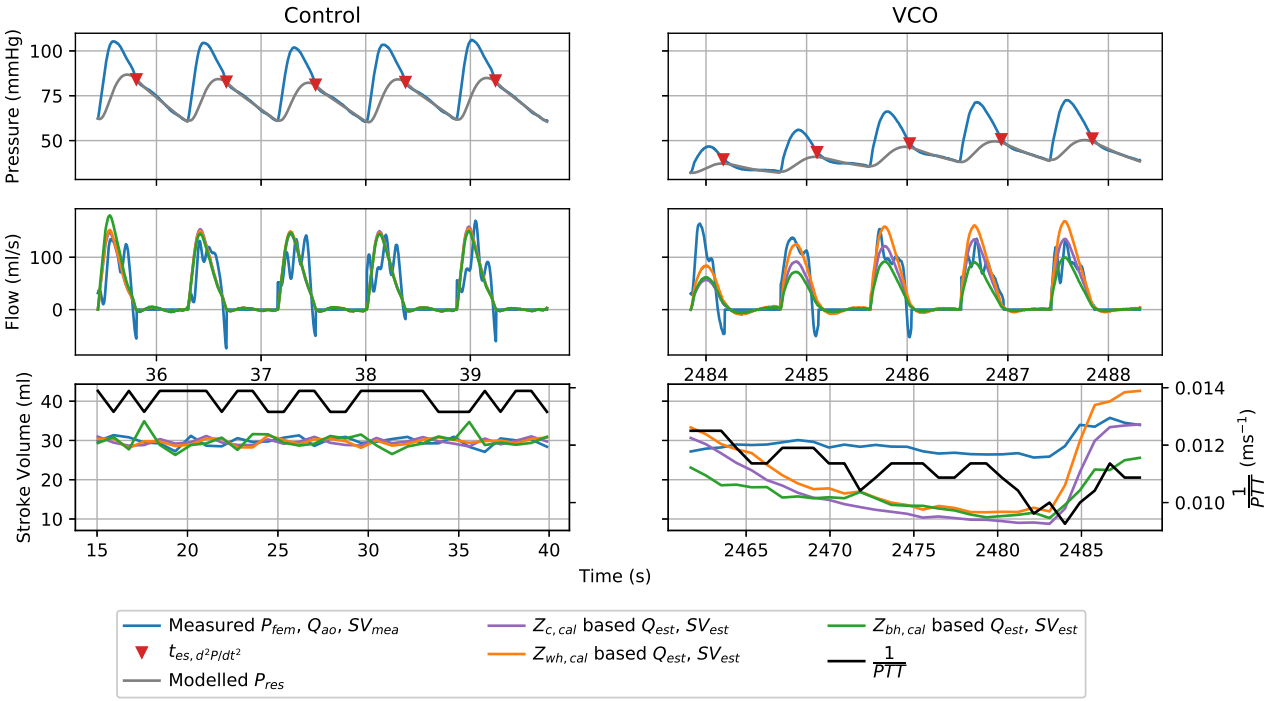

(a) Pig V1 pressure, flow and stroke volume and reciprocal *PTT* waveforms for each stage. Note, the 5 VCO beats illustrated for this particular pig are its recovery, as occlusion is slowly reduced, hence the increasing pressure.

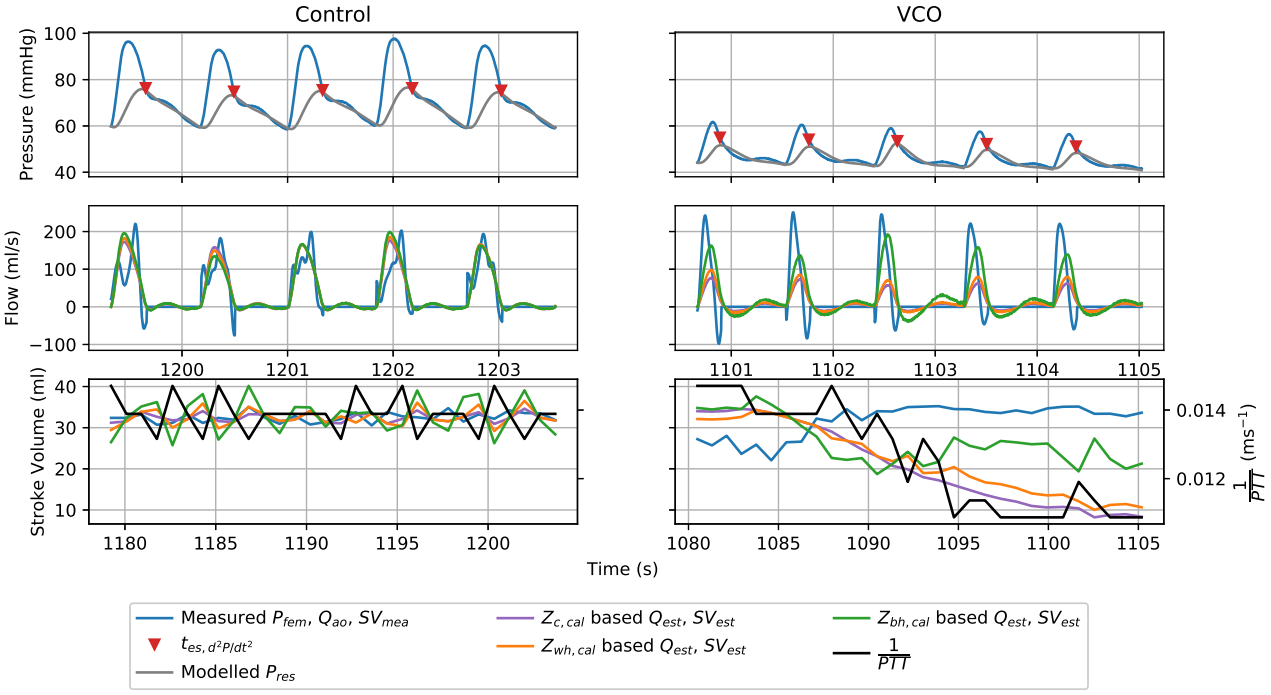

(b) Pig V2 pressure, flow and stroke volume and reciprocal *PTT* waveforms for each stage.

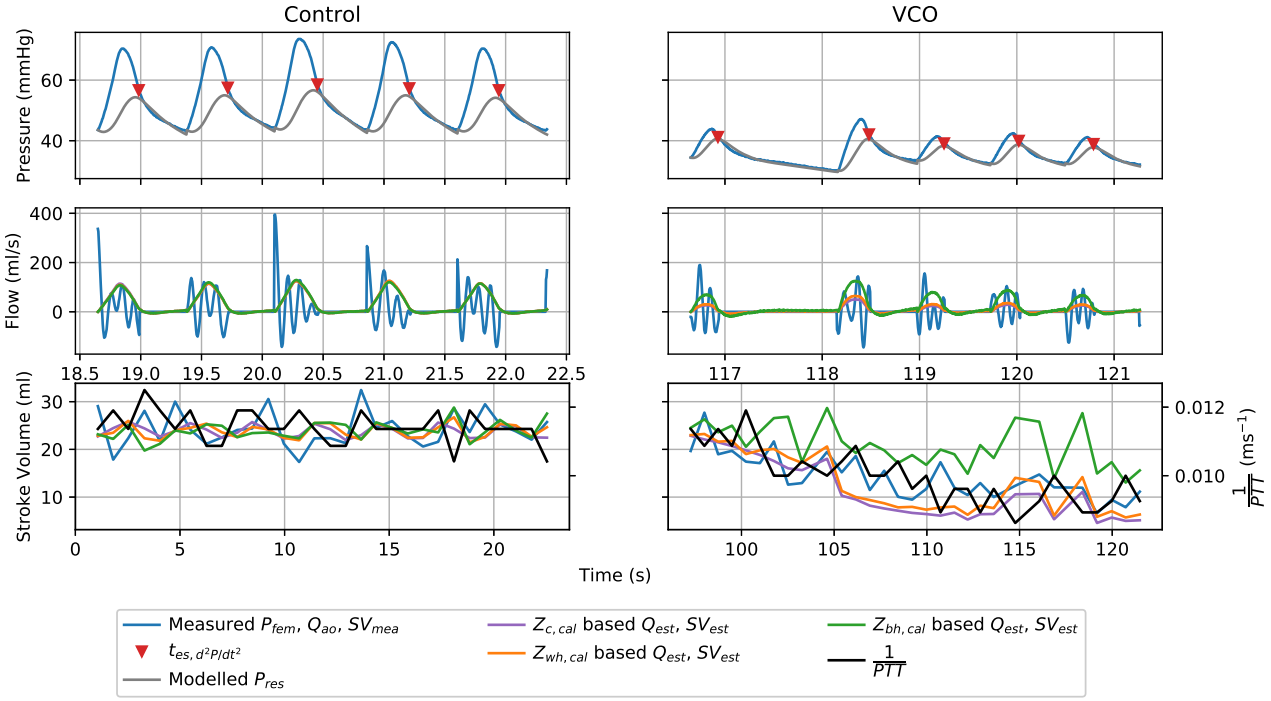

(c) Pig V3 pressure, flow and stroke volume and reciprocal *PTT* waveforms for each stage.

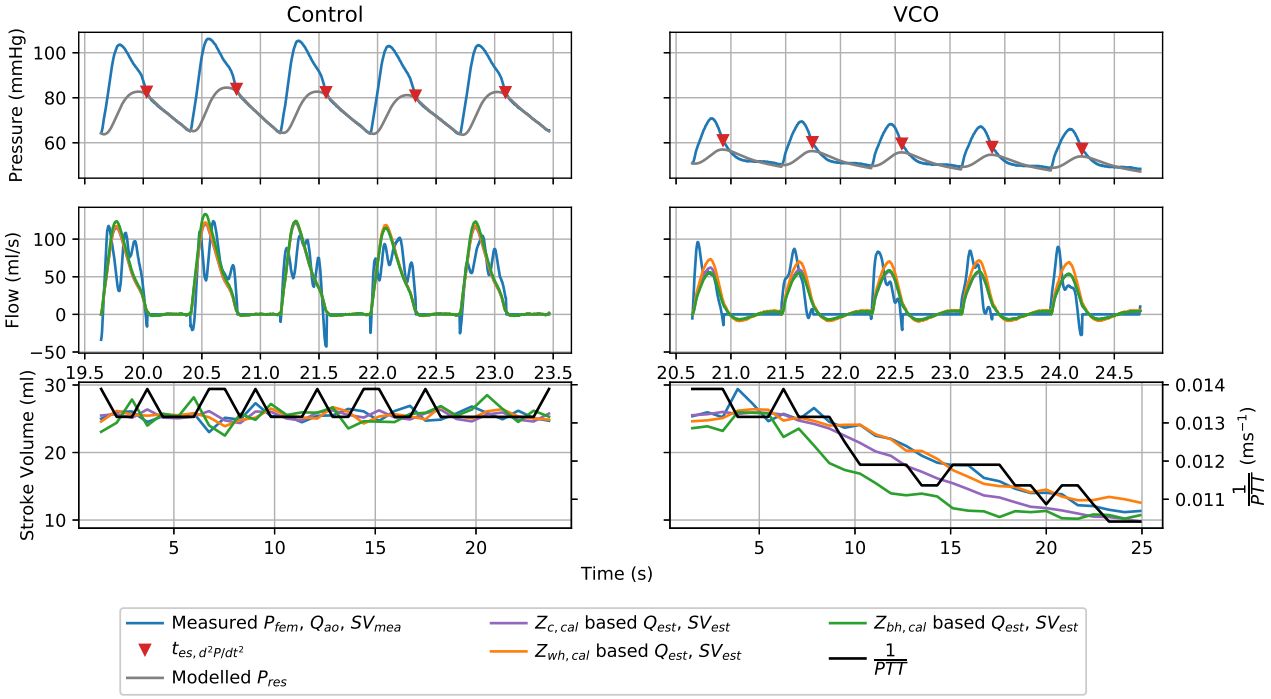

(d) Pig V4 pressure, flow and stroke volume and reciprocal *PTT* waveforms for each stage.

Figure 12.4: Each Protocol V Pig's pressure, flow, stroke volume and reciprocal *PTT* waveform for each stage. The first two rows show the last five beats of the stage to enhance clarity. The final row shows stroke volume for all 30 beats of each stage.

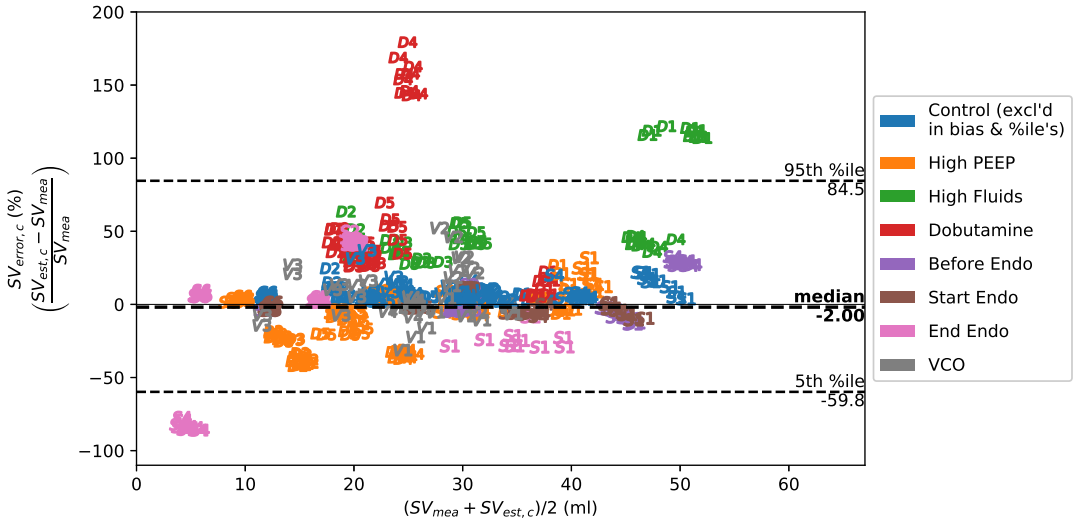

(a) *SV* error resulting from $Z_{c,cal}$

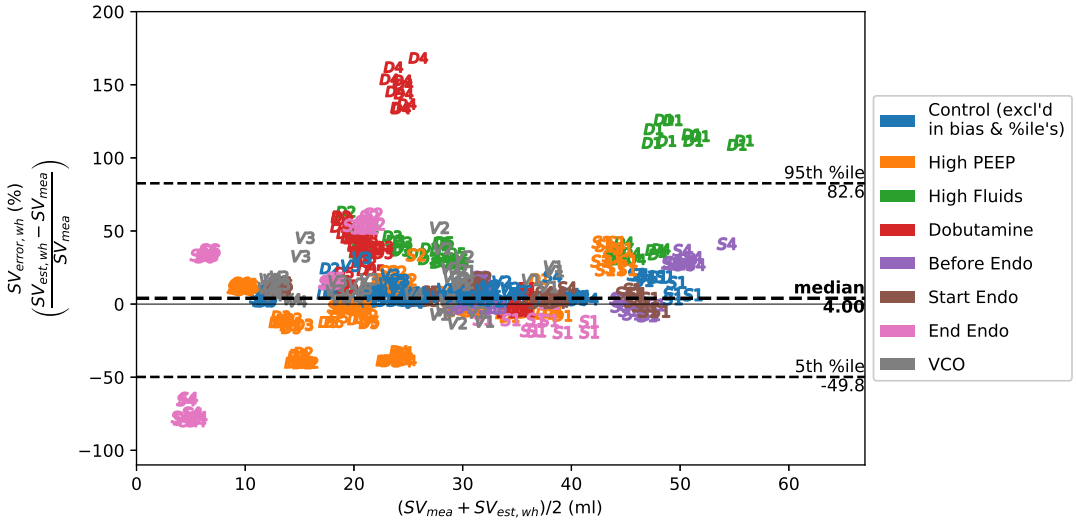

(b) *SV* error resulting from $Z_{wh,cal}$

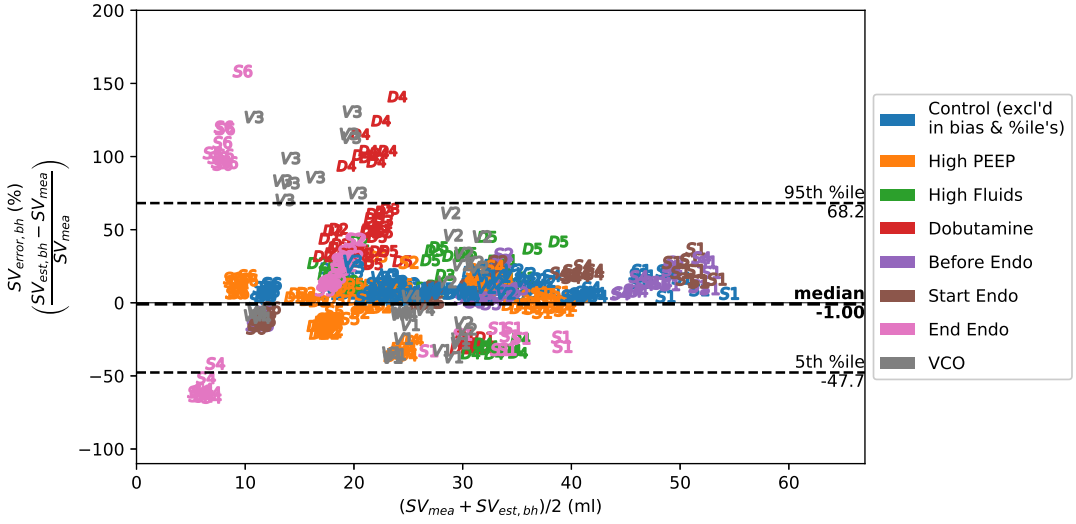

(c) *SV* error resulting from $Z_{bh,cal}$

Figure 12.5: Bland-Altman analysis assessing the *SV* estimation performance of each $Z_{c,w}$ method ($Z_{c,cal}$, $Z_{wh,cal}$ and $Z_{bh,cal}$). Pig markers are according to their labels and the median bias between the measured and estimated SV is shown, as well as the fifth and ninty-fifth percentiles, indicate the variation.

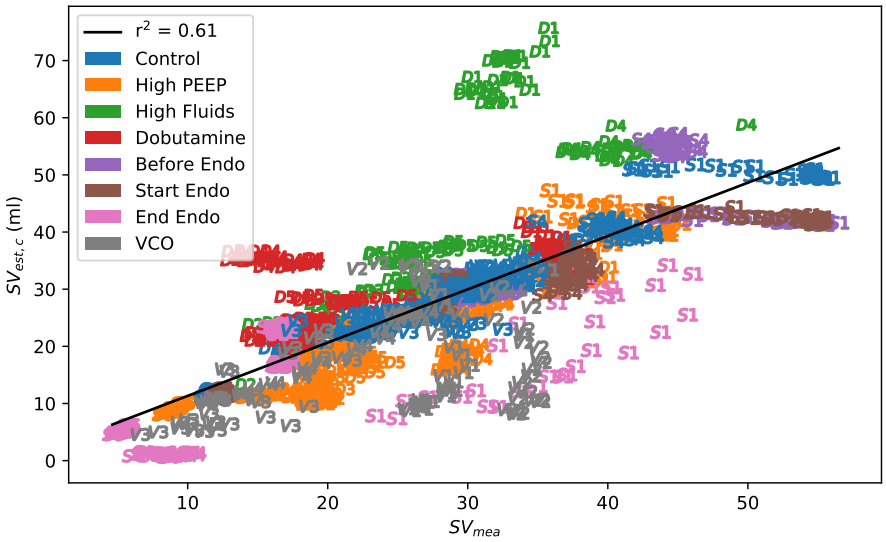

(a) Variation in $SV_{est,c}$ described by SV_{mea}

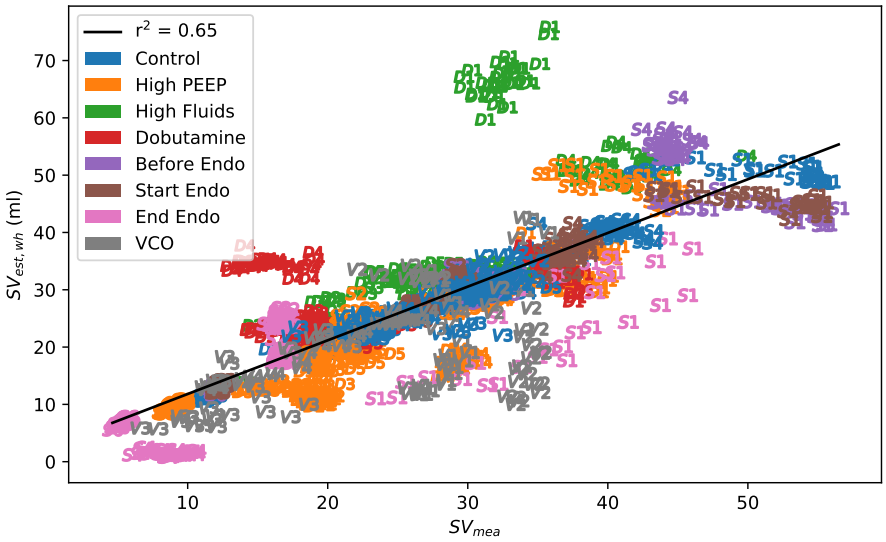

(b) Variation in $SV_{est,wh}$ described by SV_{mea}

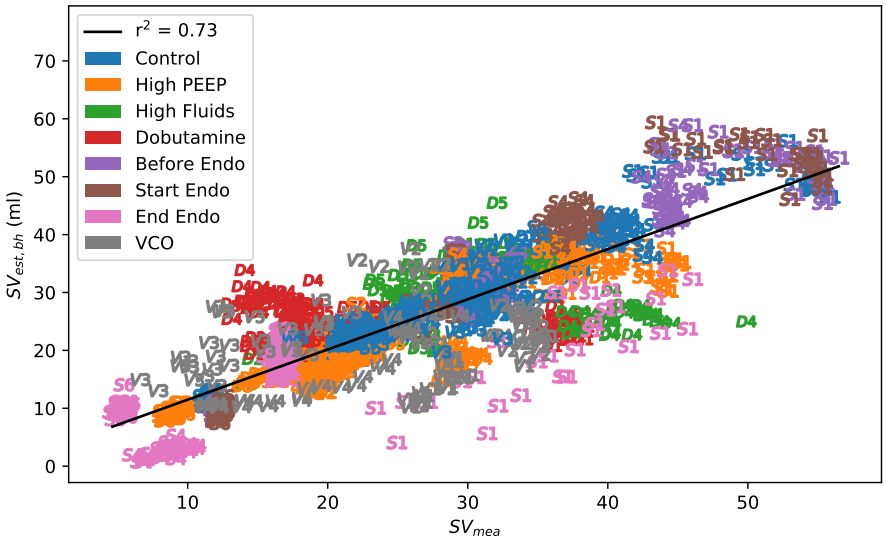

(c) Variation in $SV_{est,bh}$ described by SV_{mea}

Figure 12.6: Stroke Volume regression analysis showing the overall coefficient of determination (round to 2 d.p.) for each $Z_{c,w}$ method ($Z_{c,cal}$, $Z_{wh,cal}$ and $Z_{bh,cal}$). Pig markers are according to their label.

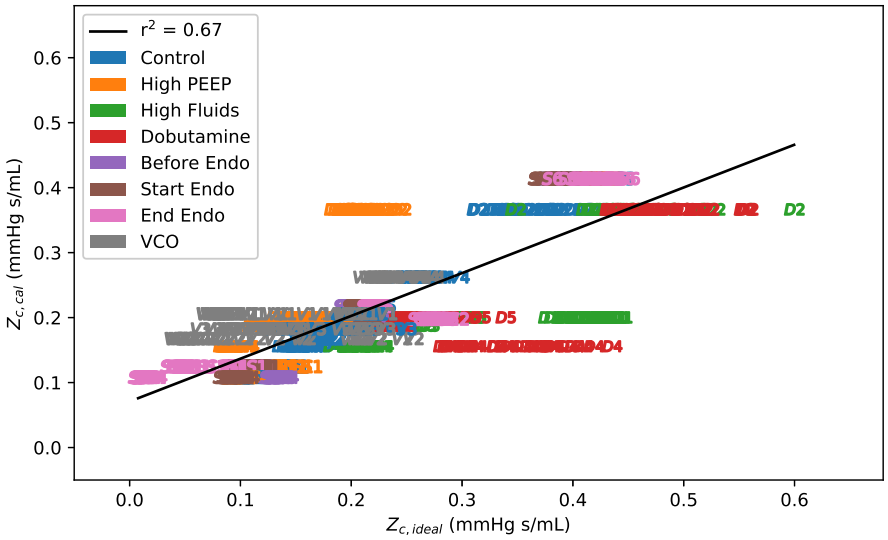

(a) Variation in $Z_{c,cal}$ described by $Z_{c,ideal}$

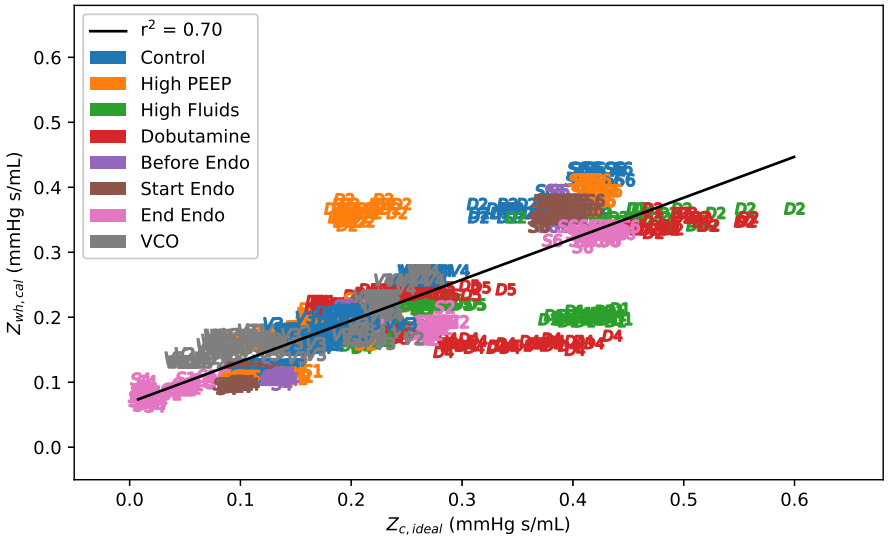

(b) Variation in $Z_{wh,cal}$ described by $Z_{c,ideal}$

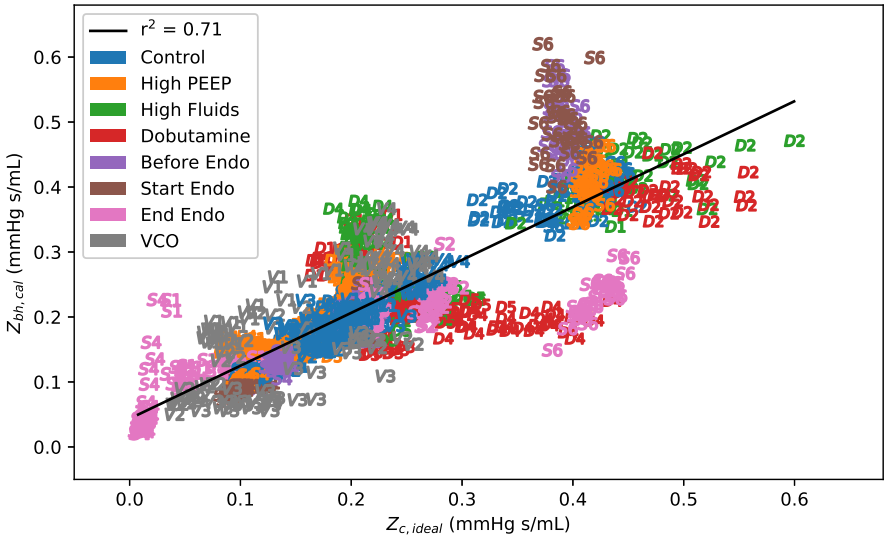

(c) Variation in $Z_{bh,cal}$ described by $Z_{c,ideal}$

Figure 12.7: Ideal versus estimated characteristic impedance regression analysis, showing the overall coefficient of determination (round to 2 d.p.) for each $Z_{c,w}$ method ($Z_{c,cal}$, $Z_{wh,cal}$ and $Z_{bh,cal}$). Pig markers are according to their label.

12.4 Discussion

12.4.1 Static versus Dynamic $Z_{c,w}$ Effect on Stroke Volume Estimation

Figure 12.5 illustrates the stroke volume estimation performance has been improved by updating $Z_{c,w}$ in a dynamic manner, using Equations 12.3 and 12.6. Notably, no method comes close to the $\pm$ 30% limits of agreement criteria outlined by Critchley and Critchley (1999) (limits of agreement not shown). This result is partly due to the severity of the interventions, where the stages of high error represent more dramatic deliberate changes in hemodynamics than is typically encountered in a clinical environment. However, these same dramatic changes enable more robust testing of the different $Z_{c,w}$ methods and thus suit this study's aim.

Water hammer based $Z_{c,w}$ method, $Z_{wh,cal}$

Overall, the median bias of each SV_{est} is similar, but the percentiles are narrower for both $SV_{err,wh}$ and $SV_{err,bh}$, compared with $SV_{err,c}$. However, the improvement shown in Figure 12.5b when using $Z_{wh,cal}$ ($SV_{err,wh}$), is slight compared with $Z_{c,cal}$ (Figure 12.5a). The minimal change in $SV_{err,c}$ versus $SV_{err,wh}$ means $Z_{c,cal}$ and $Z_{wh,cal}$ had similar values, confirmed when comparing Figures 12.7a and 12.7b. Notice their respective overall coefficient of determination, $r^2 \approx 0.7$, suggesting a reasonable and similar relationship between the $Z_{c,cal}$/$Z_{wh,cal}$ and $Z_{c,ideal}$. However, the overall r^2 result can be misleading and the similarity of the two results is not a good outcome for the $Z_{wh,cal}$ method. For example, the very motivation for developing a dynamic $Z_{c,w}$ method is shown in Figure 12.7a, where no variation in $Z_{c,ideal}$ is reflected in $Z_{c,cal}$, since the latter is treated as a constant for each pig. Therefore, and similarly, the lack of variation in $Z_{wh,cal}$ compared with the pigs $Z_{c,ideal}$, shown in Figure 12.7b confirms $Z_{wh,cal}$ actually failed to updated $Z_{c,cal}$ in a meaningful way. The individual pig's r^2 values in Table 12.2, confirm the conclusion that updating $Z_{c,cal}$ via Equation 12.3 did little to improve model performance. Since Equation 12.3 relied on PTT the same conclusions are drawn from regression analysis of PTT versus $Z_{c,ideal}$, were the overall r^2 = 0.08 and

the individual pig's r^2 values are very similar to those of $Z_{wh,cal}$ in Table 12.2 (results not shown).

Interestingly Figures 12.2 – 12.4 still do suggest a relationship between PTT and SV, as previously found in literature (Kamoi et al., 2015). However, it seems the $Z_{wh,cal}$ method employed in Section 12.2.4, does not improve model performance significantly enough to justify the additional model complexity, or invasiveness of continuously monitoring PTT in a clinical environment.

PCA-Bramwell-Hill based $Z_{c,w}$ method, $Z_{bh,cal}$

Considering all the data shown in Figure 12.5c, $SV_{err,bh}$ of the $Z_{bh,cal}$ method, had the lowest median bias and narrowest percentiles of the three $Z_{c,w}$ identification methods. Thus, a general conclusion is Equation 12.6 successfully improved model performance. However, the overall result does not capture the method's performance for individual pigs. Specifically, some pig's individual stage errors were reduced, for example, Pigs D1 high fluids, D4 dobutamine and S4 end endo, while others showed an increase in SV_{err} using the $Z_{bh,cal}$ method (Pigs S1 start endo, S6 end endo, V3 VCO).

The updating of $Z_{bh,cal}$ has two avenues, $\Delta Z_{c,w}C$ or ΔPTT, both with respect to their control stage values, according to Equation 12.6. In contrast, $Z_{wh,cal}$ was only updated via PTT. Therefore, comparing the three subfigures of Figure 12.5, the fact $SV_{err,wh} \approx SV_{err,c}$ for Pigs S1 start endo, S6 end endo, V3 VCO indicates changes in $Z_{c,w}C$ were the source of the increased error associated with $SV_{err,bh}$. By the same logic, $\Delta Z_{c,w}C$ enabled the dramatic improvement in D1 high fluids stage. Specifically, as shown in Table 12.1, SV_{err} reduced from $\approx$ 100% to 8%. Thus, it is difficult to predict when estimating $Z_{c,w}$ via $Z_{c,w}C$ will lead to improved performance and when it will be detrimental.

This issue is reflected in Table 12.1, where with the exception of Protocol D High PEEP, no $Z_{c,w}$ method showed consistent performance across a pig or stage. Even in Protocol D High PEEP, only 3 of the 5 pigs showed significant improvement due to $Z_{bh,cal}$.

Therefore, despite the overall performance shown in Figure 12.5, individual protocol Bland-Altman analyses showed a different result. Specifically, only Protocol D stroke volume estimation is significantly improved using Equation 12.6, where the median bias was improved from 6% ($SV_{err,c}$) to 1% ($SV_{err,bh}$), and the 5th – 95th percentiles were improved from -42% – 113.1% ($SV_{err,c}$) to -38.5% – 54.5% ($SV_{err,bh}$), respectively (results not shown). Individual Bland-Altman analysis for Protocols S and V showed very similar model performance between $Z_{c,cal}$, $Z_{wh,cal}$ and $Z_{bh,cal}$ (results not shown).

The regression analysis for $Z_{bh,cal}$ versus $Z_{c,ideal}$ in Figure 12.7c once more shows an overall result similar to $Z_{c,cal}$ versus $Z_{c,ideal}$. However, the variability in $Z_{bh,cal}$ is significantly increased compared with either $Z_{c,cal}$ or $Z_{wh,cal}$. However, Table 12.2 shows generally for individual pigs, variability in $Z_{bh,cal}$ does not describe change in $Z_{c,ideal}$ well, consistent with the variable impact of $Z_{bh,cal}$ on stroke volume estimation. Therefore, like $Z_{wh,cal}$, $Z_{bh,cal}$ does not appear to significantly improve flow (Q_{est}) and subsequent stroke volume estimation (SV_{est}) in a reliable manner. The added model complexity and invasion of monitoring *PTT* outweighs the small apparent benefit.

12.4.2 Limitations

One of the limitation of this analysis was the 250 Hz data acquisition sampling rate for Protocols S and V, alluded to in Section 12.2.1. Given both $Z_{wh,cal}$ and $Z_{bh,cal}$ depend on *PTT*, the 250 Hz sampling rate limited time resolution to 4 ms, possibly affecting results. However, Protocol D was sampled at 1000 Hz, and, while the higher rate did make for finer *PTT* measurement, the results did not change. It is thus unlikely 1000 Hz sampling of all data would have change the results and conclusions.

12.5 Summary

In Chapter 11 *PWV* did not feature in the improved three-element windkessel implementation, contrary to the Kamoi model of Chapter 6. However, Chapter 11, unlike Kamoi

et al. (2017) only used a static calibration of $Z_{c,w}$, rather than update it via PWV. Thus, with P_{res}/P_{ex} now robustly identified, this chapter sought to re-introduce PWV/PTT as a means of updating the only static parameter in Chapter 11's implementation, $Z_{c,w}$. The first dynamic method of updating $Z_{c,w}$ was $Z_{wh,cal}$ whose Equation 12.3 was derived from the water hammer equation (Equation 2.7). It appeared that ΔPTT were insignificant relative to the changes in the ideal characteristic impedance, $Z_{c,ideal}$, which was back-calculated from the measured stroke volume per Equation 12.7. Thus, unsurprisingly, the model estimated stroke volume of $Z_{wh,cal}$ had similar performance to that seen already when using the constant $Z_{c,w}$ calibration ($Z_{c,cal}$) which had previously been used in Chapter 11.

The other dynamic method of calculating $Z_{c,w}$ used a hybrid PCA-Bramwell-Hill equation approach, via Equation 12.6. Specifically, the hypothesis was changes in the PCA identified $Z_{c,w}C$ could be used to estimate $Z_{c,w}$, where the Bramwell-Hill equation (Equation 2.2) was used to account for the ΔC component of the parameter product. However, while this method showed improved performance compared with the $Z_{wh,cal}$ method, $Z_{bh,cal}$ did not significantly improve stroke volume estimation over $Z_{c,cal}$. Moreover, on an individual pig basis, there were times where the approach increased, rather than reduced error.

As covered in Section 7.1, PTT is not monitored continuously in a clinical environment. Thus, implementing either $Z_{wh,cal}$ or $Z_{bh,cal}$ clinically would represent increased clinician workload and potentially increased patient invasion. Since neither method showed significant stroke volume estimation improvement over the calibrated constant $Z_{c,cal}$ method, the additional complication of using PTT seems unjustified.

CHAPTER 13

Conclusions

Cardiovascular disease is the second leading cause of mortality in New Zealand and its treatment represents a significant portion of healthcare costs. The complex nature of the cardiovascular system means disease can be multifaceted, making diagnosis of the individual disease mechanisms difficult. This difficulty is exacerbated by common clinical measures, such as pressure, heart rate and electrocardiogram (*ECG*), changing in response to many different factors. In an ideal case, more direct measures of cardiac performance, such as stroke volume (*SV*) and cardiac output (*CO*), would be available and monitored continuously, for a clearer, more unambiguous picture of a patient's current state.

This issue informed the thesis goal of developing a clinically applicable *SV* estimation method. Specifically, this research opted to use a three-element windkessel, pulse contour analysis (PCA), model-based approach, so the overall method was non-additionally invasive and increased the utility of already ubiquitous arterial pressure measurements.

Historically, the potential of PCA model-based methods to estimate flow and stroke volume, had already been shown (Wesseling et al., 1993). However, many of the commercial devices incorporating windkessel theory, only output the clinically relevant *SV* and/or *CO*, even though the windkessel model predicts *SV* from a flow waveform estimate. Further-

more, many of the commercial devices use a calibrating *SV* measure to identify patient specific parameters, but subsequent accuracy is conditional on the patient's hemodynamic state remaining relatively constant. If a specific implementation's parameters are not dynamic, then really, its performance becomes contingent on the *SV* calibration and is thus more similar to the likes of the *characteristic impedance method* developed by Wesseling (1983), than the windkessel model theory.

Therefore, this thesis focused on developing a model whose implementation closely resembled the foundational three-element windkessel theory. The first barrier to achieving robust model parameter identification and thus overall implementation, was the end-systole detection in the arterial pressure waveform input to the model. Initially, a novel dicrotic notch detection method was developed, which successfully increased the robustness of systolic duration estimation, with both high accuracy and precision. However, it also unveiled further underlying limitations of the windkessel model and PCA based parameter identification. Specifically, the three-element windkessel model predicts diastolic pressure as exponential decay, but cannot describe reflected wave behaviour, such as a dicrotic notch or other distinct reflected waves. Thus, using a measured pressure waveform to back-calculate windkessel parameters via PCA, was made much more difficult in the presence of the dicrotic notch.

The identification of this issue in this research, also somewhat inadvertantly answered the question as to how Wesseling et al. (1993) had managed to successfully use the three-element windkessel model using an aortic pressure waveform. The answer lay in Wesseling et al. (1993) identifying parameters via population based empirical equations, rather than relying solely on PCA. The Wesseling et al. (1993) implementation thereby mitigated the impact of the windkessel model limitations on the parameter identification process and produced better than expected results.

However, parameter identification via PCA has the distinct advantage of being patient specific and enables parameters to be identified beat-to-beat, helping the model monitor flow

and *SV* during and post changes in hemodynamic state. Thus, PCA was seen as a crucial means of achieving the clinical desire for the method to be reliable at monitoring changes in patient state, be it disease progression or recovery.

Therefore, after identifying the challenges imposed by dicrotic notch presence for PCA parameter identification, the next step was to overcome this issue using the femoral pressure waveform. Specifically, the attenuated, or near dicrotic notch-less nature of the clinically more common femoral artery pressure waveform, made it resemble a shape similar to that predicted by the three-element windkessel model. Hence, it was hypothesised the femoral pressure would lend itself to easier windkessel model parameter identification via PCA. The caveat was end-systole detection became more difficult, as the method developed for dicrotic notch detection worked poorly when notches were not present. Thus, the thesis developed a second, more robust end-systole detection method, with high accuracy and precision, capable of detecting both dicrotic notches and end-systole in notch-less pressure waveforms, like the femoral artery. In achieving a robust end-systole detection method, the femoral pressure could now be used with PCA parameter identification and the windkessel model. Moreover, the femoral pressure being more common clinically than the aortic pressure waveform, meant the model implementation was better aligned with the clinically applicable goal of the thesis.

Focusing on implementing a three-element windkessel model, in a manner aligned with the foundational theory, meant this thesis was able to resolve *"the parameter identification sensitivity resulting in the prediction of unphysiological flow profiles"*, a thesis goal in Section 1.4. The novelty associated with achieving this goal, was the illustration of *how* the windkessel models inability to describe spatially varying dynamics (reflected wave phenomena), significantly impacted PCA parameter identification techniques. In particular this thesis illustrated the detrimental effects of the dicrotic notch and early diastolic distinct reflected wave behaviour on parameter identification. While it successfully implemented a method of parameter identification in the presence of these phenomena, ulti-

mately it illustrated waveforms without this behaviour, like the femoral artery, were more compatible with the PCA-based windkessel models. Furthermore it hypothesised the even more ubiquitous radial artery pressure would present the same issues as the aortic waveform, since it contains notches in diastole due to wave reflection that could cause similar parameter identification issues as the dicrotic notch. Thus, as part of identifying and resolving the parameter identification issues arising from the different pressure waveform shapes, this thesis also achieved the secondary goal of establishing *"the impact of pressure waveform measurement location on model implementation and performance"*.

Ultimately, having resolved both the end-systole detection and parameter identification issues, the thesis subsequently achieved its overall goal to *develop a clinically, applicable, non-additionally invasive, model-based method for accurately estimating arterial flow waveforms and subsequent SV*, per Section 1.4. The only measure necessary for flow and stroke volume estimation was the clinically common femoral artery pressure waveform.

The resulting model was also simpler than the Kamoi model method, which required continuously measured pulse wave velocity (*PWV*) (Kamoi et al., 2017), and whose performance was a benchmark/starting point for this thesis. *PWV* is a metric this thesis tried and failed to estimate in a clinically applicable manner. Specifically, a gold standard *PWV* measure can use dual arterial catheterisation to measure pulse transit time (*PTT*), but dual catheterisation is undesirable in a clinical environment. However, some literature had assumed pulse arrival time (*PAT*) was a suitable surrogate of *PTT*. This research explored the option of using *PAT* to achieve the secondary thesis goal of *"resolving the outstanding issues around the [Kamoi] model's need for PWV"*, per Section 1.4. However, this research found *PAT* variation was equally caused by pre-ejection period (*PEP*), a variable with little apparent relationship to *PTT*. Therefore, this analysis found *PAT* to be an inappropriate surrogate for *PTT*, despite it being used in this role in some literature.

However, without a clinical means of identifying *PWV*, the Kamoi model would not meet this thesis's goal of being non-additionally invasive and clinically applicable. Thus, it was

fortunate the model developed by the author was found to not require *PWV*, only requiring more careful implementation, in line with the three-element windkessels model theory, and thereby resolving the outstanding *PWV* issue.

After the thesis goals were achieved, the re-introduction of *PWV* was attempted to see if it offered further improvements, despite a clinical means of implementing such a model having not been found. Specifically, the model developed in this thesis for flow and *SV* estimation, still had a single static calibration parameter, windkessel characteristic impedance ($Z_{c,w}$). Analysis had shown, treating $Z_{c,w}$ as a constant and assuming the other parameters would capture changing hemodynamics, was generally sufficient. However, there were instances where an updated $Z_{c,w}$ parameter would have improved performance. Two methods of updating the calibrated $Z_{c,w}$ value were attempted, both relying on *PWV*/*PTT*. However, neither dynamic $Z_{c,w}$ method significantly improved model performance over the static calibration. Hence it was concluded the additional invasiveness currently required for accurate *PTT* monitoring, was not worth the potential benefits.

While the analyses used clinically applicable disease states (sepsis, vena cava occlusions (VCO)) and therapies (recruitment manoeuvre (RM), fluid and dobutamine admission), the protocols often included intervention cases more severe than may typically be observed in a clinical environment. Thus, the cardiovascular model implementation developed in this thesis, with the *worst case* experimental data, was unable to met the clinically applicable criteria for new *SV*/*CO* methods outlined by Critchley and Critchley (1999). Specifically, the criteria is $\pm$30% limits of agreement with respect to a reference method. The model performance fell just outside this criteria ($\pm$32%) using the porcine trial data were aortic flow was measured (Protocol S). Specifically, it was only during the most severe intervention, the rapid onset of a septic shock like response, where errors were outside the criteria, and this was only for 2 of the 5 pigs[1]. For all other pigs and hemodynamic interventions, the model implemented showed mean beat-to-beat error $<$24%, with excellent tracking and

[1]Where once more the -7.5ml error of Pig S4 end endo is considered highly accurate despite the percentage error being -87.5%, for the reasons explained in Section 11.4.2.

was thus able to reflect changes in state well. Therefore, it would be beneficial to test the model in a observational clinical trial to better assess whether the method could meet the clinical criteria of Critchley and Critchley (1999), rather than judge based on the severe experimental protocols.

Finally, if the model implementation developed in this thesis were successfully implemented in a intensive care unit (ICU) setting, it could significantly improve patient monitoring and care. Specifically, the patient specific manner in which the model is implemented, in conjunction with its beat-to-beat nature, enables a personalised approach to titration of treatment, informed by the quantitative estimation of cardiac function via aortic flow and ventricular SV.

CHAPTER 14

Future Work

14.1 Introduction

This chapter explores the avenues of potential future work. Some of the avenues seek to overcome the short comings identified but unresolved within this thesis. Others avenues seek to translate the work from an experimental to the clinical setting, which is the ultimate end goal for the research in the institute from which this research was conducted.

14.2 Observational Clinical Trial

Thanks to the hard work of Shun Kamoi and his supervisors (Kamoi et al., 2017), the Kamoi model was a successful proof of concept, illustrating the possibility of using a cardiovascular model, *nearly* simple enough to be clinically applicable and whose theory was interpretable by any and all clinical staff. Unfortunately, the one draw back of the method was it required pulse wave velocity (PWV) to be continuously monitored, and thus was not able to be easily implemented in a clinical environment. However, this thesis build on the previous work of Kamoi et al. (2017) and others outlined in Chapter 4, to develop a model which truly could be implemented in a non-additionally invasive manner.

Thus, the first proposal would be to run an observational clinical trial, where femoral artery pressure data is captured in humans in a variety of clinical scenarios likely to alter stroke volume (*SV*)/cardiac output (*CO*), the likes of cardiac surgery and intensive care. The trial need not influence clinical practice in any significant manner, it would only seek to assess the performance of the model against some form of common, clinically accurate, *SV* measure, the likes of thermodilution or trans-esophageal doppler, both covered in Chapter 3.

From this data, the *true* clinical potential of the method could be assessed, overcoming one of the challenges in this thesis. Specifically, this thesis used a variety of clinically applicable interventions, but at times in a severe manner. The severe hemodynamic changes were crucial in the development and testing of the model, as without them the limitations of the implementation would remain unknown. However, the experimentally induced and therefore highly controlled scenario, meant the model in this thesis at times had error higher than the clinically acceptable requirement of Critchley and Critchley (1999), by with other methods and devices have been assessed. However, based on the results of this research, it seems plausible the model will perform within the criteria in a clinical setting.

However, a clinical setting will also likely present different challenges to model implementation, than the experimental settings the model has currently been implemented in. For example, the first foreseeable challenge is getting both enough *SV* variability in a clinical trial, but also capturing that variability with frequent and reliable *SV* measures. After all, this is essentially the challenge this model is trying to overcome, and therefore validation itself is a barrier to creating clinically applicable methods.

A second challenge will be the reliability of the pressure waveforms measured in the clinical environment. This thesis used data captured from high fidelity pressure catheters where the sensor was mounted at the tip, ensuring a high degree of accuracy and precision. In contrast, fluid filled catheters are common in a clinical setting, and are vulnerable to under-damped frequency response behaviour. In the time domain, an under-damped

pressure waveform results in notches in the pressure signal (Watson and Wilkinson, 2012). Like the dicrotic notch in an aortic pressure waveform, or the reflected wave in the radial waveform, notches due to an under-damped catheter would likely increase the difficulty of identifying end-systole, estimating reservoir pressure (P_{res})/excess pressure (P_{ex}), and ultimately flow and SV.

This also highlights the authors reasoning for suggesting the clinical trial begin focusing on patients with a femoral arterial measurement. Doing so minimises the number of new variables introduced into the model implementation. When implementation differs from the steps previously used successfully, the cause of any issues that arise are more difficult to discern. For example, if the model is tested on patients with radial arterial pressure measurements and performs poorly, this may not reflect poor model theory, only new implementation issues to be overcome. Thus, the suggestion first and foremost is to *initially* minimise the potential for new implementations issues. This may mean forgoing the testing of the most desirable common pressure measurement, the radial artery, but only in the short term. Success in the femoral artery would re-enforce the potential for the model, instilling confidence in both the developers and end users. Thus early success in a clinical setting could create the momentum necessary to take the model much further.

14.3 Radial Artery Implementation

Despite Section 14.2's suggestion that initial clinical focus should use the femoral artery, the radial artery does present the most desirable arterial pressure measurement location from a clinical perspective. Specifically, the radial artery is the most commonly catheterised artery for hemodynamic monitoring (Cousins and O'Donnell, 2004), thus explaining its ubiquity in clinical care. Therefore, when the goal is to develop a truly non-additional invasive, pulse contour analysis (PCA) model-based method, the radial artery represents the pinnacle arterial measurement.

As outlined in Section 11.4.5 and 14.2, the challenge of the radial pressure waveform will

be the identification of end-systole and subsequently calculation of P_{res} per Equation 4.12. Failure to achieve the latter would lead to a P_{ex} that inaccurately predicts the flow profile, per Chapter 9. The issue is the possible reflected wave behaviour causing notches in diastole that do not represent end-systole, but whose curvature will be detected by the weighted second derivative based estimate of the time of end-systole ($t_{es,d^2P/dt^2}$), developed in Chapter 10. A potential avenue to overcome this problem is using a transfer function (Gao et al., 2016), to estimate a central arterial pressure waveform without reflected wave behaviour.

A second potential challenge of using the radial artery may be its lower arterial compliance, compared with the larger central arteries. Section 2.2.2 stated most of the arterial compliance is associated with the aorta, and since the windkessel model mechanism centers around a compliant reservoir, many previous implementation, including this thesis, focused on large central arteries. However, when comparing Figures 4.3 and 4.4 in Section 4.3.2, the three-element windkessel applied to the femoral artery predicted a the lower proportion of P_{res}, reflecting its reduced compliance, compared with P_{res} in the proximal aortic signal (P_{ao}) (Balmer et al., 2018b). Thus, it is possible the same behaviour will occur in the radial artery, where the proportion of P_{res} and P_{ex} reflects the model theory of reduced compliance and higher impedance to drive blood to a more peripheral location. Since Wesseling et al. (1993) successfully predicted physiological flow profiles from the radial artery pressure waveform, it seems likely the lower compliance will not present a problem. However, this hypothesis was not tested in this thesis.

A final potential challenge when using the radial pressure waveform will be the much smaller proportion of SV that reaches the radial artery. While the calibration of windkessel characteristic impedance ($Z_{c,w}$) using a SV measurement would account for this, if the proportion of blood to the radial artery changes after calibration, due to disease progression or treatment, the $Z_{c,w}$ value *may* no longer be optimal.

14.4 Dynamic $Z_{c,w}$ Parameter Identification and a Non-invasive *PWV* Measurement

In Chapter 12, the parameter $Z_{c,w}$ was unsuccessfully updated via pulse transit time (*PTT*). Given the already established relationship between (general) characteristic impedance (Z_c) and *PWV* via the water hammer equation (Equation 2.7) and compliance (C & C_A) via Bramwell-Hill (Equations 2.2 and 2.3), it seems plausable these relationships could be leveraged to improve model performance. Indeed, these relationships have already been used in other windkessel implementations covered in this thesis (Wesseling et al., 1993; Wang et al., 2003; Kamoi et al., 2017).

More specifically, the model developed in this thesis found it unnecessary to use *PWV* to calculate P_{res}/P_{ex}, and the subsequent flow and *SV* estimation. The fact the implementation did not require a continuous *PWV* measurement for its performance was cited as an advantage. However, the implementation did rely on an independent *SV* measurement to calibrate $Z_{c,w}$. In a clinical environment, while it is possible to estimate *SV*, it is not common and does present an added workload in order to implement the model. In an ideal implementation, the model would require only the arterial pressure measurement and possibly some other simple means of identifying the $Z_{c,w}$ parameter. Thus, *PWV* may still prove a useful metric for this purpose. To realise this potential, further testing and development of *PWV*/*PTT* with the windkessel model would be require. Moreover, a method of monitoring *PWV* in a clinically applicable manner would be required. This latter challenges is already being addressed by research from within the institute, but as yet results are unpublished.

Bibliography

Abel FL. **Maximal negative dP/dt as an indicator of end of systole**. *Am J Physiol - Hear Circ Physiol* 1981. **240**(4):H676—-H679.

Aguado-Sierra J, Alastruey J, Wang JJ, Hadjiloizou N, Davies J, Parker KH. **Separation of the reservoir and wave pressure and velocity from measurements at an arbitrary location in arteries**. *Proc Inst Mech Eng Part H J Eng Med* 2008. **222**(4):403–416. ISSN 0954-4119.

Alastruey J. **On the mechanics underlying the reservoir-excess separation in systemic arteries and their implications for pulse wave analysis**. *Cardiovasc Eng* 2010. **10**(4):176–189. ISSN 15678822.

Asmar RG, Brunel PC, Pannier BM, Lacolley PJ, Safar ME. **Arterial distensibility and ambulatory blood pressure monitoring in essential hypertension.** *Am J Cardiol* 1988. **61**(13):1066–70. ISSN 0002-9149.

Balmer J, Pretty C, Amies A, Desaive T, Chase JG. **Accurate dicrotic notch detection using adaptive shear transforms**. *10th IFAC Symp Biol Med Syst* 2018a. **51**(27):74–79. ISSN 24058963.

Balmer J, Pretty C, Davidson S, Desaive T, Habran S, Chase JG. **Effect of arterial pressure measurement location on pulse contour stroke volume estimation , during a rapid change in hemodynamic state**. *10th IFAC Symp Biol Med Syst* 2018b. **51**(27):162–167. ISSN 24058963.

Balmer J, Pretty C, Davidson S, Desaive T, Kamoi S, Pironet A, Morimont P, Janssen N, Lambermont B, Shaw GM, Chase JG. **Pre-ejection period, the reason why the electrocardiogram Q-wave is an unreliable indicator of pulse wave initialization**. *Physiol Meas* 2018c. **39**(9):095005. ISSN 1361-6579.

Balmer J, Pretty C, Kamoi S, Davidson S, Pironet A, Desaive T, Shaw GM, Chase JG. **Electrocardiogram R-wave is an Unreliable Indicator of Pulse Wave Initialization**. *IFAC-PapersOnLine* 2017. **50**(1):856–861. ISSN 24058963.

Bataille B, Bertuit M, Mora M, Mazerolles M, Cocquet P, Masson B, Moussot PE, Ginot J, Silva S, Larché J. **Comparison of esCCO and transthoracic echocardiography for non-invasive measurement of cardiac output intensive care**. *Br J Anaesth* 2012. **109**(6):879–886. ISSN 00070912.

Ben-Shlomo Y, Spears M, Boustred C, May M, Anderson SG, Benjamin EJ, Boutouyrie P, Cameron J, Chen CH, Cruickshank JK, Hwang SJ, Lakatta EG, Laurent S, Maldonado J, Mitchell GF, Najjar SS, Newman AB, Ohishi M, Pannier B, Pereira T, Vasan RS, Shokawa T, Sutton-Tyrell K, Verbeke F, Wang KL, Webb DJ, Willum Hansen T, Zoungas S, McEniery CM, Cockcroft JR, Wilkinson IB. **Aortic pulse wave velocity improves cardiovascular event prediction: An individual participant meta-analysis of prospective observational data from 17,635 subjects**. *J Am Coll Cardiol* 2014. **63**(7):636–646. ISSN 07351097.

Bendjelid K, Suter PM, Romand JA. **The respiratory change in preejection period: a new method to predict fluid responsiveness.** *J Appl Physiol* 2004. **96**(1):337–42. ISSN 8750-7587.

Bewick V, Cheek L, Ball J. **Statistics review 7: Correlation and regression**. *Crit Care* 2003. **7**(6):451–459. ISSN 13648535.

Blacher J, Asmar R, Djane S, London GM, Safar ME. **Aortic Pulse Wave Velocity as a Marker of Cardiovascular Risk in Hypertensive Patients**. *Hypertension* 1999a. **33**(5):1111–1117. ISSN 0194-911X.

Blacher J, Guerin AP, Pannier B, Marchais SJ, Safar ME, London GM. **Impact of aortic stiffness on survival in end-stage renal disease.** *Circulation* 1999b. **99**(18):2434–9. ISSN 1524-4539.

Bland JM, Altman D. **Statistical Methods for Assessing Agreement Between Two Methods of Clinical Measurement**. *Lancet* 1986. **327**(8476):307–310. ISSN 01406736.

Borlotti A, Khir A. **Wave speed and intensity in the canine aorta: Analysis with and without the Windkessel-wave system**. *Proc Annu Int Conf IEEE Eng Med Biol Soc EMBS* 2011:219–222. ISSN 1557170X.

Bramwell JC, Hill AV. **The Velocity of the Pulse Wave in Man**. *Proc R Soc B Biol Sci* 1922. **93**(652):298–306. ISSN 0962-8452.

Buhre W, Weyland A, Kazmaier S, Hanekop GG, Baryalei MM, Sydow M, Sonntag H. **Comparison of cardiac output assessed by pulse-contour analysis and thermodilution in patients undergoing minimally invasive direct coronary artery bypass grafting**. *J Cardiothorac Vasc Anesth* 1999. **13**(4):437–440. ISSN 10530770.

Bulpitt CJ, Cameron JD, Rajkumar C, Armstrong S, Connor M, Joshi J, Lyons D, Moioli O, Nihoyannopoulos P. **The effect of age on vascular compliance in man: which are the appropriate measures?.** *J Hum Hypertens* 1999. **13**(11):753–758. ISSN 0950-9240.

Cameron JD, Bulpitt CJ, Pinto ES, Rajkumar C. **The aging of elastic and muscular arteries: A comparison of diabetic and nondiabetic subjects**. *Diabetes Care* 2003. **26**(7):2133–2138. ISSN 01495992.

Cecconi M, De Backer D, Antonelli M, Beale R, Bakker J, Hofer C, Jaeschke R, Mebazaa A, Pinsky MR, Teboul JL, Vincent JL, Rhodes A. **Consensus on circulatory shock and hemodynamic monitoring. Task force of the European Society of Intensive Care Medicine**. *Intensive Care Med* 2014. **40**(12):1795–1815. ISSN 14321238.

Cecconi M, Hofer C, Teboul JL, Pettila V, Wilkman E, Molnar Z, Della Rocca G, Aldecoa C, Artigas A, Jog S, Sander M, Spies C, Lefrant JY, De Backer D, on behalf of the FENICE In-

vestigators. **Fluid challenges in intensive care: the FENICE study: A global inception cohort study**. *Intensive Care Med* 2015. **41**(9):1529–1537. ISSN 14321238.

Chaney JC, Derdak S. **Minimally invasive hemodynamic monitoring for the intensivist: current and emerging technology.** *Crit Care Med* 2002. **30**(10):2338–2345. ISSN 0090-3493.

Chase JG, Moeller K, Shaw GM, Schranz C, Chiew YS, Desaive T. **When the value of gold is zero.** *BMC Res Notes* 2014. 7(1):404. ISSN 1756-0500.

Chase JG, Preiser JC, Dickson JL, Pironet A, Chiew YS, Pretty CG, Shaw GM, Benyo B, Moeller K, Safaei S, Tawhai M, Hunter P, Desaive T. **Next-generation, personalised, model-based critical care medicine: A state-of-the art review of in silico virtual patient models, methods, and cohorts, and how to validation them**. *Biomed Eng Online* 2018. **17**(1):1–29. ISSN 1475925X.

Chua CP, Heneghan C. **Pulse transit time-derived respiratory parameters and their variability across sleep stages**. *Conf Proc Eng Med Biol Soc* 2005:6153–6. ISSN 1557-170X.

Connors AF, Speroff T, Dawson NV, Thomas C, Jr FEH, Wagner D, Desbiens N, Goldman L, Wu AW, Califf RM, Fulkerson WJ, Vidaillet H, Broste S, Bellamy P, Lynn J, Knaus WA. **The Effectiveness of Right Heart Catheterization in the Initial Care of Critically Ill Patients**. *J Am Med Assoc* 1996. **276**(11):889–897. ISSN 0002-9955.

Cousins TR, O'Donnell JM. Arterial cannulation: A critical review. 2004.

Critchley LA, Critchley JA. **A meta-analysis of studies using bias and precision statistics to compare cardiac output measurement techniques**. *J Clin Monit Comput* 1999. **15**(2):85–91. ISSN 13871307.

Cunnion RE, Schaer GL, Parker MM, Natanson C, Parrillo JE. **The coronary circulation in human septic shock.** *Circulation* 1986. **73**(4):637–644. ISSN 0009-7322.

Dalen JE, Bone RC. **Is it time to pull the pulmonary artery catheter?** *Jama* 1996. **276**(11):916–918. ISSN 00987484.

Dark PM, Singer M. **The validity of trans-esophageal Doppler ultrasonography as a measure of cardiac output in critically ill adults**. *Intensive Care Med* 2004. **30**(11):2060–2066. ISSN 03424642.

Davidson S, Pretty C, Kamoi S, Desaive T, Chase JG. **Beat-by-Beat Estimation of the Left Ventricular Pressure–Volume Loop Under Clinical Conditions**. *Ann Biomed Eng* 2018. **46**(1):171–185. ISSN 15739686.

Dawber TR, Thomas HE, McNamara PM. **Characteristics of the Dicrotic Notch of the Arterial Pulse Wave in Coronary Heart Disease**. *Angiology* 1973. **24**(4):244–255. ISSN 0003-3197.

de Wilde RBP, van den Berg PCM, Jansen JRC. **Review of the PiCCO device; our experience in the ICU**. *Netherlands J Crit Care* 2008. **12**(2):60–64. ISSN 15693511.

Dean DA, Jia CX, Cabreriza SE, D'Alessandro DA, Dickstein ML, Sardo MJ, Chalik N, Spotnitz HM. **Validation study of a new transit time ultrasonic flow probe for continuous great vessel measurements.** *Asaio* 1996. **42**(5):M671–6. ISSN 1058-2916.

Dickstein K. **Diagnosis and assessment of the heart failure patient: The cornerstone of effective management**. *Eur J Heart Fail* 2005. **7**(3 SPEC. ISS.):303–308. ISSN 13889842.

Dogui A, Kachenoura N, Frouin F, Lefort M, De Cesare A, Mousseaux E, Herment A. **Consistency of aortic distensibility and pulse wave velocity estimates with respect to the Bramwell-Hill theoretical model: a cardiovascular magnetic resonance study**. *J Cardiovasc Magn Reson* 2011. **13**(1):11. ISSN 1532-429X.

Ellender TJ, Skinner JC. **The Use of Vasopressors and Inotropes in the Emergency Medical Treatment of Shock**. *Emerg Med Clin North Am* 2008. **26**(3):759–786. ISSN 07338627.

Eren H. **Accuracy in real time ultrasonic applications and transit-time flow meters**.

IMTC/98 Conf Proceedings IEEE Instrum Meas Technol Conf Where Instrum is Going (Cat No98CH36222) 1998. **1**:568–572. ISSN 1091-5281.

Evans DC, Doraiswamy VA, Prosciak MP, Silviera M, Seamon MJ, Rodriguez Funes V, Cipolla J, Wang CF, Kavuturu S, Torigian DA, Cook CH, Lindsey DE, Steinberg SM, Stawicki SP. **Complications associated with pulmonary artery catheters: A comprehensive clinical review**. *Scand J Surg* 2009. **98**(4):199–208. ISSN 14574969.

Frank O. **The basic shape of the arterial pulse. First treatise: mathematical analysis. 1899.** *J Mol Cell Cardiol* 1889. **22**(3):255–77. ISSN 00222828.

Fung P, Dumont G, Ries C, Mott C, Ansermino M. **Continuous noninvasive blood pressure measurement by pulse transit time**. *26th Annu Int Conf IEEE Eng Med Biol Soc* 2004. **3**(4):738–741. ISSN 1557-170X.

Gao M, Rose WC, Fetics B, Kass DA, Chen CH, Mukkamala R. **A Simple Adaptive Transfer Function for Deriving the Central Blood Pressure Waveform from a Radial Blood Pressure Waveform**. *Sci Rep* 2016. **6**(September):1–9. ISSN 20452322.

Geddes LA, Voelz MH, Babbs CF, Bourland JD, Tacker WA. **Pulse transit time as an indicator of arterial blood pressure**. *Psychophysiology* 1981. **18**(1):71–74. ISSN 00485772.

Gemignani V, Bianchini E, Faita F, Giannoni M, Pasanisi E, Picano E, Bombardini T. Assessment of cardiologic systole and diastole duration in exercise stress tests with a transcutaneous accelerometer sensor. In *2008 Comput. Cardiol.*, volume 35. IEEE. ISBN 978-1-4244-3706-1. ISSN 02766574, 153–156.

Gödje O, Friedl R, Hannekum a. **Accuracy of beat-to-beat cardiac output monitoring by pulse contour analysis in hemodynamical unstable patients.** *Med Sci Monit* 2001. 7(6):1344–50. ISSN 1234-1010.

Godje O, Peyerl M, Seebauer T, Dewald O, Reichart B. **Reproducibility of double indicator dilution measurements of intrathoracic blood volume compartments, extravascular lung water, and liver function**. *Chest* 1998. **113**(4):1070–1077. ISSN 00123692.

Goedje O, Hoeke K, Lichtwarck-Aschoff M, Faltchauser A, Lamm P, Reichart B. **Continuous cardiac output by femoral arterial thermodilution calibrated pulse contour analysis: Comparison with pulmonary arterial thermodilution**. *Crit Care Med* 1999. **27**(11):2407–2412. ISSN 0090-3493.

Grensemann J. **Cardiac Output Monitoring by Pulse Contour Analysis, the Technical Basics of Less-Invasive Techniques**. *Front Med* 2018. **5**(March):1–6.

Gust R, Gottschalk A, Bauer H, Böttiger BW, Böhrer H, Martin E. **Cardiac output measurement by transpulmonary versus conventional thermodilution technique in intensive care patients after coronary artery bypass grafting**. *J Cardiothorac Vasc Anesth* 1998. **12**(5):519–522. ISSN 10530770.

Guyton AC, Hall JE. *Textbook of Medical Physiology*. January. Elsevier Saunders, Philadelphia, 11 edition, 2011. ISBN 9781455770052.

Habran S, Desaive T, Morimont P, Lambermont B, Dauby P. **Mathematical modeling of extracorporeal CO2 removal therapy: A validation carried out on ten pigs**. *Med Biol Eng Comput* 2018. **56**(3):421–434. ISSN 17410444.

Hadian M, Kim HK, Severyn DA, Pinsky MR. **Cross-comparison of cardiac output trending accuracy of LiDCO, PiCCO, FloTrac and pulmonary artery catheters**. *Crit Care* 2010. **14**(6). ISSN 13648535.

Hannon JP, Bossone CA, Wade CE. **Normal physiological values for conscious pigs used in biomedical research.** *Lab Anim Sci* 1990. **40**(3):293–298. ISSN 0023-6764.

Hanya S. **Validity of the Water Hammer Formula for Determining Regional Aortic Pulse Wave Velocity: Comparison of One-Point and Two-Point (Foot-to-Foot) Measurements Using a Multisensor Catheter in Human**. *Ann Vasc Dis* 2013. **6**(2):150–158. ISSN 1881-641X.

Harris WS, Schoenfeld CD, Weissler AM. **Effects of adrenergic receptor activation and**

blockade on the systolic preejection period, heart rate, and arterial pressure in man. *J Clin Invest* 1967. **46**(11):1704–1714. ISSN 00219738.

Hermeling E, Reesink KD, Kornmann LM, Reneman RS, Hoeks AP. **The dicrotic notch as alternative time-reference point to measure local pulse wave velocity in the carotid artery by means of ultrasonography**. *J Hypertens* 2009. **27**(10):2028–2035. ISSN 0263-6352.

Hoeksel S, Jansen JRC, Blom JA, Schreuder JJ. **Detection of Dicrotic Notch in Arterial Pressure Signals**. *J Clin Monit* 1997. **13**(5):309–316. ISSN 1573-2614.

Hughes AD, Parker KH. **Forward and backward waves in the arterial system: Impedance or wave intensity analysis?** *Med Biol Eng Comput* 2009. **47**(2):207–210. ISSN 01400118.

Ifeachor EC, Jervis BW. *Digital Signal Processing: A Practical Approach*. Pearson Education (US), New Jersey, United States, 2nd edition, 2001. ISBN 9780201596199.

Jansen JRC, Wesseling KH, Settels JJ, Schreuder JJ. **Continuous cardiac output monitoring by pulse contour during cardiac surgery**. *Eur Heart J* 1990. **11**(suppl I):26–32. ISSN 0195-668X.

Johnson NL, Kotz S, Balakrishnan N. Beta Distributions. In *Contin. univariate Distrib.*, chapter 21. Wiley, New York, 2nd edition. ISBN 978-0-471-58494-0, 1994.

Joseph J, Nabeel PM, Shah MI, Sivaprakasam M. Arterial compliance probe for calibration free pulse pressure measurement. 2016.

Kamoi S. Model-Based Hemodynamic Monitoring in Critical Care for Improved Diagnosis and Treatment. Ph.D. thesis, University of Canterbury, 2016.

Kamoi S, Pretty C, Balmer J, Davidson S, Pironet A, Desaive T, Shaw GM, Chase JG. **Improved pressure contour analysis for estimating cardiac stroke volume using pulse wave velocity measurement**. *Biomed Eng Online* 2017. **16**(1):51. ISSN 1475-925X.

Kamoi S, Pretty C, Chiew YS, Davidson S, Pironet A, Desaive T, Shaw GM, Chase JG. **Rela-**

tionship between stroke volume and pulse wave velocity. *IFAC-PapersOnLine* 2015. **28**(20):285–290. ISSN 24058963.

Kamoi S, Pretty C, Docherty P, Squire D, Revie J, Chiew YS, Desaive T, Shaw GM, Chase JG. **Continuous Stroke Volume Estimation from Aortic Pressure Using Zero Dimensional Cardiovascular Model: Proof of Concept Study from Porcine Experiments**. *PLoS One* 2014. **9**(7):e102476. ISSN 1932-6203.

Kasza J, Moran JL, Solomon PJ. **Evaluating the performance of Australian and New Zealand intensive care units in 2009 and 2010**. *Stat Med* 2013. **32**(21):3720–3736. ISSN 02776715.

Katz ES, Lutz J, Black C, Marcus CL. **Pulse transit time as a measure of arousal and respiratory effort in children with sleep-disordered breathing**. *Pediatr Res* 2003. **53**(4):580–588. ISSN 00313998.

Khir AW, Parker KH. **Wave intensity in the ascending aorta: Effects of arterial occlusion**. *J Biomech* 2005. **38**(4):647–655. ISSN 00219290.

Kim JS, Chee YJ, Park JW, Choi JW, Park KS. **A new approach for non-intrusive monitoring of blood pressure on a toilet seat**. *Physiol Meas* 2006. **27**(2):203–211. ISSN 09673334.

Knaapen P, Germans T, Knuuti J, Paulus WJ, Dijkmans PA, Allaart CP, Lammertsma AA, Visser FC. **Myocardial energetics and efficiency: Current status of the noninvasive approach**. *Circulation* 2007. **115**(7):918–927. ISSN 00097322.

Langewouters GJ, Wesseling KH, Goedhard WJA. **The static elastic properties of 45 human thoracic and 20 abdominal aortas in vitro and the parameters of a new model**. *J Biomech* 1984. **17**(6):425–435. ISSN 0021-9290.

Laurent S, Boutouyrie P, Asmar R, Gautier I, Laloux B, Guize L, Ducimetiere P, Benetos A. **Aortic Stiffness Is an Independent Predictor of All-Cause and Cardiovascular**

Mortality in Hypertensive Patients. *Hypertension* 2001. **37**(5):1236–1241. ISSN 0194-911X.

Laurent S, Cockcroft J, Van Bortel L, Boutouyrie P, Giannattasio C, Hayoz D, Pannier B, Vlachopoulos C, Wilkinson I, Struijker-Boudier H. **Expert consensus document on arterial stiffness: Methodological issues and clinical applications**. *Eur Heart J* 2006. **27**(21):2588–2605. ISSN 0195668X.

Lazaro J, Bailon R, Laguna P, Mazoras V, Rapalis A, Gil E. **Difference in Pulse Arrival Time at Forehead and at Finger as a Surrogate of Pulse Transit Time**. *Comput Cardiol* 2016. **43**:269–272. ISSN 2325887X.

Lewis T. **The factors influencing the prominence of the dicrotic wave**. *J Physiol* 1906. **34**(6):414–429. ISSN 1469-7793.

Lighthill MJ. 2. One-Dimensional Waves in Fluids 2.1. In *Cambridge Univ. Press.*, chapter 2. Cambridge University, Cambridge, 1978. 90–99.

Liu J, Yan BPY, Dai WX, Ding XR, Zhang YT, Zhao N. **Multi-wavelength photoplethysmography method for skin arterial pulse extraction**. *Biomed Opt Express* 2016. 7(10):4313. ISSN 2156-7085.

London GM, Pannier B. **Arterial functions: How to interpret the complex physiology**. *Nephrol Dial Transplant* 2010. **25**(12):3815–3823. ISSN 09310509.

Loukogeorgakis S, Dawson R, Phillips N, Martyn CN, Greenwald SE. **Validation of a device to measure arterial pulse wave velocity by a photoplethysmographic method**. *Physiol Meas* 2002. **23**(3):309. ISSN 09673334.

Luecke T, Pelosi P. **Clinical review: Positive end-expiratory pressure and cardiac output**. *Crit Care* 2005. **9**(6):607–621. ISSN 1364-8535.

Marik PE. **Hemodynamic parameters to guide fluid therapy**. *Transfus Altern Transfus Med* 2010. **11**(3):102–112. ISSN 12959022.

Marik PE. **Noninvasive cardiac output monitors: A state-of the-art review**. *J Cardiothorac Vasc Anesth* 2013. **27**(1):121–134. ISSN 10530770.

Matthieu B, Karine NG, Vincent C, Alain V, François CJ, Philippe R, François S. **Cardiac Output Measurement in Patients Undergoing Liver Transplantation: Pulmonary Artery Catheter Versus Uncalibrated Arterial Pressure Waveform Analysis**. *Anesth Analg* 2008. **106**(5):1480–1486. ISSN 0003-2999.

McKay RG, Miller MJ, Ferguson JJ, Momomura SI, Sahagian P, Grossman W, Pasternak RC. **Assessment of left ventricular end-systolic pressure-volume relations with an impedance catheter and transient inferior vena cava occlusion: Use of this system in the evaluation of the cardiotonic effects of dobutamine, milrinone, posicor and epinephrine**. *J Am Coll Cardiol* 1986. **8**(5):1152–1160. ISSN 07351097.

Merx MW, Weber C. **Sepsis and the heart**. *Br J Anaesth* 2010. **104**(1):3–11. ISSN 00070912.

Michard F, Teboul JL. **Predicting Fluid Responsiveness in ICU Patients**. *Chest* 2002. **121**(6):2000–2008. ISSN 00123692.

Millasseau SC, Stewart AD, Patel SJ, Redwood SR, Chowienczyk PJ. **Evaluation of carotid-femoral pulse wave velocity: Influence of timing algorithm and heart rate**. *Hypertension* 2005. **45**(2):222–226. ISSN 0194911X.

Ministry of Health. *Mortality and Demographic Data 2011*. New Zealand Ministry of Health, 2013. ISBN 9780478402599.

Moise SF, Sinclair CJ, Scott DHT. **Pulmonary artery blood temperature and the measurement of cardiac output by thermodilution**. *Anaesthesia* 2002. **57**(6):562–566. ISSN 00032409.

Montenij LJ, de Waal EE, Buhre WF. **Arterial waveform analysis in anesthesia and critical care**. *Curr Opin Anaesthesiol* 2011. **24**(6):651–656. ISSN 0952-7907.

Motulsky HJ. *Intuitive biostatistics: a nonmathematical guide to statistical thinking*. Oxford University Press, New York, 3rd edition, 2010. ISBN 0199730067.

Mozaffarian D, Benjamin EJ, Go AS, Arnett DK, Blaha MJ, Cushman M, De Ferranti S, Després JP, Fullerton HJ, Howard VJ, Huffman MD, Judd SE, Kissela BM, Lackland DT, Lichtman JH, Lisabeth LD, Liu S, Mackey RH, Matchar DB, McGuire DK, Mohler ER, Moy CS, Muntner P, Mussolino ME, Nasir K, Neumar RW, Nichol G, Palaniappan L, Pandey DK, Reeves MJ, Rodriguez CJ, Sorlie PD, Stein J, Towfighi A, Turan TN, Virani SS, Willey JZ, Woo D, Yeh RW, Turner MB. **Heart disease and stroke statistics-2015 update : A report from the American Heart Association**. *Circulation* 2015. **131**(4):e29–e39. ISSN 15244539.

Muehlsteff J, Aubert XL, Schuett M. **Cuffless estimation of systolic blood pressure for short effort bicycle tests: The prominent role of the pre-ejection period**. *Annu Int Conf IEEE Eng Med Biol - Proc* 2006:5088–5092. ISSN 05891019.

Murgo JP, Westerhof N, Giolma JP, Altobelli SA. **Aortic input impedance in normal man: relationship to pressure wave forms**. *Circulation* 1980. **62**(1):105–116. ISSN 0009-7322.

Mynard JP, Penny DJ, Davidson MR, Smolich JJ. **The reservoir-wave paradigm introduces error into arterial wave analysis: A computer modelling and in-vivo study**. *J Hypertens* 2012. **30**(4):734–743. ISSN 02636352.

Mynard JP, Smolich JJ. **The case against the reservoir-wave approach**. *Int J Cardiol* 2014a. **176**(3):1009–1012. ISSN 18741754.

Mynard JP, Smolich JJ. **Wave potential and the one-dimensional windkessel as a wave-based paradigm of diastolic arterial hemodynamics**. *Am J Physiol Circ Physiol* 2014b. **307**(3):H307–H318. ISSN 0363-6135.

Mynard JP, Smolich JJ. **Wave potential: A unified model of arterial waves, reservoir phenomena and their interaction**. *Artery Res* 2017. **18**:55–63. ISSN 18764401.

Mynard JP, Smolich JJ, Avolio A. **The ebbing tide of the reservoir-wave model**. *J Hypertens* 2015. **33**(3):461–464. ISSN 14735598.

Newlin DB, Levenson RW. **Pre-ejection Period: Measuring Beta-adrenergic Influences Upon the Heart**. *Psychophysiology* 1979. **16**(6):546–552. ISSN 14698986.

Nguyen HB, Rivers EP, Abrahamian FM, Moran GJ, Abraham E, Trzeciak S, Huang DT, Osborn T, Stevens D, Talan DA. **Severe Sepsis and Septic Shock: Review of the Literature and Emergency Department Management Guidelines**. *Ann Emerg Med* 2006. **48**(1):54.e1. ISSN 01960644.

Nichols WW. **Clinical measurement of arterial stiffness obtained from noninvasive pressure waveforms**. *Am J Hypertens* 2005. **18**(1 SUPPL.):3–10. ISSN 08957061.

Nichols WW, O'Rourke MF, Vlachopoulos C. Aging. In *McDonald's blood flow Arter. Theor. Exp. Clin. Princ.*, chapter 19. CRC Press, 6 edition. ISBN 9780340985014, 2011. 412–446.

Nishikawa T, Dohi S. **Errors in the measurement of cardiac output by thermodilution**. *Can J Anaesth* 1993. **40**(2):142–153. ISSN 0832610X.

Nye ER. **The Effect of Blood Pressure Alteration on the Pulse Wave Velocity**. *Br Heart J* 1964. **26**(2):261–265. ISSN 0007-0769.

Obata Y, Mizogami M, Nyhan D, Berkowitz DE, Steppan J, Barodka V. **Pilot study: Estimation of stroke volume and cardiac output from pulse wave velocity**. *PLoS One* 2017. **12**(1):1–12. ISSN 19326203.

Oppenheim MJ, Sittig DF. **An Innovative Dicrotic Notch Detection Algorithm Which Combines Rule-Based Logic with Digital Signal Processing Techniques**. *Comput Biomed Res* 1995. **28**(2):154–170. ISSN 0010-4809.

Paeme S. Mathematical Modelling of the Mitral Valve - THESIS. 2013.

Pandian NG, Roelandt J, Nanda NC, Sugeng L, Cao QL, Azevedo J, Schwartz SL, Vannan Ma, Ludomirski A, Marx G. **Dynamic three-dimensional echocardiography: methods and clinical potential.** *Echocardiography* 1994. **11**(3):237–259. ISSN 0742-2822.

Papageorgiou GL, Jones NB. **Wave reflection and hydraulic impedance in the healthy**

arterial system: a controversial subject. *Med Biol Eng Comput* 1988. **26**(3):237–242. ISSN 01400118.

Payne RA, Symeonides CN, Webb DJ, Maxwell SRJ. **Pulse transit time measured from the ECG: an unreliable marker of beat-to-beat blood pressure**. *J Appl Physiol* 2006. **100**(1):136–141. ISSN 8750-7587.

Pearl MD, PhD RG, Rosenthal MD MH, Nielson RN L, Ashton CPT JPA, Brown PhD BW. **Effect of Injectate Volume and Temperature on Thermodilution Cardiac Output Determination**. *Anesthesiol J Am Soc Anesthesiol* 1986. **64**(6):798–801. ISSN 0003-3022.

Pereira T, Correia C, Cardoso J. **Novel methods for pulse wave velocity measurement**. *J Med Biol Eng* 2015. **35**(5):555–565. ISSN 21994757.

Peyton PJ, Chong SW. **Minimally Invasive Measurement of Cardiac Output during Surgery and Critical Care: A Meta-analysis of Accuracy and Precision**. *Anesthesiol J Am Soc Anesthesiol* 2010. **113**(5):1220–1235. ISSN 0003-3022.

Philips Electronics North America Corporation. Hemodynamic Monitoring using the PiCCO Method. 2002.

Pironet A, Dauby PC, Chase JG, Docherty PD, Revie JA, Desaive T. **Structural identifiability analysis of a cardiovascular system model**. *Med Eng Phys* 2016. **38**(5):433–441. ISSN 18734030.

Pironet A, Desaive T, Kosta S, Lucas A, Paeme S, Collet A, Pretty CG, Kolh P, Dauby PC. **A multi-scale cardiovascular system model can account for the load-dependence of the end-systolic pressure-volume relationship.** *Biomed Eng Online* 2013. **12**(1):8. ISSN 1475-925X.

Pitson D, Chhina N, Knijn S, Stradling J. **Changes in pulse transit time and pulse rate as markers of arousal from sleep in normal subjects**. *Clin Sci* 1994. **87**:269 273. ISSN 0143-5221.

Porterfield JE, Kottam ATG, Raghavan K, Escobedo D, Jenkins JT, Larson ER, Treviño RJ, Val-

vano JW, Pearce Ja, Feldman MD. **Dynamic correction for parallel conductance, GP, and gain factor, alpha, in invasive murine left ventricular volume measurements.** *J Appl Physiol* 2009. **107**(6):1693–1703. ISSN 8750-7587.

Rajzer MW, Wojciechowska W, Klocek M, Palka I, Brzozowska-Kiszka M, Kawecka-Jaszcz K. **Comparison of aortic pulse wave velocity measured by three techniques: Complior, SphygmoCor and Arteriograph**. *J Hypertens* 2008. **26**(10):2001–2007. ISSN 02636352.

Reuter DA, Felbinger TW, Kilger E, Schmidt C, Lamm P, Goetz AE. **Optimizing fluid therapy in mechanically ventilated patients after cardiac surgery by on-line monitoring of left ventricular stroke volume variations. Comparison with aortic systolic pressure variations**. *Br J Anaesth* 2002. **88**(1):124–126. ISSN 00070912.

Reuter DA, Kirchner A, Felbinger TW, Weis FC, Kilger E, Lamm P, Goetz AE. **Usefulness of left ventricular stroke volume variation to assess fluid responsiveness in patients with reduced cardiac function**. *Crit Care Med* 2003. **31**(5):1399–1404. ISSN 0090-3493.

Rödig G, Prasser C, Keyl C, Liebold A, Hobbhahn J. **Continuous cardiac output measurement: pulse contour analysis vs thermodilution technique in cardiac surgical patients.** *Br J Anaesth* 1999. **82**(4):525–530. ISSN 0007-0912, 1471-6771.

Ruffolo RR. **Review: The Pharmacology of Dobutamine**. *Am J Med Sci* 1987. **294**(4):244–248. ISSN 00029629.

Sagawa K. **The ventricular pressure-volume diagram revisited.** *Circ Res* 1978. **43**(5):677–687.

Sakka SG, Reinhart K, Wegscheider K, Meier-Hellmann A. **Is the placement of a pulmonary artery catheter still justified solely for the measurement of cardiac output?** *J Cardiothorac Vasc Anesth* 2000. **14**(2):119–24. ISSN 1053-0770.

Sato T, Shishido T, Kawada T, Miyano H, Miyashita H, Inagaki M, Sugimachi M, Sunagawa K. **ESPVR of in situ rat left ventricle shows contractility-dependent curvilinearity.** *Am J Physiol* 1998. **274**(5 Pt 2):H1429–34. ISSN 0002-9513.

Segal E, Katzenelson R, Berkenstadt H, Perel A. **Transpulmonary thermodilution cardiac output measurement using the axillary artery in critically ill patients**. *J Clin Anesth* 2002. **14**(3):210–213. ISSN 0952-8180.

Segers P, Swillens A, Vermeersch S. **Reservations on the reservoir**. *J Hypertens* 2012. **30**(4):676–678. ISSN 0263-6352.

Segers P, Taelman L, Degroote J, Bols J, Vierendeels J. **The aortic reservoir-wave as a paradigm for arterial haemodynamics: Insights from three-dimensional fluid-structure interaction simulations in a model of aortic coarctation**. *J Hypertens* 2015. **33**(3):554–563. ISSN 14735598.

Silverman AM, Wang VJ. **Shock: A Common Pathway For Life-Threatening Pediatric Illnesses And Injuries**. *Pediatr Emerg Med Pract* 2005. **2**(10).

Slagt C, Malagon I, Groeneveld ABJ. **Systematic review of uncalibrated arterial pressure waveform analysis to determine cardiac output and stroke volume variation**. *Br J Anaesth* 2014. **112**(4):626–637. ISSN 14716771.

Smith BW, Chase JG, Nokes RI, Shaw GM, Wake G. **Minimal haemodynamic system model including ventricular interaction and valve dynamics**. *Med Eng Phys* 2004. **26**(2):131–139. ISSN 13504533.

Smith BW, Chase JG, Shaw GM, Nokes RI. **Experimentally verified minimal cardiovascular system model for rapid diagnostic assistance**. *Control Eng Pract* 2005. **13**(9):1183–1193. ISSN 09670661.

Sorensen MB, Bille-Brahe NE, Engell HC. **Cardiac output measurement by thermal dilution: reproducibility and comparison with the dye-dilution technique.** *Ann Surg* 1976. **183**(1):67–72. ISSN 0003-4932.

Stergiopulos N, Young DF, Rogge TR. **Computer simulation of arterial flow with applications to arterial and aortic stenoses**. *J Biomech* 1992. **25**(12):1477–1488. ISSN 00219290.

Stevenson D, Hann C, Chase G, Revie J, Shaw G, Desaive T, Lambermont B, Ghuysen A, Kolh

P, Heldmann S. Estimating the driver function of a cardiovascular system model. In *UKACC Int. Conf. Control 2010*, volume 2010. Institution of Engineering and Technology. ISBN 978-1-84600-038-6, 1008–1013.

Stevenson D, Revie J, Chase J, Hann CE, Shaw GM, Lambermont B, Ghuysen A, Kolh P, Desaive T. **Algorithmic processing of pressure waveforms to facilitate estimation of cardiac elastance**. *Biomed Eng Online* 2012a. **11**(1):28. ISSN 1475-925X.

Stevenson D, Revie J, Chase JG, Hann CE, Shaw GM, Lambermont B, Ghuysen A, Kolh P, Desaive T. **Beat-to-beat estimation of the continuous left and right cardiac elastance from metrics commonly available in clinical settings**. *Biomed Eng Online* 2012b. **11**(1):73. ISSN 1475-925X.

Takazawa K, Tanaka N, Takeda K, Kurosu F, Ibukiyama C. Underestimation of vasodilator effects of nitroglycerin by upper limb blood pressure. In *Hypertension*. ISSN 0194911X.

Talley RC, Meyer JF, McNay JL. **Evaluation of the pre-ejection period as an estimate of myocardial contractility in dogs**. *Am J Cardiol* 1971. **27**(4):384–391. ISSN 00029149.

Tibby SM. **Monitoring cardiac function in intensive care**. *Arch Dis Child* 2003. **88**(1):46–52. ISSN 00039888.

Tibby SM, Hatherill M, Marsh MJ, Morrison G, Anderson D, Murdoch IA. **Clinical validation of cardiac output measurements using femoral artery thermodilution with direct Fick in ventilated children and infants**. *Intensive Care Med* 1997. **23**(9):987–991. ISSN 03424642.

Townsend RR, Wilkinson IB, Schiffrin EL, Avolio AP, Chirinos JA, Cockcroft JR, Heffernan KS, Lakatta EG, McEniery CM, Mitchell GF, Najjar SS, Nichols WW, Urbina EM, Weber T. *Recommendations for Improving and Standardizing Vascular Research on Arterial Stiffness: A Scientific Statement from the American Heart Association*, volume 66. 2015. ISBN 0000000000000.

Transonic Sys Inc. Pressure-Volume Technology Theory of Operation. 2013.

Tyberg JV, Bouwmeester JC, Parker KH, Shrive NG, Wang JJ. **The case for the reservoir-wave approach**. *Int J Cardiol* 2014. **172**(2):299–306. ISSN 01675273.

Vieillard-Baron A, Cecconi M. **Understanding cardiac failure in sepsis**. *Intensive Care Med* 2014. **40**(10):1560–1563. ISSN 14321238.

Wallace aG, Mitchell JH, Skinner NS, Sarnoff SJ. **Duration of the Phases of Left Ventricular Systole**. *Circ Res* 1963. **12**:611–619. ISSN 0009-7330.

Wang JJ, O'Brien AB, Shrive NG, Parker KH, Tyberg JV. **Time-domain representation of ventricular-arterial coupling as a windkessel and wave system**. *Am J Physiol - Hear Circ Physiol* 2003. **284**(4):H1358–H1368. ISSN 0363-6135.

Wang JJ, Parker KH. **Wave propagation in a model of the arterial circulation**. *J Biomech* 2004. **37**(4):457–470. ISSN 00219290.

Watson CA, Wilkinson MB. **Monitoring central venous pressure, arterial pressure and pulmonary wedge pressure**. *Anaesth Intensive Care Med* 2012. **13**(3):116–120. ISSN 18787584.

Wei CL, Valvano JW, Feldman MD, Pearce JA. **Nonlinear conductance-volume relationship for murine conductance catheter measurement system**. *IEEE Trans Biomed Eng* 2005. **52**(10):1654–1661. ISSN 00189294.

Weissler AM, Harris WS, Schoenfeld CD. **Systolic Time Intervals in Heart Failure in Man**. *Circulation* 1968. **37**(2):149–159. ISSN 0009-7322.

Wesseling KH. **A simple device for the continuous measurement of cardiac output. Its model basis and experimental varification**. *Adv Cardiovasc Phys* 1983. **5**:16–52.

Wesseling KH, Jansen JR, Settels JJ, Schreuder JJ. **Computation of aortic flow from pressure in humans using a nonlinear, three-element model**. *J Appl Physiol* 1993. **74**(5):2566–2573. ISSN 8750-7587.

Westerhof N, Bosman F, De Vries CJ, Noordergraaf A. **Analog studies of the human systemic arterial tree.** *J Biomech* 1969. **2**(2):121–43. ISSN 0021-9290.

Westerhof N, Elzinga G, Sipkema P. **An artificial arterial system for pumping hearts.** *J Appl Physiol* 1971. **31**(5):776–781. ISSN 8750-7587.

Westerhof N, Lankhaar JW, Westerhof BE. **The arterial windkessel**. *Med Biol Eng Comput* 2009. **47**(2):131–141. ISSN 01400118.

Westerhof N, Stergiopulos N, Noble MI. *Snapshots of Hemodynamics*. Springer, Boston, MA, 2010a. ISBN 978-1-4419-6362-8.

Westerhof N, Stergiopulos N, Noble MIM. Cardiac Muscle Mechanics BT - Snapshots of Hemodynamics: An Aid for Clinical Research and Graduate Education. Springer US, Boston, MA. ISBN 978-1-4419-6363-5, 2010b. 69–76.

Westerhof N, Stergiopulos N, Noble MIM. Transfer of Pressure - Snapshots of Hemodynamics: An Aid for Clinical Research and Graduate Education. Springer US, Boston, MA. ISBN 978-1-4419-6363-5, 2010c. 189–195.

Westerhof N, Stergiopulos N, Noble MIM. Wave Travel and Reflection BT - Snapshots of Hemodynamics: An Aid for Clinical Research and Graduate Education. Springer US, Boston, MA. ISBN 978-1-4419-6363-5, 2010d. 147–153.

Westerhof N, Stergiopulos N, Noble MIM. Waveform Analysis BT - Snapshots of Hemodynamics: An Aid for Clinical Research and Graduate Education. Springer US, Boston, MA. ISBN 978-1-4419-6363-5, 2010e. 155–160.

Westerhof N, Westerhof BE. **The reservoir wave paradigm discussion**. *J Hypertens* 2015. **33**(3):458–460. ISSN 14735598.

Westerhof N, Westerhof BE. **Waves and Windkessels reviewed**. *Artery Res* 2017. **18**(2017):102–111. ISSN 18764401.

Wetterslev M, Møller-Sørensen H, Johansen RR, Perner A. **Systematic review of cardiac output measurements by echocardiography vs. thermodilution: the techniques are not interchangeable**. *Intensive Care Med* 2016. **42**(8):1223–1233. ISSN 14321238.

Yamashina A, Tomiyama H, Takeda K, Tsuda H, Arai T, Hirose K, Koji Y, Hori S, Yamamoto

Y. **Validity, reproducibility, and clinical significance of noninvasive brachial-ankle pulse wave velocity measurement.** *Hypertens Res* 2002. **25**(3):359–364. ISSN 09169636.

Yang XX, Critchley LA, Rowlands DK, Fang Z, Huang L. **Systematic error of cardiac output measured by bolus thermodilution with a pulmonary artery catheter compared with that measured by an aortic flow probe in a pig model**. *J Cardiothorac Vasc Anesth* 2013. **27**(6):1133–1139. ISSN 10530770.

Yelderman ML. **Continuous measurement of cardiac output with the use of stochastic system identification techniques**. *J Clin Monit* 1990. **6**:322–332.

Young JD. **The heart and circulation in severe sepsis**. *Br J Anaesth* 2004. **93**(1):114–120. ISSN 00070912.

Zhang G, Gao M, Xu D, Olivier NB, Mukkamala R. **Pulse arrival time is not an adequate surrogate for pulse transit time as a marker of blood pressure**. *J Appl Physiol* 2011. **111**(6):1681–1686. ISSN 8750-7587.

Zierler KL. **Theoretical Basis of Indicator-Dilution Methods For Measuring Flow and Volume**. *Circ Res* 1962. **10**(3):393–407. ISSN 0009-7330.